Title
Seismic and infrasonic source processes in volcanic fluid systems

Author
Matoza, Robin S.

Publication Date
2009

UNIVERSITY OF CALIFORNIA, SAN DIEGO

Seismic and infrasonic source processes in volcanic fluid systems

A dissertation submitted in partial satisfaction of the
requirements for the degree Doctor of Philosophy
in
Earth Sciences

by

Robin S. Matoza

Committee in charge:

Michael A.H. Hedlin, Chair
Bernard A. Chouet
Yuri Fialko
Milton A. Garcés
Stefan G. Llewellyn Smith
Peter M. Shearer
Clinton D. Winant

2009

The dissertation of Robin S. Matoza is approved, and it is acceptable in quality and form for publication on microfilm and electronically:

Chair

University of California, San Diego

2009

In memory of my mother, Christine Ann Matoza (1955-2009), who would have been so proud to hold these pages.

"The subject of volcanic seismology is not only the most beautiful and spectacular, but also the most difficult to study of all the subjects seismologists have encountered on Earth." - *Keiiti Aki (1930-2005)*

TABLE OF CONTENTS

LIST OF FIGURES

LIST OF TABLES

ACKNOWLEDGEMENTS

Five years ago, I arrived at Scripps with some half-baked ideas about studying the infrasound produced by volcanoes. Without the help and guidance of many people, these ideas would not have matured into the work contained in this dissertation. The first person I would like to thank in this regard is Michael Hedlin, for being an excellent advisor. Shortly after my arrival at Scripps in September 2004, Mount St. Helens began erupting. As quickly as possible, Michael and a network of colleagues deployed the infrasound arrays and seismometers that provided the data for this dissertation. During 2004-2005 Michael and I started to process this data and we started to get very excited. Michael has always been fascinated by this research, supportive and selfless in my career development, and well organized and generous with his time. He has encouraged me to develop a sense of independence, yet has always been there to provide critical and careful insights that have allowed me to see the woods from within the trees. Furthermore, his enthusiasm for science is contagious.

I would also like to thank Milton Garces of the Infrasound Laboratory, University of Hawaii at Manoa (UHM). My first interaction with Milton was in writing the proposal to NSF that would eventually fund the full exploration of this dataset. This proposal had been a dream of Milton's for some time, and in this respect I am honored that he entrusted so much to me by channeling most of the funds into my PhD work. Milton quickly became a mentor and source of many ideas developed in this dissertation. I have learned a great deal from both Michael and Milton over the past years, both on how to conduct research, and the practicalities of getting science done in today's world.

Next, I would like to thank Bernard Chouet of the Volcano Hazards Team, US Geological Survey (USGS), Menlo Park. Bernard took a keen interest in this research from the very beginning, and he has contributed greatly to it. The clarity and depth of Bernard's knowledge is both impressive and inspiring, and this dissertation owes a huge debt to his willingness to openly share ideas with me, to the generosity with which he has given me his time, and to his virtuous patience. Bernard has helped to shape some of my more speculative ideas into sound quantitative models.

In addition, I would like to thank the rest of my committee: Peter Shearer, Yuri Fialko, Clinton Winant, and Stefan Llewellyn Smith, for their careful and extremely helpful reviews of this work. I also thank the many people comprising the Acoustic Surveillance for Hazardous Eruptions (ASHE) teams at the Geological Survey of Canada (GSC), UHM, the National Center for Physical Acoustics (NCPA) at the University of Mississippi, and UCSD for deploying, maintaining, and operating the arrays at Mount St. Helens and Tungurahua. In particular, I thank David McCormack, Phil Munro, Calvin Andrews, Isa Asudeh, John Ristau, Issam Al-Khoubbi, Jim Helferty, Kadircan Aktas, Mike Patton, Tim Cote, and Luc Saumure of the GSC, and Clint Coon and Eric Blum of UCSD for doing an excellent job on the Mount St. Helens array installations. I would also like to thank the Cascades Volcano Observatory (CVO), the Hawaiian Volcano Observatory (HVO), and the Instituto Geofisico, Escuela Politecnica Nacional (IG-EPN) for allowing us to deploy these arrays at Mount St. Helens, Kilauea, and Tunguraha, and for the open sharing of ideas and data. In particular, Seth Moran (CVO, USGS) has shared data and many ideas, and I appreciate greatly his welcoming my research and making it part of the story at Mount St. Helens.

I especially thank my numerous co-authors on the papers that have been reformatted to form the chapters of this dissertation. David Fee (UHM) has been an endless resource, first on array installations and data processing when he was working as a field system engineer, and then on modeling topics when he became a fellow graduate student. Luca D'Auria of Osservatorio Vesuviano (OV), Naples, Italy, provided his seismo-acoustic finite differences code ASTAROTH which is an integral component of chapter 3. Catherine De Groot-Hedlin provided her ray-tracing codes and wealth of expertise on acoustic propagation in a moving medium. Greg Waite (Michigan Technological University) provided his point source inversion results from LPs at Mount St. Helens and several other tools that helped to speed progress. Patricio Ramon of IG-EPN provided numerous photographs and infrared images of the eruptions of Tungurahua, and some measurements of crater and jet dimensions using satellite and field observations. Jack Seiner gave David Fee and me a one-week crash-course in jet aeroacoustics at NCPA in Oxford, MS. Chapter 4 is dedicated to Hank Bass of NCPA, who acted as mentor on the subjects of infrasound and jet noise, but sadly passed away before seeing the research come to fruition. There are countless others who have contributed in various ways to this work, and I try to acknowledge the remainders in the individual chapter acknowledgments.

Chapter 2, in part, contains material as it appears in Matoza, R.S., M.A.H. Hedlin, and M.A. Garces (2007), An Infrasound Array Study of Mount St. Helens, *J. Volcanol. Geotherm. Res.*, **160**, 249–262; Copyright 2006 Elsevier. Chapter 3, in full, has been published as Matoza, R.S., M.A. Garces, B.A. Chouet, L. D'Auria, M.A.H. Hedlin, C. De Groot-Hedlin, and G.P. Waite (2009), The source of infrasound associated with long-period events at Mount St. Helens, *J. Geophys. Res.*, **114**, B04305; Copyright 2009 American Geophysical Union. Chapter 4, in full, has been published as Matoza, R.S., D. Fee, M.A. Garces, J.M. Seiner, P.A. Ramon, and M.A.H. Hedlin (2009), Infrasonic jet noise from volcanic eruptions, *Geophys. Res. Lett.*, **36**, L08303; Copyright 2009 American Geophysical Union. Chapter 5, in part, has been submitted for publication as Matoza, R.S., Fee, D., and Garces, M.A., Infrasonic tremor wavefield of the Pu‘u Ō‘ō crater complex and lava tube system, Hawaii, in April 2007, *J. Geophys. Res.*, *submitted.* The dissertation author was the primary investigator and author of each of these papers. The work was funded by NSF grant EAR-0609669.

I would also like to thank my friends and colleagues at Scripps. In particular, I thank Kris Walker for all the little tips that greatly improved my efficiency; Delia Constant for much appreciated admin assistance; my office mates: Leah Ziegler, Matt Wei, Danny Brothers, Lindsay Smith, and Jose Otero for a fun work environment; Chris Takeuchi and Brent Wheelock for reminding me that it was time to take a break and go surfing; and Joseph Ribaudo for a musical friendship.

Most importantly, I thank my wife, Emily, for her untiring love, patience and support while I completed this task, and for being exactly the sort of person I would want to go home to after a long day at the office. In addition, I thank the Crawford family for their warm enthusiasm for my chosen career, and I must acknowledge influential conversations with Bryan concerning water hammer and the noises produced inside hot water boilers. I am deeply grateful to my father, Sam, for all the sacrifices and hard work over the years, and the endless encouragement. I also wish to thank my sister, Lucy, and brother-in-law, Paul, for their love and energy. My mother, Chris, instilled in me from an early age the value of education. She thought volcanoes were wonderful, and would always get a smile on her face when we talked about them. This work is dedicated to her.

Robin Matoza
La Jolla, California

VITA

2004	M.Geophys. Geophysics (First Class Honors) University of Leeds
2004–2009	Graduate Student Researcher Scripps Institution of Oceanography, University of California, San Diego
2009	Teaching Assistant Scripps Undergraduate Education Department, University of California, San Diego
2009	Ph.D., Earth Sciences Scripps Institution of Oceanography, University of California, San Diego.

PUBLICATIONS

Matoza, R.S., Fee, D., and Garces, M.A., Infrasonic tremor wavefield of the Pu‘u Ō‘ō crater complex and lava tube system, Hawaii, in April 2007, *J. Geophys. Res.*, *submitted.*

Matoza, R.S., M.A. Garces, B.A. Chouet, L. D'Auria, M.A.H. Hedlin, C. De Groot-Hedlin, and G.P. Waite (2009), The source of infrasound associated with long-period events at Mount St. Helens, *J. Geophys. Res.*, **114**, B04305, doi:10.1029/2008JB006128.

Matoza, R.S., D. Fee, M.A. Garces, J.M. Seiner, P.A. Ramon, and M.A.H. Hedlin (2009), Infrasonic jet noise from volcanic eruptions, *Geophys. Res. Lett.*, **36**, L08303, doi:10.1029/2008GL036486.

Matoza, R.S., M.A.H. Hedlin, and M.A. Garces (2007), An Infrasound Array Study of Mount St. Helens, *J. Volcanol. Geotherm. Res.*, **160**, 249–262, doi:10.1016/j.jvolgeores.2006.10.006.

Garces, M.A., Fee, D., and Matoza, R.S., Volcano Acoustics, in "Modeling Volcanic Processes", ed. S.A. Fagents, T.K.P. Gregg, and R.M.C. Lopes, Cambridge University Press, *submitted.*

Moran, S.C., R.S. Matoza, M.A. Garces, M.A.H. Hedlin, W.E. Scott, D.R. Sherrod, J.W. Vallance, and D. Bowers (2008), Seismic and acoustic recordings of an unusually large rockfall at Mount St. Helens, Washington, *Geophys. Res. Lett.*, **35**, L19302, doi:10.1029/2008GL035176.

Garces, M., D. Fee, D. McCormack, R. Servranckx, H. Bass, C. Hetzer, M. Hedlin, R. Matoza, and H. Yepes (2008), Prototype ASHE volcano monitoring system captures the acoustic fingerprint of stratospheric ash injection, EOS Trans. AGU (article), **89**, no. 40, 377–388, doi:10.1029/2008EO400001.

PRESENTATIONS

Matoza, R.S.*, D. Fee, M.A. Garces, and M.A.H. Hedlin, 2008. Large-Scale Volcanic Jet Noise. Fall 2008 AGU meeting, San Francisco.

Matoza, R.S., M.A. Garces*, B.A. Chouet, L. D'Auria, and M.A.H. Hedlin, 2008. Source process for infrasonic and seismic 'drumbeat' LP events at Mount St. Helens, IAVCEI, Iceland.

Matoza, R.S.*, M.A. Garces, B.A. Chouet, L. D'Auria, M.A.H. Hedlin, 2007. Integrating seismic and acoustic source models for long period events (Poster). Cities on Volcanoes 5, Shimabara, Japan.

D. Fee*, M. Garces, R. Matoza, T. Orr, and Richard Hoblitt, 2007. Seismoacoustic Tremor Recordings At The Pu'u O'o Crater Complex, Kilauea Volcano, Hawaii (Poster). Cities on Volcanoes 5, Shimabara, Japan.

Garces, M.*, D. Fee, A. Steffke, M. Hedlin, R. Matoza, H. Yepes, P. Palacios, D. McCormack, H. Bass, C. Hetzer, R. Servranckx, J. Kauahikaua, T. Orr, S. Moran, R. Hoblitt, B. Chouet, G. Waite, D. Streett, and G. Swanson, 2007. Tuning infrasound arrays for automated remote sensing of hazardous eruptions (Poster). Cities on Volcanoes 5, Shimabara, Japan.

Matoza, R.*, and M. Hedlin, 2007. Volcano-acoustic recordings at Mount St. Helens. Second International Workshop on Acoustic Remote Sensing of Volcanoes, Shimabara, Japan.

Matoza, R.S.*, M.A. Garces, B.A. Chouet, L. D'Auria, and M.A.H. Hedlin, 2007. Numerical investigations of the source of infrasound from long period events at Mount St. Helens. 2007 Infrasound Technology Workshop, Tokyo, Japan.

Fee, D.*, M. Garces, and R. Matoza, 2007. Characterization of Explosion Signals from Tungurahua Volcano, Ecuador. 2007 Infrasound Technology Workshop, Tokyo Abstract.

Bass, H.*, M. Garces, et al., 2007. Regional arrays for automatic remote sensing of hazardous volcanic eruptions. 2007 Infrasound Technology Workshop, Tokyo Abstract.

Matoza, R.*, 2007. Broadband seismic and infrasonic array studies at Mount St. Helens, Tungurahua, and Kilauea. Istituto Nazionale Di Geofisica E Vulcanologia, Osservatorio Vesuviano - Napoli, Italy. *(invited)*

Garces, M.*, D. Fee, R. Matoza, and M. Hedlin, 2007. Infrasonic Tremor Variability from Pu‘u O‘o, Hawaii. IUGG XXIV General Assembly, Perugia, Italy.

Garces, M.A.*, D. Fee, M.A.H. Hedlin, R.S. Matoza, H. Yepes, D. Mccormack, R. Servranckx, and H.E. Bass, 2007. Recent Progress in Infrasonic Early Warning Systems. IUGG XXIV General Assembly, Perugia, Italy.

Matoza, R.S.*, M.A. Garces, B.A. Chouet, L. D'Auria, and M.A.H. Hedlin, 2007. Numerical investigations of the seismic-acoustic coupling mechanism for long period events. IUGG XXIV General Assembly, Perugia, Italy.

Garces, M.*, R. Matoza, M. Hedlin, B. Chouet, and L. D'Auria, 2007. Theoretical and Numerical Modeling of Volcanic Sounds. Invited paper to the 8th International Conference on Theoretical and Computational Acoustics, Heraklion, Crete, Greece, July 2-6, 2007

Matoza, R.S., M.A.H. Hedlin, M.A. Garces*, B.A. Chouet, L. D'Auria, and H. Bass, 2007. Seismoacoustic signatures of fluid oscillations in the volcanic plumbing system and eruption column. AGU 2007 Joint Assembly: Acapulco, Mexico.

Garces, M.*, D. Fee, A. Steffke, R. Matoza, M. Hedlin, Y. Yepes, D. McCormack, H. Bass, C. Hetzer, and R. Servranckx, 2007. Acoustic remote sensing of volcanic eruptions in Washington, Ecuador, and Colombia: New tools for covering observational gaps. AGU 2007 Joint Assembly: Acapulco, Mexico.

Moran, S.C.*, R.S. Matoza, M.A. Garces, M.A.H. Hedlin, W.E. Scott, D.R. Sherrod, J.W.Vallance, D. Bowers and D. Green, 2007. Recordings of acoustic and seismic signals associated with a large rockfall event at Mount St. Helens on May 29, 2006. SSA 2007 Annual Meeting, Kona, Hawaii.

Matoza R.*, M. Garces, M. Hedlin, and D. Fee, 2007. Joint seismic and acoustic recordings of eruptions at Mount St. Helens, USA and Tungurahua, Ecuador. SSA 2007 Annual Meeting, Kona, Hawaii.

Fee, D.*, M. Garces, and R. Matoza, 2007. Infrasonic tremor variability at Pu‘u O‘o crater complex, Kilauea Volcano, Hawaii. SSA 2007 Annual Meeting, Kona, Hawaii.

Matoza, R.S.*, M.A. Garces, and M.A.H. Hedlin, 2006. Infrasound associated with long period events at Mount St. Helens. Fall 2006 AGU meeting, San Francisco.

Garces, M.*, D. Fee, A. Steffke, M. Hedlin, R. Matoza, J. Kauahikaua, S. Moran, B. Chouet, H. Yepes, and G. Vincente, 2006. Integrating infrasound into studies of eruption processes at Kilauea, Mount St. Helens, and Tungurahua Volcanoes. Fall 2006 AGU meeting, San Francisco.

Matoza, R.*, M. Hedlin, M. Garces, D. Fee, D. McCormack, and H. Bass, 2006. Infrasonic and seismic signatures of Mount St. Helens activity. 2006 Infrasound Technology Workshop, Fairbanks, Alaska.

Matoza, R.*, M. Hedlin, M. Garces, and D. Fee, 2006. Constraints on the source mechanism of long period events, tremor, and eruptions from simultaneous seismic and acoustic observations. The Physics of Fluid Oscillations in Volcanic Systems Workshop, Lancaster, UK.

Matoza, R.*, and M. Hedlin, 2006. An infrasound array study of Mount St. Helens. First International Workshop on Acoustic Remote Sensing of Volcanoes, Quito, Ecuador.

Matoza, R.*, and M. Hedlin, 2006. An infrasound array study of Mount St. Helens (Poster). Cities on Volcanoes 4, Quito, Ecuador.

Matoza R., and M. Hedlin*, 2005. Seismo-acoustic study of Mount St. Helens. 2005 Infrasound Technology Workshop, Tahiti.

* *presenter*

ABSTRACT OF THE DISSERTATION

Seismic and infrasonic source processes in volcanic fluid systems

by

Robin S. Matoza
Doctor of Philosophy in Earth Sciences
University of California, San Diego, 2009
Michael A.H. Hedlin, Chair

Volcanoes exhibit a spectacular diversity in fluid oscillation processes, which lead to distinct seismic and acoustic signals in the solid earth and atmosphere. Volcano seismic waveforms contain rich information on the geometry of fluid migration, resonance effects, and transient and sustained pressure oscillations resulting from unsteady flow through subsurface cracks, fissures and conduits. Volcanic sounds contain information on shallow fluid flow, resonance in near-surface cavities, and degassing dynamics into the atmosphere. Since volcanoes have large spatial scales, the vast majority of their radiated atmospheric acoustic energy is infrasonic (<20 Hz). This dissertation presents observations from joint broadband seismic and infrasound array deployments at Mount St. Helens (MSH, Washington State, USA), Tungurahua (Ecuador), and Kilauea Volcano (Hawaii, USA), each providing data for several years. These volcanoes represent a broad spectrum of eruption styles ranging from hawaiian to plinian in nature. The catalogue of recorded infrasonic signals includes continuous broadband and harmonic tremor from persistent degassing at basaltic lava vents and tubes at Puʻu Ōʻō (Kilauea), thousands of repetitive impulsive signals associated with seismic long-period (0.5-5 Hz) events and the dynamics of the shallow hydrothermal system at MSH, rockfall signals from the unstable dacite dome at MSH, energetic explosion blast waves and gliding infrasonic harmonic tremor at Tungurahua volcano, and large-amplitude and long-duration broadband signals associated with jetting during vulcanian, subplinian and plinian eruptions at MSH and Tungurahua.

We develop models for a selection of these infrasonic signals. For infrasonic long-period (LP) events at MSH, we investigate seismic-acoustic coupling from various buried source configurations as a means to excite infrasound waves in the atmosphere. We find that linear elastic seismic-acoustic transmission from the ground to atmosphere is inadequate to explain the observations, and propose that the signals may result from sudden containment failure of a pressurized hydrothermal crack. For the broadband eruption tremor signals, we propose that the infrasonic signals represent a low-frequency form of jet noise, analogous to the noise from man-made jet engines, but operating with larger spatial scales and consequently longer time-scales. For the persistent hawaiian tremor signals, we propose that bubble cloud oscillation in the upper section of a roiling magma conduit and vortex dynamics in the shallow degassing region act as broadband and harmonic tremor sources. We also consider infrasound propagation effects in a dynamic atmosphere and discuss their effects on recorded signals. This dissertation demonstrates that combined seismic and infrasonic data provide complementary perspectives on eruptive activity.

1. Introduction

Volcanoes are manifestations of the dynamic nature of our planet. Almost all terrestrial volcanoes are distributed along plate boundaries, or above regions of mantle upwelling, as direct consequences of plate tectonics and mantle convection. Melt formed at depth migrates to the surface through a complicated network of cracks, fissures and conduits to form surface volcanism. On timescales of hours to years, this migration may be tracked by ground deformation recorded with tiltmeters, GPS, and satellite radar interferometry. However, on timescales of a few hundred seconds down to tenths of a second, subsurface oscillations of the fluids are optimally captured with broadband seismometry, while the shallow fluid activity and its eruption into the atmosphere are well recorded by acoustic sensors. Changes in volcano seismic and acoustic signal characteristics over month to year timescales can be used to infer longer-term eruption dynamics.

1.1 Volcano seismology

Since the advent of broadband seismometer deployments at volcanoes [Kawakatsu et al., 1992; Neuberg et al., 1994; Kaneshima et al., 1996], recorded volcano-seismic signals have been classified according to their frequency content, or the timescales involved in producing the signal. Typically in volcano seismology, the following definitions are used: 1) >100s, ultra-long-period (ULP), 2) 2-100 s, very-long-period (VLP), 3) 0.2-2 s, long-period (LP), 4) 0.2-0.05 s, short-period

(SP) [Ohminato et al., 1998]. Ultra-long-period signals have been observed in relation to large-scale processes such as energetic mass injection into the atmosphere [Kanamori et al., 1994], or the collapse of a volcanic edifice [Green and Neuberg, 2005]. Very-long-period signals are usually attributed to inertial volume changes and forces from mass advection in fluid conduits [e.g., Ohminato et al., 1998; Kawakatsu et al., 2000; Hidayat et al., 2002; Aster et al., 2003; Chouet et al., 2003, 2005]. Gas slugs rising through a fluid-filled tube, for instance, can generate strong oscillatory forces when encountering an increase in the tube diameter [James et al., 2006], and the results of moment tensor and single-force vector inversions of some VLP events can be explained in this framework [Chouet et al., 2003]. Long-period seismicity at volcanoes, including individual long-period events and tremor, is often ascribed to the activity of magmatic and hydrothermal fluids in subsurface conduits and cracks [e.g., Chouet, 1985, 1988; Garces, 1997; Neuberg et al., 2000, Kumagai et al. [2005]; *discussed in detail below*]. Shallow (<2 km) LP seismicity has demonstrated its utility in short-term eruption forecasting because changes in the timing and vigor of the signals accompany the pressurization of the magmatic and hydrothermal systems prior to and during eruption [e.g., Chouet et al., 1994; Chouet, 1996a; Miller et al., 1998; Pinatubo Volcano Obsevatory Team, 1991]. Finally, processes operating in the short-period band include the broadband onsets of LP events, and volcano-tectonic (VT) events (see below). Other volcanic processes such as rockfalls, landslides, lahars, pyroclastic flows, and explosions can generate signals with a wide range of frequency contents [McNutt, 2000].

In addition to the classification based on frequency content, volcano-seismic signals are also named according to the physical processes generating the signal [Lahr et al., 1994]. The most important distinction is between shear or tensile sources that occur in the elastic solid, and volumetric sources that actively involve a fluid. Volcano tectonic (VT) events belong to the former category. They are named for their resemblance to ordinary tectonic earthquakes, having distinct

P- and S-wave arrivals. VTs can result from the brittle failure of country rock in response to the stress of an intruding magma body [Moran, 2003] or from tensile cracking due to cooling and solidification of magma [Chouet, 1979]. Locations of VTs sometimes map linear faults and other structures accommodating stress, and it has been proposed that temporal and spatial variations in their b-values[1] can give information on the thermal evolution of a magma body [Wiemer and McNutt, 1997; McNutt, 2005]. Recently, analyses of fault-plane solutions of VT events have revealed information about the mechanism of stress accommodation surrounding a magma conduit [Roman and Cashman, 2006]. For instance, the pressure axis in VT fault-plane solutions has been observed to be orthogonal to the dominant regional stress orientation in some cases, indicating that these VTs may result from dike inflation in the direction of minimum compressive stress [Roman and Cashman, 2006]. Temporal changes in VT hypocenter locations and the orientation of fault-plane solutions have also been attributed to pressurization of the mid-level conduit system prior to eruption [Roman et al., 2006, 2008]. Hybrid events have properties of both categories. They may result from shear failure of melt at a conduit margin, and consist of a shear failure (i.e., mixed first motions) followed by a long-period coda from the fluid response [Lahr et al., 1994]. Long-period events and tremor belong to the latter category, and are discussed in detail below.

1.1.1 Long-period seismicity

Long-period (LP) events and tremor are closely related. LP events are transient signals, lacking in S-waves, with a broadband onset lasting ~10 s, followed by a decaying harmonic coda lasting tens of seconds to a few minutes in duration, and containing pronounced spectral peaks that are independent of azimuth and distance to the source [Chouet, 1996a]. This is usually interpreted as a broadband pressure excitation mechanism, followed by the resonant response of

---

[1] The slope of the Gutenberg-Richter frequency-magnitude relation.

a fluid-filled conduit or crack. The high-frequency energy observed in the onset is strongly affected by attenuation, and consequently the first motions are often emergent and difficult to define. The positions of the defined spectral peaks in the coda differ for each volcano, and can vary as a function of time at a particular volcano. The LPs of Galeras volcano (Colombia), for instance, are quasi-monochromatic [Gil Cruz and Chouet, 1997], while the LPs of Mount St. Helens have more complex polychromatic spectral structure [Waite et al., 2008]. This rich variety in LP signals is likely a consequence of differing conduit and crack geometries, structural and topographic heterogeneity, and variations in the fluid composition and attenuation properties [Kumagai and Chouet, 1999, 2000]. Typical fluids include bubbly magma, hot water, steam, and dusty gases.

Tremor is a more continuous disturbance lasting from minutes to days. The spectral content of tremor is often the same as the individual LP events, which led to the interpretation that both result from a common fluid resonator in response to different driving mechanisms [Chouet, 1985]. LPs are attributed to the response of the system to an impulsive pressure transient, while tremor is interpreted as the result of a more sustained pressure fluctuation. Below I summarize the history and development of these quantitative models for shallow[2] long-period seismicity.

1.1.1.1 Volcanic tremor

One of the earliest observations of volcanic tremor was that of Luigi Palmieri in 1856. He observed "continuous tremor" on electromagnetic seismometers deployed on Vesuvius, recognising that volcano-seismic signals can be different in character from ordinary crustal earthquakes [Gasparini et al., 1992]. Omer [1950] provided one early quantitative model for the source mechanism of volcanic tremor. He attributed tremor to a path effect: the reverberation of volcanic strata

---

[2] Deep (>10 km) LP activity is well documented in volcanic [Koyanagi et al., 1987] and non-volcanic [Obara, 2002] settings. However, the source processes operating at those depths are currently not well understood, and are isolated from the atmosphere.

excited into motion by lava moving though feeding conduits. Shima [1958] and Kubotera [1974] instead proposed that a peaked tremor spectrum was a result of free oscillations of a spherical magma chamber, while Shimozuru [1961] modelled it as the longitudinal resonance of a cylindrical magma column. Steinberg and Steinberg [1975] attributed tremor to pulsating "flow crises" of gas in volcanic vents undergoing the transition from subsonic to supersonic flow. However, these early models did not adequately quantify the driving force of the fluid or predict the elastic radiation from the source region [Chouet, 1981], and required implausibly large dimensions for the resonating cavities [Ferrazzini and Aki, 1987].

1.1.1.2 Jerky crack models

The first rigorous treatment of volcanic tremor was given by Aki et al. [1977], who proposed a mechanism for volcanic tremor at Kilauea (Hawaii) consisting of the jerky extension of dry and fluid-filled tensile cracks. Two models were proposed: 1) the jerky extension and propagation of a single crack; 2) the random jerky openings of narrow channels connecting a chain of pre-existing cracks. The fluid did not support acoustic waves and merely acted as a cushion to the vibration of the crack, while the crack geometry was considered 2-dimensional. Near-field and far-field displacements computed by finite-difference calculations replicated the general properties of observed tremor. Properties of the synthetic signals were dependent on the "crack stiffness":

$$C = \frac{bL}{\mu d}, \tag{1.1}$$

where b is the bulk modulus of the fluid in the crack, L is the crack length, μ is the elastic shear modulus and d is the aperture of crack opening. The single-crack model (1) was rejected because the growing crack length predicted a significant increase in tremor period, which was not observed. Model (2) was further developed for deep tremor occurring at 30-50 km beneath Kilauea by Aki and Koyanagi [1981]. They defined a measure of tremor amplitude related to the magma flux known as reduced displacement:

$$u_{reduced} = A\frac{r}{2\sqrt{2}}, \tag{1.2}$$

where A is the peak-to-peak amplitude of ground motion ($\frac{A}{2\sqrt{2}} = A_{rms}$, root mean square amplitude), and r is the source-receiver distance. Measurement of the reduced displacement as a function of time implied a magma flow rate of an order of magnitude lower than that derived from geological observations.

Chouet [1979] interpreted seismic signals observed in the cooling lava lake of Kilauea-Iki as the result of vertically-aligned penny-shaped cracks resulting from the formation of columnar basalt joints. Later, Chouet [1981] developed the crack model of Aki et al. [1977], calculating near-field and surface displacements for a single crack extension while accounting for interaction with the free-surface, and near surface velocity structure. The effects of varying the structure of the elastic media, source depth, and bulk modulus of the fluid in the crack were explored. This model was expanded into 3-dimensions and further described in Chouet [1982, 1983]. However, these models still assumed no active participation of the fluid. The fluid could not transmit acoustic waves, and the dynamics of the fluid were not considered in significant detail. Consequently, the spectral peaks obtained by these models were too weak and too broad, and the long duration of observed LP signals could not be reproduced [Chouet, 1988].

1.1.1.3 Fluid resonance models and “crack waves”

The 1980s Mount St. Helens eruption provided new observations of LPs and tremor, at a time when very few models existed for LP events [Fehler and Chouet, 1982; Fehler, 1983]. Fehler and Chouet [1982] reported LP events with duration ~30 s, spectra peaked in the range 1.7-2.3 Hz, and depths between 0-5 km. Production of the spectral peaks by a path effect [Malone, 1983] was dismissed because the position of the spectral peaks did not change significantly with station location, and a VT earthquake located in the vicinity of the crater observed with the same instruments did not have the same spectral structure as the LPs [Fehler and Chouet, 1982]. Fehler and Chouet [1982] proposed that the peaked spectra originated from excitation of a fixed[3] cavity under the active crater. Following Latter [1979], Fehler [1983] also noted the spectral similarity of LP events and tremor, and proposed that tremor consisted of a superposition of randomly occurring LP events.

These observations rejuvenated interest in LP and tremor models in which the fluid plays an active role. Lawrence and Qamar [1979] and Ferrick and Qamar [1982] proposed a mechanism involving volcanic fluids analogous to the water-hammer effect in a cavity connecting a magma chamber to the surface. This model consisted of resonance of a conduit in response to unsteady flow conditions (fluid transients). These studies were motivated by seismic observations of type-II “icequakes” in glaciers and seismic events originating from a malfunctioning power plant that bore resemblance to LP events. Chouet [1985] recognised the importance of the fluid in sustaining resonance, and interpreted LP events as the impulse response of a tremor-generating system. Accordingly, he proposed a conceptual system consisting of a “trigger”, a “resonator”, and a “radiator”: in this case a hemispherical trigger[4] overlying a cylindrical conduit (with “organ pipe” modes), terminated at the base by a circular radiator. An LP event corresponded to a single triggering of the system, while a continuous tremor would result from continuous triggering. Therefore, the quest to understand the complex source mechanism of volcanic tremor was superceded by the more tractable task of understanding individual LP events.

Chouet and Julian [1985] and Chouet [1986, 1988] further developed the crack models initiated by Aki et al. [1977] and Chouet [1981, 1982, 1983], but now

---

[3] Note that, unlike the jerky crack propagation model (section 1.1.1.2), this is consistent with recent cross-correlation studies on repetitive LP waveforms [e.g., Stephens and Chouet, 2001].

[4] It was speculated that the trigger mechanism was the rapid exsolution of gases from the fluid phase during ascent of magma, or flashing of a subsurficial layer of phreatic water to steam due to the shallow intrusion of magma.

allowed the fluid to transmit acoustic energy. These models were formulated using the equations of elastodynamics in the elastic solid and conservation of momentum and equations of continuity for the fluid. These fluid-filled crack models were applied to non-double couple earthquakes observed near Long Valley Caldera between 1978-1983, hydrofracture events as used for enhanced recovery in the oil industry, and LPs and tremor. The most significant feature of these models was the presence of an interface wave propagating through the fluid and reflecting back and forth at the crack tips (Figure 1.1). The velocity of this "crack wave" is slower than the acoustic velocity of the fluid at all wavelengths, and is inversely dispersive (velocity decreases as wavelength increases). The properties of the crack wave are analogous to those of tube waves propagating in a fluid-filled borehole [Biot, 1952]. However, unlike the tube wave, as the wavelength increases to infinity, the velocity of the crack wave approaches zero in inverse proportion to the square root of wavelength [Ferrazzini and Aki, 1987]. In the short wavelength limit, the crack wave reduces to the Stoneley wave propagating along a fluid-solid interface. Figure 1.1 shows an example of a calculation with the model of Chouet [1986]. This figure shows the normal component of velocity at the wall of a fluid-filled crack embedded in an infinite elastic solid at eight snapshot times in the finite-differences simulation. The crack is excited by an arbitrary step function in pressure applied at a small patch located in this example at the center of one tip of the crack (snapshot 1). As time progresses in the calculation, the lateral and longitudinal resonant modes of the crack are excited (snapshot 5), and crack waves propagate up and down the crack, reflecting at the crack tips (snapshots 7, 8). The fluid-filled crack is specified by the parameters α/a, b/μ, W/L, and the crack stiffness C (eqn. 1.1), where α is the P-wave velocity of the elastic solid, a is the sound speed of the fluid in the crack, and W is the width of the crack [Chouet, 1986]. The reader is referred to chapter 3, section 3.5.1.1, for a full explanation of this calculation and the values of parameters used.

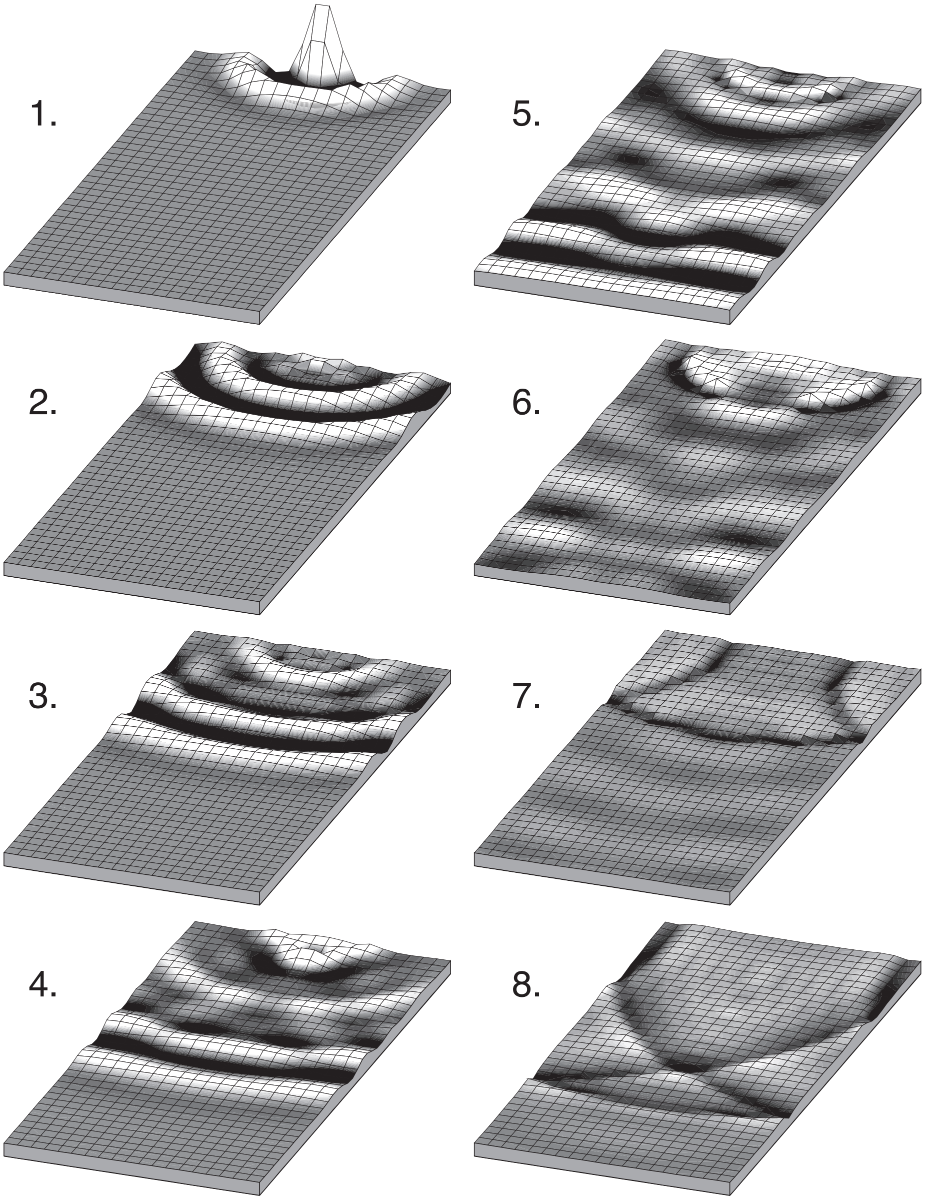

Figure 1.1: Normal component of velocity at the wall of a fluid-filled crack with $\alpha/a = 17.5$, $b/\mu = 0.0018$, $W/L = 0.5$, and $C = 7.5$ calculated with the model of Chouet [1986]. See text for explanation of symbols. Numbers 1–8 represent different snapshot times in the finite-difference calculation. The time step has scale $dt = 0.00625L/\alpha$ and the snapshots shown correspond to N time steps where: (1) $N = 50$, (2) $N = 100$, (3) $N = 150$, (4) $N = 200$, (5) $N = 300$, (6) $N = 500$, (7) $N = 1000$, and (8) $N = 2000$.

Ferrazzini and Aki [1987] found analytic expressions of the crack waves by considering normal modes in a fluid layer sandwiched between two homogeneous half-spaces. These expressions produced dispersion relations in harmony with the numerical results of Chouet and Julian [1985] and Chouet [1986]. These studies showed that "slow waves" or "crack waves" can produce long-period elastic radiation from only a modest-sized resonating cavity. For instance, Kubotera [1974] determined the source of 3.5-7 s period tremor at Mount Aso to be a resonating spherical magma chamber of 4-6 km radius. By considering crack waves, Ferrazzini and Aki [1987] and Chouet [1988] could model this same tremor signal as resulting from a modest-sized magma body 0.5 m thick and 0.5 km long. Analysis of the radiation properties from the resonating crack by Chouet [1988] demonstrated the stability of the dominant period in the far-field, while the frequency and width of this spectral peak was a strong function of the crack stiffness and trigger amplitude, area, and location. The crack stiffness affects the dispersion characteristics and therefore the resonance frequencies of the crack, while the frequency and duration of the signals are also affected by the impedance contrast between solid and fluid:

$$Z = \frac{\rho_s}{\rho_f}\frac{\alpha}{a}, \tag{1.3}$$

where ρ_s and ρ_f are the density of the elastic solid and fluid respectively. The duration of the LP signal is also related to the viscous damping loss at the fluid-solid boundary:

$$F = \frac{12\eta L}{\rho_f d^2 \alpha}, \tag{1.4}$$

where η is the viscosity of the fluid. Accordingly, the LP coda contains information on the attenuation properties of fluids in the crack source volume. However, as formulated, the crack model accounts for radiation and viscous drag losses only. Intrinsic losses due to dissipation mechanisms within the fluid are treated separately as described in the following section.

1.1.1.4 Attenuation in volcanic fluid-filled cracks

Attenuation in the fluid-filled crack model was investigated by Kumagai and Chouet [1999, 2000, 2001] and Morrissey and Chouet [2001]. By treating the coda of the LP event as a decaying harmonic oscillation, it is possible to determine the complex frequencies using the Sompi method [Kumazawa et al., 1990; Nakano et al., 1998]. The complex frequencies $f - ig$, where f is the frequency, g is the growth rate, and $i = \sqrt{-1}$, are related to the quality factor Q by

$$Q^{-1} = -2g/f. \tag{1.5}$$

Sompi utilizes an autoregressive (AR) equation in the complex frequency domain, equivalent to the linear differential equation of a linear dynamic system [Kumazawa et al., 1990; Nakano et al., 1998]. Sompi can be applied to observed LP waveforms to recover the trigger source-time function initiating resonance [Nakano et al., 1998] and to determine the Q of the resonator. The observed Q is composed of two components:

$$Q^{-1} = Q_r^{-1} + Q_i^{-1}, \tag{1.6}$$

where Q_r^{-1} and Q_i^{-1} are the radiation and intrinsic losses respectively. Q_r^{-1} is a function of the resonator geometry and sound speed and density of the fluid, and can be evaluated using the fluid-filled crack model [Kumagai and Chouet, 1999, 2000; Morrissey and Chouet, 2001; Kumagai and Chouet, 2001]. The intrinsic attenuation Q_i^{-1} corresponds to intrinsic losses in the fluid, e.g., viscous, thermal and acoustic damping. Calculation of Q_i^{-1} requires knowledge of the thermodynamic equations of state for multiphase fluids [e.g., Commander and Prosperetti, 1989]. Kumagai and Chouet [2000, 2001] evaluated Q_r^{-1} and Q_i^{-1} for various gas-gas mixtures, ash-gas mixtures and liquid-gas mixtures. They found that Q_i^{-1} is negligible compared to Q_r^{-1} for gas-gas mixtures, but that Q_i^{-1} can be important in bubbly liquids when the bubble radius is larger than 1 mm, and in dusty and misty gases where particles larger than 100 μm are considered. Furthermore, they found that the high Q values of dusty and misty gases with small particles ($\sim$1 μm) were consistent with the values of Q observed for long-lasting LP codas observed at several volcanoes, highlighting the importance of these fluids in sustaining LP events. By analyzing Q in a sequence of 35 LP events as a function of time, Kumagai et al. [2002] were able to infer possible changes in the fluid composition of the LP resonator as a function of time at Kusatsu-Shirane Volcano, Japan.

1.1.1.5 Pressure excitation mechanisms for LP events

In all of these models, the impulsive trigger mechanism for LPs was an arbitrary step function in pressure. To date, the physical process producing this pressure transient and the true trigger source-time function remain incompletely understood. This is also the case for the sustained pressure fluctuations that drive tremor. Cross correlation of thousands of LP events demonstrates a high degree of similarity between individual events within a swarm (correlation coefficients typically >0.9 [e.g., Stephens and Chouet, 2001; Green and Neuberg, 2006; Thelen et al., 2008; Waite et al., 2008]). These studies indicate the repetitive action of a non-destructive source with only gradually evolving properties.

Proposed trigger mechanisms have included: 1) rapid phase changes associated with magma ascent [Chouet, 1985], 2) shocks formed by flow acceleration through a channel constriction [Morrissey and Chouet, 1997b], 3) explosions analogous to underwater explosions [Buckingham and Garces, 1996], 4) saturated and subcooled hydrothermal boiling [Leet, 1988], 5) magma-water interactions such as flashing of water to steam [Fehler and Chouet, 1982], 6) brittle failure of melt in the glass transition phase [Goto, 1999; Neuberg et al., 2006], 7) non-linear mechanisms such as periodic degassing, vortex shedding [Hellweg, 2000] and other flow-induced oscillation [Julian, 1994; Garces et al., 1998], and 8) steady flow cavitation due to a bend in a conduit [Garces, 2000]. It is feasible that some or all of these processes may be operating in different volcanological settings, while a similar crack stiffness for drastically different fluid compositions and resonator geometries ensures that the resultant signals remain in the long-period band. In any case, understanding the excitation mechanisms of LP events and tremor remains a major challenge facing volcano seismology [Chouet, 2003].

1.1.2 Note on imaging of fluid pathway geometry

Seismic tomography of volcanoes is another major focus of volcano seismology, but due to funding and logistics considerations, only tens of seismometers have so far been utilized in these studies [Lees and Crosson, 1989; Benz et al., 1996; Chouet, 2003]. The latest studies have achieved resolutions of 0.5 km [Dawson et al., 1999] and 0.25 km [McNutt, 2005]. The length scales of the fluid pathways needed to produce LP seismicity are typically smaller than this, while resolving shallow, vertical features such as vertical conduits can be difficult in the absence of crossing rays for this geometry.

Some clues can be obtained from locations of LP events and tremor that map finite volumes. Both tremor and LPs can be located by analyzing wavefront properties with small-aperture seismic arrays [Almendros et al., 2001], or spatial amplitude distributions corrected for site effects [Battaglia et al., 2005], while relative relocation analysis using waveform similarity can be used for repetitive LPs [Battaglia et al., 2003]. Another way to image fluid pathway geometry comes from waveform inversion for the forces producing VLP and LP signals. The representation theorem for seismic waves from a point source may be expressed as [Aki and Richards, 2002; Chouet, 1996b]:

$$u_n(\underline{x}, t) = F_p * G_{np} + M_{pq} * G_{np,q}, \tag{1.7}$$

where the summation convention is assumed, u_n is the nth-component of displacement at a receiver location $\underline{x}$ at a time t, F_p is a single force applied in the p-direction at the source, M_{pq} is a pair of opposing forces pointing in the p-direction, separated in the q-direction, with a dimension of force times distance at the source (the moment tensor), and G_{np} is the elastodynamic Green's function relating the nth-component of displacement at the receiver to the pth-component of force applied at the source. The linearity of equation (1.7) allows inversions for the moment tensor M_{pq} and single force F_p components of the source from seismic observations u_n given knowledge of the Green's functions G_{np}. Since influence from strong topographic heterogeneity is unavoidable in volcanic settings [Ohminato and Chouet, 1997; Neuberg and Pointer, 2000], the functions G_{np} connecting the source-time functions to the observed seismic displacements are usually computed using time-domain finite-differences [Ohminato and Chouet, 1997; Chouet et al., 2003, 2005; Kumagai et al., 2005].

We note that volcanic sources, unlike ordinary tectonic earthquakes, may consist of single-force sources F_p, resulting from, for instance, the reaction force down on the earth from an erupted jet of fluid [Kanamori et al., 1984], or large-scale mass advection in a fluid conduit [Chouet et al., 2003, 2008]. The moment tensor M_{pq} can be used to assess whether the source is a double-couple (shear-faulting) source or a volumetric source. The relative magnitudes of the eigenvalues, and orientations of the eigenvectors, of a volumetric moment tensor can be interpreted in terms of the orientation of idealized geometrical structures such as a crack plane, cylindrical pipe, or a sphere [Chouet, 1996b]. For instance, the moment tensor for a spherical source is [Chouet, 1996b]:

$$\boldsymbol{M} = \Delta V \begin{pmatrix} \lambda + \frac{2}{3}\mu & 0 & 0 \\ 0 & \lambda + \frac{2}{3}\mu & 0 \\ 0 & 0 & \lambda + \frac{2}{3}\mu \end{pmatrix}, \tag{1.8}$$

where ΔV is the volume change at the source, and λ and μ are the Lamé parameters. The moment tensor for a vertical pipe is [Chouet, 1996b]:

$$\boldsymbol{M} = \Delta V \begin{pmatrix} \lambda + \mu & 0 & 0 \\ 0 & \lambda + \mu & 0 \\ 0 & 0 & \lambda \end{pmatrix}, \tag{1.9}$$

and the moment tensor for the volumetric opening of a horizontal crack is given by [Chouet, 1996b]:

$$\boldsymbol{M} = \Delta V \begin{pmatrix} \lambda & 0 & 0 \\ 0 & \lambda & 0 \\ 0 & 0 & \lambda + 2\mu \end{pmatrix}. \tag{1.10}$$

By modeling volumetric moment tensors obtained by inversion of seismic data in terms of these geometrical idealizations, it is possible to infer the possible geometries of subsurface fluid bodies [Chouet et al., 2003, 2008]. The resolution of these inversions critically depends on the velocity models used. The latest studies involve moment tensor and single-force vector inversions for source-time functions up to 2 Hz [Kumagai et al., 2005; Waite et al., 2008]. It is anticipated that as the density of seismic stations monitoring volcanoes increases, the resolution of velocity models and accuracy of the source locations will improve, moment tensor inversions will be able to quantify the forces from fluid motion with finer temporal and spatial resolution, and the pathways of fluid migration could be tracked in increasing detail. For instance, Nakano et al. [2007] have recently proposed a method for the inversion for an extended seismic source (i.e., beyond the assumption of a point source), that could be exploited with a larger density of seismic stations.

1.1.3 Recent laboratory and numerical studies

1.1.3.1 Analogue laboratory experiments

Although seismology can give information on the geometry of fluid-filled cavities, and quantify the forces exerted in the ground by the oscillations of the fluids, the fluid dynamics driving the excitation of LPs and tremor are not amenable to direct observation. Significant advances have been made in scaled laboratory experiments using analogue fluids. Lane et al. [2001] conducted experiments using vertical glass tubes filled with gas-gum rosin mixtures. Optical and pressure sensors along the length of the tubes tracked changes in the fragmentation dynamics and radiated acoustic signals associated with flow regimes dependent on the gas supersaturation. Signals in strongly supersaturated liquids were associated with bubble coalescence and bursting, gas pockets forming at conduit margins, gas-at-wall annular flow, and fragmented flow. LP-like signals associated with longitudinal and radial resonances of the tube were observed when a stable, slow-moving foam layer developed, and were also observed in the unfragmenting, low Reynolds number, weakly supersaturated flow.

James et al. [2004, 2006] investigated the pressure changes associated with slug flow through vertical and inclined conduits, and conduits with changing cross-sectional area. These studies are relevant to the production of LPs and VLPs in low viscosity magmas such as basaltic strombolian (see Table 1.1) systems, where the fluid may be considered Newtonian. When an inertia-dominated slug encounters a flare in the tube diameter, the slug nose expands horizontally into the flare. A characteristic pinching of the slug tail is then seen to occur synchronous with recorded pressure and acceleration transients. This is consistent with the downward and inward motion of a liquid piston formed by the thickening film of liquid falling past the slug expanding in the wider tube. The sudden deceleration of the liquid annulus as it impinges the narrow inlet of the lower tube generates a pressure pulse in the liquid below the flare and also induces a downward force on the apparatus. The magnitudes and repeatability of these forces and pressure oscillations are scalable to observed VLP and LP signals [Chouet et al., 2003, 2008] under reasonable conditions [James et al., 2006].

Signals analogous to VTs, LPs, and tremor were also observed in association with thermal cracking by Burlini et al. [2007] in a 3 mm-thick disk of mid-ocean ridge basalt heated in a gas rig to a temperature of 1200 °C at a confining pressure of 300 MPa. This particular study highlights the possibility that real volcanic materials may be used in future experiments.

1.1.3.2 Numerical simulation

Where scaling of laboratory studies up to volcanic length-scales, temperatures and pressures is not possible, numerical simulations coupling fluid dynamics with wave propagation hold great promise. Nishimura and Chouet [2003] used a finite-difference method to solve the equations for mass and momentum conservation simultaneously in a compressible fluid and the elastodynamic equations for seismic propagation and ground deformation. Flow in a pressurized conduit-reservoir system was initiated by instantaneous removal of either a lid at the top of the conduit, or a plug between the lower reservoir and base of the conduit. Magma pressure was found to decrease as the magma migrated upward in response to the pressure change, while LP oscillations resulted from acoustic resonance in the conduit.

D'Auria [2006] and D'Auria and Martini [2009] produced numerical simulations of gas slug ascent using a numerical implementation of diffuse-interface theory. These simulations accurately reproduced the complex flow behavior observed by James et al. [2006] and produced force-time functions similar to those determined by Chouet et al. [2003]. The ultimate goal of these studies is numerical simulation of the multiphase fluid dynamics, validated by analogue experiments, and able to simultaneously solve for seismic and acoustic wave propagation for direct comparison with source-time functions [Lane and Gilbert, 2007].

1.2 Volcano acoustics

Seismometers measure ground motion, so the signals result preferentially from buried sources. In contrast, acoustic sensors sample the atmospheric wavefield and record signals from shallow buried sources and subaerial sources radiating directly into the atmosphere. Although some coupling does occur, these wavefields are mostly separated by the strong impedance contrast at the ground-air inter-

Table 1.1: Idealized types of volcanic eruption referred to in this dissertation.

Type	Description
Hawaiian	Effusive basaltic eruptions with low viscosity magma. Fissures, fire fountains and lava flows.
Strombolian	Basaltic and basaltic andesite eruptions with low viscosity magma. Repetitive series of explosions at fairly regular intervals.
Vulcanian	Small to moderate explosions lasting from seconds to minutes in duration. Discrete, violent explosions accompanied by ballistics of blocks and bombs. Ash content often significant.
Plinian	Moderate to large sustained mass discharge characterized by formation of tall eruptive columns. Significant ash content.
Phreatic	Eruption involving groundwater or surface water, i.e., seawater, meteoric water, hydrothermal water, or lake water. Ash can be entrained.
Magmatic	Eruption involving rapid release of juvenile gas dissolved in magma by fragmentation.

face, and thus contain separate information on volcanic activity. Interestingly, the earliest studies gave equal emphasis to seismic and acoustic wavefields, and it is only since the 1970's that volcano seismology research has rapidly outpaced volcano acoustics. Volcano acoustics received relatively few contributions until it was revived in the 1990's.

1.2.1 Early work

1.2.1.1 Barograph studies

In 1883, the eruption of Krakatau produced low-frequency pressure signals that were recorded on barometers distributed around the world [Strachey, 1888]. This event simultaneously awakened the world to the existence of subaudible sound, and the concept of volcanoes as immense[5] acoustic sources. Later, in a pioneering study of earthquakes and airborne explosions ("detonations") from the Asama-Yama, Japan, Omori [1912] used permanent seismometers and barometers to make a distinction between seismic signals associated with explosions, and non-explosion earthquakes. Many of the explosion events were audible in settlements at radial distances of ∼200-300 km, and some were powerful enough to knock out doors and windows. Omori used this information to map the sound propagation and acoustic shadow zones, and even considered the effects of wind and topography. The use of weather barometers to study low-frequency ($<$1 Hz) atmospheric pressure waves from volcanoes at intermediate to long range (tens to thousands of kilometers) was continued throughout the 20th century, e.g., the 1902 eruption of Mount Pelee, Martinique [Tempest and Flett, 1903]; 1956 Bezymianni, Russia [Gorshkov, 1960]; 1980 Mount St. Helens, USA [Reed, 1987; Delclos et al., 1990]; 1988 Mount Tokachi, Japan; 1989 Sakurajima, Japan; 1991 Mount Pinatubo, Philippines; and 1995 Ruapehu, New Zealand [Morrissey and Chouet, 1997a].

---

[5] Cannon-like sounds were audible as far away as 5000 km, while acoustic gravity waves (periods $> \sim$1 minute) performed at least seven laps of the globe [Strachey, 1888].

1.2.1.2 Microphone studies

In 1906, Frank Perret began the first recordings of volcano acoustic signals using moving-coil microphones at Vesuvius [Perret, 1950]. By 1911, Thomas Jagger and Perret had established a permanent monitoring station at Kilauea, Hawaii. Jagger[6] focussed on volcano seismology [e.g., Jagger, 1920], while Perret continued his work on volcano acoustics, eventually also recording signals at Etna, Stromboli, Sakurajima, Pelee, and Montserrat [Perret, 1950]. Wilcox [1947] provided a detailed, qualitative classification of volcanic sounds, but did not make any recordings. The first tape recordings of volcanic sounds were apparently made by the NHK Broadcasting Bureau of Japan [Snodgrass and Richards, 1956]. In 1952, a program of volcanic acoustics was initiated at the Scripps Institution of Oceanography by James Snodgrass, leading to a decade's worth of underwater and atmospheric acoustic recordings of volcanic sounds [Richards, 1963], but the sonobuoy-based recording systems had a poor frequency response below 50 Hz.

Woulff and McGetchin [1976] provided the first quantitative link between acoustic radiation and fluid mechanics at volcanoes. They postulated that the three basic types of acoustic radiation: 1) monopole, 2) dipole, and 3) quadrupole [Lighthill, 2001] would be generated by different styles of volcanic degassing, and derived relations between the radiated acoustic power and gas exit velocity. Examples of these processes were: 1) explosions, 2) interaction of gas flow with a solid volcanic vent, and 3) jet noise. Unfortunately, the data quality was poor, and regrettably this work was never continued.

1.2.2 Recent work

As in volcano seismology, the richest band for volcano acoustics is the long-period band (0.5-5 Hz). These frequencies are below the hearing threshold of

---

[6] Jagger was responsible for classifying volcanic tremor into the categories of "harmonic" (more rhythmic vibrations) and "spasmodic" (irregular vibrations).

the human ear (<20 Hz), which in acoustic terminology is known as *infrasound*. Little progress was made in the field of volcano acoustics until microphones targeting these frequencies were deployed near active volcanoes.

1.2.2.1 Infrasonic microphone arrays

Goerke et al. [1965], Wilson et al. [1966] and Wilson and Forbes [1969] provided some of the first infrasonic microphone array observations of volcanic infrasound[7] (1963 eruption of Mount Agung, Bali recorded 14,700 km away in Boulder, Colorado; and the 1967 eruptions of Redoubt and Trident, recorded at College, Alaska). The main emphasis of these studies, however, was the atmospheric propagation of the signals. Infrasonic microphone arrays were also installed at Kariya, Japan [Tahira, 1982] and Windless Bight, Antarctica [Dibble, 1989]. Although limited to the band 0.1-1 Hz, the Kariya array routinely detected explosions from Sakurajima volcano at a range of 710 km, while the Windless Bight array recorded explosions from Mount Erebus (26 km).

1.2.2.2 Volcano monitoring using infrasound in Japan

Following Tahira [1982], the utility of infrasound for regional volcanic monitoring has been understood in Japan [Kamo et al., 1994]. The array at Kariya recorded the 1991 Pinatubo (Philippines) eruptions at a range of 2,770 km, and these data were used to infer the eruptive time history when visual or instrumental observations close to the volcano were impossible [Tahira et al., 1996]. Iguchi and Ishihara [1990] and Yamasato [1997] installed infrasonic microphones at distances of 2-5 km from Sakurajima, Suwanosejima, and Unzen volcanoes, recording numerous explosions, pyroclastic flows [Yamasato, 1997], harmonic tremor [Sakai et al., 1996], and impulsive signals associated with LP events [Iguchi and Ishihara, 1990; Yamasato, 1998; Garces et al., 1999; *see chapter 3*]. The successful volcanic

---

[7] The frequencies of these signals were in the low infrasound band (0.01-0.1 Hz).

monitoring system at Sakurajima has integrated deformation data (tilt and strain meters) for information on the inflation prior to eruption, seismometers for the detection of LP swarms associated with eruptive activity, and infrasonic microphones to detect the occurrence of eruptions [Kamo et al., 1994].

1.2.2.3 Strombolian and vulcanian explosions

Explosions at Stromboli volcano (Aeolian Islands) are believed to result from the coalescence of bubbles in a foam at depth in the conduit, the rise of this gas as a slug flow, and the bursting of this slug at the magma surface [Harris and Ripepe, 2007]. Braun and Ripepe [1993] and Ripepe et al. [1996] deployed the first infrasonic microphones at Stromboli, determining that bursting of the large gas bubbles at the surface of the magma column was responsible for simultaneous seismic and acoustic signals. This idea was developed by Vergniolle and Brandeis [1994, 1996] and Vergniolle et al. [1996], who suggested that oscillation of the bubble immediately prior to bursting and kinematic waves on the magma surface after the burst were the significant acoustic sources rather than the bubble burst itself. Waveforms from such strombolian explosions usually consist of an initial compressional onset followed by a rarefaction, with extended coda reverberation in some cases [e.g., Firstov and Kravchenko, 1996; Ripepe et al., 1996; Johnson et al., 2003; Johnson, 2003; Ripepe and Marchetti, 2002; Ripepe et al., 2007; Johnson et al., 2008; Jones et al., 2008]. Ripepe and Marchetti [2002] proposed that the initial compression is related to the sudden pressure release at the burst of the overpressurized bubble, while the prolonged coda ($\sim$15 s) for some explosions may relate to sustained degassing following the initial bubble rupture. At Stromboli, the explosions occur within a conduit, and are not amenable to direct observation. However, at Mount Erebus (Antarctica) similar strombolian explosions occur in a phonolite lava lake (“Ray Lake”) that can be observed from the crater rim with simultaneous visual, seismic, acoustic and radar observations [Aster et al., 2004; Gerst et al., 2006]. Doppler radar observations of such explosion events indicate that the bubble does not vibrate prior to bursting [Gerst et al., 2006, 2008a], at odds with the model proposed by Vergniolle and Brandeis [1994, 1996] and Vergniolle et al. [1996]. Prior to bursting, a volumetric expansion of the bubble membrane is observed, but the membrane rips before equilibrium pressure is reached [Gerst et al., 2008a]. Furthermore, radar [Gerst et al., 2008b], visual, and infrasound data [Johnson et al., 2008] suggest the presence of directivity effects during bubble rupture. These appear to be manifest as non-monopole (dipole) radiation patterns in the acoustic pulses recorded on a network of 3 infrasonic sensors [Johnson et al., 2008]. At Stromboli, microphone arrays deployed close to the active craters are now able to locate and track activity at vents separated by a few hundred meters, and have also detected lower-amplitude infrasound signals associated with smaller-scale degassing activity [Ripepe et al., 2007].

The acoustic waveforms from "weak" impulsive vulcanian[8] explosions at more silicic and closed-vent volcanoes can be similar to those from strombolian explosions [e.g., Garces et al., 1999; Johnson et al., 2003; Ruiz et al., 2006; Johnson, 2007; Sahetapy-Engel et al., 2008; Garces et al., 2008], probably since both result from a rapid release of gas into the atmosphere. For instance, Johnson and Lees [2000] proposed that pyroclastic explosions at Karymsky represent a sudden pressure release as gas escapes past a solid plug in a conduit. In fact, differentiating between strombolian and weak vulcanian explosions simply from acoustic measurements can be difficult, and other data such as thermal infrared time series may be needed to determine whether an event is strombolian or vulcanian in nature [Marchetti et al., 2009]. Recently, experiments using explosions at a water-air interface have been performed to understand air waves from volcanic explosions [Ichihara et al., 2009]. In addition, the passage of infrasonic pressure waves from explosions is manifest as flashing arcs, condensation clouds, or luminescence changes

---

[8] See Table 1.1.

in video recordings [Yokoo and Taniguchi, 2004; Yokoo and Ishihara, 2007; Yokoo et al., 2009]. These modeling and additional data constraints represent promising new methods to further probe the source of infrasound from impulsive volcanic explosions.

1.2.2.4 Shallow conduit resonance

Garces [1995] and Buckingham and Garces [1996] recognized the importance of resonance in a magma column for the upgoing sound field, and derived a full wave-theoretical analytic solution for the airborne Green's function from a resonant magma conduit. In order to obtain a tractable analytic solution, a number of simplifying assumptions were made, including two-dimensional cylindrical symmetry (source in the center of the conduit), the treatment of the elastic solid bounding the conduit as acoustically rigid (i.e., no seismic wave propagation), the neglect of volcano topography, neglect of distortion effects at the magma surface, and the assumption that magma filled the conduit to the brim in order that sound radiation into the atmosphere may be treated as a piston set in an infinite baffle. In addition, the magma surface was treated as a pressure-release boundary in order to allow the separation of the acoustic wavefield (the Green's function) in the magma and the acoustic wavefield in the atmosphere. The geometrical idealization of the conduit was similar to that of Chouet [1985], with the exception that the "radiator" was now a diaphragm-like motion of the magma surface radiating sound into the atmosphere. This formulation demonstrated that high-frequency ($>$50 Hz) acoustic energy is propagated preferentially in a narrow beam of sound vertically above a conduit with radius $\sim$10 m, while infrasonic frequencies ($<$10 Hz) diffract spherically from the conduit opening. This partially explains why these frequencies are more readily recorded on ground-based sensors, and helped to rekindle interest in volcano infrasonics.

The model was further developed by Garces and McNutt [1997] and

Garces [1997, 2000] to eventually consider a depth-dependent conduit composed of an arbitrary number of sections, each specified by its: 1) radius, 2) material properties (viscosity, sound speed, density), and 3) fluid velocity (including high Mach numbers). The fluids were treated as multiphase (magma with exsolving H_2O and CO_2 gas), and seismic radiation from coupling at the walls of the conduit was calculated. Different pressure driving mechanisms were also investigated, including the effects of spectral interference from the repetitive excitation of the conduit by an impulsive forcing function.

These models were used to interpret seismic and acoustic recordings of eruptions at Arenal [Garces et al., 1998] and Pavlof [Garces and Hansen, 1998; Garces et al., 2000]. The model at Pavlof, for instance, was that ground-coupled air waves resulted from explosions in an upper conduit section, while seismic tremor originated from fluid flow in a deeper section of the conduit. The layers could be interpreted as a gas-rich, fragmenting foam layer overlying an equilibrium degassing conduit. These two layers resulted in a strong impedance contrast, isolating the downgoing seismic and upgoing acoustic energy[9]. At Arenal, gliding[10] harmonic tremor was recorded on both seismic and acoustic channels, demonstrating conclusively that the spectral structure of this tremor was due to resonance in a finite source volume, and not a seismic propagation effect.

Of particular relevance to the observation of infrasonic harmonic tremor at silicic stratovolcanoes [Johnson and Lees, 2000; Garces et al., 2008] may be the non-negligible Mach number formulation of Garces et al. [2000]. This solution deals with the resonant properties of a tube of gas moving at high velocity relative to the sound speed of the flow. To a first order approximation, the (gliding) spacing between frequency peaks is given by [Garces et al., 1998, 2000]:

$$\Delta f = \frac{c(1 - M^2)}{2L}, \tag{1.11}$$

---

[9] This was also observed in the laboratory experiments of Lane et al. [2001].

[10] A commonly observed phenomenon of volcanic tremor in which spectral peaks vary gradually as a function of time while maintaining a constant frequency spacing between spectral peaks.

where c is the sound speed of the material in the conduit, $M = U/c$ is the Mach number of the flow, and L is the effective length of the conduit. Hence, gliding could be explained by either a change in the effective length of the conduit L, or changes in the flow velocity U or sound speed c (e.g., via changes in particulate loading).

1.2.2.5 Surface and atmospheric eruption processes

Not surprisingly, the activity of volcanic material above ground can also be a powerful infrasonic source. The partial collapse of dacitic lava domes [Green and Neuberg, 2005; Moran et al., 2008], explosive blowout of gas-charged blocks impacting the ground [Oshima and Maekawa, 2001], and pyroclastic flows [Yamasato, 1997; Ripepe et al., 2009] generate large-amplitude infrasound. The path and speed of pyroclastic flow fronts can be tracked using arrival times and Doppler shift at a microphone network or array, even if visual observation is impossible [Yamasato, 1997; Ripepe et al., 2009]. Sustained steam and ash eruptions also generate infrasound [Garces et al., 1999; Johnson et al., 2003, 2004; Ruiz et al., 2006; Vergniolle and Caplan-Auerbach, 2006; Petersen et al., 2006], and it remains possible that some of this degassing could also generate a resonant spectrum [Garces, 1995; Johnson and Lees, 2000]. To date, the majority of volcano-acoustic studies have only considered small [11]VEI 1 and VEI 2 eruptions (Table 1.2), simply because this type of activity is more abundant and reliable. Following Woulff and McGetchin [1976], some recent studies have tried to relate radiated acoustic power with mass flux [e.g., Vergniolle and Caplan-Auerbach, 2006], but others have noted poor scaling between observable proxies for mass flux (e.g., visible plume height) and acoustic intensity [Johnson et al., 2005; Petersen et al., 2006]. However, although these signals hold great promise for robust volcano monitoring and learning more about eruption column dynamics, quantitative analysis of these signals has so far

---

[11] Volcanic Explosivity Index: a semi-quantitative measure of the size of volcanic eruptions based primarily on the erupted mass or volume [Newhall and Self, 1982].

proven difficult. One major factor has been instrumental limitations, particularly bandwidth.

1.3 The infrasound renaissance

Infrasound research has seen a significant resurgence since the initiation in 1996 of the Comprehensive Nuclear Test Ban Treaty (CTBT) which strives to eliminate explosive nuclear tests anywhere on the planet or in space. To enforce this treaty, there has been development of the International Monitoring System (IMS) comprising four components: seismic, infrasonic, hydroacoustic, and radionuclide monitoring stations [Hedlin et al., 2002]. The planned 60-station global infrasound network will be entirely new, and has led to improvements in infrasound sensor technology, wind noise reduction systems, and array processing algorithms. Typical stations consist of an array of 4 to 8 high-sensitivity broadband microbarometers (flat response 0.01 to >10 Hz), arranged in various geometries (e.g., centered triangle, pentagon, quadrilateral), with spatial wind filters consisting of pipes attached to each microbarometer [Hedlin et al., 2003]. Since turbulence from wind is the dominant form of noise, site selection has also proven key, and shelter is achieved by locating the arrays in forests where possible. In future, it is anticipated that new technology will further improve infrasound data collection. Emerging technology includes optical fiber infrasonic antennas that average pressure along a line at the speed of light [Zumberge et al., 2003], distributed sensors consisting of tens of microphones deployed over a large area [Shields, 2005], and wind “shredding” turbulence reducing enclosures [Christie, 2006].

Models of sound propagation in the atmosphere, and atmospheric specifications have also improved dramatically. The Ground to Space (G2S) semi-empirical models [Drob et al., 2003], for instance, consist of time-dependent specifications of sound speed, pressure, density, temperature, and wind speed with a standard resolution of $1^\circ \times 1^\circ$ up to the stratosphere (50-55 km), and $10^\circ \times 10^\circ$

Table 1.2: Volcanic Explosivity Index (VEI) criteria, after Newhall and Self [1982] and Simkin and Siebert [1994]

<table>
<tr><th>VEI</th><th>0</th><th>1</th><th>2</th><th>3</th><th>4</th><th>5</th><th>6</th><th>7</th><th>8</th></tr>
<tr><td>General Description</td><td>Non-Explosive</td><td>Small</td><td>Moderate</td><td>Moderate-Large</td><td>Large</td><td>Very Large</td><td></td><td></td><td></td></tr>
<tr><td>Volume of Ejecta (m^3)</td><td>$<10^4$</td><td>10^4-10^6</td><td>10^6-10^7</td><td>10^7-10^8</td><td>10^8-10^9</td><td>10^9-10^{10}</td><td>10^{10}-10^{11}</td><td>10^{11}-10^{12}</td><td>$>10^{12}$</td></tr>
<tr><td>Column Height (km)</td><td><0.1</td><td>0.1-1</td><td>1-5</td><td>3-15</td><td>10-25</td><td>>25</td><td></td><td></td><td></td></tr>
<tr><td rowspan="2">Qualitative Description</td><td rowspan="2">“Gentle”</td><td rowspan="2">“Effusive”</td><td colspan="2">“Explosive”</td><td colspan="5">“Cataclysmic, Paroxysmal, Colossal”</td></tr>
<tr><td colspan="7">“Severe, Violent, Terrific”</td></tr>
<tr><td rowspan="2">Eruption type</td><td></td><td colspan="2">Strombolian</td><td></td><td colspan="4">Plinian</td><td></td></tr>
<tr><td colspan="2">Hawaiian</td><td colspan="3">Vulcanian</td><td colspan="4">Ultra-Plinian</td></tr>
<tr><td rowspan="3">Duration</td><td colspan="4"><1 hour</td><td colspan="5">>12 hours</td></tr>
<tr><td colspan="2"></td><td colspan="3">1-6 hours</td><td colspan="4"></td></tr>
<tr><td colspan="3"></td><td colspan="3">6-12 hours</td><td colspan="3"></td></tr>
<tr><td>Tropospheric Injection</td><td>Negligible</td><td>Minor</td><td>Moderate</td><td colspan="6">Substantial</td></tr>
<tr><td>Stratospheric Injection</td><td>None</td><td>None</td><td>None</td><td>Possible</td><td>Definite</td><td colspan="4">Significant</td></tr>
</table>

to above the thermosphere (170 km). A number of studies have performed source location [e.g., Le Pichon et al., 2005b], and modeled the propagation of various infrasonic signals through tropospheric, stratospheric, and thermospheric ducts using ray tracing, parabolic equation (PE), and normal mode methods, utilizing theoretical models for atmospheric attenuation [Sutherland and Bass, 2004]. Le Pichon et al. [2005a], for instance, tracked the persistent activity of volcanoes in the Vanuatu archipelago from a distance of ∼500 km, and used this to measure annual changes in high altitude winds for assessing wind models.

However, ever since the IMS infrasound network was activated, it has been clear that it would provide useful data for a broad range of research interests and practical applications [Hedlin et al., 2002]. Natural sources of infrasound include thunder, sprites, tornadoes, auroras, avalanches, earthquakes, meteors, ocean microbaroms [e.g., Willis et al., 2004; Waxler and Gilbert, 2006], tsunamis, surf, and mountain associated waves (MAW) caused by air flow over topography; while man-made sources include nuclear tests, supersonic aircraft, power plants, wind turbines, and many others [Bedard and Georges, 2000]. Since infrasound propagates with relatively little attenuation over huge distances [Sutherland and Bass, 2004], the International Civil Aviation Organization (ICAO) and the Washington DC Volcanic Ash Advisory Center (VAAC) have expressed interest in using the existing IMS infrasound network or dedicated regional networks for volcano monitoring, especially for volcanoes not monitored by other means [Garces et al., 2008]. However, to achieve this goal, it is first necessary to understand and characterize the source generation process for infrasound from large volcanic eruptions, and to differentiate this from baseline volcano-acoustic activity.

1.4 Dissertation motivation and aims

Recent advances in infrasound sensor technology, data acquisition systems, wind noise reduction, and array processing techniques have led to a dramatic improvement in the ability to record atmospheric infrasound. The first aim of this dissertation is to present data collected using this technology at intermediate (tens of kilometers) to regional (hundreds of kilometers) range from active volcanoes, including Mount St. Helens (USA), Tungurahua (Ecuador), and Kilauea (Hawaii). We show that microbarometer arrays have the potential to record low-amplitude infrasound at greater range from a volcanic edifice than is possible with conventional microphone networks, enabling improved site selection, wind noise reduction, and continous data flow during a volcanic crisis. Furthermore, the use of broadband infrasonic sensors (flat response 0.01-17 Hz for Mount St. Helens, 0.1-17 Hz for Tungurahua and Kilauea) leads to an enhanced ability to capture the acoustic radiation from volcanic fluid motions at longer timescales. This is analogous to the addition of portable broadband seismometers to volcano seismology, and enables more detailed and accurate modeling of the fluid processes at work during volcanic eruptions.

The volcanoes under investigation represent a broad range in eruptive styles[12], from effusive basaltic hawaiian volcanism (Kilauea) to sustained explosive vulcanian (Mount St. Helens) and plinian (Tungurahua) eruptions from silic stratovolcanoes. This is a significant advance on previous volcano-acoustic studies, which have typically targetted strombolian and mild vulcanian activity at close range, or large eruptions at ranges of thousands of kilometers. We observe a rich variety in recorded signals from each of these volcanoes, which we attribute to a diverse collection of volcanic fluid oscillation processes. The primary aim of this dissertation is to initiate and develop quantitative models relating shallow and subaerial volcanic fluid motions to recorded infrasound. In several cases, this is most efficiently achieved by extending and modifying existing volcano-seismic source models to include the upgoing atmospheric sound field. This combined seismo-acoustic approach leads to an improved understanding of the shallow fluid

---

[12] See Table 1.1.

processes simultaneously generating recordable seismic and acoustic signals, and will ultimately lead to a more robust volcanic monitoring system. However, in other cases, the observed infrasonic signals bear little relation to simultaneously recorded seismic signals, and these infrasound signals likely represent a separate, shallower fluid process than is responsible for the seismic signals. We have developed models for several of these signals using dimensional analysis where possible. Finally, we aim to understand infrasound propagation effects in a time-varying atmosphere for the frequencies and ranges considered. The ranges and scale-lengths considered correspond to the atmospheric mesoscale and microscale. Infrasound propagation at this scale remains a significant and ongoing challenge.

1.5 Organization of the dissertation

Chapter 2 consists of a description of the broadband microbarometer array deployment at Mount St. Helens. First, the eruptive history of Mount St. Helens is presented briefly in order to provide context to the 2004-2008 eruption and the infrasound array experiment. We then describe the experimental set up and discuss array processing techniques that are useful for analyzing volcanic signals, and are important for discriminating volcanic signals of interest from the ambient infrasonic noise field. Finally, **chapter 2** concludes with a brief overview of data highlights during the 2004-2005 initial array deployment, and a discussion of possible sources of infrasonic signals.

Chapter 3 focuses on one of the observations in **chapter 2**, namely that the source of LP seismic events at Mount St. Helens in 2004-2005 also generated impulsive infrasonic pressure signals that travelled through the atmosphere. The event waveforms, spectra, and amplitude ratios (infrasonic pressure to vertical seismic velocity) are characterized by statistical methods applied to thousands of similar LP events. We then investigate several hypotheses for the possible origin of the infrasonic pulses. The most simple hypothesis is that the infrasonic signals result from seismic-acoustic conversion at the ground-air interface, either from the volumetric moment-tensor or vertical-single-force component of the LP events. This is tested using a finite-difference simulation of the seismo-acoustic wavefield. We find that, although shallow buried seismic sources can generate infrasonic signals in the atmosphere, the predicted amplitudes from linear seismic-acoustic coupling are too low, and the characteristic differences in waveforms and spectra cannot be reproduced from a single common point source. We then investigate seismic-acoustic coupling from an extended seismic source consisting of a fluid-filled crack. We again find that simple seismic-acoustic coupling cannot explain the observations, and instead argue that a sudden fluid expansion into shallow, loosely-consolidated dome material from the LP crack source represents a plausible infrasonic source. This indicates that the impulsive infrasonic signal is a record of the broadband trigger component exciting LP resonance, which has important implications for the origin of LP events at Mount St. Helens. In **chapter 3** we also investigate observed variability in infrasonic signal amplitude with respect to the seismic amplitude. This is best explained by atmospheric variability, particularly changes in vertical wind speed gradients in the atmospheric boundary layer.

In **chapter 4** we investigate some unique acoustic signals that were found to accompany large, sustained vulcanian and plinian eruptions at Mount St. Helens and Tungurahua, Ecuador. We propose that these signals represent an infrasonic form of jet noise, generated by the same physical mechanisms that sustain sonic jet noise, but occurring at much larger length-scales and correspondingly longer time scales. This idea is tested by use of the empirically-derived similarity spectra for jet noise.

Chapter 5 describes a two-week field deployment of an infrasound array at the Pu‘u Ō‘ō crater complex and lava tube system, Kilauea Volcano, Hawaii. The aim of the experiment was to investigate the source and propagation effects of continuous infrasonic tremor from Puʻu Ōʻō. We discuss possible sources for the infrasonic tremor, proposing that a broadband component of the tremor results from the collective cloud oscillation of small bubbles in the shallow region of a degassing magma conduit, while harmonic tremor with more sharply-peaked spectra may result from vortex dynamics (Rossiter modes) resulting from steady, laminar degassing through near-surface cavities.

Finally, in **chapter 6** we discuss possible avenues for future research. In particular, we discuss several ways in which the source models initiated in this dissertation could be further tested and evaluated using analogue and numerical experiments, and more dense seismo-acoustic sensor deployments.

2. A broadband seismic and infrasound array deployment at Mount St. Helens

The 2004-2008 eruption of Mount St. Helens (MSH) provided an opportunity to study the infrasonic wavefield produced by an active, silicic stratovolcano. In late October 2004 we deployed two 4-element broadband infrasound arrays to continuously record acoustic signals from MSH. Each array was collocated with a broadband seismometer and weather station. The nearest array, Coldwater (CDWR), was deployed to the northwest of the volcano, ~13 km from the summit. The second array, Sacajawea (SCJW), was deployed ~250 km east of the volcano at a distance where stratospherically ducted acoustic waves may be expected during the winter. This chapter presents an overview of the experimental setup, application of array processing to discriminate volcanic signals of interest from coherent and incoherent ambient noise, and preliminary results from this unique data set. Eruptions on 16 January 2005 and 9 March 2005 produced strong infrasonic signals. The 16 January eruption signal lasted ~9.4 minutes beginning at ~11:20:44 01/16/05 UTC. The 9 March eruption signal lasted ~52.8 minutes beginning at ~01:26:17 03/09/05 UTC, with the main steam and ash venting stage probably lasting ~7.2 minutes. The 9 March signal was an order of magnitude larger in amplitude than the 16 January eruption, and was clearly recorded 250 km east at SCJW. Infrasonic signals associated with long-period (LP) seismic events ("drumbeats") were also intermittently observed. These impulsive signals arrived as acoustic waves that mimic the temporal sequence of the seismic LP events. The acoustic observations provide important constraints for source models of LP events and eruptions.

2.1 Mount St. Helens

2.1.1 Eruptive history

Mount St. Helens (MSH) is a young stratovolcano in the Cascade Range of the Pacific Northwest. The Cascade Volcanic Arc ultimately results from subduction of the Juan de Fuca plate[1] beneath the North American plate, and stretches from Mount Lassen in northern California, USA to Mount Garibaldi in British Columbia, Canada [Tilling et al., 1984]. Mullineaux and Crandell [1981] identified nine eruptive periods in MSH history. The volcano perhaps began erupting ∼300,000 yr ago [Clynne et al., 2008] on a glaciated Tertiary terrain, with explosive, dacitic volcanism lasting for periods of hundreds to thousands of years, punctuated by dormant intervals ranging from a few hundred to ∼15,000 yr in length. At ∼2,500 yr ago, the range of eruptive products expanded to include lava flows of andesite and basalt, pyroclastic flows and lahars of dacite and andesite, and air-fall tephra of dacite, andesite, and basalt. The majority of the modern volcanic edifice is constructed from rocks younger than 2,500 yr. Major dormant intervals in the last 2,500 yr range in length from 200 to 700 yr [Mullineaux and Crandell, 1981].

Eruptions of MSH were witnessed by indigenous people of the Pacific Northwest[2] and settlers between 1831 and 1857, and possibly as early as 1800 [Till-

---

[1] In addition to other remnants of the Farallon plate.

[2] Apparently, MSH was formerly known as "Loo-Wit Lat-Kla" or "Louwala-Clough", translated as "fire mountain" or "smoking mountain" - a hint at its active past [Pringle, 1993].

ing et al., 1984]. However, apart from minor steam explosions in 1898, 1903, and 1921, the volcano remained dormant for 123 years after 1857 until 1980 [Mullineaux and Crandell, 1981]. Prior to 1980, MSH was regarded by the general public as a serene "Fujiyama of America" [Tilling et al., 1984]. The potential for a hazardous explosive eruption had been recognized however [Crandell et al., 1975].

The reawakening of MSH was indicated in March, 1980 by an increase in seismicity levels, including a M4.2 earthquake on 20 March 1980. After two months of activity consisting of phreatic eruptions, heightened seismicity, and rapid deformation of the north flank, the volcano erupted dramatically on 18 May 1980. A M5.1 earthquake and subsequent failure of the upper north slope triggered a lateral blast that destroyed a $\sim$600 km^2 sector of conifer forests, resulting in catastrophic mud flows and floods, and the loss of 57 lives [Christiansen and Peterson, 1981; Voight, 1981; Kieffer, 1981]. In addition to the lateral blast, plinian activity injected ash into the stratosphere ($>$20 km) for more than 9 hours, and audible sounds were reportedly heard within pronounced zones of audibility to as far away as 750 km [Fairfield, 1980]. In addition to audible sounds, radiated infrasound and acoustic-gravity waves propagated globally, and were used to estimate the explosive yield of the main blast [Reed, 1987; Delclos et al., 1990]. VLP and ULP seismic energy resulting from the eruption was documented and modeled by Kanamori and Given [1982] and Kanamori et al. [1984].

The volcano remained active throughout 1980 with a series of smaller magmatic eruptions that produced pyroclastic flows, intermittent growth and destruction of dacitic domes that appeared to act as leaky plugs to gas emissions, and occasional violent gas emissions producing minor plumes between the major eruptions [Christiansen and Peterson, 1981]. Between October 1980 to October 1986, dome growth continued in a series of 17 eruptive episodes [USGS, 2000]. This dome building activity was accompanied by minor explosions (gas and steam bursts) and lahars. By November 1986, dome building had ceased. Between 1986 and 2004, the volcano remained quiescent, except for occasional bursts of increased seismicity and sometimes small explosions from the dome [USGS, 2000]. During this time, a glacier accumulated in the crater (Crater Glacier) [Major et al., 2005].

2.1.2 2004-2008 eruption

MSH began erupting again in late 2004. Seismic unrest started on 23 September 2004 with a swarm of shallow (<2 km) VT events, followed on 25 September by a dramatic increase in earthquake rates and magnitudes [Dzurisin et al., 2005]. This increase in seismicity culminated in a series of small ([3]VEI $\sim$1) phreatic eruptions on 1, 3, 4, and 5 October 2004. Some of these eruptions were referred to as "silent eruptions" owing to the relatively low-levels of seismicity accompanying them [Moran, 2005], prompting questions of whether the eruptions, like the 1980 eruption, would be significant sources of infrasound. Two episodes of harmonic tremor also occurred amidst the eruptions: a high amplitude 50-minute harmonic tremor on 2 October and a less energetic tremor on 3 October 2004. After each tremor or eruption event, seismicity dropped and then subsequently recovered [Dzurisin et al., 2005; Major et al., 2005]. This initial "vent clearing" phase of the eruption ended with a decrease in seismicity after 5 October 2004.

The remainder of the 2004-2008 eruption was characterized by a "dome building" phase consisting of solid extrusion and dacitic dome growth, deformation of Crater Glacier, a sustained sequence of repetitive LP (and sometimes VLP) seismic events, relatively low-level emissions of steam and volcanic gases, and occasional rockfalls resulting from partial collapse of the 2004-2008 lava domes [Scott et al., 2008; Major et al., 2005]. Following October 2004, only two further explosive eruptions occurred: on 16 January and 8 March[4] 2005. The 8 March 2005 event was the largest explosive event of the 2004-2008 MSH eruption and was considered VEI $\sim$2. The data presented in this chapter correspond only to the dome

---

[3] See Table 1.2.

[4] 9 March 2005 UTC.

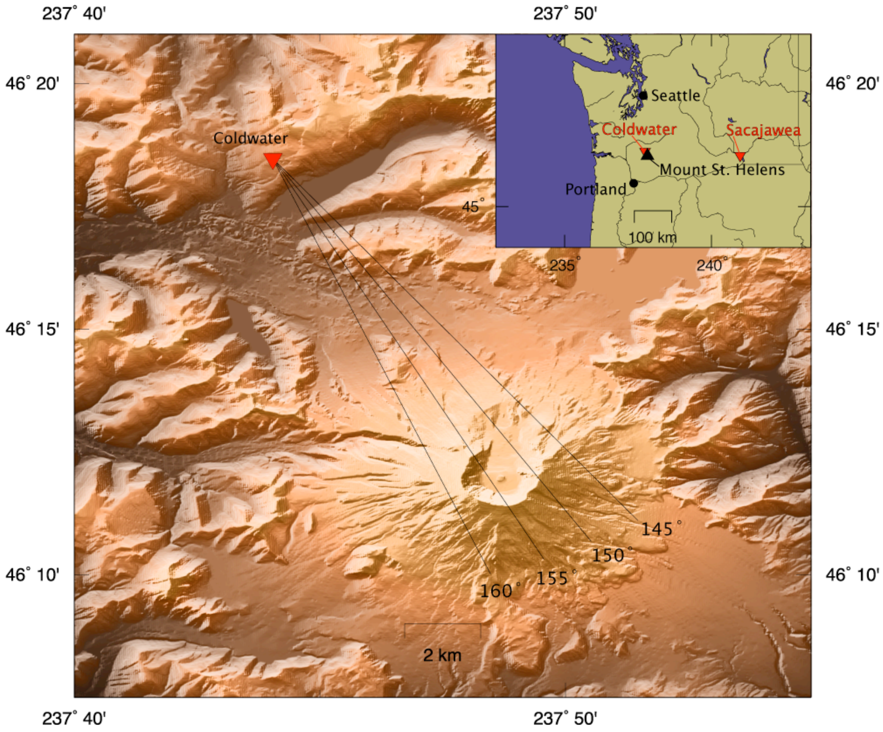

Figure 2.1: Location of the CDWR array (red triangle) with direct line-of-sight to MSH ∼13 km away. Black lines indicate the range of azimuths corresponding to MSH as observed at CDWR. Inset shows the location of both CDWR and SCJW arrays in relation to MSH and the northwestern US.

building stage of the 2004-2008 MSH eruption, as our infrasound data collection commenced on 1 November 2004.

2.2 Array deployment

In late October 2004, UCSD, in collaboration with the Geological Survey of Canada (GSC), deployed two infrasound arrays in order to record signals from MSH. This was a proof-of-concept experiment for the Acoustic Surveillance for Hazardous Eruptions (ASHE) project. The ASHE project seeks to use infrasound signals to provide eruption notification to Volcanic Ash Advisory Centers (VAACs) [Garces et al., 2008]. The deployment resulted in a high-quality and long-duration volcano-acoustic data set. The nearest array, Coldwater (CDWR), was deployed to the northwest of MSH (Figure 2.1), ∼13 km from the summit. This array was located in a young forest owned by the Weyerhaeuser forest products company and provided a direct line-of-sight into the crater, as well as excellent low-noise recordings of acoustic signals from the volcano. The second array, Sacajawea (SCJW), was deployed in Sacajawea State Park near Kennewick, WA, ∼250 km east of the volcano (Figure 2.1 inset). At this location, ray tracing for a typical winter atmosphere predicts that stratospherically ducted acoustic waves from MSH would be recorded at the array. Each array consisted of four MB2000 (DASE/Tekelec) broadband aneroid microbarometers arranged in a centered triangle with an aperture of ∼100 m (Figure 2.2). The MB2000 sensor has a flat response 0.01-27 Hz, a sensitivity of 1 mV/Pa, and a dynamic range of 134 dB. The array element locations are known to within 50 cm accuracy by differential GPS. Connected to each microbarometer were four ∼15 m microporous hoses arranged at ∼90° angles extending radially away from the sensor. These hoses act as a spatial filter to preferentially sum coherent acoustic energy, and filter out spatially uncorrelated noise from wind turbulence [Grover, 1971; Hedlin et al., 2003]. The central element was collocated with a Güralp CMG-40T broadband seismometer and Vaisala temperature, ultrasonic wind velocity, and wind direction sensors. The infrasound data sampled at 40 Hz have a flat response between 100 seconds and 17 Hz. The data were digitized using a 24-bit Nanometrics Polaris Trident digitizer and transmitted in real-time to a hub in Ottawa, Canada and then to UCSD for archiving and analysis. Both arrays were withdrawn from the field on 27 March 2005 as the equipment was needed for another experiment. They were reinstalled on 13 August 2005. In the reinstallation, SCJW was relocated to another site KNWK, in Kennewick, WA, due to site noise conditions at SCJW (see section 2.4.1). KNWK

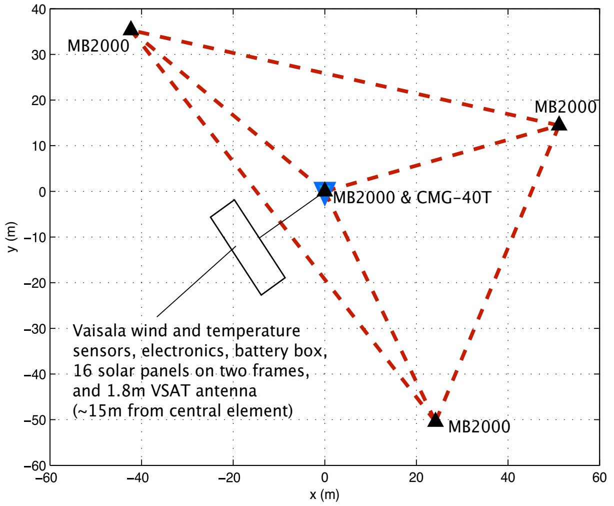

Figure 2.2: Schematic of the CDWR array geometry. Four MB2000 microbarometers (black triangles) are arranged in a centered triangle (depicted by red dashed line). The central MB2000 is collocated with a Güralp CMG-40T broadband seismometer (blue triangle) and met station. Connected to each microbarometer are four ∼15 m microporous hoses extending away from the sensor with 90° angular spacing (not shown) acting as a spatial filter. The SCJW array had a similar layout.

was removed from the field on 18 July 2007. CDWR continued to operate until 12 December 2007, when severe snowfall permanently disrupted telemetry from the array. The equipment at CDWR was removed on 8 July 2008. Dome growth and seismicity at MSH had ceased by late January 2008, and accordingly Cascades Volcano Observatory declared the end of the 2004-2008 eruption.

As outlined in chapter 1, the utility of dedicated infrasonic observations close to volcanoes has been well established [e.g., Yamasato, 1997; Garces and Hansen, 1998; Garces et al., 1998, 1999; Hagerty et al., 2000; Ripepe and Marchetti, 2002; Johnson et al., 2003, 2004; Green and Neuberg, 2005; Johnson and Aster, 2005]. However, to date, most volcano-infrasound studies have focused on small strombolian or weak vulcanian explosions, simply because this type of activity is most abundant and reliable. Consequently, very little is known about the infrasound produced by large eruptions from silicic volcanoes. In addition, a large number of volcano-infrasound studies have acquired data using networks of low-cost microphones deployed near active vents [Johnson et al., 2003]. Data acquired in this way are prone to wind noise and have a limited ability to discriminate volcanic sources of infrasound from other sources [Johnson et al., 2006]. Furthermore, microphones deployed close to vents are at risk of being destroyed during eruptions [Moran et al., 2008], causing data loss at critical moments. The use of infrasound arrays as remote monitoring systems yields significant advantages in wind noise reduction and signal discrimination, as well as the ability to observe explosive eruptions at a safe distance. In addition, the MB2000 microbarometers used in this study are well-calibrated, phase-matched instruments, suitable for quantitative acoustic analysis.

Microbarometer arrays have advantages over conventional networks of microphones. In particular, arrays have the ability to discriminate signals on the basis of azimuth (angle clockwise from North), and conventional or adaptive beamforming techniques (Appendix A) may then be applied to boost the signal-to-noise ratio (SNR) of signals from a particular azimuth. Furthermore, arrays yield the ability to estimate the phase velocity of signals, and therefore separate purely acoustic energy from mechanical shaking of the sensor by seismic energy. This ability to detect, discriminate, and enhance the signal-to-noise ratio of low-amplitude signals also allows the array to be located at a greater distance from the volcanic edifice. In turn, this enables more flexibility in site selection, so the array may be located in a wind-protected site such as a forest [Garces et al., 2003]. In contrast, sensors placed on top of a volcanic edifice are typically exposed to strong and variable winds, often obscuring the signals of interest. The microporous hoses attached to each array element also serve an essential role in suppressing wind noise, which exists at smaller spatial scales than coherent infrasound [Grover, 1971; Hedlin et al., 2003]. This combination of spatial filters, wind-protected site selection, and array processing is effective in separating coherent infrasound from incoherent wind noise. We note that networks show success in recording transient volcano-acoustic signals with high signal-to-noise ratios (see chapter 1). Microbarometer arrays are particularly suitable when recording continuous volcano-acoustic signals (see chapter 5) and when recording signals with low signal-to-noise ratios.

2.3 Array processing

The ambient infrasound field consists of many forms of coherent and incoherent "noise" that are simultaneously recorded with volcanic infrasound signals. A single coherent source of infrasound that is not of specific interest is referred to as an *interferer* [Van Trees, 2002], while the general collection of these interferers forming the coherent ambient background noise field has been termed *clutter* [Hetzer and Garces, 2003]. Array processing can be used to identify coherent signals within incoherent noise and to separate volcanic signals of interest from coherent ambient noise. Below we discuss one useful array processing method and its application to the MSH small-aperture array data. A comparison with other array processing methods can be found in Appendix A.

2.3.1 Progressive multi-channel correlation method

A detailed description of the Progressive Multichannel Correlation Method (PMCC) algorithm can be found in Cansi [1995], Cansi and Klinger [1997] and Garces et al. [2003]. PMCC uses correlation in the time domain to determine the time-delay Δt between different groupings of sensors i, j, k. Detections are assessed by seeking small values of r in the closure relation:

$$r_{ijk} = \Delta t_{ij} + \Delta t_{jk} + \Delta t_{ki}. \tag{2.1}$$

A detection is registered if the consistency r is below a threshold value. This calculation is initially performed on a subset of three array elements, resulting in an

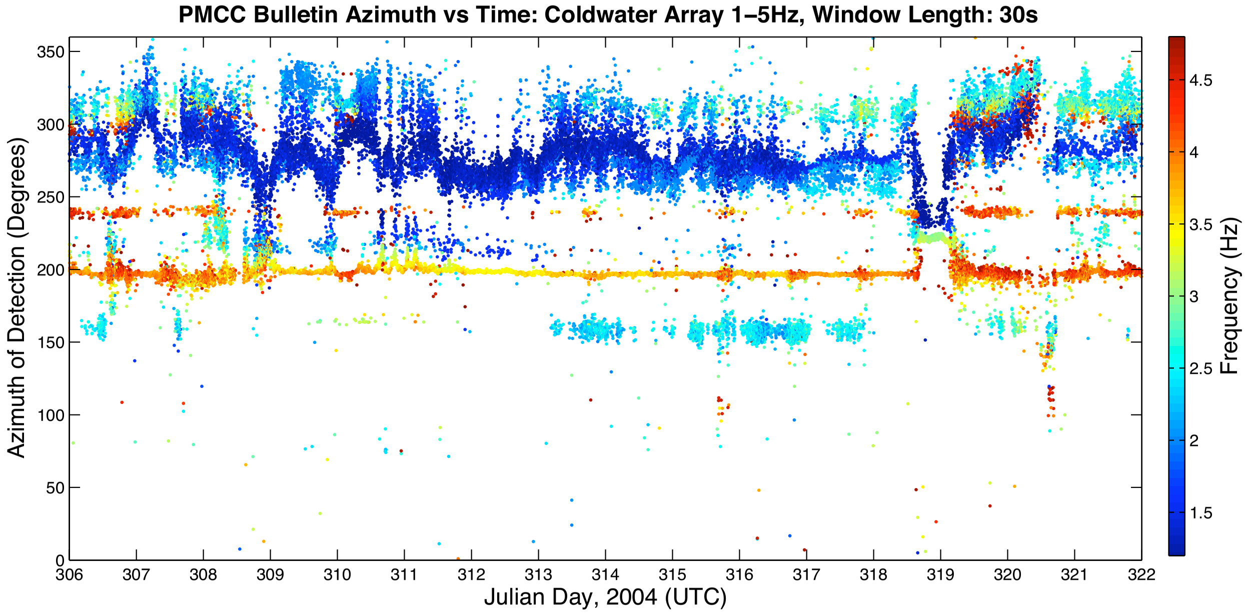

Figure 2.3: Summary of PMCC processing results for CDWR, showing the arrival azimuth and frequency content (color) of coherent infrasound signals during 1-16 November 2004 in the band 1-5 Hz (30 s time window). The continuous sequence of high-frequency (3.5-5 Hz, red, orange and yellow dots) infrasound arrivals at ~200° and ~240° point directly at the nearby settlements of Portland (OR) and Kelso/Longview (WA). The lower-frequency (1 Hz, dark blue dots) arrivals from a distributed source to the west (between 250° and 360°) point towards the Pacific Ocean. The bursts of 2-3 Hz arrivals at ~153° (especially between JD 313 and 318), are LP signals from MSH.

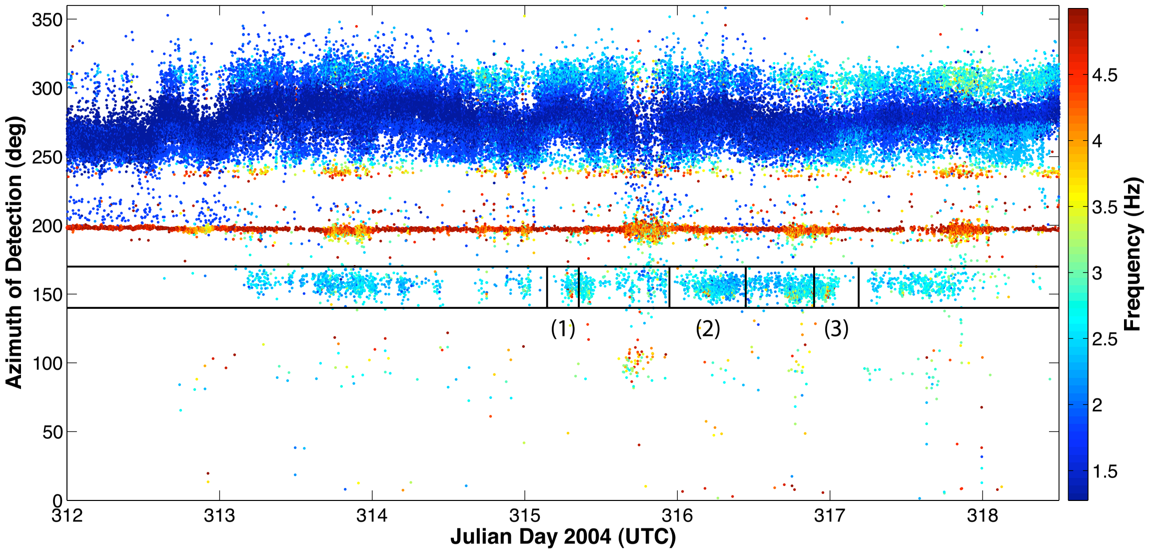

Figure 2.4: Expanded view of Figure 2.3 showing more detail of arrivals (1-5 Hz, 10 s time window) between JD 312 and 319 2004 UTC. Horizontal black lines indicate azimuth limits of MSH signals (140° to 170°). Vertical black lines indicate time range of infrasonic LP arrivals depicted in (1) Figure 2.8, (2) Figure 2.9 and (3) Figure 2.10.

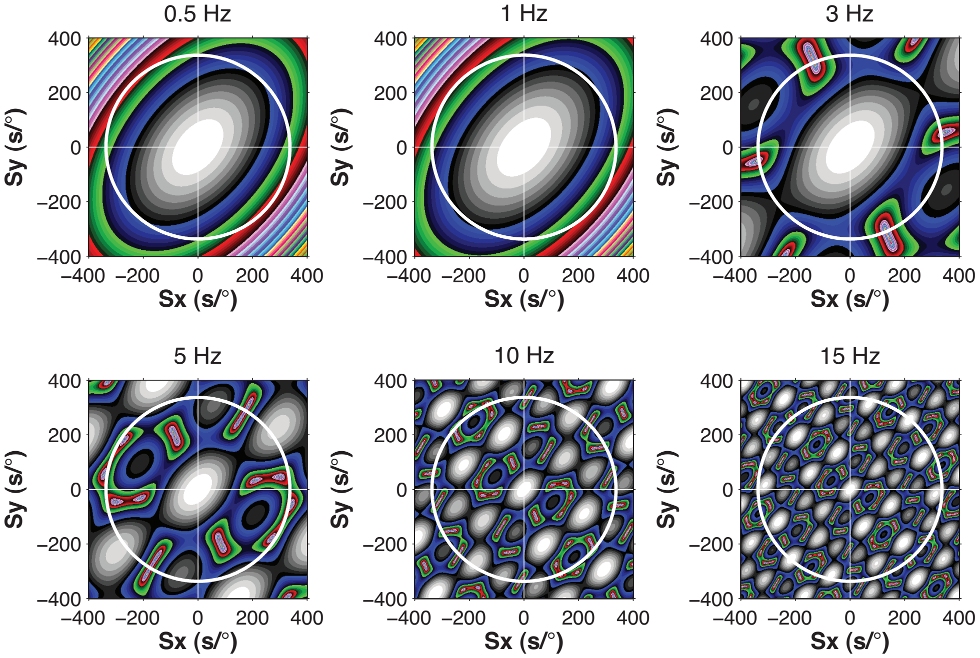

Figure 2.5: CDWR array response to a vertically incident plane wave ($c = \infty$, center) as a function of slowness (s/°) at various frequencies (0.5-15 Hz). The radius of the white circle corresponds to a slowness of 337 s/°, equivalent to a horizontal acoustic sound speed of 330 m/s. Spatial aliasing (indicated by repetition of the central beam pattern at greater radii) begins at a frequency of ∼5 Hz for this array. At 15 Hz, the array is heavily spatially aliased. The ∼SW-NE trend of the array response results from the asymmetrical array geometry (Figure 2.2). Azimuthal resolution is unfortunately worse in the direction of MSH and optimal to the SW and NE (e.g., signal from Portland, Oregon, Figure 2.3).

initial azimuth and slowness estimate. Additional subsets of array elements are then progressively included in the calculation. If this results in a significant variation in the azimuth, velocity, or origin time estimate of a particular detection, the detection is discarded. The PMCC calculation is repeated for a series of time windows at a designated number of frequency bands. The final result is a list of arrival times, azimuth of arrival, frequency content, speed, and amplitude of any coherent energy traveling across the array. PMCC can be run in batch processing mode on long data segments. Any acoustic signals arriving at the desired azimuth (e.g., from MSH) can then be examined in more detail using beamforming (Appendix A) and other conventional signal processing techniques.

Array processing with PMCC enables discrimination between signals from MSH and coherent ambient noise provided that each source of infrasound arrives with a unique azimuth. Differences in frequency content, amplitude, and phase velocity can be used as additional event discrimination criteria. We primarily use arrival backazimuth to initially identify infrasound sources. For example, Figure 2.3 shows a summary of PMCC detections at CDWR between 1-16 November 2004 in the frequency band 1-5 Hz. The plot is typical of the data collected throughout the deployment. At all times we observe high-frequency (3.5-5 Hz) noise at ∼200° (city of Portland) and 240° (town of Kelso/Longview), and lower-frequency (∼1 Hz) signals from the Pacific Ocean (between 250° and 360°). The 2-3 Hz detections at ∼153°, most notably between Julian days 313 and 318, are LP signals from MSH (discussed below). The degree of scatter in the azimuth values for the separate sources is a complicated function of array response (section 2.3.2), signal frequency content, signal-to-noise ratio, signal duration, (cross) wind conditions, source-receiver distance, and point source vs. distributed source effects. For instance, higher frequency signals have a narrower beamwidth, and signals from sources closer to the array would arrive with a greater azimuthal swath than signals arriving from more distant sources. Figure 2.4 shows an expanded view of

Julian days 312-318 with the same data reprocessed using a shorter (10 s) PMCC time window, yielding better time resolution for the signal variability.

2.3.2 Array response

The infrasound arrays deployed at MSH have a maximum aperture of ∼100 m (Figure 2.2), corresponding to one wavelength for an acoustic wave traveling at ∼330 m/s with a frequency of 3.3 Hz. The arrays therefore perform optimally at ∼3 Hz. To evaluate the performance of the array geometry at different frequencies, a plot of the array response to a vertically incident plane wave ($c = \infty$) can be useful. The theory and application of the array response function is fully described in Evers [2008]. The array response for CDWR (Figure 2.2) is shown in Figure 2.5. The response is shown at various frequencies from 0.5 to 15 Hz. A radially symmetric array would have a circular response pattern. However, since the array is elongated in the SE-NW direction, the array response is elongated in the perpendicular SW-NE direction. This means that azimuthal resolution is unfortunately worse in the direction of MSH and is actually optimal to the SW and NE. This partially explains why the signals from Portland, Oregon, (section 2.3.1, Figure 2.3) have a very sharply defined azimuth, while there is greater azimuthal scatter for the signals originating from MSH. Other factors also contribute to these observed differences in azimuthal scatter (section 2.3.1). The white circle shown in Figure 2.5 represents a horizontally traveling plane wave with acoustic speed 330 m/s. Once the central beam pattern for a particular frequency begins to repeat within the radius corresponding to the horizontal acoustic slowness (white circle), the array is spatially aliased. We note that this occurs at ∼5 Hz for the CDWR array, so we cannot expect to estimate signal azimuth and slowness values reliably for frequencies >5 Hz with CDWR or other ASHE arrays with similar geometry. Nevertheless, PMCC performs well for frequencies above the spatial aliasing frequency for many signals analyzed in this study (e.g., see section 2.4.3.2), probably because it incorporates the use of multiple smaller-aperture sub-networks [Cansi, 1995].

2.4 Preliminary analysis of signals

2.4.1 Overview

The CDWR and SCJW arrays were deployed at different distances from MSH to observe signals at close and long range respectively. The aim of this configuration was to evaluate the potential for infrasonic monitoring at regional distances as part of the ASHE project [Garces et al., 2008]. This section presents results from the first deployment (30 October 2004 to 27 March 2005). Data from the second deployment (13 August 2005 to 8 July 2008) are not discussed. Observations at CDWR have included:

1. Infrasound associated with long-period (LP) seismic events ("drumbeats")
2. Infrasound associated with well-documented eruptions on 16 January and 9 March 2005
3. Low-amplitude infrasound occurring prior to the 16 January 2005 eruption
4. Infrasound from rockfalls off the 2004-2008 dacite lava spines [Moran et al., 2008]

As discussed in the previous section, CDWR also recorded coherent ambient noise in the form of low-frequency noise from the direction of the Pacific Ocean, and high-frequency infrasound noise coming from the direction of the city of Portland and other surrounding settlements (Figure 2.3). Given the ∼1 Hz frequency content of the detections coming from the direction of the Pacific, these signals are possibly surf-generated infrasound [Arrowsmith and Hedlin, 2005; Garces et al., 2006], rather than microbaroms [e.g., Willis et al., 2004; Waxler and Gilbert,

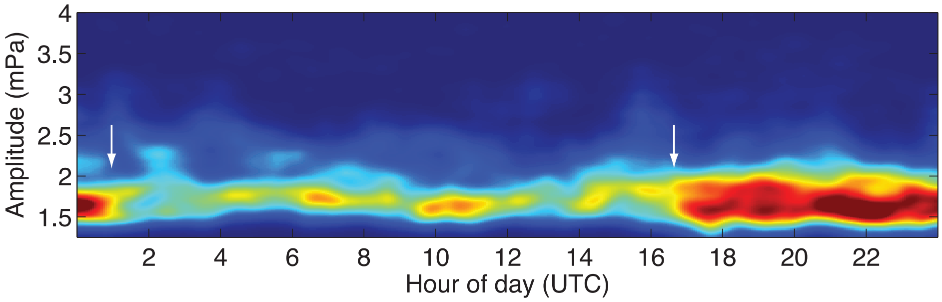

Figure 2.6: Density of PMCC detections (10 s window length) within an azimuth of 180° $\leq \theta \leq 210°$ as a function of hour of day (UTC) at CDWR during 4 to 14 November 2004 (Julian day 309-319). This azimuth swath corresponds to the direction of Portland, OR. The detections are plotted against their amplitude. Warm colors in the plot indicate increasing density of detections. Detections occur throughout the day from this azimuth with little amplitude variation, but more detections are observed between the hours of 16:00 and 02:00 UTC (white arrows), corresponding to 8 am to 6 pm local time (PST). This suggests a cultural origin for the signals.

2006], although it is possible that the energy observed at 1 Hz corresponds to the upper tail of frequencies produced by a lower-frequency oceanic source. The signals from the urban areas (Portland and Kelso/Longview) could be generated by a number of sources, including airplanes during take off and landing at airports, power plants, traffic noise, or other industrial activity. The signals from this azimuth occur throughout the day, but there are more detections originating from this azimuth during the hours of 8 am to 6 pm local time (PST), (Figure 2.6). This suggests a cultural origin for these signals.

SCJW recorded the 9 March 2005 eruption signal, which was the signal with largest amplitude produced by the volcano during the deployment (section 2.4.3.2). SCJW was also subject to continuous infrasound from a nearby wind farm. This noise appears at multiple discrete frequencies and may be analogous to continuous propeller or rotary fan noise [Magliozzi et al., 1991].

2.4.2 Infrasonic long-period events ("drumbeats")

Seismicity during the 2004-2008 eruption of MSH has been characterized by a sustained sequence of long-period (LP) seismic events (0.5-5 Hz, see Chapter 1) occurring beneath the 2004-2008 lava dome. These LP events have also been named seismic "drumbeats" because of their highly repetitive and regular nature and the relatively constant delay time between successive events [Moran, 2005]. We find that these LP events have intermittent infrasonic arrivals. When observed, the infrasonic signals arrive after the seismic event with a velocity and time-delay appropriate for an acoustic wave. A clear example of this occurred in November 2004. Figure 2.3 shows a summary of PMCC detections between 1-16 November 2004 in the frequency band 1-5 Hz. Bursts of 2-3 Hz detections coming from the direction of MSH ($\sim$153°, see Figure 2.1), occur between Julian days 313 and 318 (8 November and 13 November 2004). To examine the waveforms of these signals, Figure 2.7a shows one hour of time-delay beamformed infrasound data from 11 November 2004, compared with the collocated vertical seismic record. Both the infrasound and seismic data were filtered 2-4 Hz to isolate the LP signals. The infrasound beam is computed using a conventional time-delay beamformer [Appendix A.1, DeFatta et al., 1988], where the gain in signal amplitude due to beamforming has been set to unity. The time-delay beamformer is used throughout the remainder of this chapter. Figure 2.7b shows an expansion of 500 seconds of the record shown in Figure 2.7a (indicated by box in Figure 2.7a). In the lower panel of Figure 2.7b, the acoustic and seismic records have been normalized with respect to their amplitude, and the acoustic trace has been time-advanced by 38 seconds. This is the approximate time delay for an acoustic wave following a seismic wave if both were sourced simultaneously at the volcano 13 km away. Once aligned in this manner, the infrasound signals mimic the seismic waveforms in amplitude and sequencing. However, the characteristic long-period coda observed in the seismic waves is less prominent in the infrasonic records. We emphasize that the signals are propagating at acoustic velocities and are not caused by vibration of the pressure sensor by passing seismic waves (see Appendix A.1, Figure A.2). The amplitudes of the infrasonic LP events are typically $\sim 1 \times 10^{-2}$ pascals (Pa).

Not all seismic LP events have associated infrasonic arrivals. In November 2004 (Figure 2.3), the infrasound arrivals were observed for five days between 8-12 November. For the following two days they were absent, after which they reappeared for a further day on 14 November. The seismic channel was constantly recording LP events during this time. This is clearly illustrated in Figures 2.8-2.10, which show the time series data during the time periods where PMCC detections are switching on and off (Figure 2.4). These figures clearly show the infrasonic LP events fading in and out above and below ambient noise while the seismic LP signals are continuously recorded with relatively constant amplitude.

2.4.3 Eruption infrasound

Two eruptions occurred during the November 2004–March 2005 deployment: on 16 January and 9 March 2005. The 16 January 2005 eruption occurred during the night, while the volcano was visually obscured by cloud cover. This eruption was effectively aseismic at many seismic stations (low-amplitude tremor was recorded on seismic stations within the crater [Moran et al., 2008a]). The primary evidence that an eruption had occurred was loss of radio contact with US Geological Survey (USGS) instruments deployed in the summit region, and visual evidence of ash deposits the following morning [Moran et al., 2008a]. The 9 March 2005 eruption was a larger, dominantly phreatic [Moran et al., 2008], explosive eruption that produced a plume of steam and ash in the atmosphere extending ~9 km above the dome. However, this event was still relatively "small" for a volcanic eruption[5] (VEI ~2). The infrasonic signals from both of these eruptions were recorded in full, with an excellent signal-to-noise ratio, on all four sensors

---

[5] See chapter 4 for comparison to larger-volume eruptions at Tungurahua.

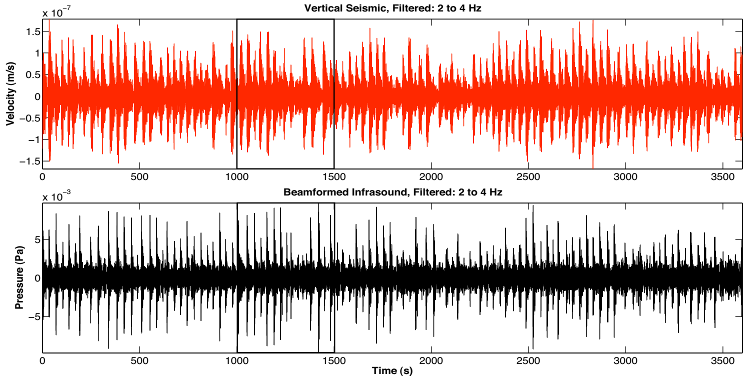

(a) One hour of vertical seismic (top, red) and beamformed infrasound (bottom, black) recordings of LP events (drumbeats), on 11 November 2004. Both series are filtered 2-4 Hz. The similarity of the two records is striking. Box indicates the time range covered in Figure 2.7b.

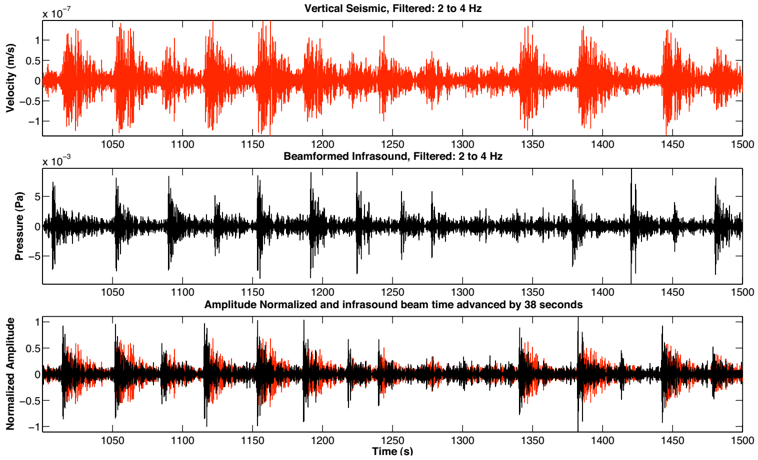

(b) 500 seconds of vertical seismic (top, red) and beamformed infrasound (middle, black) LP events from the time indicated in Figure 2.7a. In the bottom panel, both signals have been amplitude-normalized, and the infrasound beam (black) has been time advanced by 38 seconds (predicted time delay for the 13 km distance) and overlain with the collocated vertical seismic data (red). The infrasound waveforms mimic the seismic waveforms in amplitude and relative arrival time, indicative of a common source mechanism.

Figure 2.7: Long-period events recorded in seismic and acoustic data.

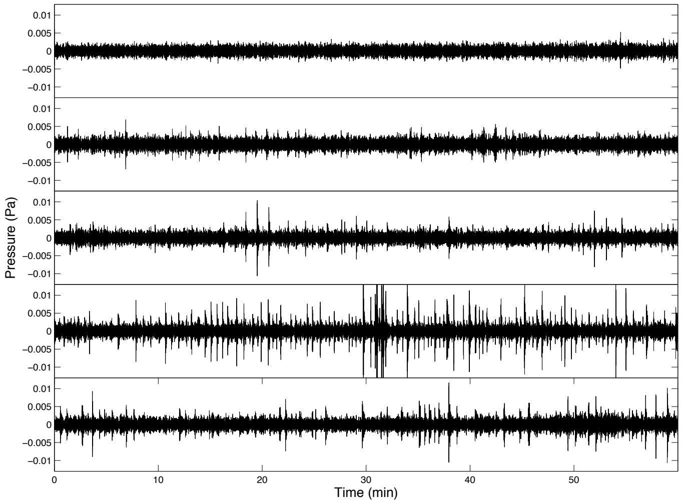

(a) Infrasound beamed data. Infrasonic LP events gradually emerge out of ambient noise and reach maximum amplitude in hour 4.

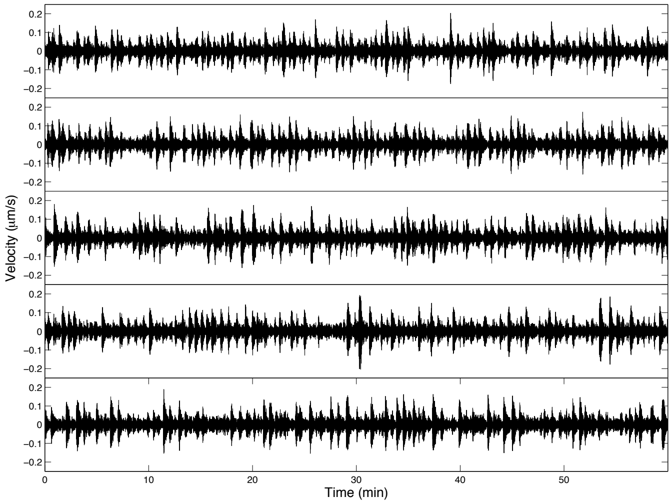

(b) Vertical seismic data. Seismic LP events are observed throughout with only minor fluctuations in amplitude, in contrast to the infrasonic data shown in Figure 2.8(a).

Figure 2.8: CDWR data during the time period 2004/11/10 03:30 to 08:30 UTC. Vertical panels represent consecutive hours of data.

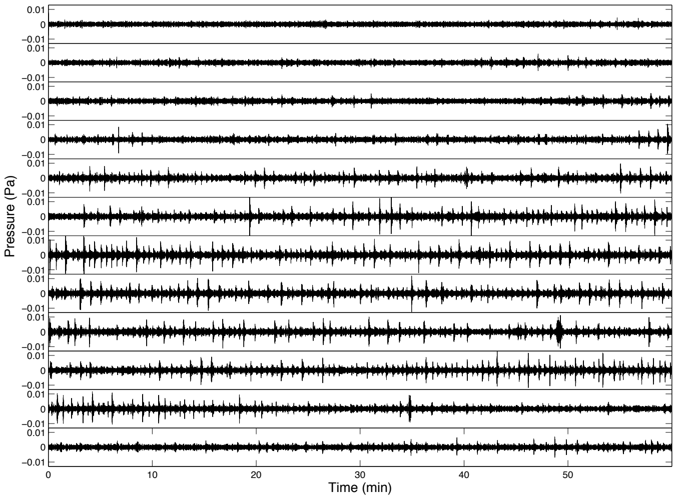

(a) Infrasound beamed data. Infrasonic LPs gradually fade in for the first four hours, are detected continuously during hours 5-10, then begin to fade out during hour 11.

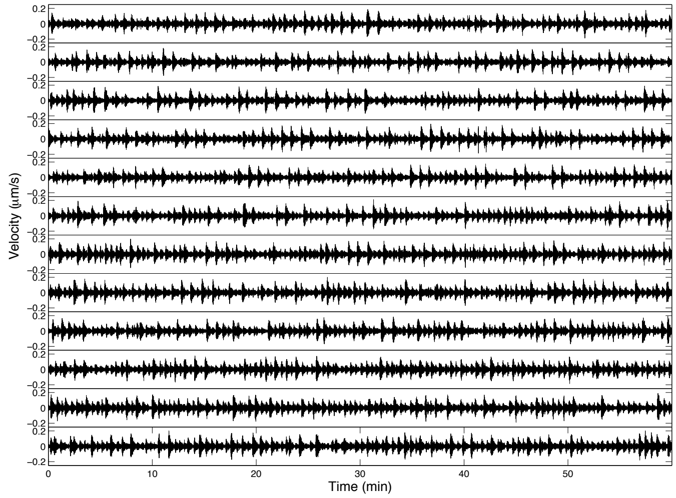

(b) Vertical seismic data. Seismic LP events are observed continuously throughout this time period.

Figure 2.9: CDWR data during the time period 2004/11/10 22:45 to 2004/11/11 10:45 UTC. Vertical panels represent consecutive hours of data.

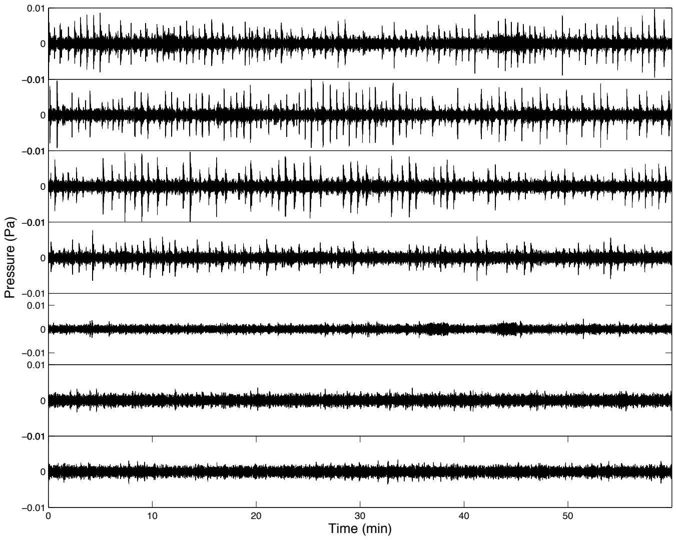

(a) Infrasound beamed data. Infrasonic LPs are present with high amplitude for the first 3 hours, decline in amplitude during hour 4, and then fade into ambient noise by hour 5.

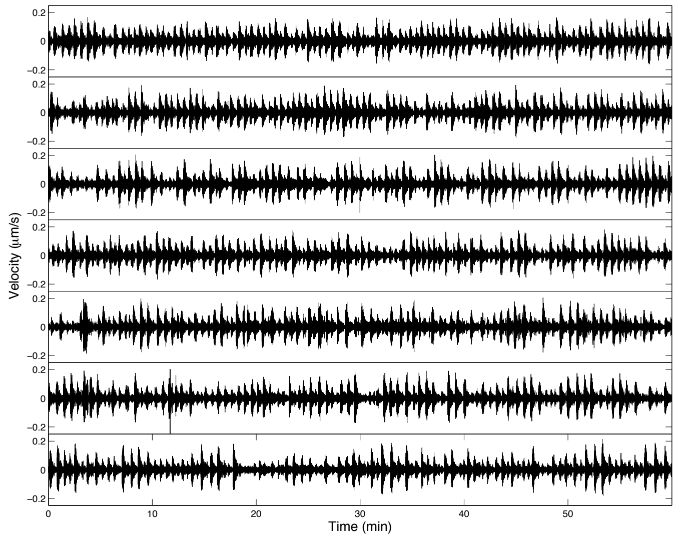

(b) Vertical seismic data. Seismic LP events are observed throughout this time period.

Figure 2.10: CDWR data during the time period 2004/11/11 21:30 to 2004/11/12 04:30 UTC. Vertical panels represent consecutive hours of data.

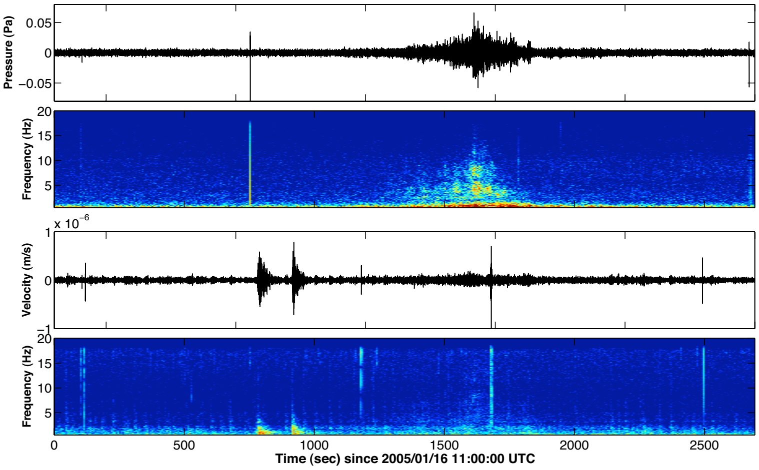

Figure 2.11: Infrasound beam and collocated vertical seismic data for the 16 January 2005 eruption observed at CDWR (filtered 1-10 Hz). The eruption is distinguished by a clear infrasonic signal between ∼1300 seconds and ∼1800 seconds. The eruption is preceded by two seismic LP events without infrasonic arrivals. No significant seismicity is associated with the eruption. Spikes near 750 s in the pressure record and 2500 s in the seismic record are spurious noise.

of the CDWR array (Figures 2.11, 2.14, 2.16). The 9 March eruption was also recorded on all four sensors of SCJW (Figures 2.15, 2.17). In each case, PMCC processing yields a signal arriving directly from the direction of the summit area (Figures 2.12, 2.15, 2.17).

2.4.3.1 16 January 2005 eruption

Figure 2.11 shows the beamformed infrasound data compared with the collocated vertical seismic channel from CDWR during the 16 January 2005 eruption. The data are shown filtered 1-10 Hz. The infrasound signal from the 16 January eruption lasted ∼9.4 minutes starting with an emergent onset at ∼11:21:22 UTC and ending at ∼11:30:47 UTC. Note that the travel time for infrasound from the volcano to the array is ∼38 s, so the inferred eruption onset is ∼11:20:44 UTC. The maximum amplitude of the infrasound signal at CDWR was ∼0.065 Pa.

The 16 January eruption was also preceded by ∼7 hours of coherent infra-

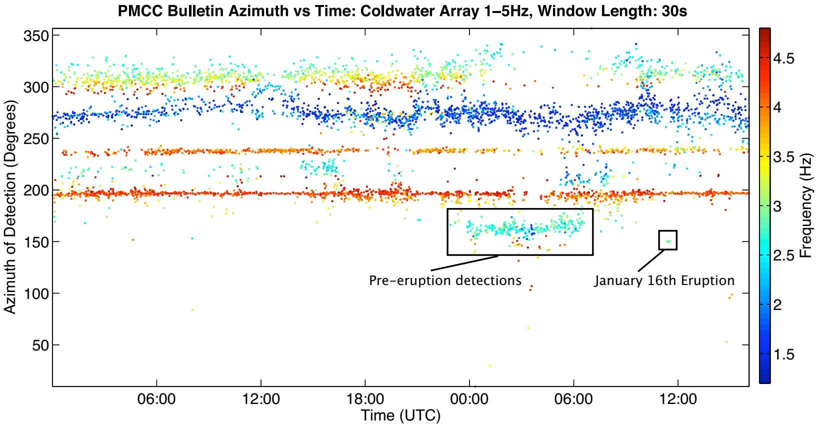

Figure 2.12: PMCC detections ∼36 hours prior to the eruption on 16 January 2005. Each coherent infrasound detection is plotted at its arrival azimuth and color-scaled for its mean frequency. The main eruption is observed as a small cluster of turquoise-blue (∼2-3 Hz) dots at the appropriate time. Beginning at ∼00:00 01/16/05 UTC, a series of coherent infrasound events are detected for ∼7 hours from the direction of MSH (∼160°).

sound detections coming from the direction of MSH. Figure 2.12 shows a summary of PMCC detections at the CDWR array, spanning ∼36 hours prior to the eruption. Each coherent infrasound detection, regardless of amplitude, is plotted as a dot with color-scale corresponding to frequency content. The main eruption is observed as a small cluster of turquoise-blue dots (∼2-3 Hz) at ∼11:21:22 UTC. Beginning at ∼00:00 2005/01/16 UTC, a continuous series of coherent infrasound events are detected for ∼7 hours from the direction of MSH (∼160°). The detections are not associated with an increased level of seismicity and are not infrasound arrivals from LP events. The main burst of activity ends ∼5 hours prior to the eruption. Figure 2.13 shows the results of detailed PMCC analysis on 20 minutes of these signals. The top four panels in Figure 2.13 show the frequency content of the signal vs. time, color-scaled according to the parameter labeled on the right-hand side. Correlation is that between different sensors of the array. Amplitude, azimuth, and speed describe how the signal propagated across the array. The lowermost four panels in Figure 2.13 show the sensor time series data. The events

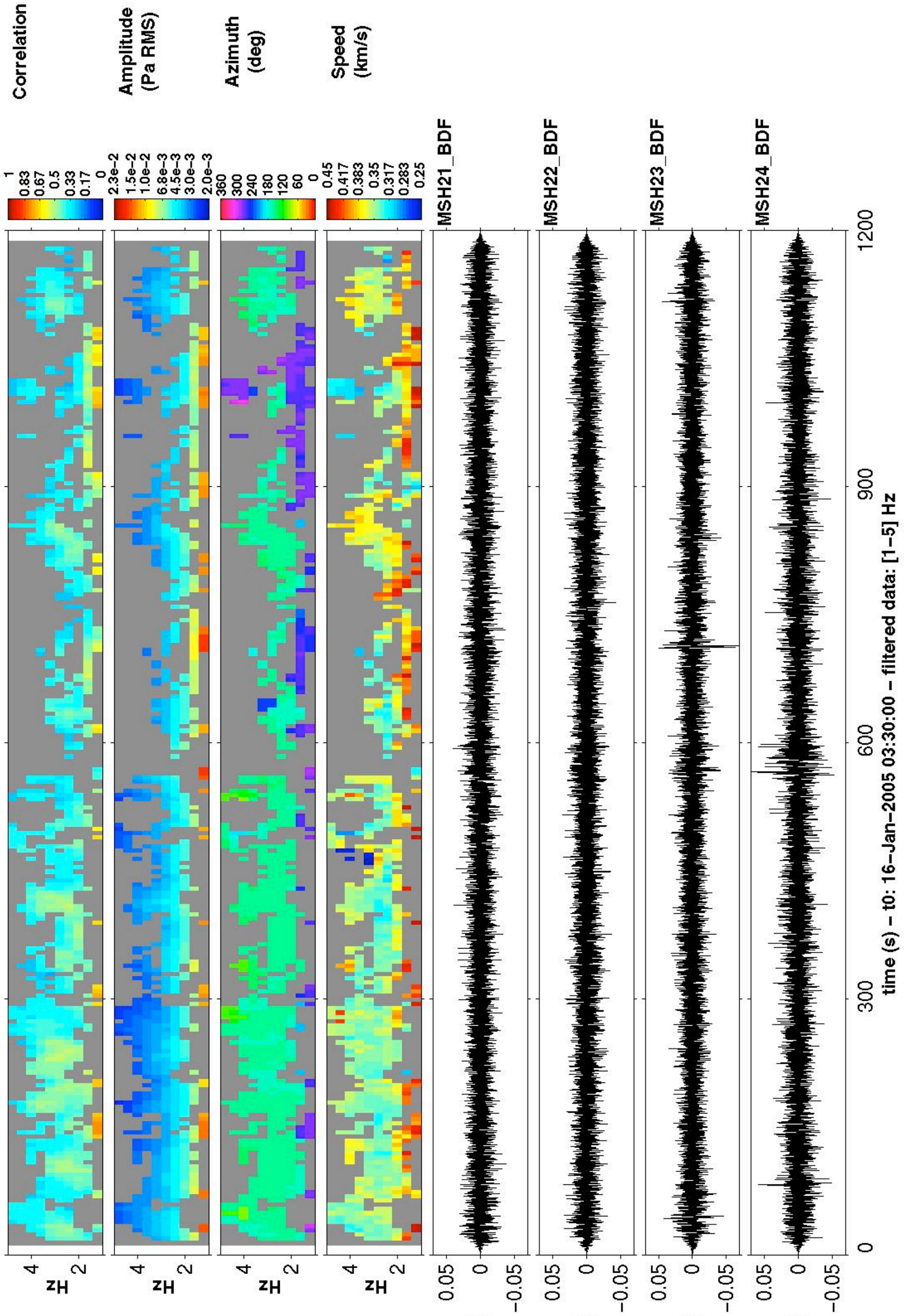

Figure 2.13: PMCC analysis of a 20-minute selection of events preceding the 16 January 2005 eruption (Figure 2.12).

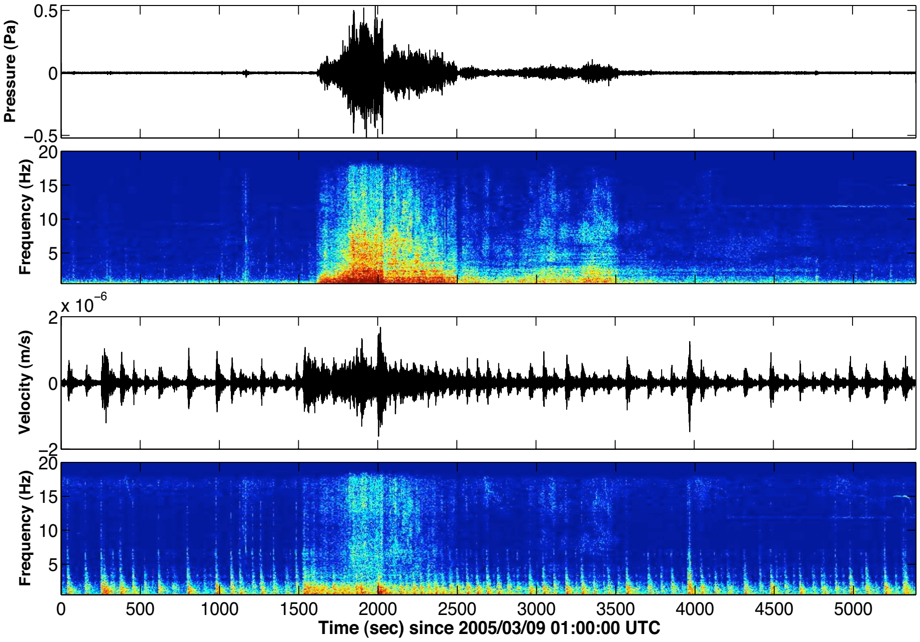

Figure 2.14: Waveforms and spectrograms for the 9 March 2005 eruption sequence observed in collocated infrasound (top) and vertical seismic (bottom) sensors at CDWR. The seismic data consist of highly repetitive, discrete LP events occurring before and after the eruption, and merging much closer together in time during the eruption. In contrast, the infrasound data consist of a quasi-continuous sound observed only during the eruption. An initial ∼7.2 minute stage with increasing amplitude might result from rapid gas thrusting. This amplitude drops off suddenly and is replaced by a ∼45.6 minute coda with three distinct sections (see text) which may reflect the subsequent evolution of the gas plume or less vigorous venting from the volcano. Much of this coda contains spectral peaks at ∼1.5 Hz, ∼2.5 Hz and other frequencies.

have low signal-to-noise ratio and cannot be distinguished in the raw waveform data. However, PMCC clearly detects coherent energy at ∼2-3 Hz coming from the direction of MSH (∼160° indicated by lime green in the azimuth panel). The source of these signals is therefore not well understood.

2.4.3.2 9 March 2005 eruption

Figure 2.14 shows data recorded at CDWR during the 9 March 2005 eruption. The top two panels show the beamformed infrasound data and its cor-

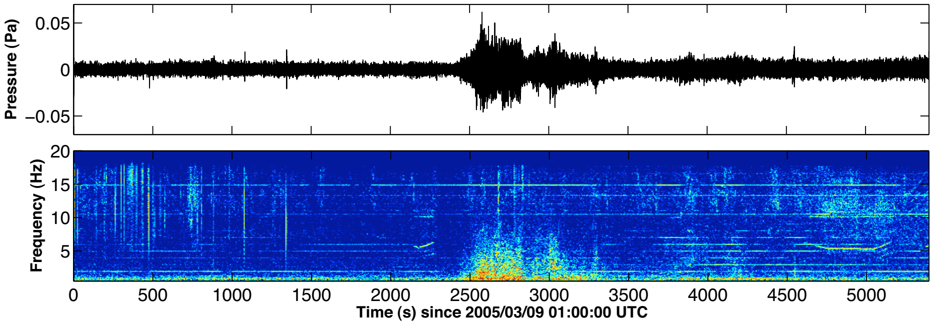

Figure 2.15: The 9 March 2005 eruption signal as observed at SCJW, ∼250 km east of MSH. The beamformed infrasound data are shown filtered 1-5 Hz. Impulsive signals at the beginning of the record are noise on one channel of the array (see Figure 2.17). The lines of constant frequency present in the spectrogram correspond to the continuous harmonic windfarm noise. A clear signal originating from the direction of MSH begins at ∼2500 seconds (∼01:40 UTC), and lasts ∼18 minutes until ∼3500 seconds (∼01:58 UTC).

responding spectrogram, while the lower two panels show the collocated vertical seismic channel and its spectrogram. The time series data are shown high pass filtered >1 Hz. Figure 2.16 shows the results of detailed PMCC analysis on this time window. Figure 2.16 is organized in the same way as Figure 2.13. A coherent signal associated with the eruption, and coming from the direction of MSH (lime green in the azimuth panel) is detected for ∼52.8 minutes from 01:26:55 UTC until 02:19:48 UTC. The lower amplitude detection preceding the eruption at ∼01:20 UTC is not sourced by MSH (wrong azimuth). The 9 March 2005 eruption signal was initially observed at CDWR at 01:26:55 UTC, with a coherent signal detectable for ∼53 minutes until 02:19:48 UTC. The majority of energy is <5 Hz, but the signal is fairly broadband across the infrasound range (signal above noise from ∼0.03 Hz to >10 Hz, see chapter 4). The lower amplitude detection at ∼01:20 UTC is not sourced by MSH (wrong azimuth). The waveform is constructed of four distinct stages. The first stage lasts ∼430 s between 01:26:55 UTC and 01:34:06 UTC (1615 s to 2045 s on Figure 2.14), and consists of a rapid increase in pressure oscillation amplitude up to a maximum of ∼0.54 Pa, followed by a sudden drop in pressure amplitude. We interpret this to be the duration of rapid gas thrusting, during which the volcano was ejecting steam and ash at high velocity. At 2045 s, a second broadband packet of energy is present, abruptly terminating at 2515 s. This is followed by a third, lower amplitude stage (2515 s to 3520 s) with spectral structure evolving between ∼2900 s and 3520 s to include higher frequencies. Finally, after 3520 s, a low amplitude coda rings on for ∼20 minutes, which is clearly identified in the PMCC analysis (Figure 2.16).

There is some spectral structure evident in the latter three stages. Well-defined spectral peaks at ∼1.5 Hz, and ∼2.5 Hz are present in every stage after the initial ∼430 s “gas thrusting” stage along with other transiently appearing spectral peaks. The peaks at ∼1.5 Hz and ∼2.5 Hz are most visible in the final ∼20 minute phase (Figure 2.14). These subsequent stages may correspond to either the evolution of the gas plume as it continued to generate infrasound by turbulent convection, or a lower amplitude jetting noise associated with slower, steadier venting.

Figure 2.15 shows the beamformed infrasound at SCJW. The time series is shown bandpass filtered between 1 and 5 Hz. Impulsive signals at the beginning of the record are noise local to channel 1 of the array (Figure 2.17). The lines of discrete constant frequency present in the spectrogram are a record of continuous windfarm noise. A clear signal originating from the direction of MSH begins at ∼01:40 UTC, and lasts ∼18 minutes until ∼01:58 UTC. The signal is easily distinguished from the background noise by the arrival azimuth derived from PMCC and its spectral signature (Figure 2.17). The spectral signature is similar to that recorded at CDWR, except that much of the energy >10 Hz has been attenuated. In the time domain, approximately the same waveform structure is apparent but with a lower amplitude of ∼0.05 Pa, and the detectable signal is shorter in duration. The signal arrives at SCJW ∼13 minutes later than at CDWR, which is consistent with the ∼250 km geographic distance between the array sites.

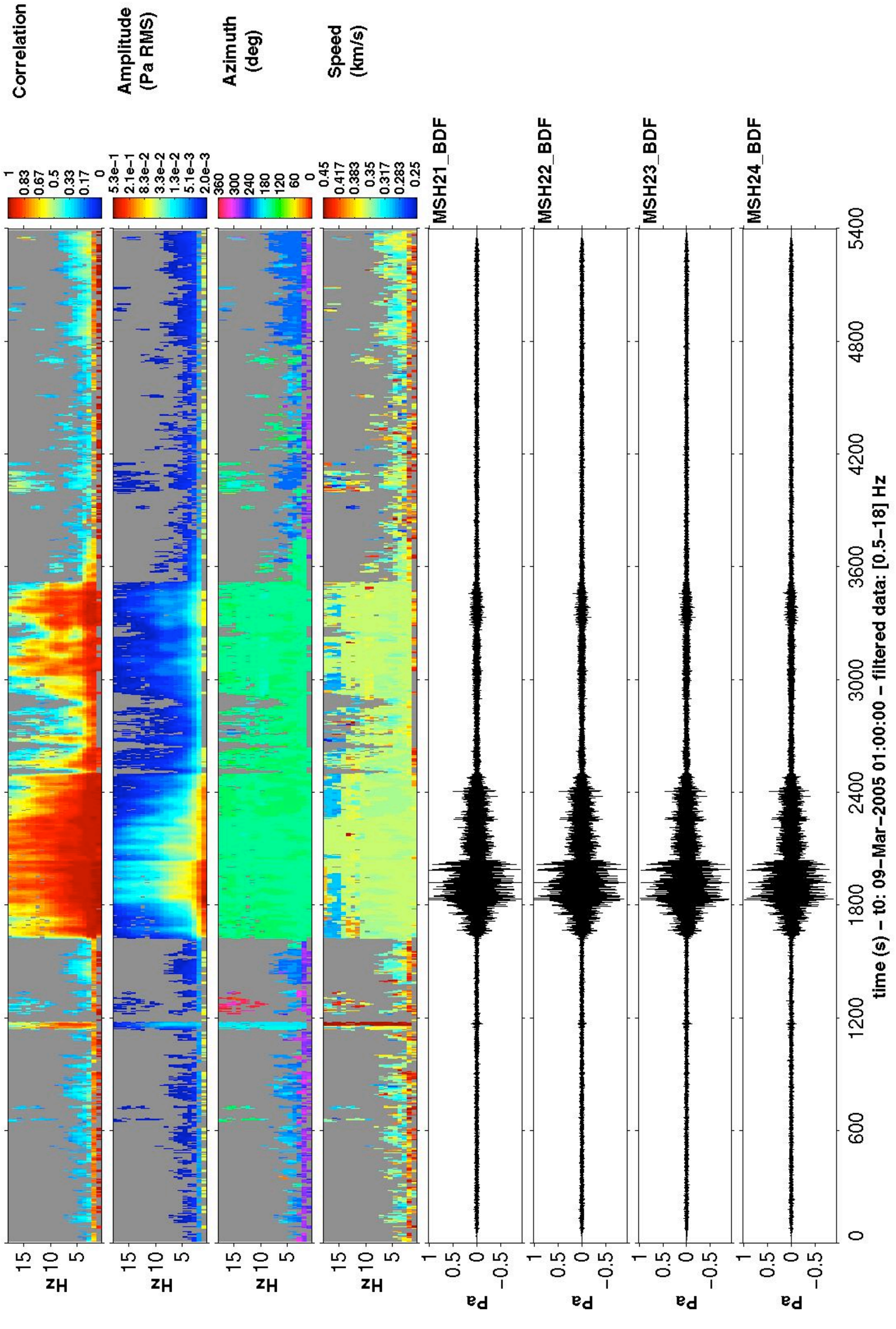

Figure 2.16: Detailed PMCC analysis of the 9 March 2005 eruption signal. Time range is identical to that shown in Figure 2.14.

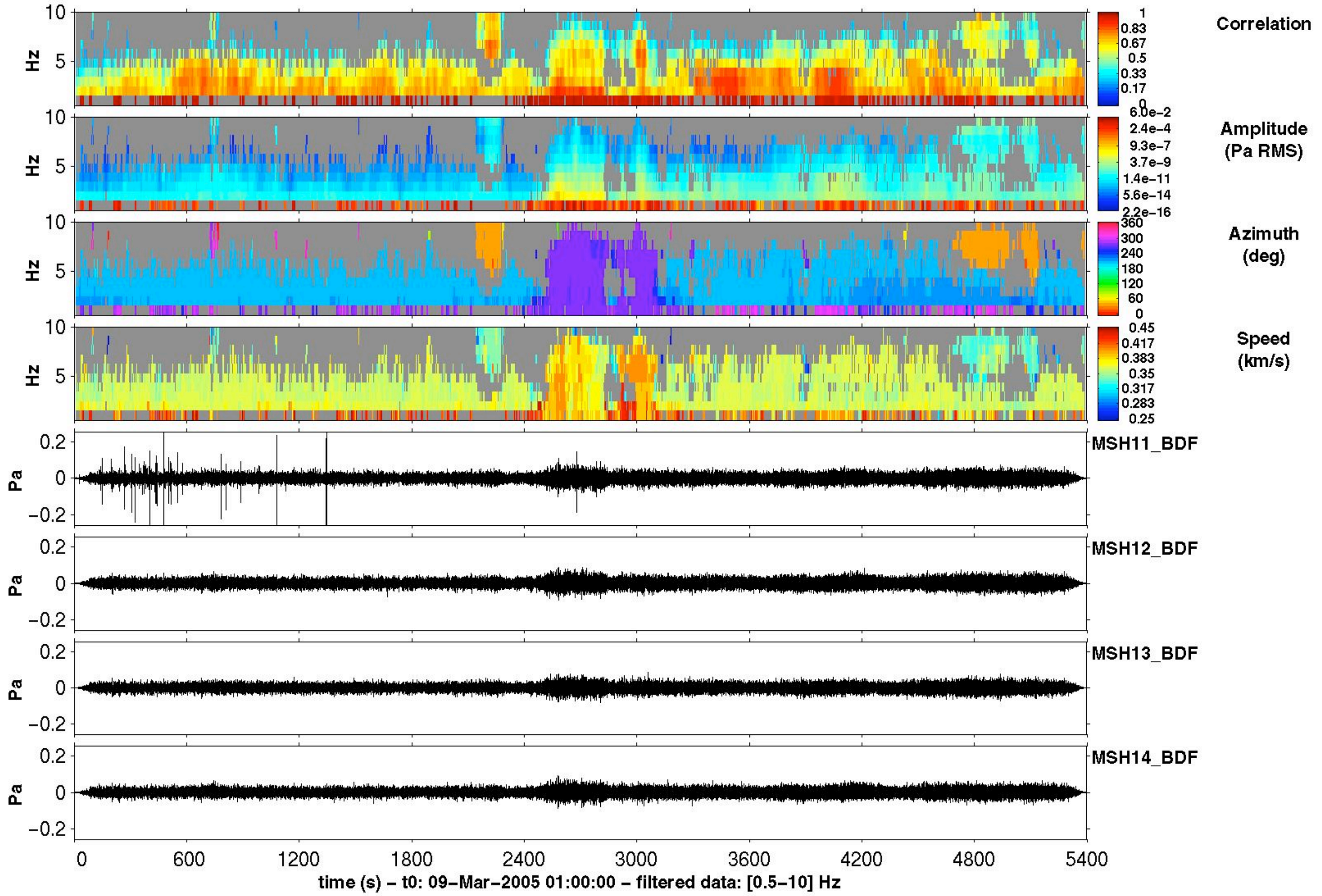

Figure 2.17: Detailed PMCC analysis of the 9 March 2005 eruption signal observed at SCJW ~250 km from MSH. A coherent signal associated with the eruption, and coming from the direction of MSH (purple in the azimuth panel) is detected for ~18 minutes from ~01:40 UTC until ~01:58 UTC.

In addition to CDWR and SCJW, this eruption was recorded by two other stations. The first, SEP, was a microphone deployed in the MSH crater by the Cascades Volcano Observatory (USGS). SEP was destroyed during this eruption [Moran et al., 2008a], but the telemetered data capture the origin time (emergent onset at ∼01:26:20 UTC) and the first ∼90 s of the eruption (Figure 2.18). The eruption was also recorded at the IMS station I56 Newport (I56US) (Figure 2.19) [Campus, 2006], with relatively low signal-to-noise ratio. The celerity (total horizontal distance travelled from source to receiver divided by the total travel time) of the recorded signals is ∼0.3 km/s (Figure 2.18), which is typical for infrasonic energy ducted in the stratosphere [Garces and Le Pichon, 2009]. Stratospheric propagation of the 9 March 2005 signal is also predicted by modeling with a parabolic equation method (RAMPE) [Lingevitch et al., 2002] and 2D ray tracing through G2S atmospheric specifications [Drob et al., 2003], with attenuation coefficients given by Sutherland and Bass [2004] (Figure 2.20, *codes provided by Douglas P. Drob, NRL*). We note that Le Pichon et al. [2009] showed that ∼80 % of global infrasound detections at IMS stations in the 0.2-2 Hz bandpass are associated with downwind propagation in the dominant stratospheric wind direction. The dominant stratospheric wind direction during the 9 March 2005 event was from west to east, resulting in efficient stratospheric ducting to the east, and enabling this relatively low amplitude signal to propagate to the large range of ∼445 km (I56US).

2.5 Discussion

2.5.1 Infrasonic long-period events

The observation that the source that generates LP seismic events also generates infrasound is of high significance. In November 2005, an observer standing in the summit region reported feeling ground vibrations from seismic LP events, and

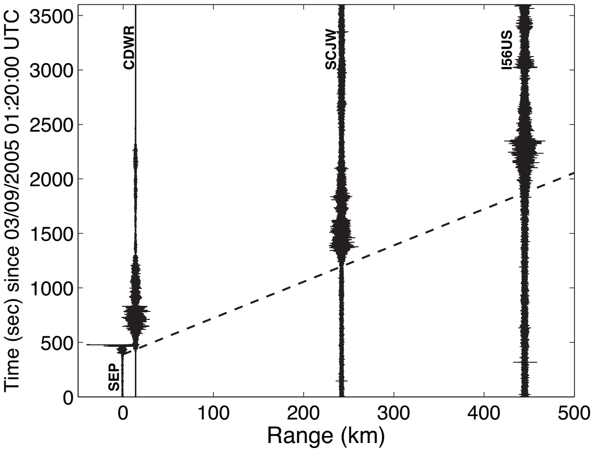

Figure 2.18: Record section of infrasound data for 9 March 2005 phreatic eruption at MSH. Time series at arrays CDWR, SCJW and I56US are time-domain beams. Station SEP in the crater of MSH was destroyed by the event. The signal travelled with a celerity of approximately 300 m/s (dashed lined), which is typical of stratospherically ducted arrivals.

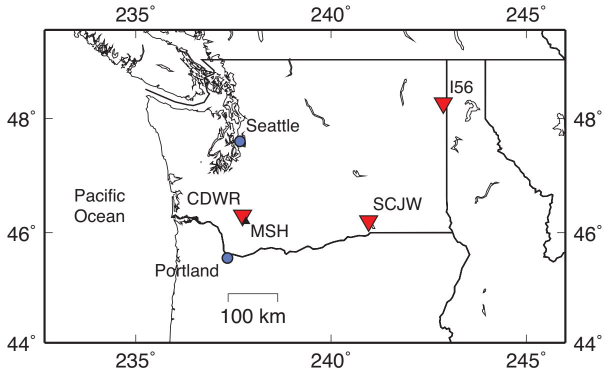

Figure 2.19: Location of IMS station I56 (inverted solid red triangle) ~445 km to the northeast of MSH. CDWR and SCJW are also shown (inverted solid red triangles). SEP was located in the crater of MSH (black triangle).

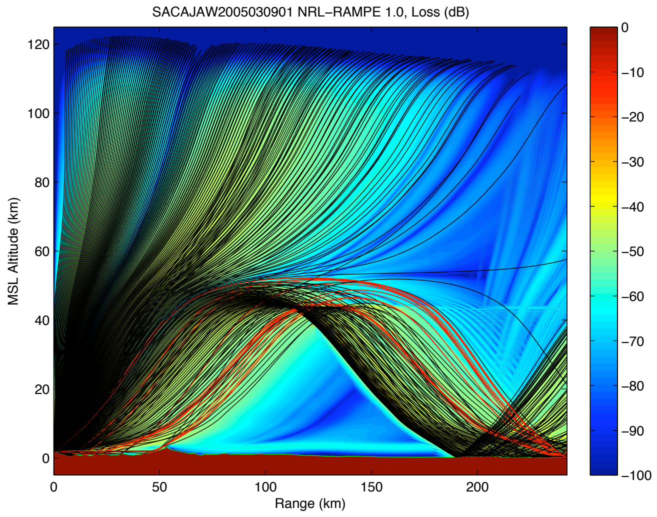

(a) MSH to SCJW: arrivals are predicted at SCJW (242 km range) as a first stratospheric bounce.

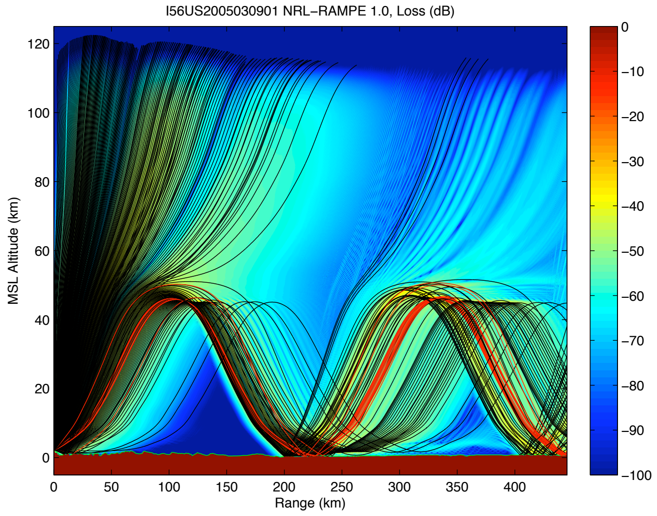

(b) MSH to I56 Newport: predicted arrivals at I56 (445 km range) correspond to a second stratospheric bounce.

Figure 2.20: RAMPE model runs (color scale, loss in dB) with G2S atmospheric specification for propagation from MSH to Sacajawea and MSH to IMS station I56 (Newport) at 01:00 UTC 9 March 2005, overlain by 2D ray tracing results (solid lines). Altitude is in km above mean sea level (MSL). Rays terminate in the thermosphere when the loss exceeds 120 dB. Eigenrays (rays connecting source to receiver) are shown in red.

hearing associated acoustic “booms” (Seth Moran, CVO/USGS, personal communication). This suggests that close to the source, at least some of the energy was also in the audible acoustic range (>20 Hz). LP events are often modeled by an initial pressure excitation mechanism, followed by a coda resulting from resonance in a fluid-filled conduit or crack [Chouet, 1985, 1988, 1992, 1996a; Garces, 1997; Neuberg et al., 2000]. LP events may also be considered the impulse response of the resonant tremor-generating system [Chouet, 1985], although the excitation mechanisms involved in both cases remain incompletely understood [Chouet, 1996a]. The absence of a prominent infrasound coda (Figure 2.7b) may indicate that the infrasound is more representative of the excitation mechanism of the LP events. Also, it is necessary to explain the observation that not all seismic LP events have associated infrasonic arrivals (Figure 2.3, or compare Figures 2.7b and 2.10).

The most plausible explanations for the infrasonic arrivals from LP events can be broadly categorized as follows:

1. direct seismic-acoustic conversion at the ground-air interface from a buried source,
2. vertical motions or pistoning of the ground surface or lava dome above a buried LP source,
3. a pressure excitation function in a shallow-buried fluid cavity that produces acoustic oscillations in the fluid (leading to seismic LP events), and a pressure wave in the air (leading to the infrasound), or
4. a pressure disturbance accompanied by a rapid release of gas, which travels to the surface through a permeable medium and generates infrasound.

In cases (1) and (2), the cessation and reemergence of infrasound may be attributed to factors influencing the propagation of the seismic wave to the ground surface or the amount of pistoning at the surface. Examples of factors include changes in the source depth or magnitude, or changes in the impedance contrast at the ground-air interface. In cases (3) and (4), the switching on and off of LP infrasound may possibly reflect changes in the permeability of the system. Observation of infrasonic arrivals might indicate that the pathways for infrasound or gas transmission are more open, while absence of infrasound might indicate that the pathways are sealed. Further work will need to focus on the role of earthquake magnitude and location (particularly depth) in influencing seismic to acoustic coupling, and a more detailed comparison of the waveforms and spectra of seismic and infrasonic LP events is required (see chapter 3).

Alternatively, variations in the detection of infrasonic LP events may be controlled by variations in atmospheric conditions between the volcano and CDWR, or a change in the background noise level at the array. In many cases infrasonic LP events emerge and disappear without correlation with wind speed or direction, temperature, or a change in the background noise level at the array, and without change in detections from other sources (Figure 2.3). This suggests that this is not a propagation or a detection SNR effect. We note that moderate winds induce azimuthal scatter in all detections at the array simultaneously, while very strong winds result in the loss of all coherent signal. This said, the wind sensor was collocated with the array in a dense forest, and was somewhat protected from regional winds. The data from this sensor do not represent wind at altitude along the path between the source and receiver. The switching on and off of LP infrasound is further investigated in chapter 3, while infrasonic propagation effects at this scale are further discussed in chapter 5. In future experiments, data on the atmospheric conditions along the propagation path between the volcano and the array would help to assess propagation effects at this scale ($\sim$10 km, mesoscale-microscale). This question could have been addressed more easily at MSH with the addition of an exposed wind sensor between the volcano and CDWR, and the addition of more infrasonic sensors placed closer to the volcano. We note that, although some microphones were located around MSH [Moran et al., 2008], noise conditions and the short seismic-acoustic time delay at these sites made it difficult to distinguish between true acoustic energy and vibration of the microphones by seismic ground motion (section 3.2.2). An array of sensors may have been able to identify true acoustic signals within a few hundred meters of the source.

2.5.2 Eruption infrasound

The observation of clear infrasonic signals associated with the 16 January and 9 March 2005 eruptions is interesting from both a scientific and monitoring perspective. Infrasound places tight constraints on the exact timing of eruptive activity because a drastic surge in infrasonic energy coincides with the eruption duration. The 16 January eruption further demonstrates the utility of infrasound observations for monitoring, as the eruption was essentially aseismic, and visually obscured by cloud cover. In contrast, the acoustic record reveals a 7-hour duration of heightened infrasound activity prior to the eruption, and a clear record of the eruption. In addition, the observation of the 9 March eruption at SCJW ($\sim$250 km away) and I56 ($\sim$450 km away) suggests that infrasound could be used as a long range monitoring tool for modest-sized eruptions with relatively small aperture arrays.

Infrasound also provides a means to compare quantitatively the power of eruptions [Johnson et al., 2003]. At CDWR, the 16 January eruption signal reached a maximum amplitude of $\sim$0.065 Pa. Assuming a spherical spreading factor of $1/r$ for the 13.41 km distance from volcano to array, the amplitude $\sim$1 m from the source would have been $\sim$872 Pa, or $\sim$153 dB re 20 μPa. If this sound were in the audible frequency range, it would be as loud[6] as a jet engine during takeoff. The amplitude of the 9 March eruption signal reached 0.54 Pa, an order of magnitude larger than that of the 16 January eruption. In this case, using $1/r$ to correct for

---

[6] Note that the threshold of human hearing 20 μPa is here used as a reference pressure even though the acoustic signals considered are infrasonic and therefore inaudible to the human ear.

spherical spreading, the amplitude ∼1 m from the source would have been ∼6571 Pa, or ∼171 dB re 20 μPa.

Figures 2.11 and 2.14 also reveal that acoustic signals from eruptions are notably different from the seismic signals. For the 9 March eruption (Figure 2.14), the acoustic signal consists of a four-stage, broadband, quasi-continuous signal with evolving spectral structure. In contrast, the seismicity consisted of an intense swarm of individual LP events, merging closer together in time during the eruption. The acoustic data may therefore represent the shallower processes of pressure release, gas and ash venting, and perhaps subsequent evolution of the volcanic plume (see chapter 4), and not the deeper processes that act as seismic sources. In this respect, joint seismic and acoustic studies are capable of recording a more complete representation of the wavefields generated by a volcano. Waveform modeling of joint infrasound and seismic observations may therefore lead to an enhanced understanding of the physics of the eruption process.

2.6 Conclusions

Infrasonic and seismic data analysis result in complementary perspectives on eruptive activity. MSH almost continuously generated infrasound during the November 2004–March 2005 deployment. Infrasound associated with seismic long-period (LP) events must be sourced simultaneously, but not necessarily by simple seismo-acoustic coupling and conversion. Models of the source mechanism for LP events should therefore explain the radiated infrasound. In contrast, infrasound observed during eruptions is of different character to simultaneous seismic data. The active gas and ash venting stage of the eruption appears to generate a very large, unambiguous surge in infrasonic energy, which can be detected at long range (up to ∼450 km in the case of the 9 March 2005 VEI 2 eruption). In contrast, the seismicity observed during the 9 March 2005 eruption was of about the same amplitude as the preceding seismicity. Infrasound can therefore play a key role in separating surface processes from deeper processes, and in identifying the timing and vigor of eruptions.

Chapter acknowledgments

This experiment would not have been possible without the Geological Survey of Canada (the GSC). The GSC provided most of the equipment for this experiment. The team is led by David McCormack (Head, Earthquake Tsunami and Volcano Hazard Assessment and the Nuclear Monitoring Program). Phil Munro helped in locating the arrays and obtaining permission to use the land. Calvin Andrews, John Ristau, Issam Al-Khoubbi, Jim Helferty, Kadircan Aktas, and Mike Patton deployed the arrays. Tim Cote and Luc Saumure provided assistance with data acquisition and archiving. Clint Coon and Eric Blum (UCSD) helped to deploy the arrays. David Norris (BBN) performed ray tracing to determine the SCJW location. Discussions with David Fee, Sara McNamara, Claus Hetzer, Seth Moran, Kris Walker, and David Green helped to shape ideas. RAMPE and 2D ray tracing codes were provided by Douglas Drob (NRL). Chapter 2, in part, contains material as it appears in Matoza, R.S., M.A.H. Hedlin, and M.A. Garces (2007), An Infrasound Array Study of Mount St. Helens, *J. Volcanol. Geotherm. Res.*, **160**, 249–262, doi:10.1016/ j.jvolgeores.2006.10.006.

3. The source of infrasound associated with long-period events at Mount St. Helens

During the early stages of the 2004-2008 Mount St. Helens eruption, the source process that produced a sustained sequence of repetitive long-period (LP) seismic events also produced impulsive broadband infrasonic signals in the atmosphere. To assess whether the signals could be generated simply by seismic-acoustic coupling from the shallow LP events, we perform finite-difference simulation of the seismo-acoustic wave field using a single numerical scheme for the elastic ground and atmosphere. The effects of topography, velocity structure, wind, and source configuration are considered. The simulations show that a shallow source buried in a homogeneous elastic solid produces a complex wave train in the atmosphere consisting of P/SV and Rayleigh wave energy converted locally along the propagation path and acoustic energy originating from the source epicenter. Although the horizontal acoustic velocity of the latter is consistent with our data, the modeled amplitude ratios of pressure to vertical seismic velocity are too low in comparison with observations, and the characteristic differences in seismic and acoustic waveforms and spectra cannot be reproduced from a common point source. The observations therefore require a more complex source process in which the infrasonic signals are a record of only the broadband pressure excitation mechanism of the seismic LP events. The observations and numerical results can be explained by a model involving the repeated rapid pressure loss from a hydrothermal crack by venting into a shallow layer of loosely consolidated, highly permeable material. Heating by magmatic activity causes pressure to rise, periodically reaching the pressure threshold for rupture of the "valve" sealing the crack. Sudden opening of the valve generates the broadband infrasonic signal and simultaneously triggers the collapse of the crack, initiating resonance of the remaining fluid. Subtle waveform and amplitude variability of the infrasonic signals as recorded at an array 13.4 km to the NW of the volcano are attributed primarily to atmospheric boundary layer propagation effects, superimposed upon amplitude changes at the source.

3.1 Introduction

Shallow (<2 km) long-period (0.5-5 Hz) seismicity at volcanoes, including individual long-period (LP) events and tremor, is often attributed to the activity of magmatic and hydrothermal fluids in subsurface conduits and cracks [e.g., Chouet, 1985, 1988; Garces and McNutt, 1997; Neuberg et al., 2000; Kumagai et al., 2005]. LP events are transient, volumetric signals, with a broadband onset lasting ∼10 s, followed by a decaying harmonic coda lasting tens of seconds to a few minutes and containing pronounced spectral peaks that are independent of azimuth and distance to the source [Chouet, 1996a]. This is usually interpreted as a broadband pressure excitation mechanism, followed by the resonant response of a fluid-filled cavity. Although the fluid response is understood quantitatively in terms of solid-fluid interface waves or "crack waves" [Chouet, 1986; Ferrazzini and Aki, 1987], the physics of the driving mechanism initiating LP resonance remains a major challenge [Chouet, 2003].

The 2004-2008 eruption at Mount St. Helens was accompanied by a sustained sequence of shallow, repetitive LP events that were also named "drumbeats" owing to their precise regularity and high degree of waveform similarity [Moran et al., 2008b]. Although initially ascribed to stick-slip motion along the margins of the solid lava extrusion [Iverson et al., 2006; Harrington and Brodsky, 2007], these earthquakes were shown to have all-dilatational first motions where distinguishable, common spectral peaks observed on multiple stations, long-duration oscillatory source-time functions, and a volumetric moment tensor, which are all characteristic of LP events [Waite et al., 2008]. The moment tensor inversions of a subset of these LP events were found to be consistent with a sub-horizontal, steam-filled crack located at the elevation of the old 1980s crater floor and directly below the new lava dome (Figure 3.1). Inversion of very-long-period (VLP) events that accompanied some of the LPs also pointed to reaction forces in a dike-sill composite located ∼400 m to the NW of the LP source (underneath the old 1980s lava dome), and ∼250 m deeper [Waite et al., 2008].Waite et al. [2008] proposed that the LP source may consist of a shallow hydrothermal crack, filled with a mixture of meteoric and juvenile steam, and pressurized by the magmatic activity. Periodically, pressure is lost, causing the crack to partially collapse and resonate (LP events), and triggering a response in the magmatic system (VLP events).

In addition, in chapter 2 we reported infrasound signals (acoustic waves <20 Hz) associated with LP events at Mount St. Helens during November 2004–March 2005, radiating away from the volcano through the atmosphere at acoustic velocity. Whenever present, the infrasonic LP events were more impulsive than the seismic LP events and lacked a prominent long-period coda. It was also observed that not all seismic LP events had a clear infrasonic arrival because the infrasonic signal amplitude faded in and out over timescales of hours to days without a change in the background noise levels.

In this chapter, we attempt to understand: 1) the source process generating the infrasonic signals, and 2) the intermittency of the infrasonic signals. Since the seismic and infrasonic signals from LP events are sourced simultaneously, an understanding of (1) would yield additional information on the source process of

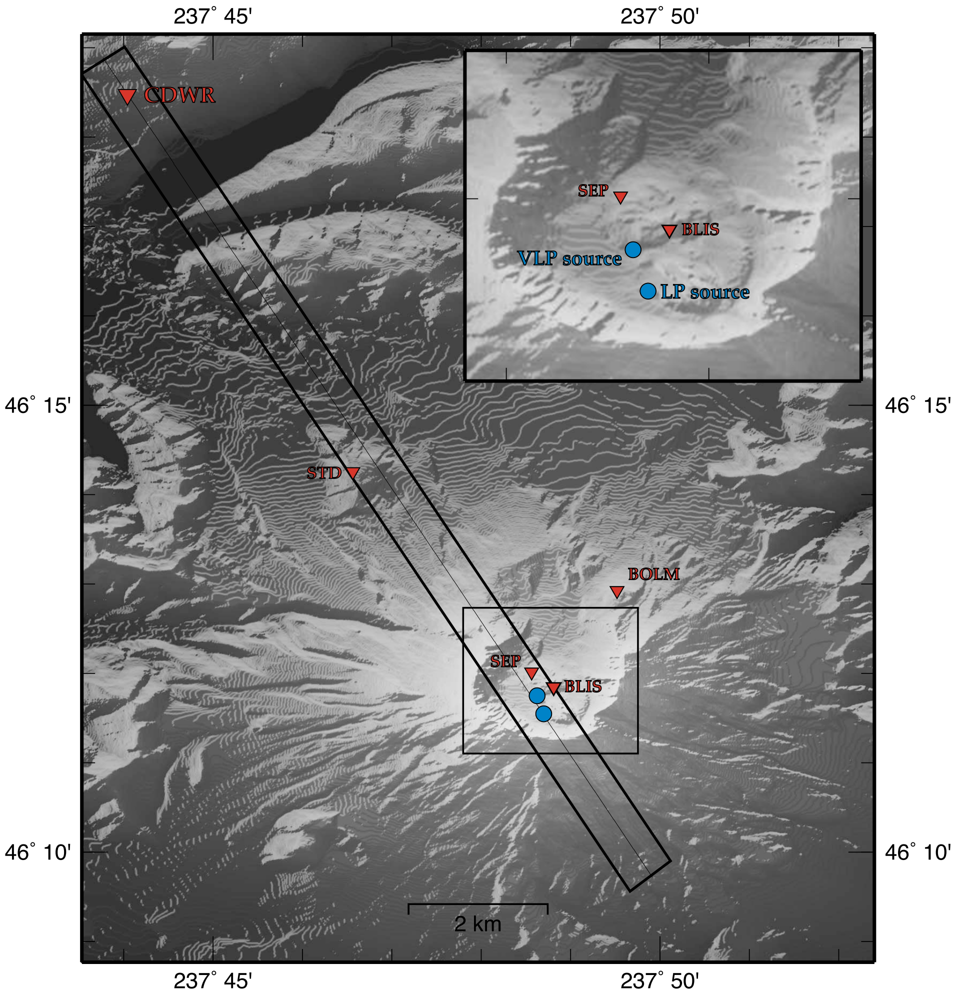

Figure 3.1: Location of CDWR, in a forest 13.4 km to the NW of Mount St. Helens (MSH). Microphones operated by CVO (BLIS, SEP, BOLM, STD) are also shown. The long box trending NW is 750 m wide, and represents the region of the 2.5D FD calculations described in section 3.4. The line down the center of this box intersects the LP source location and CDWR, and represents the profile used in the 2D FD simulations. The box centered on the MSH crater indicates the area of the inset, which shows the LP and VLP point source locations obtained by Waite et al. [2008]. The topography data in the crater are from 19 April 2005 [Schilling et al., 2008].

seismic LP events. The simplest explanation for the infrasonic signals is that they are sourced by seismic-acoustic conversion at the ground-air interface. It is known that infrasound and acoustic-gravity waves are generated by large tectonic earthquakes both from strong ground displacement and deformation near the source epicenter [e.g., Bolt, 1964; Mikumo, 1968] and interaction of surface waves with topography [Le Pichon et al., 2002, 2003, 2006; Mutschlecner and Whitaker, 2005]. In addition, P/SV and Rayleigh wave energy can be locally radiated into the atmosphere for even relatively small magnitude earthquakes [e.g., Press and Ewing, 1951; Kitov et al., 1997; Mutschlecner and Whitaker, 2005; Sylvander et al., 2007], providing an explanation for reports of low-frequency sounds accompanying earthquakes [Benioff et al., 1951]. Seismic-acoustic conversion is expected for LPs at Mount St. Helens because the source is very shallow (∼200 m below the topography surface used in the moment tensor inversion), extended horizontally, and consists of a moment tensor with diagonal elements in the ratio M_{xx}:M_{yy}:$M_{zz} \sim$ 1:1:3 [Waite et al., 2008], which propagates proportionally more energy vertically than horizontally. Furthermore, Waite et al. [2008] imaged a strong (∼9 GN) oscillatory vertical single-force component (F_z) to the LP source. This was attributed to the vertical elastic oscillations of the rock mass perched above the crack, and could be a significant source of acoustic energy by analogy with a piston.

However, if these elastodynamic processes cannot explain the observed infrasonic signals, other mechanisms may be invoked for the source. The "trigger" [Chouet, 1985], or pressure excitation mechanism initiating LP resonance, may be propagated directly into the atmosphere through shallow porous material, or a secondary process such as rapid gas release from the LP source may generate the acoustic signals (chapter 2).

When infrasound has been observed in relation to LP events at other volcanoes [Iguchi and Ishihara, 1990; Yamasato, 1998; Garces et al., 1999; Petersen and McNutt, 2007], it has typically been attributed to gas release. Yamasato [1998] analyzed impulsive infrasonic signals associated with hybrid long-period events (LPs with mixed first motions and pronounced broadband onsets [Lahr et al., 1994]) at Unzen Volcano, Japan. The observed infrasonic amplitude at Unzen could not be explained by a simple volume change (acoustic monopole source) due to ground displacement above the seismic source, so it was concluded that the infrasound was generated by the emission of volcanic gas during seismic rupture and fracture of the gas-charged lava dome material. Petersen and McNutt [2007] also observed impulsive infrasonic signals associated with LP events at Shishaldin Volcano, Alaska. In this case, the seismo-acoustic events were correlated with visual observations of discrete "gas puffing" from the open-conduit system, and so were attributed to degassing explosions in a shallow hydrothermal conduit system.

Before invoking such a mechanism for LPs at Mount St. Helens, we investigate whether seismic-acoustic conversion can produce the observed amplitude ratio of acoustic pressure to seismic vertical velocity (P/V_z) and replicate the general characteristics of the observed waveforms and spectra. Since influence from strong topographic heterogeneity is unavoidable in volcanic settings [Ohminato and Chouet, 1997; Neuberg and Pointer, 2000], we use a 3D staggered-grid finite-differences representation of the velocity-stress elastodynamics equations, which allows for heterogeneous medium properties, arbitrary moment tensor and single-force sources with an arbitrary source-time function, and implicit modeling of wave propagation across solid-fluid boundaries without the use of explicit boundary conditions [D'Auria and Martini, 2007].

Interpretation of the infrasound source mechanism is further complicated by the intermittency of the signals (2 above). This intermittency may be caused by acoustic propagation effects in a time-varying atmosphere, and/or time-varying source effects. To gain more understanding of the relative contributions from these effects, we consider infrasonic propagation in a time-varying atmosphere at the range of interest (13.4 km) using ray tracing and finite-difference methods. We also track the observed time evolution of both seismic and infrasonic waveforms using waveform cross-correlation, providing additional insights into source and propagation effects.

3.2 Data

In chapter 2 we described the broadband infrasound array deployment at Mount St. Helens (MSH). In this chapter, we use data from the Coldwater (CDWR) array located in a forest 13.4 km to the NW of the volcano, with direct line-of-sight to the open crater (Figure 3.1). This array consisted of four DASE/Tekelec MB2000 broadband aneroid microbarometers (flat response 0.01-17 Hz with anti-aliasing filter) arranged in a centered triangle with an aperture of ∼100 m. Four 15-m porous hoses were attached to each microbarometer for spatial wind filtering [Hedlin et al., 2003]. The central element was collocated with a Güralp CMG-40T broadband seismometer (0.033-17 Hz with anti-aliasing filter) and a weather station (wind speed, direction, and temperature). The data were digitized at 40 Hz using a 24-bit Nanometrics Polaris Trident digitizer, and transmitted to the Geological Survey of Canada, Ottawa using a VSAT antenna. The array configuration permits evaluation of wavefront properties of recorded signals. Azimuth is used to discriminate between signals of interest and coherent background noise, while horizontal velocity is used to separate infrasonic signals from co-seismic shaking.

The U.S. Geological Survey Cascades Volcano Observatory (CVO) also operated a network of short-period (1 Hz) infrasonic microphones at distances of 400 m to 4 km from the LP source region (BLIS, SEP, BOLM, STD; Figure 3.1), with some overlap in data coverage with the CDWR array [McChesney et al., 2008; Moran et al., 2008a]. Noise conditions at these wind-exposed sites and strong co-seismic shaking hinder unambiguous identification of infrasonic LP events in these data. Nevertheless, infrasound signals associated with M_d 2–3 earthquakes were recorded at STD during the vent-clearing phase prior to 5 October 2004 [Moran et al., 2008a], and impulsive signals resembling the infrasonic LP events observed at CDWR were recorded at BLIS in November 2004. However, BLIS was deployed on a “spider” platform [McChesney et al., 2008] prone to co-seismic shaking, and the signals were not recorded at the other microphone stations due to noise conditions, so care must be taken to identify these as true infrasonic signals [S.C. Moran, CVO, personal communication]. The STD microphone telemetry was disconnected on 12 October 2004 [McChesney et al., 2008] .

3.2.1 Observations at CDWR

Infrasonic signals associated with LP events were observed intermittently at CDWR throughout the time period 1 November 2004 to 27 March 2005 (first CDWR deployment), and much less frequently from 13 August 2005–8 July 2008 (second CDWR deployment). The time periods with the clearest, largest signal-to-noise ratio events were November 2004 and late February to March 2005. These time periods correspond to the largest seismic amplitudes during the CDWR data coverage [Moran et al., 2008b], indicating that clear observation of the infrasonic signals depends to a first order on a seismic amplitude “threshold” (see section 3.3). CDWR was deployed at a range optimized for large-amplitude eruption signals. Since infrasonic LP events are relatively weak signals, it is not surprising that only the largest amplitude examples are clearly detected above noise.

3.2.1.1 Waveforms

When the infrasonic signals were clearly observed, their waveform and spectral features were distinct from those of the seismic signals. Figure 3.2 shows the waveforms for a typical LP event recorded by CDWR at 08:18:35 4 March 2005 UTC. An acoustic signal is seen to arrive $\sim$38 s after the onset of the seismic signal, consistent with the 13.4 km source-receiver range. No coincident seismo-acoustic arrival is observed in the infrasonic pressure data (also true when beamforming

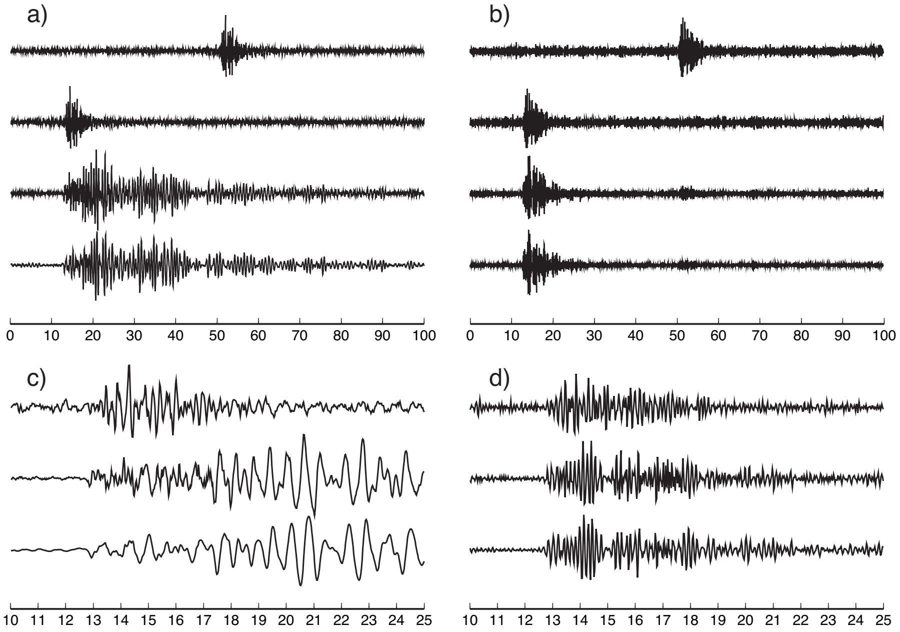

Figure 3.2: Infrasonic and seismic waveforms at CDWR for an LP event with high SNR. Origin time of plot: 08:18:35 4 March 2005 UTC, time in seconds. a) all signals filtered 1-15 Hz, from top to bottom: 1) infrasonic beam (azimuth 153°, speed 330 m/s), 2) infrasonic beam time advanced by 38 s, 3) vertical seismic velocity, 4) vertical seismic displacement (integrated velocity). c) lower three traces in (a) expanded to show time from 10 to 25 s. (b, d) same as (a, c) but filtered 5-15 Hz. Note the following features: i) no coincident seismo-acoustic arrival observed in the infrasound data of upper trace in (a), ii) in band 1-15 Hz, infrasonic signal has the same duration as the broadband trigger onset in seismic LP event (c), iii) in band 1-15 Hz, at $\sim$17 s, infrasonic amplitude is decaying into noise while resonant oscillations of the crack are becoming dominant in seismic record (c), iv) dilatational first motion observed in seismic displacement (c), consistent with Waite et al. [2008], v) in band 5-15 Hz, infrasonic and seismic waveforms have similar duration (b, d), vi) air-ground coupled energy observed in seismic data at $\sim$50 s in (b). The waveforms shown in this figure have normalized amplitudes. See Figure 3.3 for the waveforms shown at their correct amplitudes.

at seismic velocity), indicating that local seismic-acoustic conversion [Press and Ewing, 1951] or mechanical sensitivity of the MB2000 sensor is not significant in this study. When filtered in the band 1-15 Hz, the infrasonic waveforms have duration ∼10 s, with the dominant portion of energy lasting ∼5 s. This duration corresponds to the duration of the broadband pressure excitation mechanism or LP "trigger" observed in the seismic records. After 5 s, the infrasonic amplitudes decay rapidly, while in the seismic records the resonant oscillations of the crack become increasingly dominant. This is further exemplified by considering data filtered at 5-15 Hz, which effectively filters out the crack resonance signature from the seismic data and leaves only the higher frequency components of the broadband trigger. In this band, the seismic and acoustic waveforms have the same duration. We also note that a) the seismic first motion is dilatational, consistent with Waite et al. [2008], and b) the infrasound signal is apparently seen in the 5-15 Hz filtered seismic record, which may represent shaking of the seismic sensor by the passing infrasonic wave or local air-ground coupling. While dispersion may add to the length of the seismic waveform at this range (see section 3.4.2.1), a long-duration source-time function (>20 s [Waite et al., 2008]) is required to produce such a long-duration seismic signal. The observed waveform differences require a mechanism to separate the trigger and resonance components at the source (sections 3.5 and 3.7.1).

The waveforms in Figure 3.2 are shown with normalized amplitudes. In Figure 3.3, the same waveforms are shown with their correct amplitudes. Figure 3.3 illustrates that the 5-15 Hz infrasonic waveforms have amplitudes lower by a factor of ∼3 than the 1-15 Hz filtered infrasonic waveforms, demonstrating that the majority of energy in the impulsive infrasonic signals is in the 1-5 Hz band. This is the same band in which the seismic signals have the majority of their energy, and indicates that the observed differences in waveform cannot be attributed simply to a difference in frequency content and attenuation effects (see

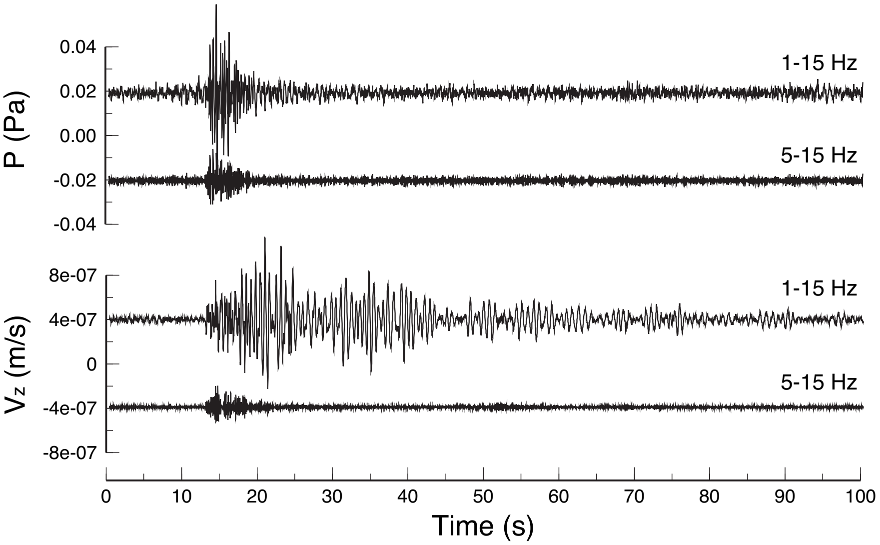

Figure 3.3: Pressure and velocity waveforms shown in Figure 3.2 without amplitude normalization. From top to bottom: 1) infrasonic beam filtered 1-15 Hz, 2) infrasonic beam filtered 5-15 Hz, 3) vertical seismic velocity filtered 1-15 Hz, 4) vertical seismic velocity filtered 5-15 Hz. The infrasonic data have been time advanced 38 s. The 1-15 Hz filtered infrasonic waveform has amplitude ∼3 times greater than the 5-15 Hz filtered infrasonic waveform, indicating that a large portion of the energy in the impulsive infrasonic signal is emitted in the 1-5 Hz band. Similarly, the seismic waveform has amplitude ∼4 times greater in the 1-15 Hz band than the 5-15 Hz band, indicating that the majority of energy is in the 1-5 Hz band.

sections 3.5 and 3.7.1).

3.2.1.2 Power spectra

Figure 3.4 shows power spectral density (PSD) estimates for infrasonic and seismic LPs. Only seismic LPs with a clear infrasonic arrival were included. Infrasound array data were beamformed at an azimuth of 153° and speed of 330 m/s using a conventional time-delay (time-domain) beamformer, with the array gain due to beamforming set to 1.0 [DeFatta et al., 1988]. The PSD estimates were formed by picking 1116 events on 11 November 2004 and 432 events on 4 March

2005 with a Short Term Average / Long Term Average (STA/LTA) detector (STA length: 3 s, LTA length: 10 s, STA/LTA ratio for detection: 2.0), isolating a 12 second window of unfiltered data around the pick (1 s pre-trigger, 11 s post-trigger), and estimating the power spectrum of each using a multitaper method [Riedel and Sidorenko, 1995; implemented in program PSD provided by R. L. Parker, IGPP, SIO]. This method applies frequency-dependent minimization of the sum of variance and bias, making it particularly suitable for spectra with sharp peaks, such as LP resonance spectra. The same spectral parameters were used for infrasonic and seismic data and were chosen to smooth the spectra and show only the grossest and most robust spectral details. The individual event spectra were progressively stacked, emphasizing the repeatable spectral features and reducing the influence of random noise. A transfer function was then obtained by dividing the final seismic stack by the infrasonic stack, which serves to illustrate the differences between the two spectra.

The infrasonic signals have a relatively flat spectrum in the 1-5 Hz band, with noise from the ocean dominating below ~1 Hz (chapter 2). The seismic signals have significant spectral peaks in the 1-5 Hz band, broadly consistent with Waite et al. [2008]. The 11 November 2004 data have a dominant peak at 1.4 Hz, while the 4 March 2005 data have a dominant peak at 1.7 Hz (cf. Waite et al. [2008], who also observed a dominant peak at 1.7 Hz on multiple stations for events on 22 July 2005). Such a change over a timescale of months is expected for spectral features of the source process, but not for those due to propagation effects. The transfer functions for both November 2004 and March 2005 further indicate that the seismic data are enriched in the resonant oscillation signature of the crack, while the infrasonic data are not. The roll-off at higher frequencies (>3 Hz) is more pronounced in the seismic data than infrasonic data, emphasizing that the infrasonic data may be more representative of the broadband trigger signal. This may also relate to frequency-dependent anelastic attenuation and scattering, which

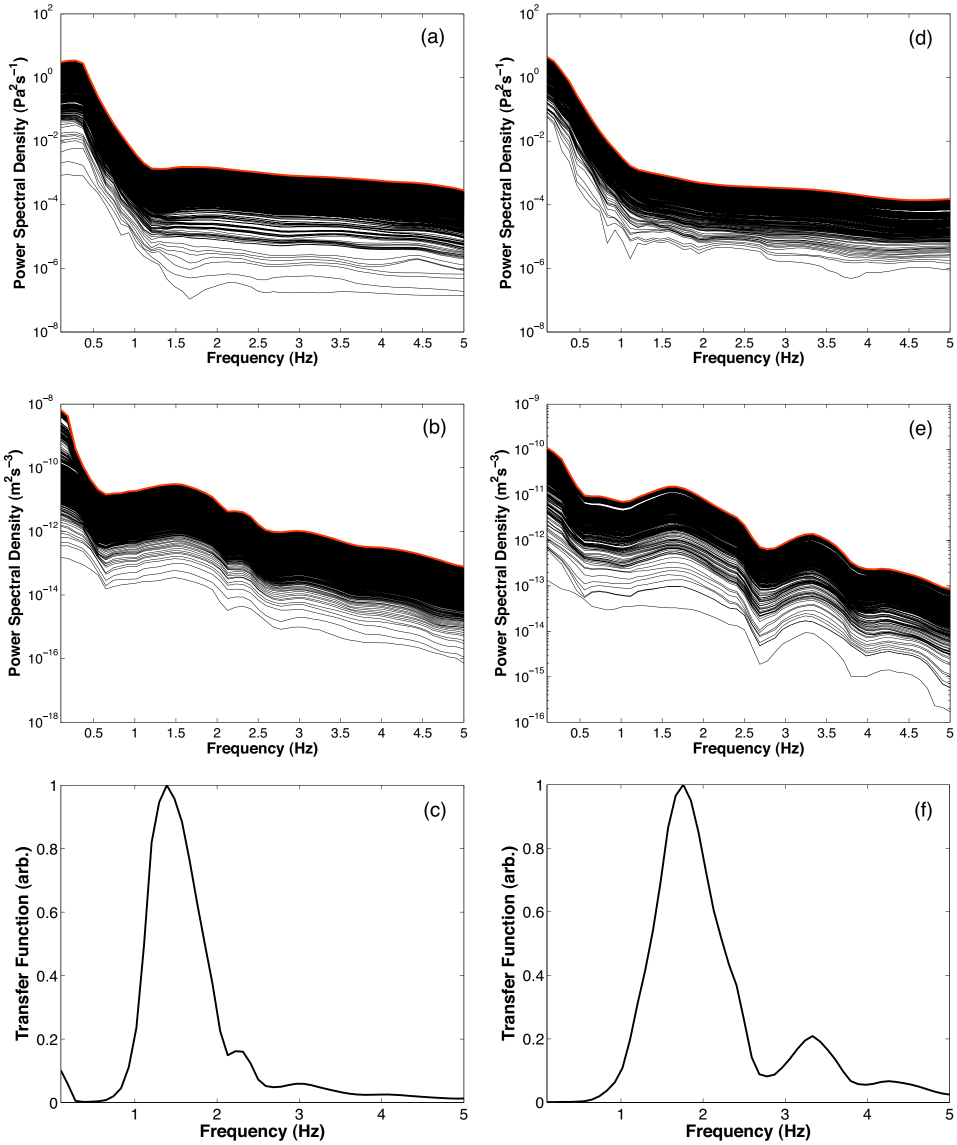

Figure 3.4: Power spectrum estimates for infrasonic and seismic LPs observed at CDWR on 11 November 2004 and 4 March 2005. Events were picked with an STA/LTA detector, and a multitaper method applied to a 12 s window surrounding the pick (1 s pre-trigger, 11 s post-trigger). The spectra for the individual events were then progressively stacked (thick red line shows final stack). a) 1116 infrasonic LP events on 11 November 2004, b) vertical component seismic LP events corresponding to infrasonic events in (a), c) transfer function formed by dividing final seismic spectrum stack (b) by final infrasonic spectrum stack (a). (d-f) same as (a-c) but for 432 events on 4 March 2005. The energy below ∼1.2 Hz in (a) and (d) and below ∼0.5 Hz in (b) and (e) is ambient noise, and not LP signal.

is more severe for seismic energy in the volcanic edifice than in the air [Thelen et al., 2008; Sutherland and Bass, 2004].

3.2.1.3 Amplitudes

Since the amplitudes of infrasonic LPs observed at CDWR vary significantly, we consider the distribution of infrasonic to vertical seismic amplitude (P/V_z) ratios for a large number of events sampling a wide range of atmospheric conditions. Figure 3.5a shows a scatter plot of peak infrasonic pressure amplitude (P) vs. peak vertical seismic velocity amplitudes (V_z) for 2963 LP events from 1-16 November 2004, 16 December 2004, 1-10 and 24-28 February 2005, and 1-19 March 2005. The unit-gain beamformed data were filtered at 2-4 Hz (found to be an optimal band for picking), and events were picked using the STA/LTA detector described in the previous section. Subsequently, the beamed data were re-filtered at 1-5 Hz, and the maximum absolute amplitude in a 20 s window following the pick was assigned to each event. Since the maximum seismic amplitude does not coincide with the time-delayed maximum infrasonic amplitude but appears later in the waveform during the resonance coda (Figure 3.2), the P/V_z we measure should be considered a lower bound. In order to exclude spurious picks not associated with LP events at MSH, only events consisting of a seismic pick followed by an infrasonic pick 38 ± 4 s later were included. However, for the large quantity of data considered, picks related to transient noise occasionally match the selection criteria. This is responsible for the small number of detections with $P/V_z > 10^5$ Pa·s/m. However, compared to the number of detections associated with LP events, these occurrences are insignificant.

Figure 3.5a demonstrates that the vast majority of events have P/V_z between 5×10^3 and 5×10^4 Pa·s/m. Figure 3.5b shows a histogram of P/V_z ratios for the events shown in Figure 3.5a, better illustrating the distribution of values. A smoother estimate of the underlying probability density function (PDF)

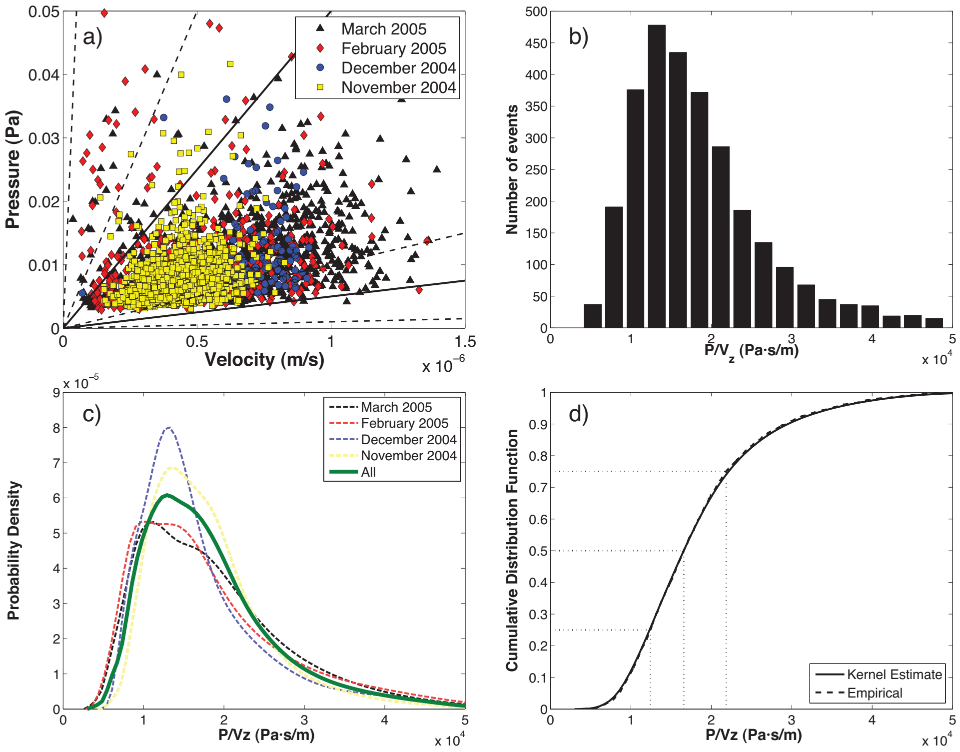

Figure 3.5: A comparison of infrasonic and seismic amplitudes for 2963 LP events observed during 1-16 November 2004, 16 December 2004, 1-10 and 24-28 Februrary 2005, and 1-19 March 2005. a) Scatter plot of infrasonic amplitude (Pa) vs. vertical seismic amplitude (m/s). Dashed lines correspond to constant values of P/V_z, clockwise from top: 10^6, 10^5, 10^4, 10^3 Pa·s/m. The vast majority of events have P/V_z between 5×10^3 and 5×10^4 Pa·s/m (solid lines). b) Histogram of P/V_z values for data shown in (a). Long tail of events with $P/V_z > 5 \times 10^4$ Pa·s/m not shown. Note the unimodal distribution with a peak at 1.3×10^4 Pa·s/m. c) (Gaussian) kernel density estimate of the probability density function of P/V_z for the different time periods. d) Kernel estimate and empirical cumulative distribution functions for all data. The median is: 1.7×10^4 Pa·s/m, and the interquartile range is 9.4×10^3 Pa·s/m.

was obtained using a kernel density estimator with a Gaussian kernel (Figure 3.5c). The PDF has a long tail at high values and a shorter tail at lower values, likely caused by the artifact of the infrasonic amplitudes falling below the detection threshold of the STA/LTA detector. However, we note that the P/V_z values form a unimodal distribution with a maximum at 1.3×10^4 Pa·s/m (Figure 3.5c). We take this mode as the P/V_z ratio that would be observed under "average" atmospheric conditions for which infrasonic signals associated with seismic LPs are detected. The mode differs from the median (1.7×10^4 Pa·s/m) by a negligible amount (Figure 3.5d). We attribute the spread in values about this peak primarily to random dynamic atmospheric propagation effects, i.e., random variations in the wind, temperature, and sound speed profiles, and scattering from atmospheric turbulence [Bass, 1991]. However, it remains possible that part of this spread is attributable to variable seismic-acoustic energy partitioning at the source (see section 3.7). Regardless of the physical cause of spread, a P/V_z of 1.3×10^4 Pa·s/m at 13.4 km range is taken as the target in modeling the elastodynamic seismic-acoustic coupling for a static atmosphere (section 3.4).

3.2.1.4 Larger (M_d >2) events

The sustained LP sequence at MSH is occasionally punctuated by events with larger magnitude (M_d >2.0) that often caused rockfalls and subsequent ash plumes rising above the crater rim [Moran et al., 2008b]. These events have similar spectral content to the ordinary LPs, but in general have dissimilar waveforms [Moran et al., 2008b; Waite et al., 2008], so their relationship to the ordinary LPs is unclear. Here we show that, like the typical LP events, these larger events also produce infrasound. Figure 3.6 shows a sequence of LP events from 4 March 2005, which contains one event with much larger seismic amplitude (2.2 μm/s) than the others. The infrasound signal corresponding to this event has an amplitude of 32 mPa, comparable to some of the events seen earlier in the sequence. However, we note that for the time period shown, P/V_z varies between 2.0×10^4 Pa·s/m (for the larger event) and 5.3×10^4 Pa·s/m, consistent with the variability illustrated in Figure 3.5 and discussed above. Like the infrasound from other LPs, the infrasonic signal from the larger event is impulsive, and lacks a prominent coda. This suggests that the larger events and ordinary LPs have a similar source mechanism.

3.2.2 Observations at BLIS

The instruments deployed at station BLIS (Figure 3.1) consisted of an accelerometer and an 18-element electret infrasonic microphone deployed on a "spider" platform [McChesney et al., 2008]. The predicted seismic-acoustic time delay at BLIS (400 m from LP source, Figure 3.1) is too short to provide clear separation of an acoustic arrival vs. co-seismic shaking. In addition, infrasound associated with LPs was not recorded at SEP or BOLM due to site noise conditions.

However, Figure 3.7 shows data from the microphone and accelerometer at BLIS. The typical seismic LPs have coincident infrasonic signals. The amplitudes of these signals ($\sim$0.8 Pa at 400 m), and the amplitudes at CDWR ($\sim$0.01 Pa at 13.4 km) for the same time period, are broadly consistent with acoustic spherical spreading (amplitude $\sim 1/r$). In addition, small events are recorded on the seismic channel that are not mimicked in the acoustic record. These smaller events are recorded at other times, such as during the 8 March 2005 phreatic explosion (chapter 2), and do not occur with a constant delay time in relation to the typical LP events. Instead, the smaller events appear to be part of a separate random process loosely coupled to the LP generation (unlike at other volcanoes where the small event may be considered a coupled precursor with more consistent time-delay, e.g., Gil Cruz and Chouet [1997]; Caplan-Auerbach and Petersen [2005]). If each typical LP corresponds to the sudden loss of pressure and collapse in a hydrothermal crack, these smaller events may be related to the recharge of fluid pressure, or the fine-scale adjustments in the hydrothermal system in response to this sudden

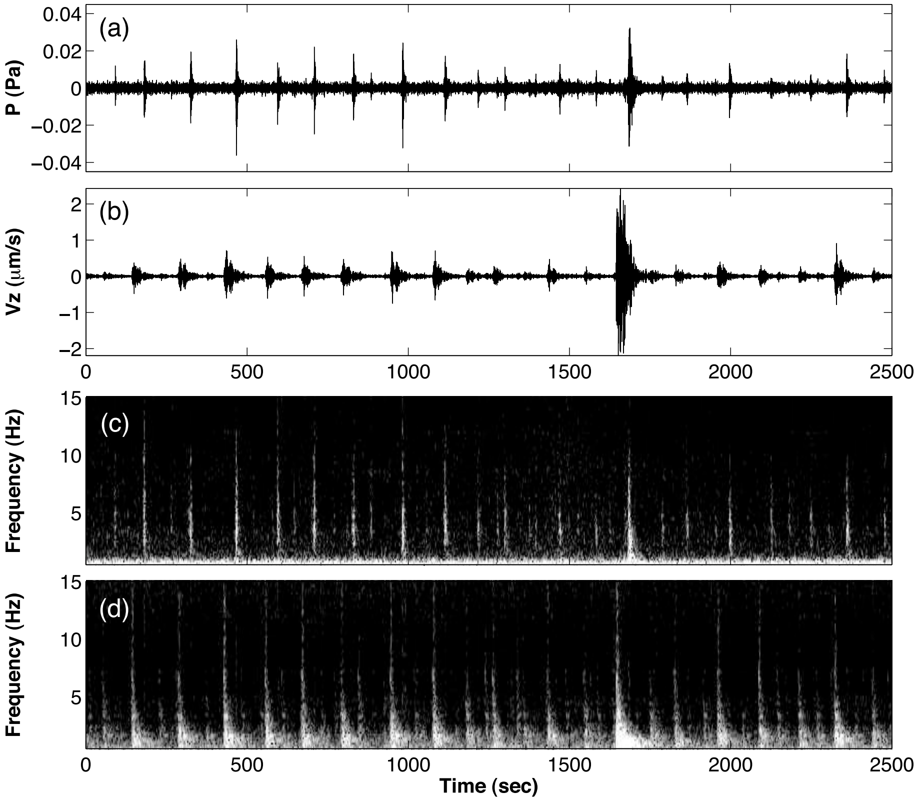

Figure 3.6: A sequence of LPs punctuated by a larger M_d >2 seismic event observed at CDWR. The larger event is also accompanied by an impulsive infrasound signal. Origin time of plot: 4 March 2005, 08:11:40 UTC. a) Beamformed CDWR infrasound data (azimuth 153°, speed 330 m/s, filtered 1-5 Hz), b) CDWR vertical seismic data filtered 1-5 Hz, c) spectrogram of unfiltered infrasonic beam, d) spectrogram of unfiltered vertical seismic data. The large seismic event at 1645 s has an amplitude 2.4 times greater than the next largest event in the sequence, while the infrasonic arrival has an amplitude comparable to the preceding events. However, the P/V_z ratio varies only between 2.0×10^4 and 5.3×10^4 Pa·s/m, consistent with the variability shown in Figure 3.5. Note in the spectrograms how the seismic events contain a long-duration resonant coda, while the infrasonic events consist of a short-lived broadband impulse.

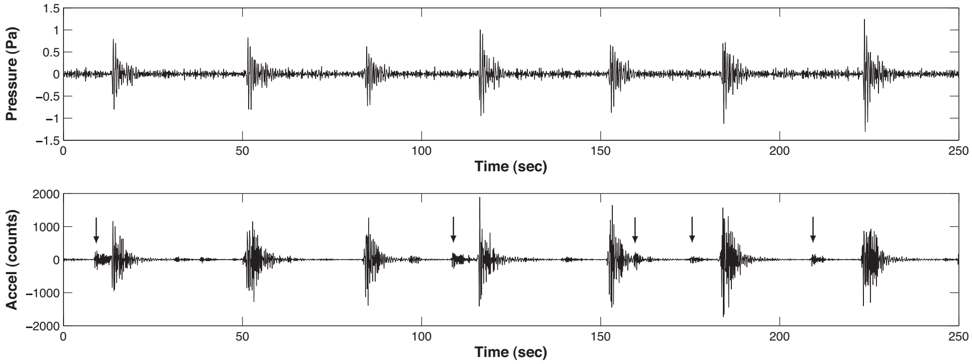

Figure 3.7: Waveforms (filtered 1-5 Hz) observed on the BLIS spider platform ~400 m from the LP source (origin time of plot: 19:12:30 11 November 2004 UTC). Impulsive signals appear in the microphone data ~coincident with each typical LP event. However, smaller seismic events (some indicated by arrows) do not appear on the microphone channel, suggesting that co-seismic shaking of the microphones is not significant. The lack of long-period coda for LP events in the accelerometer record is a result of instrument response.

disturbance of the hydraulic pressure. The disruption of hydraulic pressure may induce cavitation inception [Leighton, 1994], perhaps producing signals via bubble collapse similar to those produced by hydrothermal boiling [Leet, 1988].

Assuming a linear scaling between recorded apparent pressure and amplitude of microphone shaking, the small events should appear with amplitudes above noise on the acoustic channel. This suggests that microphone shaking is not significant, and the BLIS microphone was recording "true" infrasonic signals for the LPs like those recorded at CDWR. However, the possibility remains that an amplitude threshold for ground-shaking is required to induce apparent signals on the microphones.

Given the ambiguity associated with these data, we do not attempt a detailed analysis. However, we determined amplitudes for 4811 LP events during 7-13 November 2004 using the method described in section 3.2.1.3. Acceleration data were integrated to velocity, both P and V_z data filtered at 1-3 Hz, and the nominal calibration values for 2 Hz applied. Only detections consisting of a seismic

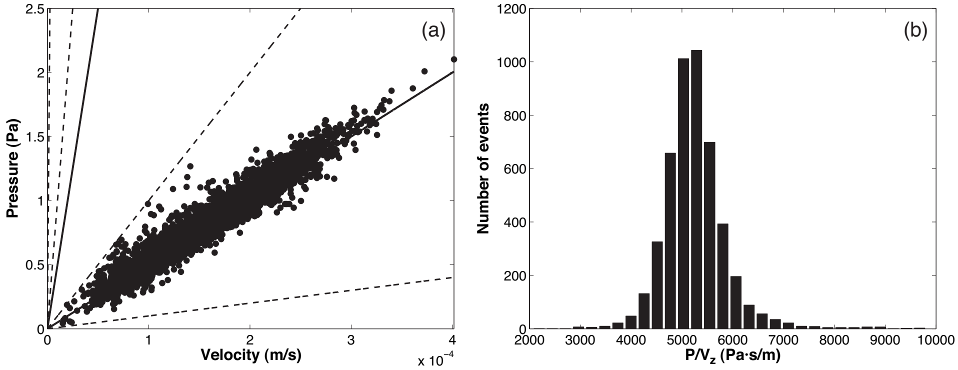

Figure 3.8: Scatter plot of infrasonic (Pa) vs. vertical seismic amplitudes (m/s) for 1-3 Hz filtered waveforms at BLIS, 7-13 November 2004. As in Figure 3.5, dashed lines correspond to constant values of P/V_z, clockwise from top: 10^6, 10^5, 10^4, 10^3 Pa·s/m, solid lines correspond to 5×10^3 and 5×10^4 Pa·s/m. The relation between P and V_z at BLIS is linear. b) Histogram of P/V_z values for data shown in (a). Some variability is present due to measurement error, but a clear mode is present at 5.3×10^3 Pa·s/m.

detection and an infrasonic detection ± 2 s were included. At BLIS, P is clearly linearly related to V_z, with a modal P/V_z ratio of 5.3×10^3 Pa·s/m in the 1-3 Hz band[1] (Figure 3.8). Furthermore, the infrasonic LPs were continuously observed during this time at BLIS, with both infrasonic and seismic amplitudes gradually increasing in proportion such that the amplitude ratio remained relatively constant. This indicates that the amplitude variations at CDWR during this time period are related to atmospheric effects superimposed upon changes in the amplitude at the source. BLIS was destroyed in January 2005, so direct comparisons cannot be made for March 2005.

3.3 Waveform cross correlation

Waveform cross correlation at a single station has been used previously on sequences of seismic LP events to demonstrate the repetitive action of a non-

---

[1] In the band of the LP signals (∼0.5-5 Hz), the electret microphones and accelerometer used at BLIS have a sharp roll-off in frequency response. Therefore, this P/V_z value is not compared to the numerical calculations in section 3.4.2.3.

destructive source [e.g., Stephens and Chouet, 2001; Green and Neuberg, 2006; Petersen, 2007; Waite et al., 2008; Thelen et al., 2008]. Gradual evolution of observed waveforms implies a change either in the Green's function describing all propagation from source to receiver, or in the source-time function. For seismic data, a change in waveform correlation over time typically implies a change in the source location or source-time function. Acoustic propagation is further subject to time-dependent variability in atmospheric conditions, especially changes in temperature and wind. In this case, a change in the waveform correlation with time can imply a change in the source location, source-time function, or a change in the atmospheric conditions.

3.3.1 Waveform changes 1-16 November 2004

We analyze CDWR data for 1-16 November, or Julian Day (JD) 306-322, 2004 (Figure 3.9). This corresponds to the time period depicted in Figure 2.3 of chapter 2, where Progressive MultiChannel Correlation (PMCC) [Cansi, 1995] detection of infrasound from LPs was observed to switch on and off while the seismic LP events were continuously observed (see Figure 3.11). We also analyzed data from 1-19 March 2005 using the same method and obtained similar results. All data were bandpass filtered at 2-4 Hz and the infrasound data were beamformed (azimuth 153°, speed 330 m/s). Events were picked using the STA/LTA detector, then progressively selected for correlation with the master event using 11 s windows (3 s pre-trigger, 8 s post-trigger). In Figure 3.9, the master event (seismic: 18:03:38, infrasonic: 18:04:16, 11 November 2004 UTC) was an event arbitrarily chosen from a time period of good seismic and infrasonic signal-to-noise ratio. The maximum linear correlation coefficient (CC) between each event and the master is shown in Figure 3.9. For clarity, we emphasize that the infrasound and seismic data were considered separately. Correlation between infrasonic pressure and seismic velocity or displacement waveforms was always low (CC <0.1).

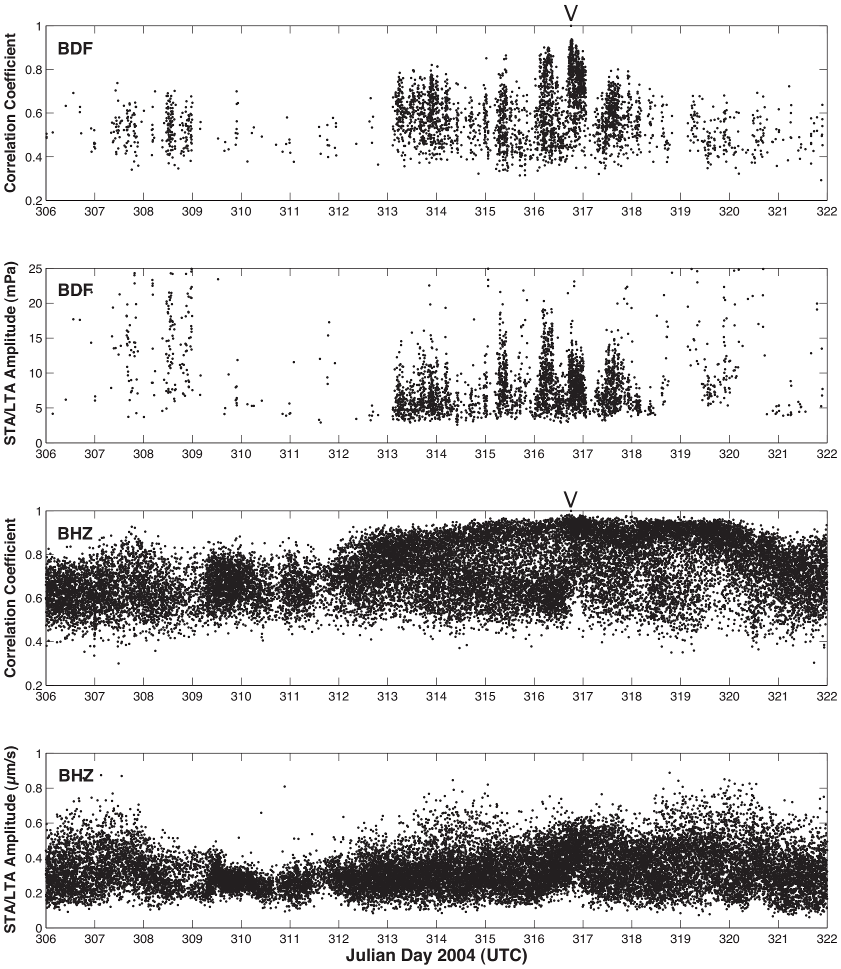

Figure 3.9: Waveform changes observed at CDWR 1-16 November (JD 306-322) 2004 UTC. Top two panels show infrasonic (BDF = broadband infrasound data) correlation coefficient (CC) with master event (location indicated by "V"), and event amplitude. Lower two panels show seismic (BHZ = broadband vertical seismic data) CC and amplitude. The seismic CC gradually evolves with time, peaking at the location of the master event, while the infrasonic events appear in discrete "bursts" of signal (especially JD 315-318). The occurrence of infrasonic detections depends to first order on the seismic amplitude (infrasonic detections are more likely when the seismic amplitude is higher).

The seismic LP sequence during this time period is characterized by a gradually evolving waveform, with the CC values peaking at the time of the chosen master event, and sloping off before and after. We found that choosing a different master event simply caused the peak in CC values to occur at the location of the new master. This is reminiscent of the results of Stephens and Chouet [2001], who observed a gradual evolution in correlation between individual LP events comprising a 23-hour swarm preceding the 14 December 1989 eruption of Redoubt (Alaska). Our results are also consistent with Thelen et al. [2008], who analyzed the same time period at MSH using station ELK (∼17.3 km from MSH). Thelen et al. [2008] separated events with CC >0.8 into "multiplets", and found that new multiplets continuously appeared during this time period, with the CC decreasing as a function of time during the lifespan of the multiplet.

In contrast, the infrasonic LPs for the same time period occur in discrete "bursts" of signals. Generally, events within each burst are well correlated with one another, but poorly correlated with signals in bursts at other times. The correlation falls off more rapidly in time than in the seismic data. Of the 3530 infrasonic triggers in this 15-day time period, only 750 (21%) were correlated with the master with CC above 0.7. For the 24753 seismic triggers, 13317 (54%) were correlated with CC above 0.7. Considering only seismic LP events that had a detected infrasonic arrival, 2463 (70%) of the 3530 events had CC greater than 0.7. Therefore, we conclude that the infrasonic waveform is less stable than the seismic waveform – changing on fine timescales while the seismic waveform is stable for days to weeks. The cause of infrasonic waveform instability is most likely atmospheric variability.

3.3.2 Atmospheric influence on waveforms: 10-12 November 2004

The influence of atmospheric effects is apparent in the data between 10 to 12 November (JD 315-317) 2004. Figure 3.10 shows the cross correlation results (Figure 3.9) for this time period, directly compared with the low-frequency (<1 Hz) infrasonic spectrogram from the central element at CDWR, and wind data. The wind data are taken from CDWR, and from a meteorological station operated by the Northwest Weather and Avalanche Center (NWAC) located ~500 m south of CDWR. There is general agreement between the wind data for both sites, though the CDWR hourly maximum wind speed is higher than that for the NWAC data probably due to differences in data sampling rate (1 sample/sec for CDWR, 1 sample/10 sec for NWAC). Noise in the low-frequency infrasound data (0.02-0.3 Hz) increases with the wind speed, and may be considered a proxy for wind speed in the boundary layer [Fee and Garces, 2007].

In Figure 3.10 there are four "bursts" of infrasonic signals characterized by an increase in number of events, amplitudes, and correlation between the events. Between JD 315.5 and 316 the wind speed increases, resulting in decorrelation of the infrasonic waveforms and a decline in the number of detected events. Once the wind speed decreases, the detections return and correlation is restored. Between JD 316.5 and 317, a sharp change in the wind direction is observed. This coincides with a time of increased infrasonic detection and waveform correlation, suggesting that atmospheric conditions are somehow adjusted for stable reception of signal. However, wind blowing from source to receiver should enhance signal detection, while wind blowing from receiver to source should hinder signal detection [Reynolds, 1873]. The fact that the measured wind direction is blowing approximately from receiver to source (~330°) during the increase in signal reception from JD 316.5 to 317 suggests that the wind conditions measured near CDWR are not representative of the wind conditions along the propagation path between the LP

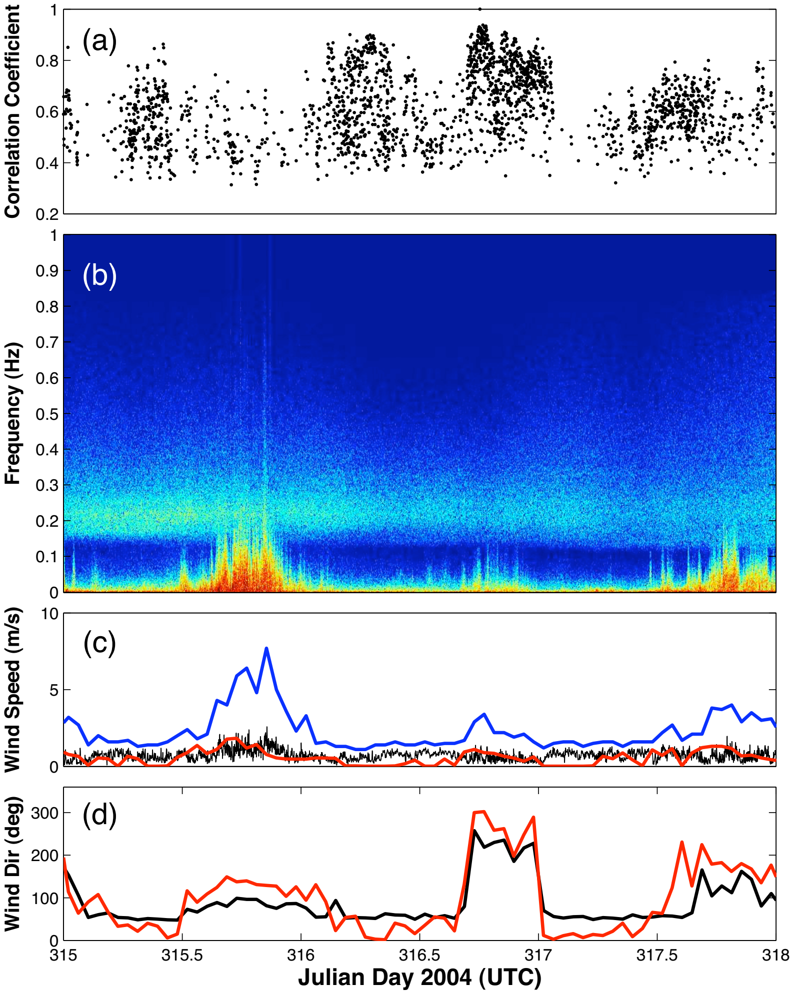

Figure 3.10: Comparison of infrasonic waveform correlation with available wind data 10-12 November (JD 315-317) 2004 UTC. a) infrasonic CC with master event (Figure 3.9), b) spectrogram of low-frequency (0-1 Hz) pressure at CDWR central infrasonic sensor element (warm colors indicate high spectral amplitudes; cool colors indicate low spectral amplitudes), c) black: 1-min wind speed average at CDWR, blue: hourly wind speed max at CDWR, red: hourly wind speed max at NWAC, d) black: hourly wind direction average at CDWR, red: hourly wind direction average at NWAC. At least one measured wind speed increase (JD 315.5-316) is associated with a loss in signal correlation. The diffuse peak at ∼0.2 Hz in the spectrogram is the microbarom peak. Wind direction is defined as the direction from which wind is blowing.

source and CDWR [see Figure 3.11 for the longer sequence of atmospheric data (1-16 November 2004)].

The effect of atmospheric conditions on waveforms is illustrated in Figure 3.12. The 2042 infrasonic and 5897 seismic events during this time period are aligned by cross correlation in chronological order for comparison (filtered 1-5 Hz). To exclude spurious automatic picks, only events having CC>0.2 with a time-evolving master event [Stephens and Chouet, 2001] have been included. A stacked master event is formed from the point-by-point 10% trimmed mean of the waveforms, and 95% confidence intervals on the mean were computed by bootstrapping with 1000 samples [Rice, 1995]. The point-by-point standard deviation and 5 and 95 percentiles of all waveforms are also shown, illustrating the observed variability in the waveforms. Individual events were not normalized by their maximum amplitude, so larger amplitude events contribute more significantly to the master than lower SNR events.

Figure 3.12a demonstrates the similarity of seismic LP waveforms during these three days. The only variability is in minor changes in the amplitude of each waveform, as evidenced in the shaded percentile region of the master stack. In contrast, the infrasonic waveforms in Figure 3.12b show continuous fluctuation and variability. Apart from amplitude changes, individual peaks and troughs in the waveforms move relative to one another – indicative of fine changes in the atmospheric propagation path, while strong winds result in decorrelation and loss of the signals. However, on average, the basic waveform structure is unchanged, even after the signals have faded and reappeared. This suggests that subtle waveform changes and “switching on and off” of the infrasonic LP detections are a result of boundary layer dynamics [Fee and Garces, 2007], rather than time-varying source effects. Also, infrasonic waveforms appear weakly correlated at low amplitude for as long as 30 s. This suggests that low-amplitude seismic-acoustic conversion from a long-duration source-time function may be important for the later stages of the

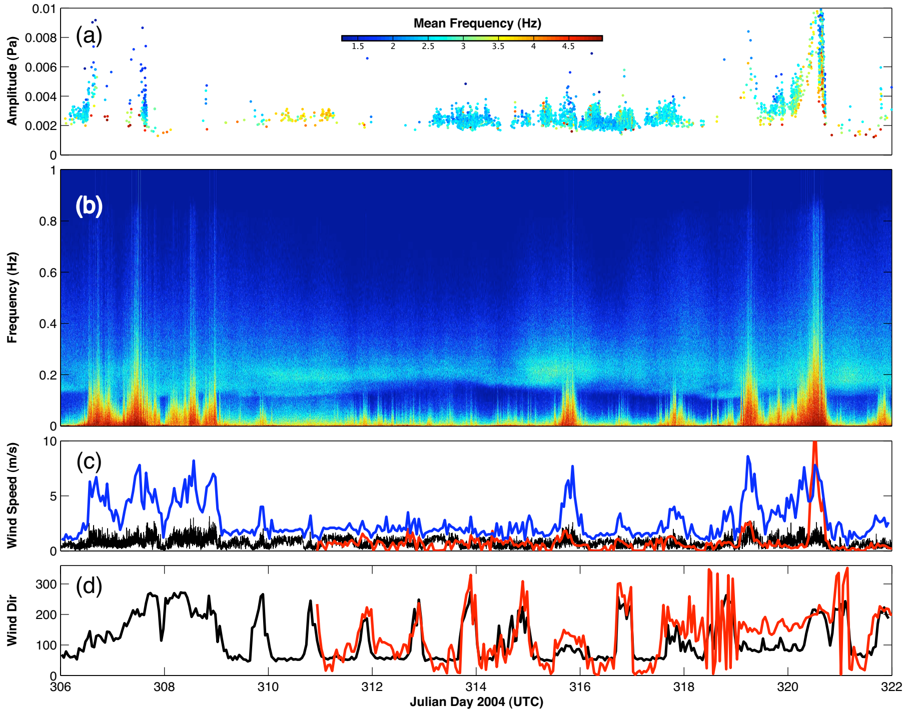

Figure 3.11: Available wind data compared with PMCC detections at CDWR (chapter 2) for 1-16 November (JD 306-322) 2004 UTC. a) amplitude of PMCC detections within an azimuth swath corresponding to MSH (145°–160°), families color-scaled for mean frequency (Hz). b) spectrogram of low-frequency (0-1 Hz) pressure at CDWR central infrasonic sensor element. The diffuse peak at ∼0.2 Hz is the microbarom peak. c) black: 1-min wind speed average at CDWR, blue: hourly wind speed max at CDWR, red: hourly wind speed max at NWAC, d) black: hourly wind direction average at CDWR, red: hourly wind direction average at NWAC. Wind direction defined as direction from which wind is blowing. NWAC data only available after JD 311. Some measured wind speed increases are clearly associated with a loss in signal correlation and detection. When the wind speed increases, noise in the 0-0.3 Hz band increases. However, detections "switch on" between JD 310 and JD 314 without an appreciable change in the atmospheric conditions, which is related to the overall increase of LP amplitude during this time period (Figure 3.9). The amplitude surge associated with wind increase on JD 320 is an artifact of PMCC processing (RMS amplitude in time window is sensitive to noise increase). Note that wind speed changes are not dominantly diurnal as in Fee and Garces [2007]

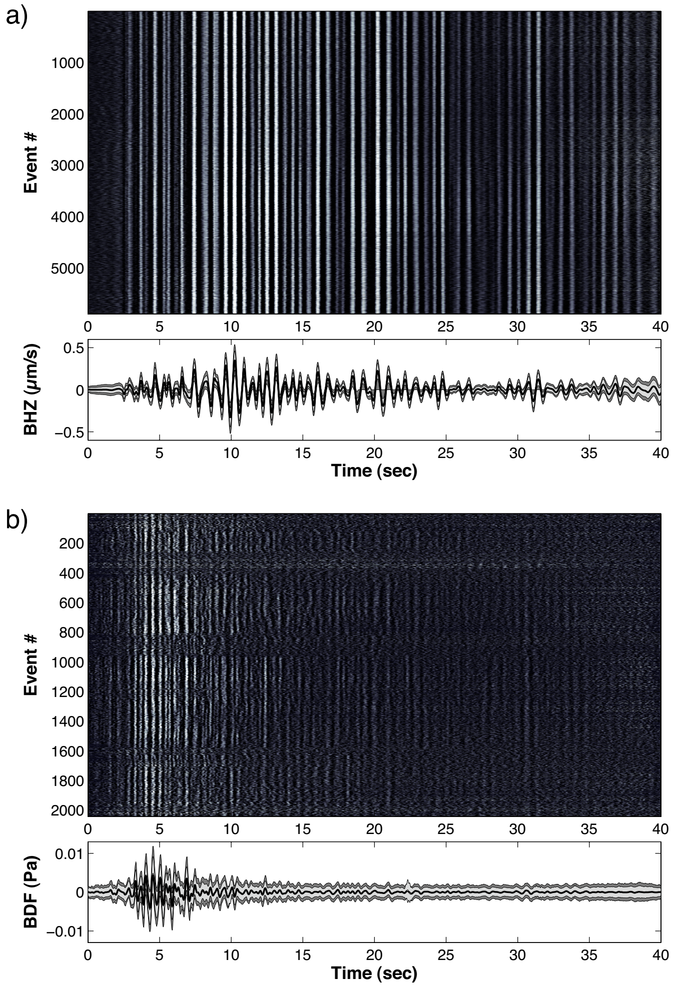

Figure 3.12: Waveform variability at CDWR 10-12 November (JD 315-317) 2004 UTC. Individual detected events (filtered 1-5 Hz) are aligned by cross correlation in chronological order (from top to bottom). There are 5897 seismic events (a) and 2042 infrasonic events (b). Lower panels show a master waveform formed from the 10% trimmed mean of all waveforms (thick black line), standard deviation of all waveforms (light gray), and 5 and 95 percentiles of all waveforms (dark gray). The bootstrapped 95% confidence intervals on the mean master event are plot in white and are thinner than the black line used on this plot. Both data are characterized by highly repetitive waveforms, but the infrasonic data are subject to subtle waveform variations. Decorrelation of infrasonic waveforms is observed between events 250 to 400, 800 to 950, and 1550 to 1750.

infrasonic waveforms.

3.4 Numerical modeling of seismic-acoustic conversion from a point source

Seismic wave propagation in volcanic settings is influenced by topography and heterogeneity in material properties. Consequently, finite-difference methods are usually used in volcano seismology to compute Green's functions for moment tensor inversions [Chouet et al., 2003] or travel times for tomographic inversions [Benz et al., 1996]. In this study, we use a finite-difference code, ASTAROTH [D'Auria and Martini, 2007], to investigate seismic-acoustic wave conversion and coupling from a shallow buried source. Following Virieux [1986], seismic propagation in the elastic solid and acoustic propagation in the (inviscid) fluid atmosphere are solved simultaneously using a single velocity-stress computational scheme. The fluid is defined by a zero S-wave velocity (V_s, $\mu = 0$), and appropriate values for the density and sound speed (P-wave velocity or V_p) of air. This approach does not require explicit free-surface boundary conditions to define the coupling at the topography surface between the solid earth and atmosphere. Seismic-acoustic conversion results from weak energy transmission controlled by effective material properties at the solid-fluid interface [van Vossen et al., 2002].

The governing equations are the equations of elastodynamics in 3D Cartesian coordinates:

$$\begin{aligned} \delta_t \tau_{ij} &= \lambda(\delta_k v_k)\delta_{ij} + \mu(\delta_i v_j + \delta_j v_i), \\ \delta_t v_i &= \rho^{-1}(\delta_j \tau_{ij} + f_i), \end{aligned} \tag{3.1}$$

where τ_{ij} is the stress tensor, v_i the (Lagrangian) particle velocity, δ_{ij} the Kronecker delta, μ and λ the Lamé parameters, ρ the density, f_i the body forces (source term), and the Einstein summation convention is assumed. The equations (3.1) are equivalent to the acoustics equations in the fluid with acoustic pressure $p = -\tau_{ii}/3$, $\mu = 0$, and $\lambda = \kappa$ (bulk modulus) $= \gamma p_0$ in an ideal gas (p_0 reference pressure, $\gamma = c_p/c_v$ ratio of specific heats) [D'Auria and Martini, 2007]. Since the acoustic wave equation is retrieved by linearizing Euler's equation [Landau and Lifshitz, 1987], static wind fields (wind speeds that vary as a function of position but not time) can be considered simply by adding advective terms [D'Auria and Martini, 2007]:

$$\begin{aligned} \delta_t \tau_{ij} &= \lambda(\delta_k v_k)\delta_{ij} + \mu(\delta_i v_j + \delta_j v_i) - (w_l \delta_k \tau_{kl})\delta_{ij}, \\ \delta_t v_i &= \rho^{-1}(\delta_j \tau_{ij} + f_i) - (w_j \delta_j v_i), \end{aligned} \tag{3.2}$$

where w_i is the wind velocity ($w_i = 0$ in the elastic nodes).

These equations are solved using a staggered-grid finite-differences scheme that is second order in space and time. Arbitrary moment tensor and single-force sources are implemented as distributions of body forces f_i on velocity nodes [Graves, 1996] with an arbitrary source-time function, and Perfectly Matched Layer (PML) absorbing boundary conditions are imposed around the edge of the computational volume [Berenger, 1996; Festa and Nielsen, 2003]. The parallel code is written in C++/MPI, and proceeds by dividing the computational volume into equal sub-volumes during each time step (master-slave implementation).

3.4.1 Model configuration

The strong velocity contrast considered leads to some practical limitations. To limit numerical dispersion, 10 grid points per minimum wavelength are required. For an atmospheric sound speed of 330 m/s, a denser grid sampling is required than in typical seismic applications. We restricted our models to frequencies <2 Hz by choosing a grid spacing of 15 m for all spatial dimensions. For this grid spacing and maximum velocity ($V_{max} = V_p = 3500$ m/s) we found empirically that a time step of 1×10^{-4} s was required for stability. Considering the 14 km source-receiver distance, this grid spacing and time step result in a significant computational effort. Hence our model geometry was chosen to minimize the computational volume.

3.4.1.1 Model geometry

Initial calculations were performed for a 2D profile connecting the LP source location and CDWR location (Figure 3.1). This profile is defined as an x-axis with positive values to the ∼southeast (Figure 3.13). Although this captures the basic properties of wave propagation (section 3.4.2.1), it does not correctly predict the geometrical spreading loss. Rather than extending to a fully 3D geometry, we use a 2.5D geometry where the x-axis runs along the 2D profile described above, and the y-dimension is restricted to 51 grid points centered on this line (Figure 3.1). The wave propagation is 2.5D in the sense that backscattering from topography outside this narrow strip is neglected. Tests showed that the PML absorbing boundaries sufficiently reduced edge reflections for this geometry. The final computational volume was $NX \times NZ = 1250 \times 261 = 326{,}250$ nodes for the 2D model, and $NX \times NY \times NZ = 1250 \times 51 \times 261 = 16{,}638{,}750$ nodes for the 2.5D model. The topography data are the same as used by Waite et al. [2008], consisting of USGS topographic map data outside the crater, and a DEM constructed from aerial photographs taken on 19 April 2005 [Schilling et al., 2008] inside the crater. The topography data were interpolated onto the regular 15 m grid (staircase approximation for topography). Discretization of the staircase boundary was sufficient to limit non-physical scattering for the topography gradients considered [de Groot-Hedlin, 2004]. Synthetic sensors were positioned at 450 m spacing along the x axis (Figure 3.13), with one sensor positioned 2 grid points above the topography surface (synthetic acoustic sensor), and one sensor positioned 2 grid points below the topography surface (synthetic seismic sensor). The coordinate system is centered on the epicenter of the LP source.

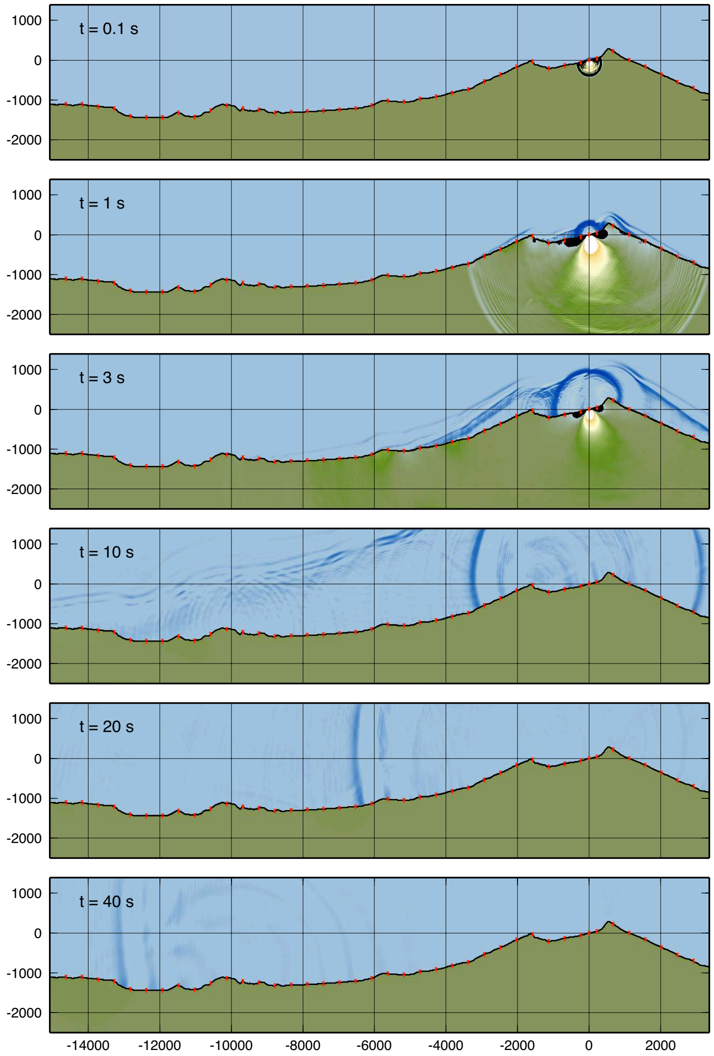

Figure 3.13: Pressure wave field snapshots for a 2D simulation. Distance in m. From top to bottom, snapshot times: 0.1 s, 1 s, 3 s, 10 s, 20 s, 40 s. An isotropic point source with an arbitrary impulsive source-time function is located 60 m below the crater floor at the position (0, 0, −60). Homogeneous material properties are assumed for the solid earth (V_p = 3500 m/s, V_s = 2020 m/s, and ρ = 2650 kg/m^3) and atmosphere (V_p = 330 m/s, V_s = 0 m/s, and ρ = 1.2 kg/m^3). Synthetic sensors are located two grid points away from either side of the ground surface (red triangles, see Figure 3.16). Two distinct atmospheric pressure waves result from the buried source: 1) locally converted or "leaky" P/SV and Rayleigh wave energy that travels along the ground surface at seismic velocity and radiates energy continuously into the overlying atmosphere, and 2) hemispherical wavefronts traveling at acoustic velocity (330 m/s) resulting from strong ground shaking in a finite region surrounding the source epicenter. *See supplementary material in Matoza et al. [2009b] for an animation of this simulation.*

3.4.1.2 Material properties

In the initial 2D and 2.5D simulations (runs 1-5, Table 3.1) we used homogeneous medium properties in the solid earth and atmosphere. For the solid: $V_p = 3500$ m/s, $V_s =$ 2020 m/s, and $\varrho = 2650$ kg/m^3, and for the fluid: $V_p =$ 330 m/s, $V_s =$ 0 m/s, and $\rho = 1.2$ kg/m^3. Waite et al. [2008] did not find an appreciable difference between results obtained with a homogeneous velocity model and those derived from the best available 3D velocity model [Waite and Moran, 2009], in part because low frequencies (<2 Hz) were considered.

We also use a homogeneous atmosphere free from density and sound velocity variation. In section 3.2.1.3 we showed that statistical averaging of waveform and amplitude properties for thousands of events sampling a wide range of atmospheric conditions removes much of the variability in the atmosphere, leaving the "average" atmosphere case. This "average" atmosphere may be interpreted in two ways. In one scenario, no particular atmospheric condition (e.g., a specific wind direction) favors detection of the signals. In this case the "average" P/V_z ratio determined in section 3.2.1.3 would correspond to acoustic propagation in a homogeneous atmosphere as considered in our numerical modeling. However, in a second scenario, a specific atmospheric condition (e.g., wind direction) could be the cause of stable signal reception. In this case, the PDFs shown in Figure 3.5c would be biased toward these conditions, and our numerical modeling with a homogeneous atmosphere may underestimate the P/V_z ratio as determined in section 3.2.1.3, as focusing by wind or temperature has been neglected. Since we do not have detailed specifications of the atmospheric conditions between the LP source and CDWR, the role of atmospheric effects are considered separately in section 3.6 where we investigate more realistic temperature, density, and wind speed profiles.

In a second set of 2.5D simulations using a smaller computational volume (runs 6-7, Table 3.1, section 3.4.2.5), we include a near-surface weathered layer of thickness 495 m, with $V_p = 2000$ m/s, $V_s =$ 1155 m/s, and $\rho = 2000$ kg/m^3 based on material properties used and evaluated by Virieux [1986]; Thelen et al. [2008], and Scheu et al. [2006]. Due to the low frequencies ($<$2 Hz) and relatively short ranges ($<$15 km) considered, we do not introduce intrinsic attenuation into any of our models.

3.4.1.3 Point sources

Of concern in our study are: 1) the sensitivity of the amplitude ratio (P/V_z) observed at CDWR to changes in the source depth and moment tensor/single-force configuration, and 2) the predicted infrasonic waveform duration at 13.4 km range from a buried impulsive and long-duration source-time function (STF). Due to computational requirements, only a small set of models could be run to investigate these effects. Therefore, only four runs (runs 2-5) were performed with the full 2.5D model, each with a different source configuration (Table 3.1, Figure 3.14). In runs 1–2, a source was placed 4 nodes (60 m) below the topography surface (as close to the surface as possible without the source body force nodes interacting with the free surface directly). In these runs, an arbitrary pulse-like STF was used with an isotropic moment tensor: $M_{xx} = M_{yy} = M_{zz} = 1$ (off-diagonal elements $= 0$). In runs 3–5 the source was moved to 195 m depth (13 grid points) below the topography surface. This is the source location obtained by Waite et al. [2008] using the same topography. Runs 3–5 differ in the STF used. Run 3 used the arbitrary pulse STF with isotropic moment tensor (same as runs 1-2). Run 4 used the STF and moment tensor obtained by Waite et al. [2008] by full waveform inversion, with the moment tensor rotated into our coordinate system. This source can be interpreted as the volumetric oscillations of a crack in a Poisson solid ($\lambda = \mu$), so this run gives an indication of how crack resonance at the given source location would couple into the atmosphere. In run 5, the same source location was used, but with a source corresponding to the vertical single-force component (F_z) imaged in the moment tensor and single-force inversions. In the runs using

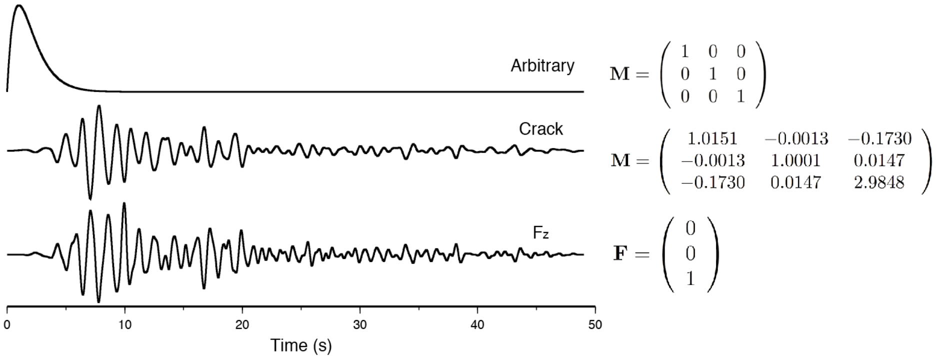

Figure 3.14: Source-time functions used in this study. Top: arbitrary pulse-like source-time function used with an isotropic moment tensor, middle: crack source-time function from Waite et al. [2008] and corresponding moment tensor components rotated into our coordinate system, bottom: vertical single-force component from Waite et al. [2008].

the impulsive STF, time stepping was performed until t = 50 s. In runs using the crack STF (∼30 s duration), time stepping was performed until t = 90 s to capture the full duration of the signal. In our representation of moment tensor and single-force, the source is a point source. Hence, the horizontal extent of the fluid-filled crack is neglected. In section 3.5 we consider the limitations of this assumption by considering the seismo-acoustic wave field resulting from an extended fluid-filled crack source.

3.4.2 Results

3.4.2.1 Wave field structure from 2D simulation

The acoustic wave field structure resulting from an impulsive shallow buried source is best illustrated in the 2D simulation results of Figure 3.13, 3.15, and 3.16.Two distinct acoustic arrivals result from this source configuration, in general agreement with the observations of Le Pichon et al. [2002, 2003]; Mutschlecner and Whitaker [2005], and Sylvander et al. [2007]. The first corresponds to locally

Table 3.1: Model configuration

Run #	Figures	Geometry	Solid Properties	Atmosphere Properties	M_{xx}:M_{yy}:M_{zz}	F_z	STF	Src. Depth (m)
1	3.13, 3.15, 3.16	2D	Homogeneous	Homogeneous	1:1:1	0	Impulse	60
2	3.18	2.5D	Homogeneous	Homogeneous	1:1:1	0	Impulse	60
3	3.19	2.5D	Homogeneous	Homogeneous	1:1:1	0	Impulse	195
4	3.20, 3.22	2.5D	Homogeneous	Homogeneous	1:1:3	0	Crack M_{ii}	195
5	3.21, 3.22	2.5D	Homogeneous	Homogeneous	0	1	F_z	195
6, 7	3.23	2.5D	Comparison between homogeneous and 500 m weathered layer	Homogeneous	1:1:1	0	Impulse	60
8, 9	3.25	2D	Homogeneous, flat topography	Homogeneous	Eqn. 3.6	0	WETC3D	50
10, 11	3.26	2D	Homogeneous, crater topography	Homogeneous	Eqn. 3.6	0	WETC3D	30
12	3.28a	2D	None	G2S 2004-11-01 06:00, no wind	1:1:1	0	Impulse	-160
13	3.28b	2D	None	G2S 2004-11-01 06:00, with wind	1:1:1	0	Impulse	-160
14	3.28c	2D	None	G2S 2004-11-01 18:00, no wind	1:1:1	0	Impulse	-160
15	3.28d	2D	None	G2S 2004-11-01 18:00, with wind	1:1:1	0	Impulse	-160
16	3.28e	2D	Homogeneous	G2S 2004-11-01 06:00, no wind	1:1:1	0	Impulse	60
17	3.28f	2D	Homogeneous	G2S 2004-11-01 18:00, no wind	1:1:1	0	Impulse	60
18	3.28g	2D	Homogeneous	G2S 2004-11-01 18:00, with wind	1:1:1	0	Impulse	60
19	3.28h	2D	Homogeneous	G2S 2004-11-01 18:00, with wind	1:1:1	0	Impulse	60

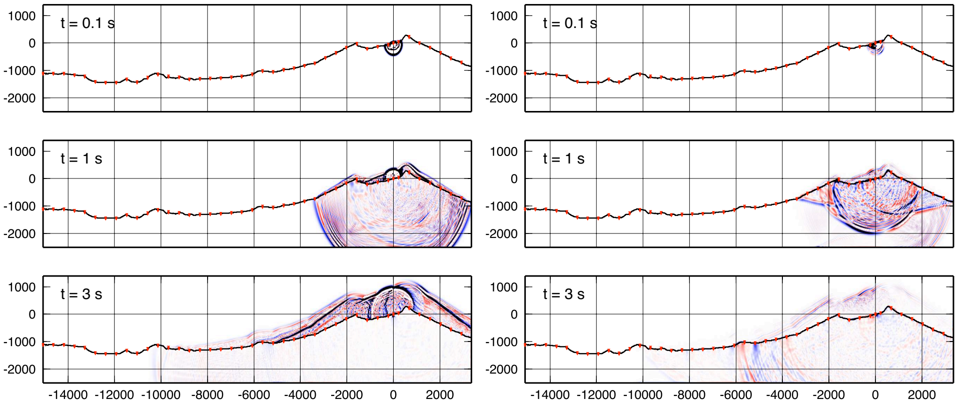

Figure 3.15: $\nabla \cdot v$ (left) and $(\nabla \times v)_y$ (right) of the vector velocity field v for the simulation shown in Figure 3.13. From top to bottom, snapshots times: 0.1 s, 1 s, 3 s. $\nabla \cdot v$ illustrates P and Rayleigh wave propagation, while $(\nabla \times v)_y$ illustrates S and Rayleigh waves. Conversion of upward P to downward SV is seen at the free surface, while local seismic-acoustic conversion is seen for both P and Rayleigh waves leaving the source. Apparent rotational components traveling at acoustic velocity in the atmosphere and P velocity in the elastic solid for $(\nabla \times v)_y$ (right) are artifacts of high-frequency numerical noise (the curl does not precisely vanish).

converted P/SV and Rayleigh wave energy (identified by particle motion analysis, see Figure 3.17), and travels along the ground surface at seismic velocity, arriving at the infrasonic sensor coincident with the seismic energy. Note in Figure 3.13, snapshot at $t = 10$ s, how the wavefronts in the atmosphere from this first arrival form at a shallow angle (which is dependent on the elastic wave speed) to the topography surface, and that amplitude increases along the wavefront in the direction away from the solid-fluid boundary. These properties are the same as those of "leaky waves" [Brekhovskikh, 1980; Viktorov, 1967] that form at a solid-fluid boundary when the elastic wave speed is higher than the sound speed in the fluid. Amplitude increases along the wavefront away from the solid-fluid boundary (i.e., in the direction towards the volcanic edifice in snapshot at $t = 10$ s in Figure 3.13) because this higher-amplitude energy has left the solid at a later time.

The second arrival corresponds to energy converted in the vicinity of

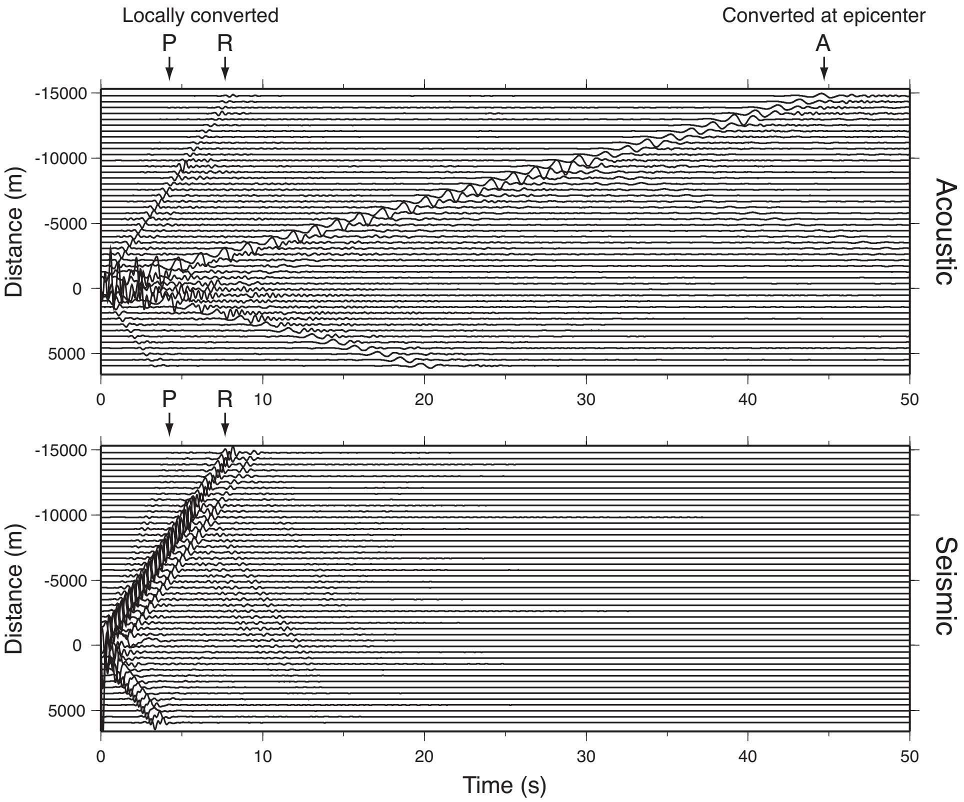

Figure 3.16: Synthetic record sections for acoustic pressure (top) and seismic vertical velocity (bottom) for a 2D simulation from an isotropic impulse point source (Figure 3.13, 3.15). The synthetic seismograms show a faint P-arrival followed by the dominant Rayleigh wave train (R). Note the backscattering from topography at ∼-10 km (see supplementary material in Matoza et al. [2009b]). The synthetic acoustic data show the arrival of two distinct packets of energy. The first corresponds to locally converted P and Rayleigh wave energy, and travels in the atmosphere along the ground surface at seismic velocity. The second corresponds to energy converted from strong ground shaking near the source epicenter, and travels through the atmosphere at acoustic velocity (A). Note the asymmetry in amplitudes of A with respect to range, resulting from asymmetry in topography. Although useful for identifying the principal acoustic arrivals from a buried source, 2D simulations do not adequately predict the amplitude loss due to geometrical spreading.

the source epicenter, and travels along the ground surface at the much slower acoustic velocity, arriving time-delayed from the seismic-acoustic coupled (first) arrival (Figure 3.16). The wavefronts for this second arrival are much steeper, and are hemispherical in the absence of topography (confirmed by a calculation not shown here). The lateral extent of the region of coupling of seismic energy into atmospheric infrasound is restricted to a radius at which the peak vertical seismic velocity reaches a limiting value for effective infrasound generation, which in turn depends on the amplitude and depth of the seismic source [Mutschlecner and Whitaker, 2005]. We note that there is an asymmetry in the amplitude of this second arrival observed in Figures 3.13 and 3.16. The acoustic signal propagating to the SE is weaker than the signal propagating to the NW. This appears to result from the asymmetry in topography. The topography in the crater is dipping to the NW (toward CDWR, left in Figure 3.13), while to the SE the wavefront must diffract over the SE crater wall, which is immediately adjacent to the epicenter of the source where the energy conversion is taking place. This illustrates the importance of topography in the immediate vicinity of the source epicenter for the radiated far-field acoustic amplitude from a buried source.

The seismic wave field structure is better illustrated in Figure 3.15. Here, the divergence

$$\nabla \cdot v = \frac{\partial v_x}{\partial x} + \frac{\partial v_z}{\partial z}$$

and y-component of the curl

$$(\nabla \times v)_y = \frac{\partial v_x}{\partial z} - \frac{\partial v_z}{\partial x}$$

of the vector particle velocity field are shown. The divergence illustrates P and Rayleigh wave propagation, while the curl illustrates S and Rayleigh waves [Ohminato and Chouet, 1997]. These plots show clearly the conversion of upward P to downward SV at the free surface, and acoustic waves in the atmosphere locally radiating from P and Rayleigh waves. There are no S waves directly radiated from the volumetric source. A weak reflection from the south crater wall (right in plot) is also apparent in the divergence (Figure 3.15, left) and pressure field (Figure 3.13) plots.

3.4.2.2 2.5D simulations

Moving from 2D to 2.5D simulation for an identical source configuration results in the same basic wave field structure, but geometrical spreading effects are correctly accounted for. In particular, we find that the acoustic energy originating from the source epicenter becomes more dominant in amplitude for the 60 m depth source within ∼10 km of the source, but both locally-converted and acoustic arrivals have very low amplitudes at ∼13.4 km (Figure 3.18). We note that the first clear arrival in Figure 3.18 corresponds to the Rayleigh wave propagating in the solid, as the P-arrival is not visible at this scale. Moving the source depth to 195 m results in equal amplitudes for the seismic-acoustic coupled waves and acoustic waves from the source epicenter at all ranges (Figure 3.19). Thus, the acoustic waveforms generated by a buried source are very sensitive to source depth. In general, we found in test 2.5D simulations that increasing the source depth caused the amplitude of the second acoustic arrival to decrease dramatically. At depths on the order of an acoustic wavelength (∼330 m), the energy from the source epicenter is mostly directed vertically upwards, with very little horizontal component. We note that all of our simulations predict that at 13.4 km, seismic-acoustic coupled energy and acoustic energy originating from conversion near the source epicenter have comparable amplitudes.

Figures 3.20-3.21 show the results of using the source parameters obtained from inversion of seismic data [Waite et al., 2008]. Here the changes are: 1) the moment tensor and single-force contributions to the source, and 2) the long-duration source-time function. The effects of these parameters on the amplitude ratio and observed waveform duration are presented below.

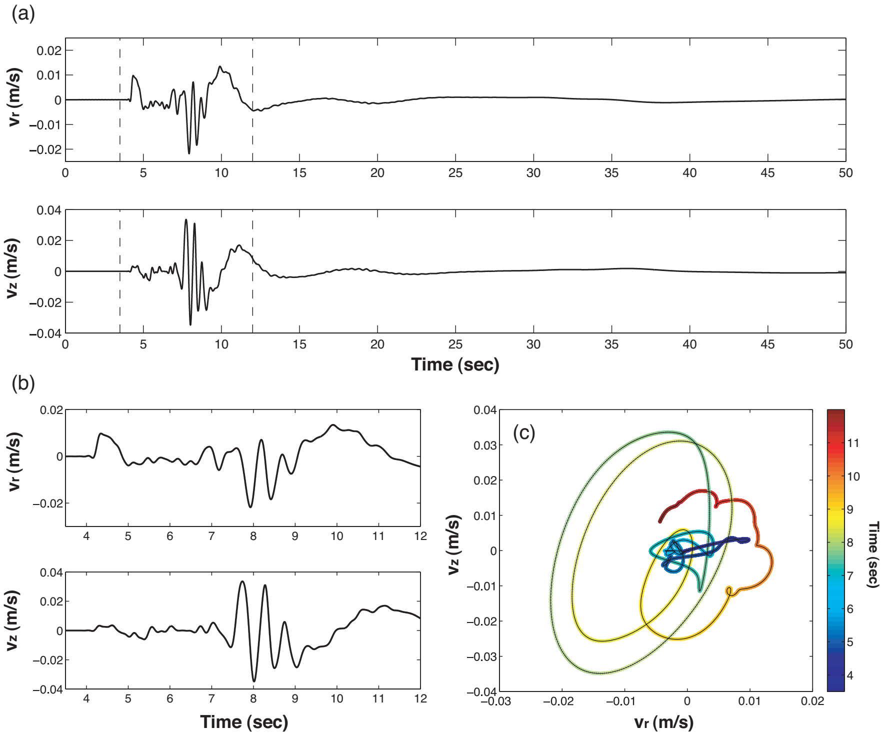

Figure 3.17: Particle motion analysis of synthetic seismic data at $x = -14625$ m, $z = -1140$ m for the 2D FD simulation of Figures 3.13, 3.15, 3.16. a) Synthetic radial (v_r, positive values pointing away from MSH) and vertical (v_z, positive upwards) velocity (m/s) seismograms. The velocity amplitudes are high as geometrical spreading effects are not correctly accounted for in 2D simulation.Vertical dashed lines indicate time range of (b) and (c). Note the strong P-arrival observed on v_r at ∼4 s that has lower amplitude on v_z. b) Zoom-in of the synthetic data shown between dashed lines in (a). c) Particle motion of data shown in (b). Color scale corresponds to time in seconds. Note the initial longitudinal particle motions (P-wave, ∼4-5 s) that subsequently evolve into retrograde elliptical particle motions (Rayleigh wave, particularly 7-9 s). The Rayleigh wave (7-9 s) is the signal with the highest amplitude on v_z in (b) and is the strongest seismic signal seen in Figure 3.16. Accordingly, this Rayleigh wave results in the highest amplitude locally-converted seismic-acoustic energy at ranges of ∼10 km.

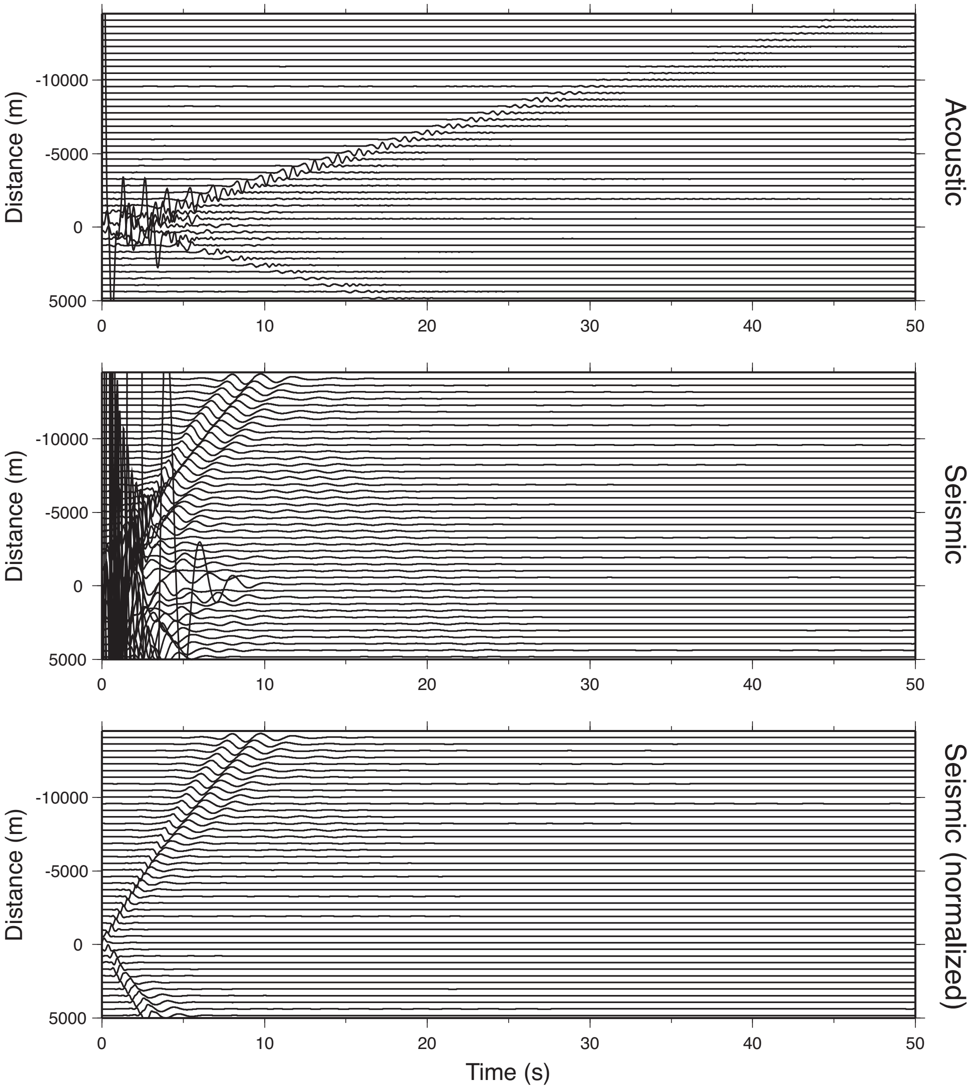

Figure 3.18: Upper two panels: same as Figure 3.16 but for a 2.5D simulation in which the model domain is extended by 51 grid points in the y-direction (see Figure 3.1). The same seismic and acoustic arrivals are present but geometrical spreading effects are now included. The first clear packet of energy corresponds to the Rayleigh wave propagating in the solid, as the P-wave is not visible at this scale. The strong ground shaking in the vicinity of the source epicenter is more significant in 2.5D than 2D, and becomes the dominant source of energy in the atmosphere within a range of ∼10 km of the source. However, pressure amplitudes at ∼-13.4 km are very low. Lower panel: same as middle panel except amplitude of each trace is normalized. Note how dispersion occurs due to interaction with topography and losses into the overlying fluid.

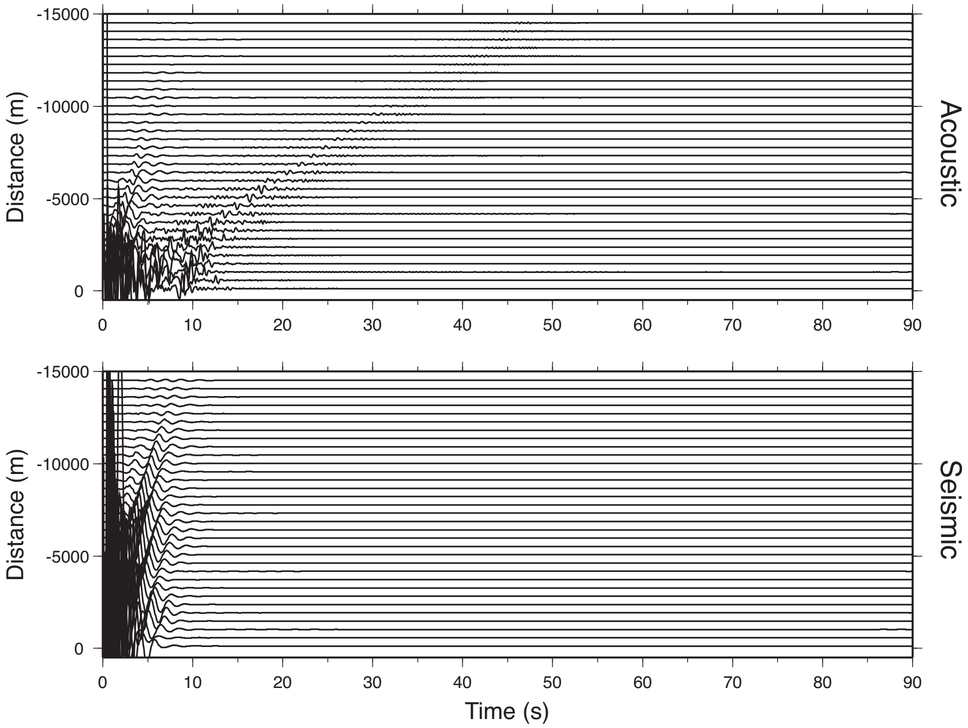

Figure 3.19: 2.5D simulation using a point source at 195 m depth below the ground surface. The source location and DEM used in the simulations are from *Waite et al.* [2008]. An isotropic source (diagonal moment tensor with $M_{xx} : M_{yy} : M_{zz}$ = 1:1:1) with arbitrary impulse source-time function is used as in Figures 3.13, 3.15, 3.16, and 3.18. The traces have not been normalized to illustrate the amplitude decay with distance. Note how the slight increase in source depth from 60 m to 195 m results in locally converted seismic-acoustic coupled arrivals having amplitudes comparable to the acoustic energy originating from the source epicenter at all ranges (compare with Figure 3.18). The acoustic energy at ∼-13.4 km is very weak.

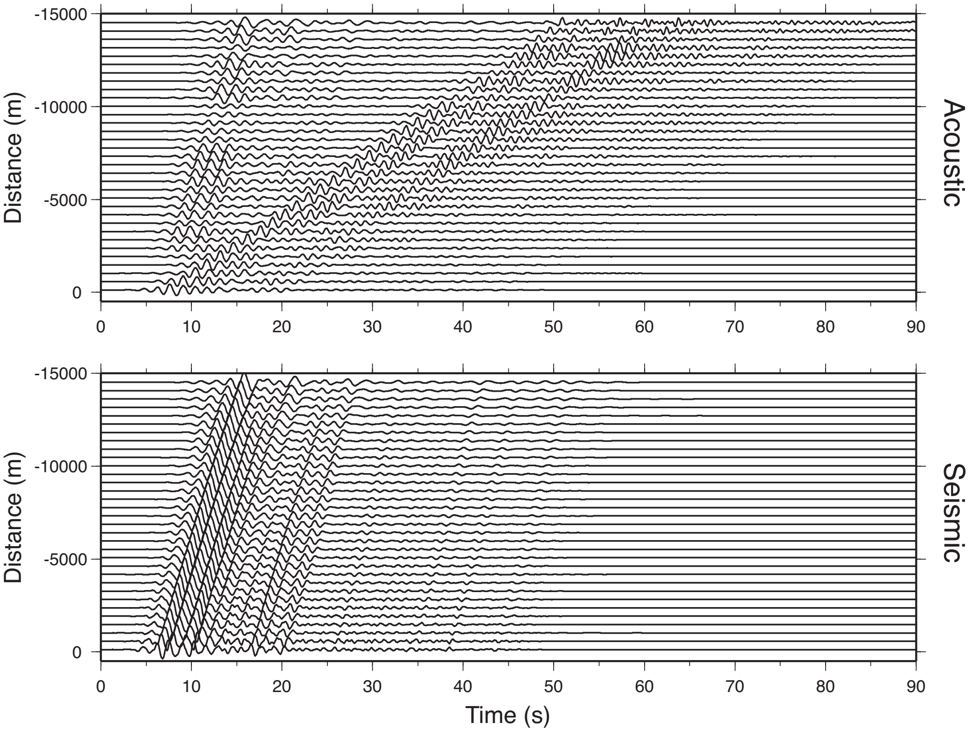

Figure 3.20: As Figure 3.19 but with sub-horizontal crack source (diagonal moment tensor with M_{xx} : M_{yy} : M_{zz} = ~1:1:3) and long-duration resonant source-time function determined from moment tensor inversion Waite et al. [2008]. Traces have been normalized to show the waveforms clearly. The long-duration source-time function generates a long-duration infrasonic signal in the atmosphere, inconsistent with our observations.

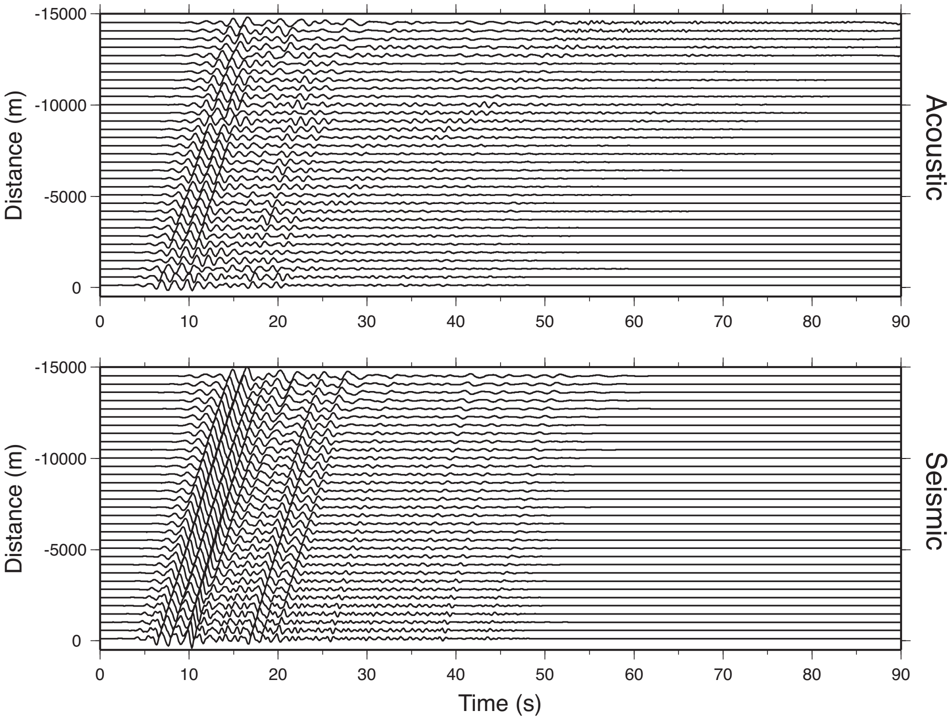

Figure 3.21: As Figures 3.19 and 3.20 but with vertical single-force component (F_z) and long-duration source-time function obtained by Waite et al. [2008]. The results are similar to the volumetric crack source (Figure 3.20), but the predicted P/V_z ratio at CDWR is smaller. Therefore, we conclude that the F_z component is less significant for horizontally propagating infrasound than the volumetric moment tensor component of the source.

3.4.2.3 P/V_z ratios

The P/V_z amplitude ratio was found to vary smoothly with range, superimposed by small local perturbations due to topography. Local topography causes focusing and defocusing of seismic energy, which affects V_z [Ohminato and Chouet, 1997]. Consequently, only order of magnitude values are considered here. We measured the P/V_z amplitude ratio at 13.4 km distance (x = -13.4 km) as the peak synthetic pressure amplitude to synthetic vertical velocity amplitude. Only the atmospheric waves traveling at acoustic velocity (from the source epicenter) are considered. For the 2D simulation of Figure 3.16, the P/V_z ratio is $\sim 10^4$ Pa·s/m. Moving to 2.5D and keeping the same source parameters (Figure 3.18), the P/V_z ratio decreases to 10^3 Pa·s/m. Staying in 2.5D but moving to a source depth of 195 m (the source depth obtained by waveform inversion, Figure 3.19), the P/V_z ratio drops to $\sim 10^2$ Pa·s/m. Changing the moment tensor from isotropic (M_{xx}:M_{yy}:M_{zz} $\sim$ 1:1:1) to that of a volumetric crack (M_{xx}:M_{yy}:M_{zz} $\sim$ 1:1:3) and using the long-duration STF (Figure 3.20) causes an increase in the P/V_z ratio to $\sim 10^3$ Pa·s/m, while the vertical single-force component (Figure 3.21) leads to a P/V_z of $\sim 10^2$ Pa·s/m. Figures 3.20-3.21 show that the F_z source component contributes less to the acoustic pressure waveforms than the volumetric components of the crack. This can be understood by comparing the pressure wave field structure of these two sources (Figure 3.22). The vertical single-force component results in energy directed vertically upwards, while the volumetric moment tensor components result in more hemispherical wavefronts with a stronger horizontally traveling component.

3.4.2.4 Long-duration source-time function

Figures 3.20-3.22 demonstrate that using a long-duration STF in the ground leads to a long-duration infrasonic waveform in the atmosphere. The seismic-acoustic conversion does not result in an impulsive infrasonic signal from some portion of the long-duration seismic source-time function. Furthermore, Figures 3.19-3.21 show that the amplitudes in the atmosphere of the locally radiating seismic wave energy should be comparable to that of the energy originating from the source epicenter for this source depth, resulting in even longer-duration and highly complex infrasonic signals. This is at odds with our observations, as we have instead recorded a simple impulsive infrasonic signal, and a more complex, longer-duration seismic LP. This suggests that the impulsive trigger and resonant crack components of the LP event are separated into infrasonic and seismic components at the source by a more complex mechanism not captured in our numerical modeling using a single point-source representation.

3.4.2.5 Effects of a near-surface weathered layer

Here we briefly consider the effects of a near-surface weathered layer on the seismic-acoustic conversion near the source epicenter. A shallow lower-velocity layer acts to match the impedance between the subsurface and the overlying atmosphere, having potentially significant effects on the ground-atmosphere wave transmission. Given lack of knowledge of the shallow subsurface materials at MSH, we specified a conceptual 495 m thick weathered layer using nominal values of V_p = 2000 m/s, V_s = 1155 m/s, and ρ = 2000 kg/m^3 [Virieux, 1986; Thelen et al., 2008; Scheu et al., 2006]. Figure 3.23 shows the results of including the weathered layer compared to the homogeneous solid used in previous simulations. These simulations use the 2.5D geometry, but a smaller subset of the computational volume extending to just 2 km from the source in the x-direction. The impulsive isotropic source is at 60 m depth below the surface. The low-impedance layer enhances the amplitude of the air pressure wave by a factor of five at 2 km, but increases the seismic amplitude in approximately the same proportion, leading to the same P/V_z amplitude ratio. Also, short-lived reverberation in this layer leads to more complex seismic and acoustic signals. The locally converted seismic-acoustic energy

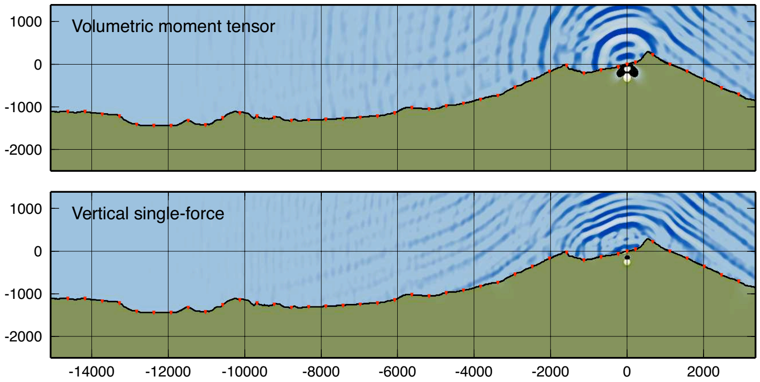

Figure 3.22: Pressure wave field structure from volumetric moment tensor (top) and vertical single-force components (bottom) of the LP source (195 m below ground surface) at t = 40 s. Note how the volumetric source results in more hemispherical wavefronts, whereas the vertical single-force component results in vertically directed energy, and weaker signals at long range.

contributes more to the waveforms for the weathered layer model.

3.5 Seismic-acoustic conversion from a shallow buried, fluid-filled crack

So far our consideration of the airborne acoustic field from a buried, fluid-filled crack has been restricted to frequencies <2 Hz according to the STF obtained by Waite et al. [2008]. This STF (Figure 3.14) captures the resonant coda of the LP waveform, but does not adequately include the broadband trigger component initiating the resonance. Chouet [1986] calculated waveforms for the normal component of velocity at the wall of a fluid-filled crack resulting from its response to a step function in pressure applied to a small patch of the crack (the "trigger patch"). The waveforms near the trigger patch have a highly-broadband onset with amplitude an order of magnitude higher than the resonance component, resulting from the pressure step function [Chouet, 1986]. This high-amplitude

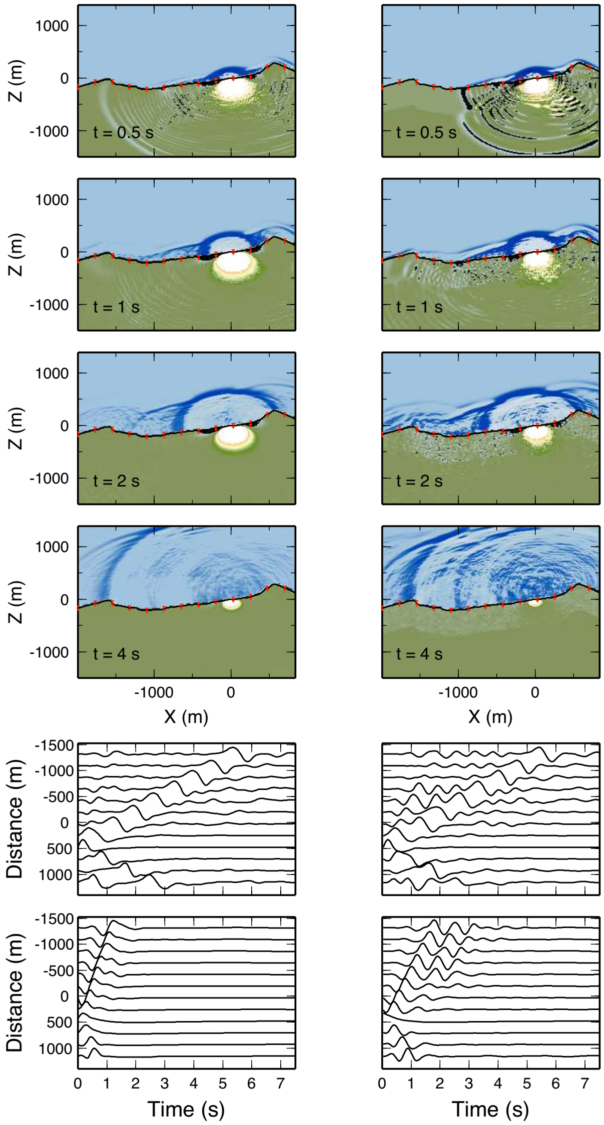

Figure 3.23: Wave field snapshots and synthetic record sections for the 2.5D conceptual weathered layer model (right) compared to a homogeneous solid model (left). For the 495 m-thick surface weathered layer: V_p = 2000 m/s, V_s = 1155 m/s, and ρ = 2000 kg/m^3, for the homogeneous solid beneath the weathered layer: V_p = 3500 m/s, V_s = 2020 m/s, and ρ = 2650 kg/m^3, and for the atmosphere: V_p = 330 m/s, V_s = 0 m/s, and ρ = 1.2 kg/m^3. Left, from top to bottom: pressure wave field snapshots at t = 0.5, 1, 2, and 4 s, synthetic acoustic (top) and seismic (bottom) record sections for the homogeneous solid model. Right: as left but for the weathered layer model. The source is placed at (0,0, −60) in each case.

broadband-trigger component dissipates rapidly in the crack due to radiation into the elastic solid and viscous attenuation in the fluid, so that the resonant fluid response becomes the dominant motion in the crack. Furthermore, once the elastic energy leaves the crack, attenuation in the elastic solid erases more of the higher frequency trigger components. The end result is that far-field seismic LP waveforms have a relatively low-amplitude broadband trigger component, and a dominant resonance component (see Figure 3.2).

The modeling results of section 3.4 indicate that infrasonic signals may be generated by seismo-acoustic conversion in the immediate vicinity of the source epicenter. In the epicentral region of a shallow (depth ∼200 m) fluid-filled crack, the trigger component of the seismic waveform may still have amplitude an order of magnitude higher than the resonance component, as the attenuation through ∼200 m of elastic solid may be negligible. This offers a potential explanation for why the infrasonic signals observed at CDWR are dominantly a record of the broadband trigger, while the seismic waveforms consist primarily of the resonance signal.

However, the broadband trigger component is only an order of magnitude higher in amplitude than the resonance component on a small area of the crack wall close to the trigger patch (see Figure 3.24). Crack resonance is the dominant motion in the remainder of the crack. Another limitation of our modeling so far has been the restriction to a point source representation, where the geometry of the trigger patch with respect to vibrations of the extended crack was not taken into account. The observed infrasonic signals have the majority of their energy in the same frequency band (1-5 Hz) as the observed seismic signals (Figure 3.3), yet have only a very low amplitude contribution that could be attributed to crack resonance (Figure 3.12). Thus, for seismic-acoustic coupling to generate the infrasonic signals, and account for the differences in infrasonic and seismic waveforms, the contribution of the small trigger patch on the crack would have to outweigh the net contribution from the remainder of the crack where resonance is the domi-

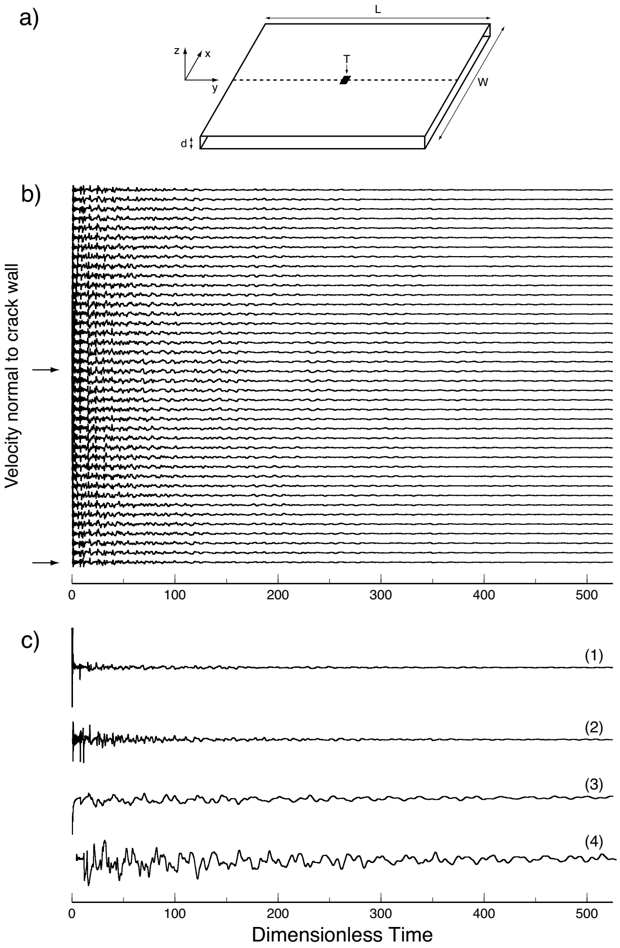

Figure 3.24: Waveforms at the wall of a fluid-filled crack with $\alpha/a = 17.5$, $b/\mu = 0.0018$, $W/L = 0.5$, and $C = 7.5$. a) Geometry of the fluid-filled crack. Dashed line represents the centerline of the crack in the y-direction and is an axis of symmetry exploited in the computation. In this case, the trigger patch (T) is located at the central position along the centerline and extends one grid point in both positive and negative directions along the x-axis. b) Normal component velocity record section along full length of crack centerline in y-direction, $x = 0$ (dashed line in a). Arrows indicate position of waveforms shown in (c). c) From top to bottom: 1) normal component of velocity at the central position of the crack (trigger patch, $x = 0$, $y = L/2$), 2) normal component of velocity at the crack tip ($x = 0$, $y = L$), 3) normal component of displacement at central position of the crack, 4) normal component of displacement at the crack tip. Note that the trigger component of the velocity and displacement waveforms at the location of the trigger patch is an order of magnitude larger in amplitude than the resonance component. At the crack tip ($y = L$), the trigger and resonance components have the same amplitude in the velocity waveform, while the resonance component is dominant in the displacement waveform.

nant motion. This might be achieved by variations in crater topography across the extent of the crack, which may allow the motion at shallower parts of the crack to couple well into the atmosphere while keeping the remainder of the crack buried deep enough that coupling to the atmosphere is negligible. In this section, we investigate these additional complexities in 2D by using the finite difference fluid-filled crack code WETC3D of Chouet [1986] to generate a distributed line source, which is then input into ASTAROTH [D'Auria and Martini, 2007] for calculation of the seismic-infrasonic coupling. A smaller grid spacing is used to allow modeling of frequencies up to 5 Hz, while the effects of trigger patch position, and variations in crater topography above the extended line source are considered.

3.5.1 Model configuration

3.5.1.1 Acoustic properties of the fluid-filled crack

The fluid-filled crack is specified by the parameters α/a, b/μ, W/L, and the crack stiffness:

$$C = \frac{bL}{\mu d}, \tag{3.3}$$

where $\alpha = V_p$ is the P-wave velocity of the elastic solid, μ is the shear modulus of the elastic solid, a is the sound speed of the fluid in the crack, b is the bulk modulus of this fluid, and L, W, and d, are the length, width and aperture of the crack respectively [Chouet, 1986]. Assuming a Poisson solid ($\lambda = \mu$), the ratios α/a and b/μ are related to the density of the fluid ρ_f and density of the solid ρ_s by:

$$\frac{\rho_f}{\rho_s} = \left(\frac{\alpha}{a}\right)^2 \left(\frac{b}{3\mu}\right). \tag{3.4}$$

For the solid, we use $\alpha = 3500$ m/s and $\rho_s = 2650$ kg/m^3 as in section 3.4, which fixes μ to ∼10 GPa. For the crack dimensions we assume $L = 200$ m, $W = 100$ m, and $d = 5$ cm as postulated by Waite et al. [2008]. The acoustic properties of the fluid are given values of $a = 200$ m/s and $\rho_f = 500$ kg/m^3, corresponding to a water-steam foam at a pressure of 5 MPa (lithostatic pressure for the shallow source depth of ∼200 m) and temperature T = 537 K [Kumagai and Chouet, 2000]. Accordingly, the model fluid-filled crack is specified by $\alpha/a = 17.5$, $b/\mu = 0.0018$, $W/L = 0.5$, and $C = 7.5$.

3.5.1.2 Waveforms at the wall of the fluid-filled crack

Since we are interested in the contribution of the broadband trigger component to infrasonic waveforms in the band 1-5 Hz, our modeling in this section includes frequencies up to 5 Hz. The finite difference calculations for the fluid-filled crack were performed for a physical grid spacing of 5 m, satisfying the minimum of five grid points per smallest wavelength (based on $a = 200$ m/s) required for stability in WETC3D. Time stepping was performed until $t = 30$ s to capture the long-duration oscillations of the crack.

Figure 3.24 shows waveforms at the wall of the fluid-filled crack in the y-direction along the centerline of the crack, $x = 0$ (dashed line in Figure 3.24a), where a trigger patch is located at the center of the crack ($x = 0$, $y = L/2$). Velocity and displacement waveforms at the trigger patch (center of the crack) have trigger components with amplitude an order of magnitude higher than the resonance component (Figure 3.24c – 1,3). In contrast, velocity and displacement waveforms at the crack tip have a much weaker contribution from the trigger, and the resonance component is more dominant here (Figure 3.24c – 2,4).

3.5.1.3 Moment tensor representation of the crack

The moment tensor for the volumetric opening of a horizontal crack is given by:

$$\boldsymbol{M} = \Delta V \begin{pmatrix} \lambda & 0 & 0 \\ 0 & \lambda & 0 \\ 0 & 0 & \lambda + 2\mu \end{pmatrix}, \tag{3.5}$$

where $\boldsymbol{M}$ is the moment tensor, ΔV is the volume change, and λ, μ are the Lamé parameters [Chouet, 1996b]. For a horizontal crack in a Poisson solid ($\lambda = \mu$), the time-dependent moment tensor is therefore given by:

$$\boldsymbol{M}(\mathrm{t}) = 2\mu LWu(t)\begin{pmatrix} 1 & 0 & 0 \\ 0 & 1 & 0 \\ 0 & 0 & 3 \end{pmatrix}, \tag{3.6}$$

where $\mathbf{M}(\mathrm{t})$ is the moment tensor as a function of time, L and W are the length and width of the crack, and *u(t)* is the normal component of displacement at the crack wall. *u(t)* was obtained by a cumulative integral of the normal component of velocity at the crack wall using the trapezium rule. Note that the factor of 2 comes from the full opening of the crack with 2 opposite walls. The time and velocity output from WETC3D were converted to dimensional form using the relations:

$$v(t) = \left(\frac{4n\alpha\Delta P}{\mu}\right)v'(t) \tag{3.7}$$

$$dt = \left(\frac{L}{\alpha}\right)dt', \tag{3.8}$$

where n is the number of grid points used to discretize the length of the crack ($n = 40$), ΔP is the magnitude of pressure step applied at the trigger patch ($= 1 \times 10^5$ Pa), and primed quantities represent non-dimensional form in WETC3D.

The extended line source in 2D is represented by a series of 40 point sources sampling the crack centerline (Figure 3.24b). Each point source has the moment tensor representation of equation (3.6), with the appropriate function *u(t)* corresponding to that location on the crack, length element $L = 5$ m, and width $W = 100$ m corresponding to the entire width of the crack. The difference in source depth ($\sim$18 m) along the $\sim$200 m length of a crack dipping $\sim 5^\circ$ as postulated by Waite et al. [2008] is small, justifying our assumption of a horizontal crack in these calculations.

3.5.1.4 Geometry of the seismo-acoustic medium

In each case, the geometry of the seismo-acoustic medium in ASTAROTH is 2D, extending 1 km in the y-direction and 500 m in the z-direction. The solid is homogeneous with V_p = 3500 m/s, V_s = 2020 m/s, and ρ_s = 2650 kg/m^3, and is overlain by a homogeneous atmosphere with V_p = 330 m/s, V_s = 0 m/s, and ρ_a = 1.2 kg/m^3. As in WETC3D, a physical grid spacing of 5 m was used in ASTAROTH, therefore avoiding spatial aliasing problems. Time stepping was performed until t = 10 s, enough to compare the contribution from the initial trigger component (t <0.5 s, see Figures 3.24, 3.25) to the resonance component of the STF (t >0.5 s). We note that the instantaneous pressure-step function used in WETC3D produces a very short-duration trigger component (<0.5 s) with amplitude an order of magnitude higher than the resonance component. In reality, the trigger may be longer in duration, and the model results would be convolved with this longer-duration trigger STF. However, the short-duration trigger is more practical for investigating trigger-resonance separation with shorter computations. The first set of runs (Figure 3.25) correspond to flat topography, while the second set of runs include variations in crater topography above the shallow buried crack (Figure 3.26, Table 3.1).

3.5.2 Results

3.5.2.1 Crack in a homogeneous half space

Figure 3.25 shows the results for a crack line source buried in a homogeneous elastic half space. In Figure 3.25a-d the trigger patch is located at the crack center, while in Figure 3.25e-h the trigger patch is located at the crack tip. In both cases, the horizontal crack is placed at 50 m depth below the ground surface. As seen in Figure 3.25c and g, seismic-acoustic conversion takes place near the epicenter of the trigger patch, resulting in propagation of the trigger signal through the

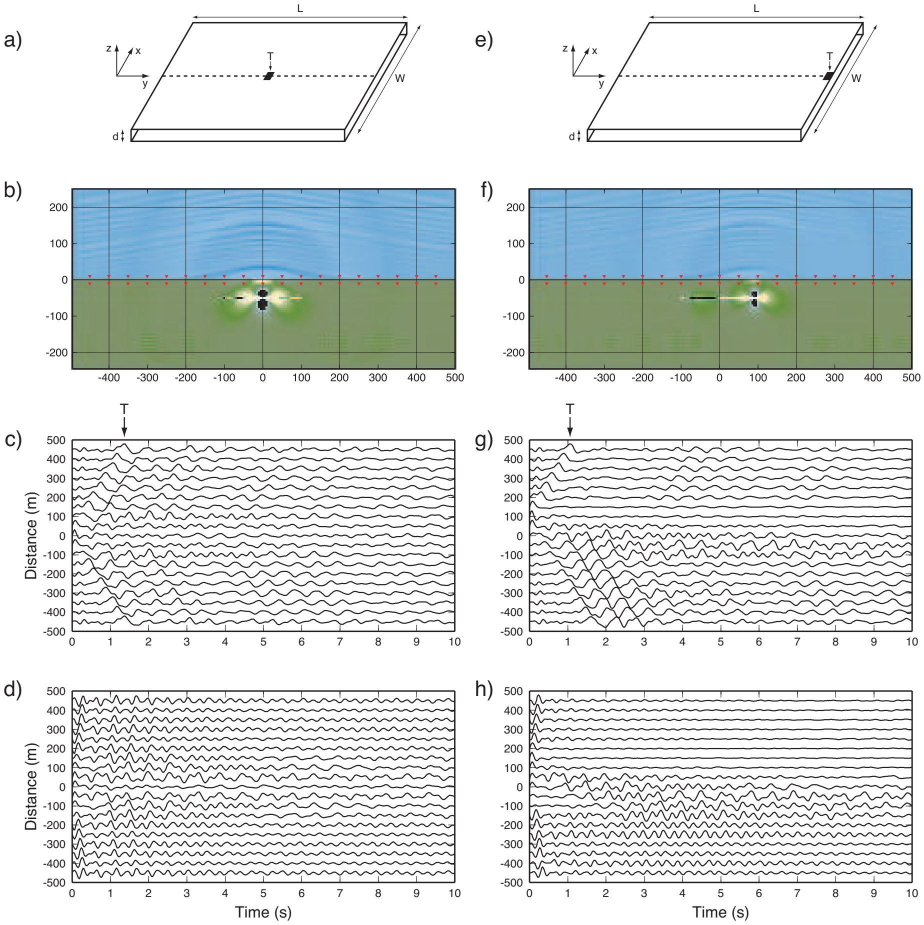

Figure 3.25: Seismo-acoustic wave field from a fluid-filled crack buried at 50 m depth in a homogeneous elastic half space, overlain by a homogeneous atmosphere. a) Geometry of the fluid-filled crack for the simulation results shown in b-d. In this run, the trigger patch is located at the crack center. b) Pressure (acoustic and elastic) wave field snapshot at $t = 1$ s for the crack geometry of (a) centered at (0,-50). Position of synthetic sensors indicated by red inverted triangles. c) Pressure record section for sensors in the atmosphere layer. The acoustic arrival corresponding to the trigger component of the LP source is indicated by a "T", all subsequent waveform features correspond to the 'resonance' component. d) Vertical component velocity record section for sensors in the elastic layer. Note that the resonance component dominates the velocity waveforms. (e-h) as (a-d) but for a trigger patch located at the crack tip. Note the asymmetry in the wave field for this source configuration (f, g). The trigger component is dominant in pressure waveforms to the right hand side of the crack, while the resonance component is dominant to the left hand side of the crack. The apparent "weak" P-arrival at distances of -50 and -100 m in (h) is a result of waveforms being displayed as normalized (energy later in the waveform at those distances is dominant in amplitude over the initial P-arrival).

atmosphere at acoustic velocity ("T") in Figure 3.25c,g). However, for a trigger patch located at the crack center, this energy is focused in the vertical direction (Figure 3.25b), and the acoustic waveforms at ground level consist of a trigger and resonance component with approximately the same amplitude except directly above the crack (Figure 3.25c). For a trigger patch at the crack tip, horizontal source-directionality is observed. Pressure waveforms to the right of the crack ($y > 100$ m) in Figure 3.25f have a stronger trigger component than resonance component, while waveforms to the left of the crack ($y < -100$ m) are dominated by the resonance component (Figure 3.25g). However, the amplitude ratio of trigger to resonance component for $y >100$ m is only ~ 2, not the order of magnitude required to explain the observed signals (Figures 3.2, 3.12b). In additional calculations not presented here, we increased the size of the trigger patch and found that this resulted in stronger resonance of the crack, and a reduction in the amplitude ratio of trigger to resonance components for the atmospheric signals. Although limited to a 2D geometry, these calculations suggest that the contribution of the trigger patch cannot outweigh the net contribution of the resonance component for a horizontal crack buried in a homogeneous elastic half space. Remaining possible ways to enhance the trigger component in the atmosphere relative to the resonance component are variable topography over the crack, or a localized increase in acoustic transmission immediately above the trigger patch by permeable/porous material. In the next section, we investigate the role of variable topography above the crack.

3.5.2.2 Crack overlain by variable topography

Figure 3.26a shows a 5 m interpolated DEM of the southern April 2005 crater [Schilling et al., 2008]. In this region, the crater wall and 2005 lava dome have the greatest topographic gradients. Accordingly, we sample two profiles along (P1) and across (P2) the 2005 lava dome, extending to the south crater wall. The

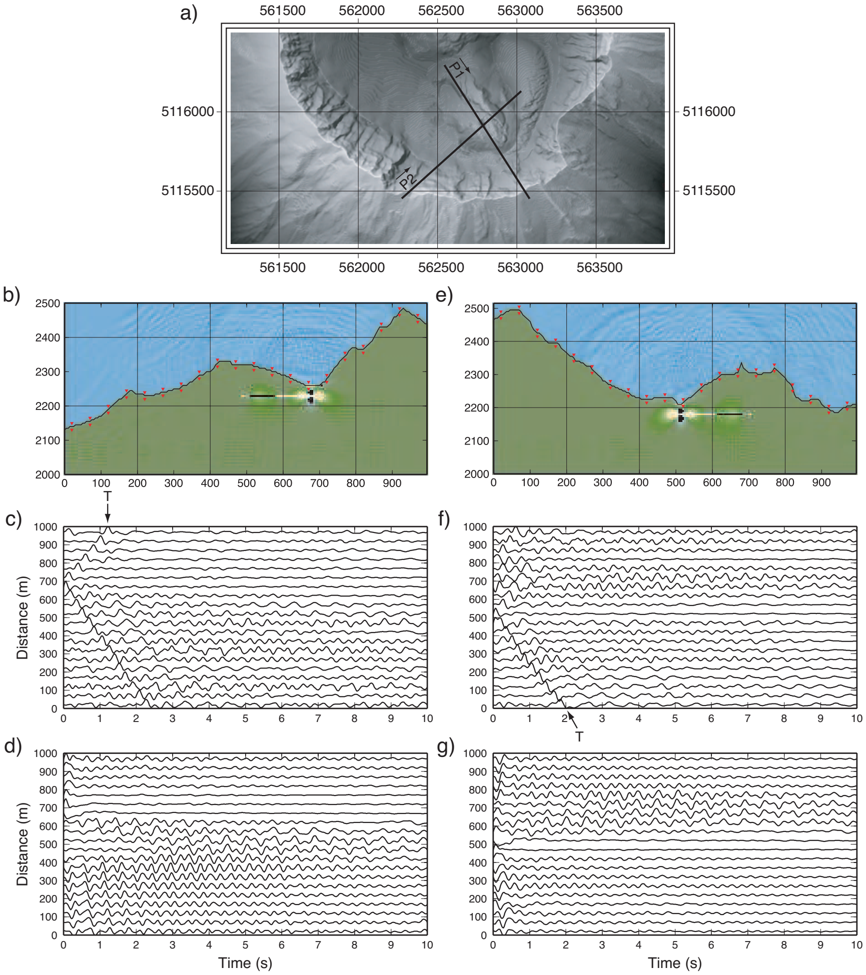

Figure 3.26: Seismo-acoustic wave field from a fluid-filled crack buried shallow beneath variable crater topography. a) Location of topography profiles within the crater of April 2005 [Schilling et al., 2008]. Profile P1 runs approximately NW-SE along the 2005 lava dome, while profile P2 runs approximately SW-NE across the 2005 lava dome. In each case, the centerline y-axis of the fluid filled crack is oriented along the profile, with the trigger patch at the crack tip underneath the shallowest point in topography (b, e). b) Pressure (acoustic and elastic) wave field snapshot at $t = 1$ s for a fluid-filled crack with trigger at the crack tip underneath topography profile P1. Red inverted triangles indicate position of synthetic sensors. c) Acoustic pressure record section for profile P1. The acoustic arrival corresponding to the trigger is indicated by a "T". d) Vertical component velocity record section for profile P1. (e-g) as (b-d) but for profile P2. In each case, the crack is located such that the trigger patch at the crack tip is the shallowest point on the crack, located 30 m below the surface. The remainder of the crack is buried beneath the deeper variable topography of the 2005 lava dome.

fluid-filled crack source with trigger patch at the crack tip (see section 3.5.2.1) is located directly beneath the 2005 lava dome, with the trigger patch located 30 m below the topography surface at that location (Figure 3.26b,e). The acoustic signal resulting from this source for profile P1 has a trigger-resonance amplitude ratio of ∼3 for profile P1 (Figure 3.26c). For profile P2, the acoustic trigger amplitude is about the same as the resonance amplitude (Figure 3.26f), even though the topography gradient is stronger along the length of the crack for P2. The reason for this is that P2 includes strong gradients in topography in the immediate vicinity of the trigger epicenter, while P1 has relatively flat topography in the vicinity of the trigger epicenter. This indicates that not only is crater topography important for controlling variable seismic-acoustic coupling along the length of a shallow crack in a homogeneous elastic medium, but the topography structure in the immediate vicinity of the source epicenter is also critical for effective infrasound generation.

In a separate calculation, we found that decreasing the depth of the crack to 15 m below the topography surface at the trigger patch increased the acoustic trigger-resonance amplitude ratio by a factor of 2, still too small to explain the observed signals (Figure 3.2, Figure 3.12). This indicates that an extremely shallow trigger source (<10 m) would be required to explain the observed signals by simple elastodynamic coupling in homogeneous media. For the LP source depth of ∼200 m obtained by Waite et al. [2008], simple elastodynamic coupling is therefore not a feasible source for the observed infrasonic signals. For a crack at a depth ∼200 m, variations in topography above the crack would be negligible (see Figure 3.26b,e) and would not cause separation of the trigger and resonance components in the acoustic pressure waves. The shallowest materials in the 2004-2005 crater of Mount St. Helens most likely consisted of a lava dome complex made up of core blocks of dense dacite with large-scale fractures, covered by a loosely-consolidated talus pile, and partially by glacier ice [Cashman et al., 2008; Pallister et al., 2008; Schilling et al., 2008; Vallance et al., 2008]. Since our models indicate that an extremely shallow source is required, this implies that the trigger would be located within this material (see section 3.7.1).

3.6 Atmospheric propagation effects and signal intermittency

The most significant time-dependent factors influencing sound propagation outdoors are: 1) refraction from vertical gradients in temperature and wind, 2) classical and molecular absorption (dependent on temperature, ambient pressure, and relative humidity), 3) effects of the ground impedance (affected by snow cover and vegetation), and 4) scattering from turbulence [Reynolds, 1873; Piercy et al., 1977; Larsson and Israelsson, 1991; Embleton, 1996; Ostashev, 1997]. Fortunately, infrasonic propagation for the frequencies and range (13.4 km) we consider in this study is much simpler: absorption is negligible [Sutherland and Bass, 2004], the surface impedance is very large so that very little energy is lost to the ground surface [Bass, 1991], and turbulence is typically disregarded. Therefore, to a first order, infrasonic propagation is governed by horizontal stratification in temperature and wind, while turbulence may result in additional fluctuations in signal amplitude and phase. Temperature affects the adiabatic or static sound speed as:

$$c = \sqrt{\frac{\gamma RT}{M}}, \tag{3.9}$$

where c is the sound speed, $\gamma = c_p/c_v$ the ratio of specific heats, R is the molar gas constant, T is the absolute temperature, and M the molar mass of air. Wind advects the acoustic fluid (see equation (3.2)), resulting in spatially dependent changes in the propagation speed. The infrasonic propagation between MSH and CDWR is confined to the atmospheric boundary layer, and is therefore controlled by mesoscale and microscale meteorology.

Ray theory applied to temperature lapse or upwind propagation results in upward refraction and the formation of a shadow zone, while temperature inversion or downwind propagation result in downward refraction and clear signal reception [Piercy et al., 1977]. Thus, ordinary lapse conditions or northwesterly winds would put CDWR in a shadow zone of MSH according to ray theory. However, ray theory is a high-frequency approximation and begins to fail for infrasonic frequencies where the wavelength approaches the scale lengths of the temperature and wind gradients. Refraction occurs but at much longer ranges [Piercy et al., 1977], and diffraction (creeping waves) and scattering from turbulence fill in the shadow zones [Bass, 1991]. This said, Fee and Garces [2007] reported diurnal variations in infrasonic tremor amplitude at a range of 12.5 km from Pu‘u ‘Ō‘ō, Hawaii, well-correlated with the formation and break up of a nocturnal boundary layer. Although the variations are not dominantly diurnal in our data (Figure 3.11), non-diurnal boundary layer dynamics are the likely cause of signal intermittency. The amplitudes of the infrasonic LP signals we consider in this study (Figure 3.5) are comparable to the amplitudes of infrasonic tremor discussed by Fee and Garces [2007] and are very low in comparison to other volcano-acoustic signals [Garces et al., 2008]. Thus atmospheric propagation effects are far more noticeable for LPs than for large-amplitude eruption signals that appear to fill in the shadow zones [Garces et al., 2008]. In this section, we briefly compare ray tracing and 2D finite-difference simulations of infrasonic propagation between MSH and CDWR. The finite-difference approach gives a more complete description of wave propagation, enabling more accurate predictions of the sound field at low frequencies.

3.6.1 Ray tracing

We performed ray tracing using the approach of Garces et al. [1998] using Ground to Space (G2S) semi-empirical atmospheric specifications for the study region [Drob et al., 2003]. The G2S specifications used in this study have a horizontal resolution of $\sim 1^\circ \times 1^\circ$, a vertical resolution of 200 m and a temporal resolution of

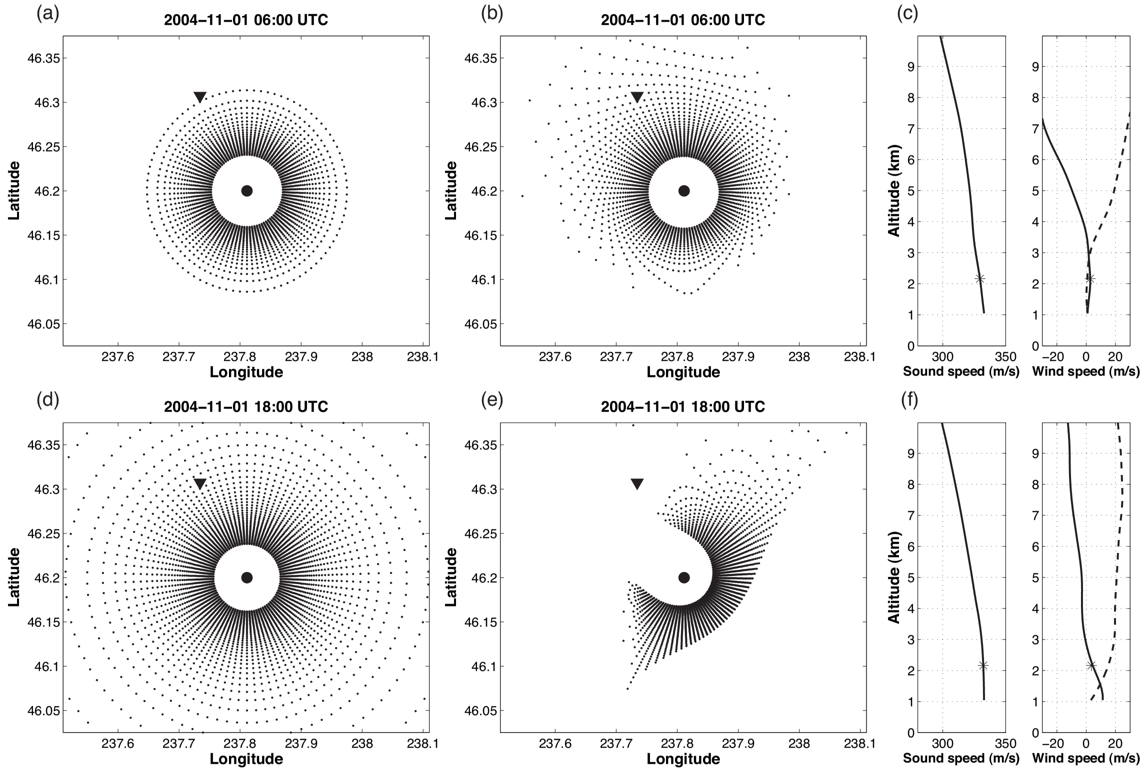

Figure 3.27: Coordinates of ray first-bounce points predicted with the G2S model. The source location (altitude 2.2 km, star in c,f) at MSH is indicated by a solid dot, CDWR location indicated by an inverted triangle. In the dotted area, clear direct signal reception is predicted, while other regions represent shadow zones where rays refract upwards before reaching the ground. a) G2S model for 2004-11-01 06:00 UTC with effects of wind neglected, b) as (a) but wind included, c) static sound speed and wind speed profiles for G2S model 2004-11-01 06:00 UTC, solid line: meridional winds (N-S), dashed line: zonal winds (E-W), d) model for 2004-11-01 18:00 UTC without wind, e) as (d) but with wind, f) as (c) but for 2004-11-01 18:00 UTC.

6 hours. They therefore lack the finer mesoscale structure required to fully resolve atmospheric propagation at this scale. Nevertheless, G2S does provide physically realizable wind and temperature profiles that are useful for assessing the effects of typical atmospheric variability.

Supplementary movie 2 in Matoza et al. [2009b] shows a plan view of tropospheric ray first-bounce points from a source just above the elevation of the LP source for the time period 1-16 November 2004. Rays are shot in 4° increments azimuthally, and 0.25° increments for the grazing angle (angle from horizontal, positive upward). Topography has been neglected, but rays have been limited to a grazing angle of >-15°, the approximate slope of the mountain along our profile (Figure 3.13). Multiple ground bounces are not permitted. Fluctuation in the spatial position of ray first-bounce points is seen. Ray bounce points extend to CDWR at certain times (e.g., 2004-11-10 06:00 UTC) predicting clear signal reception, and at other times do not (e.g., 2004-11-01 18:00 UTC), predicting CDWR is in a shadow zone and loss of signal reception. We note that these time predictions for signal loss do not match our data, indicating that the G2S atmospheric models are not sufficiently accurate at the 10 km lateral scale.

The importance of wind for the ray predictions is illustrated in Figure 3.27. Here the spatial distribution of first-bounce points for two representative time periods are shown with and without including advection due to wind. In Figure 3.27a, ray coverage does not extend to CDWR when wind is neglected, but does when wind is included (Figure 3.27b). In Figure 3.27d, rays do extend to CDWR without wind, but form a clear shadow zone when wind is included (Figure 3.27e). This can be understood by reference to the wind profiles (Figures 3.27c, 3.27f). While relatively little difference exists in the static sound speed due to temperature, the winds for the case shown in Figure 3.27b have a southeasterly component at the source altitude (winds blowing from MSH toward CDWR) and for the case shown in Figure 3.27e have a strong northwesterly component (winds blowing from

CDWR toward MSH), generating a shadow zone due to upwind propagation.

3.6.2 Finite-differences

Figure 3.28 shows the results of 2D finite-difference (FD) simulations for the four atmospheric cases shown in Figure 3.27, with and without elastic ground topography. Where topography is neglected (Figure 3.28a-d), the source altitude is the same as in the ray simulations of Figure 3.27 and all boundary conditions are absorbing (no reflections from the ground), allowing for a direct comparison of ray tracing and FD methods. Where topography is included (Figure 3.28e-h), the source is buried at a depth of 60 m within the volcano. In each case we also included a more realistic density profile for the atmosphere:

$$\rho(z) = \rho_0 e^{-0.000146(z-z_0)},$$

where ρ_0 = 1.04 kg/m^3 at z_0 = -1100 m in our coordinate system. Although the 2D geometry does not include the geometrical spreading loss, it models the wave field structure, which is more directly comparable to the ray results of Figure 3.27.

All simulations in Figure 3.28 show less pronounced effects of vertical wind and temperature gradients than the ray simulations of Figure 3.27. Rather than sharp refraction and the formation of clear shadow zones, the gradients result in a slight steepening and gradual upward turning of the wavefronts, with significant energy diffracting down into the ray shadow zones. The simulations neglecting wind (Figure 3.28a, c, e, and g) are barely distinguishable from one another, while the simulations including wind (Figure 3.28b, d, f, and h) show more pronounced differences. This is in agreement with the prediction of Figure 3.27 that wind has more significant effect on acoustic propagation at this scale than vertical temperature gradients. As in Figure 3.27e, the most significant effects are seen in Figure 3.28d, with the G2S model for 2004/11/01 18:00 UTC with wind included. In Figure 3.27e a full shadow zone for CDWR is predicted, while in

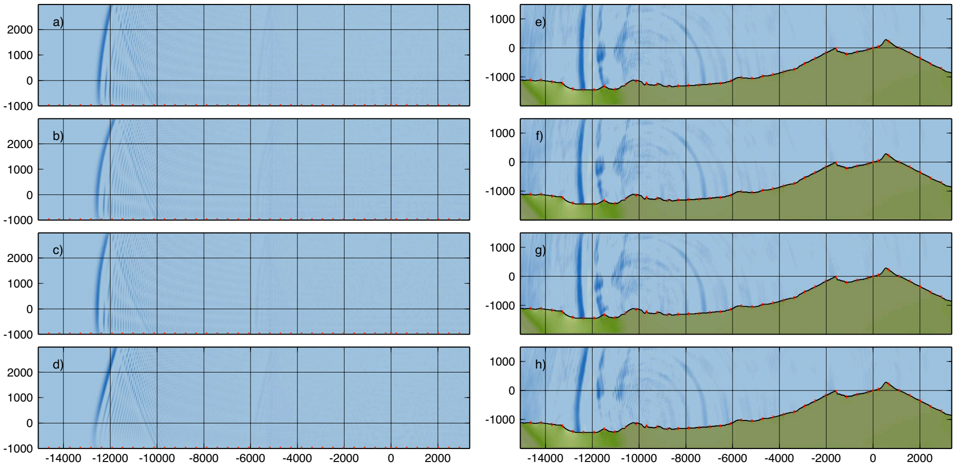

Figure 3.28: 2D FD simulation of the four atmospheric cases shown in Figure 3.27, with and without topography. All images are pressure wave field snapshots at $t = 38$ s. a) G2S model for 2004-11-01 06:00 UTC with effects of wind neglected, b) as (a) but in-profile wind included, c) G2S model for 2004-11-01 18:00 UTC with effects of wind neglected, d) as (c) but in-profile wind included, (e)-(h) as (a)-(d) but source is buried at 60 m depth in elastic topography. Note the difference in vertical scales for plots on left vs. plots on right. In all cases, the effects of wind and temperature gradients are less pronounced than in the high-frequency ray approximation, with only slight steepening and gradual refraction of wavefronts. In contrast, the ray results of Figure 3.27 predict a full shadow zone for the case shown here as (d) and (h). The effects of wind are evident in (d), where upturning of the wavefront, and weaker amplitude near the base of the model are observed. However, the simulations (e)-(h) show less sensitivity to the atmospheric conditions, suggesting that scattering from topography, in addition to diffraction, may be important for filling-in the infrasonic shadow zone.

Figure 3.28d some weak upward refraction results in a predicted lower amplitude at CDWR (energy weaker along wavefront below $z = 0$ km), but not the complete loss of signal. Thus, the ray and FD results are in qualitative agreement about which are the more dominant atmospheric effects on propagation (i.e., winds blowing receiver-source), but rays are overly sensitive to these gradients and predict full signal loss where FD predicts significant energy.

Further differences are seen in the simulations including elastic topography and a buried source (Figure 3.28e-h). Here, the effects of refraction are even less pronounced than in the simulations without topography (Figure 3.28a-d). In particular, the energy loss predicted at a ground-based receiver at 13 km in Figure 3.28h is much lower than that seen in Figure 3.28d for the same atmospheric conditions. This suggests that scattering by topography may be important for diffracting energy into shadow zones at this scale. In a separate set of simulations, we experimented with adding a thin (400 m) temperature inversion layer mantling the topography. We found that this also had no effect on the predicted infrasonic wave field, suggesting that wind and perhaps turbulence are the dominating factors.

3.7 Discussion

3.7.1 Source process

The measured lower bound on the modal amplitude ratio (P/V_z) of 1.3 $\times$ 10^4 Pa·s/m at CDWR (Figure 3.5) cannot be reproduced by the simple elastodynamic processes we have considered. For the shallowest source possible in our modeling, the predicted P/V_z is an order of magnitude lower than this, while the predicted P/V_z ratios from the point source description and location of Waite et al.

[2008] are lower still[2]. We also found that the addition of a laterally continuous near-surface weathered layer with lower impedance cannot reproduce the amplitude ratio, as the seismic amplitude in the layer increases in proportion to the amplitude of the pressure wave. However, additional complexities not considered in our modeling may affect the amplitude ratio. As discussed in sections 3.4.1.2 and 3.6, energy focusing by a wind-direction bias may lead to an increase in observed P/V_z. In addition, a low-impedance layer local to the source region would enhance infrasonic energy transmission in the vicinity of the source epicenter, without increasing seismic amplitudes at long range. Furthermore, our velocity-stress governing equations do not include nonlinear material effects such as tensile failure or spalling of near-surface layers that can be important for shallow buried sources [Stump, 1985], nor do they include the effects of porosity and permeability of the near-surface materials [Sabatier et al., 1986; Hickey and Sabatier, 1997]. In particular, Bass et al. [1980] showed that the transmission coefficient at the ground surface for acoustic energy in the 20-300 Hz band cannot be fully described by the impedance ratio of the materials. The transmission coefficient can be at least an order of magnitude higher (up to three orders of magnitude higher) when permeability and airflow through pore volumes is considered. Allowing for the presence of fractures and loosely consolidated material [Cashman et al., 2008; Pallister et al., 2008], the permeability increases substantially. Therefore, based on amplitude considerations alone, we can rule out the possibility of a deep source generating the infrasonic signals, but we cannot distinguish between a surface source venting directly to the atmosphere, and a shallow source (e.g., the ∼200 m deep source of Waite et al. [2008]) buried in a near-surface layer of highly-fractured, porous and permeable material. In addition, we find little evidence in our data for seismic-acoustic en-

---

[2] The amplitudes of the observed pressure waves at BLIS and CDWR are consistent with acoustic spherical spreading. However, the observed P/V_z at BLIS is likely affected by instrumental limitations at that station, in particular, the restricted bandwidth of the piezo-electric accelerometer and electret microphones. We therefore refrain from making inferences based on the BLIS data.

ergy converted locally along the propagation path and arriving coincident on the microbarometer and seismic records (i.e., pressure waves in the atmosphere with seismic horizontal velocity). Our numerical results indicate that these should be a prominent feature for a source buried in a homogeneous elastic medium. By allowing for high permeability and low impedance of near-surface material above the source, the acoustic energy radiating from the source epicenter may potentially dominate in amplitude over the locally converted seismic energy at ranges of ∼10 km. However, while the amplitude ratios are sensitive to several factors not included in our modeling, the observed characteristic differences in waveforms and spectra (Figures 3.2, 3.4, 3.12) are more robust indicators of source properties.

The observed waveforms and spectra (Figures 3.2, 3.4) are very difficult to reconcile with a common source-time function. The infrasonic signals are characterized by short-lived (∼5-10 s) broadband pulses, while the seismic signals are characterized by ∼5-10 s broadband pulses followed by a long-duration (>50 s) resonant coda. The resonant coda is not prominent in the infrasonic records, but a very weak long-duration signal is found to underlie the infrasonic records (Figure 3.12). Impulsive acoustic signals in the atmosphere are often observed to generate longer-duration seismic vibrations by air-ground coupling, and these can be modeled in terms of the seismic frequency response of a near-surface layered structure to the impulsive acoustic driving function [Sabatier and Raspet, 1988]. However, if a common source-time function is assumed in our study, we have the opposite of this scenario, with a longer-duration resonant seismic source-time function apparently producing an impulsive broadband acoustic signal in the atmosphere. Such a process is unlikely, and not supported by the results of sections 3.4.2.4 and 3.4.2.5.

Putting this together, a more complex integrated source process is required, one consisting of an impulsive STF for the infrasound signal and an impulsive signal plus resonance component for the seismic signal. In other words, the infrasound signal is a record of the impulsive pressure excitation mechanism or trigger mechanism of the long-period event, while the seismic signal consists of the superposition of the trigger and fluid response (crack waves). Since the broadband pulse has much stronger coupling to the atmosphere than the resonant coda, a mechanism is required for energy partitioning of the trigger and resonance components at the source.

In section 3.5, we investigated whether variable crater topography above an extended fluid-filled crack source could provide a viable mechanism for partitioning of trigger and resonance components. We found that a trigger patch located $<$10 m below the topography surface, connected to an extended fluid-filled crack buried at greater depth below a mound of crater topography such as a lava dome, would result in atmospheric acoustic signals that are enriched in the trigger component relative to the resonance component. However, the source depth required for topography to be important is extremely shallow, and requires the trigger patch to be located effectively at the surface. The trigger component from a crack buried at $\sim$200 m depth would not be isolated from the resonant component by the effect of topography alone. This leads to the conclusion that while crater topography may play a role for a very shallow crack source, the influence of porosity and permeability of the shallowest materials is inescapable. We note that strong coupling of the fluid-filled crack into the elastic solid is required for effective seismic LP signal generation. Therefore, a very shallow, horizontal crack located near the surface exclusively in loosely consolidated material, is an unlikely source for the seismic LP signals. A buried crack that is well coupled to the elastic solid, but venting at its tip into loosely consolidated material, is a reasonable source for both seismic and infrasonic waveforms. Vertical and lateral heterogeneity in crater materials therefore seem necessary for separating the trigger and resonance components from an extended source.

As proposed by Waite et al. [2008], the loss of pressure in a shallow hydrothermal crack is a feasible source for both infrasonic and seismic LP events at Mount St. Helens. Sudden, seismogenic loss of steam pressure requires a sudden opening of a pathway to allow the steam to escape. This opening is analogous to the opening of a valve, and the pressure signal resulting from this sudden pressure change, in addition to the rapid flow of gas accompanying this process, would be a significant source of infrasound. The jetting from such a source may be highly localized, perhaps involving a small patch of crack wall with a length scale of $\sim$10 m on the 100 m × 200 m crack postulated by Waite et al. [2008], and in this case would result in higher-frequency signals than those recorded. However, although the jetting may not be the dominant source of infrasound for LPs, the gas velocity would increase the total gas volume flux, and enhance the amplitude of the resultant acoustic signal [Lighthill, 2001]. If gas vents into a network of open pathways within the dome material, efficient acoustic coupling into the atmosphere is possible. Conversely, crack vibration radiates elastic energy into the solid, so this component dominates the seismic waveforms.

The periodic occurrence of drumbeat LPs can be explained conceptually by a cycle of pressure build up, the reaching of a critical pressure threshold for the valve, and the catastrophic opening of the valve which initiates rapid pressure loss (infrasound signal), collapse of the crack, and attendant resonant response of the fluid remaining in the crack (seismic LP signal). Once pressure is lost, lithostatic pressure reseals the valve and the next cycle of pressure recharge begins. A similar model was proposed by Ohminato [2006] to explain periodic VLP and high-frequency pulses associated with the hydrothermal system at Satsuma-Iwojima volcano, Japan. Ohminato [2006] also suggested that water contained in a crack in a superheated state might suddenly vaporize, providing an explanation for the sudden surge of pressure in the crack and the opening of the valve. However, in our case the pressure release valve is close enough to the surface to generate infrasound.

Periodic, rapid discharge of gas in association with seismic LP and VLP activity has been observed at numerous other volcanoes [e.g., Gil Cruz and Chouet, 1997; Neuberg et al., 2000; Chouet et al., 2005], and has also been associated with infrasound radiation when infrasonic sensors were deployed [Yamasato, 1998; Yamasato et al., 2002; Petersen and McNutt, 2007]. In the crater of Galeras volcano, Colombia, Gil Cruz and Chouet [1997] photographed explosive gas emissions along a crack bisecting the dome (120-150 m long and a few millimeters wide) that were correlated with recorded LP events. Neuberg et al. [2000] reported jets of steam and ash accompanying LP events at Soufriere Hills volcano, Montserrat, recorded on synchronized seismic and video data, suggesting that the LP source was somehow linked to gas venting.

However, the 2004-2008 eruption of Mount St. Helens was characterized by low magmatic gas emissions [Gerlach et al., 2008], with relatively low-levels of steady steam effusion leaking from cracks and openings in the lava dome [Vallance et al., 2008]. No periodic gas release was observed. The near-surface materials above the LP source most likely consisted of fractured blocks of dacite, loosely consolidated talus, and perhaps glacier ice [Cashman et al., 2008; Pallister et al., 2008; Schilling et al., 2008; Vallance et al., 2008], and so were likely to be acoustically permeable for infrasonic wavelengths. Slow diffusion, condensation, and buffering of steam through this material may result in relatively low levels of steam emissions at the surface, consistent with field observations. Darcy's law for fluid-flow through a porous medium gives an approximate diffusion timescale for steam rising through porous Mount St. Helens dacite:

$$\tau_d \sim \frac{\mu d^2}{\kappa \Delta P}, \tag{3.10}$$

where μ is the dynamic viscosity of steam, d the depth of the venting hydrothermal crack, κ the permeability of dome rock, and ΔP the pressure difference between the crack and the surface. For $\mu \sim 10^{-5}$ kg/ms, $d \sim 200$ m, $\kappa \sim 9 \times 10^{-13}$ m^2 corresponding to vesicular dacite at MSH [Cashman et al., 2008], and ΔP given by lithostatic pressure ~5 MPa ($\Delta P \sim \rho g z$ for $\rho = 2650$ kg/m^3, $g = 9.8$ m/s^2, and $z = 200$ m), τ_d is ~ 24 hours, providing adequate time for a periodic release of steam to be filtered to a steady surface effusion, and perhaps for a large portion of the steam to be condensed and buffered. However, if the flow of steam takes place through a dendritic network of cracks, the value of effective κ may be higher, decreasing τ_d. In addition, Darcy's law may not be applicable for energetic steam injection into the subsurface. Nevertheless, it seems feasible that the ascent of steam through near-surface material may be much slower than the time-scale for acoustic propagation in the same material. This may mask the periodic nature of the steam release so that only a steady steam effusion is observed at the surface. In addition, if longer time-scales are considered, steam may condense and be recycled back into the groundwater system.

Finally, we note that the weak long-duration signal underlying the dominant pulse in the infrasonic records was identified only by waveform cross correlation of many repeating events (Figure 3.12) and was too low in amplitude to be identified in individual events by array processing. This energy has a P/V_z ratio an order of magnitude or more lower than the main pulse, so is consistent with seismic-acoustic converted energy from the region around the source as calculated in our numerical models. This agrees with our interpretation that crack waves coupling into the elastic solid and subsequently into the atmosphere at the ground surface form much weaker infrasonic signals than direct mass injection through clogged pathways to the atmosphere.

The LP seismic events investigated in this study have alternatively been attributed to stick-slip motion and shear-fracture of the extruding solid lava dome [e.g., Iverson et al., 2006; Harrington and Brodsky, 2007; Tuffen et al., 2008]. This shear-faulting source process was qualitatively suggested by the presence of fault gouge and breccia on the surface of the extruded lava spines [Pallister et al., 2008], but these features may be generated aseismically. A shear-faulting (double-couple) source is inconsistent with the all-dilatational first-motions and volumetric source mechanism derived by [Waite et al., 2008]. We note that although the drumbeat LP events at MSH have been classified as “hybrid” LP events on the basis of their broadband onsets [Iverson et al., 2006; Harrington and Brodsky, 2007; *see Figure 3.6d*], a hybrid LP event was originally defined as an event with resonance features characteristic of an LP event, but with mixed first-motions characteristic of a double-couple (shear-faulting) source [Lahr et al., 1994]. Since the MSH drumbeat events do not have mixed first-motions, they are not hybrid events according to the definition of Lahr et al. [1994]. The observed broadband onsets of the MSH LP events are typical of LPs, and can be attributed to the higher modes of oscillation of a resonating source (see Figure 3.24), which dissipate more rapidly than the lower modes (leading to the long-period coda).

Furthermore, a shear-faulting source mechanism predicts seismic moments and single forces that are much smaller than those observed. Waite et al. [2008] presented inversion results for a series of similar-waveform LP events with estimated forces up to 8 × 10^9 N and moments up to 2 × 10^{13} Nm. These values are 2-3 orders of magnitude larger than the force of ∼7 × 10^7 N (for slip of 5 mm) estimated by Iverson et al. [2006] and moments of 10^9–10^{10} Nm estimated directly from fault surfaces on the lava spines [Pallister et al., 2008]. A shear-faulting source is also difficult to reconcile with the results of this study. In principle, a shear-faulting source may generate infrasound by gas release associated with the rupture of gas-charged lava dome material [Yamasato, 1998], and it has also been proposed that gas-filled cracks resulting from fracture of silicic magma may sustain seismic LP resonance [Tuffen and Dingwell, 2005]. However, the gas-poor nature of the 2004-2008 MSH extrusion [Gerlach et al., 2008] makes these scenarios implausible for MSH. A passive release of gas in response to shear-fracture would also generate a much weaker infrasonic signal than the infrasonic source mechanism outlined above. The presence of steaming cracks in the 2004-2008 lava dome [Vallance et al., 2008], as well as geoelectrical evidence for the presence and persistence of an active shallow hydrothermal system within ~200 m of the 1980s crater floor throughout the 2004-2008 MSH eruption [Bedrosian et al., 2007, 2008], provide additional qualitative yet compelling evidence in favor of a shallow hydrothermal origin for the source of seismic and infrasonic LP events at MSH.

3.7.2 Signal intermittency

The infrasound signals accompanying LP events at Mount St. Helens have relatively low amplitudes in comparison to other acoustic signals recorded from volcanoes at this range. Typical amplitudes were ~0.01 Pa at 13.4 km (Figure 3.5), which is two orders of magnitude lower than signals from phreatic explosive events and rockfalls (~1 Pa) recorded at the same array from Mount St. Helens [chapter 2; Moran et al., 2008], and three orders of magnitude lower than signals recorded at the more open-vent system at Tungurahua volcano, Ecuador, at a greater range of 37 km [Fee et al., 2007]. Therefore, it is not surprising that clear detection above noise of these signals depends on atmospheric propagation effects.

Ray tracing for reasonable atmospheric specifications provided by G2S predicted strong variability in signal detection as a function of wind, and to a lesser extent, temperature gradients. However, the ray predictions do not agree with the more complete description of wave propagation given by finite-differences. For vertical wind and temperature gradients where rays show sharp refraction and the formation of a shadow zone, finite-difference results exhibit only gradual refraction, and significant diffraction of energy into ray shadow zones. The slow refraction in some instances (Figure 3.28d) may be enough to cause low-amplitude signals to fall below background noise levels, indicating that wind provides a viable mechanism for causing the observed intermittency in infrasonic LP signal detection. We note that the finite-difference results are in agreement with predictions from normal mode theory, where frequencies of 1-5 Hz propagate as a single horizontally propagating “surface” mode for typical boundary layer wind and temperature gradients [Waxler et al., 2006, 2008].

The decorrelation, loss, and subsequent return of the same infrasonic waveform is a strong indicator of atmospheric effects. Furthermore, these changes in waveform appear to be correlated with measured changes in wind speed and direction at particular times (Figure 3.10). In addition, the observations of Fee and Garces [2007] demonstrate propagation effects on the amplitude of weak (∼0.01 Pa) infrasonic signals at ∼13 km range. While the amplitude variation at Mount St. Helens is not dominantly diurnal, this suggests that mesoscale wind structure has an important effect on infrasonic propagation at these ranges.

This said, atmospheric dynamics are clearly not the only cause of signal intermittency. Infrasonic detections are more likely when the amplitude at the source is higher (Figure 3.9), illustrating that clear signal reception requires a minimum amplitude at the source even under favorable atmospheric conditions. Hence, the signal intermittency is a superposition of a long-term trend associated with the changing source amplitude, and short-term variability due to atmospheric effects.

Finally, we comment that the source process outlined in section 3.7.1 could in principle produce another source of signal intermittency via changes in the permeability of the materials overlying the LP source (chapter 2). However, changes of this kind would be masked by the effects discussed above, and we do not have adequate data to examine this.

3.8 Conclusions

During November 2004-March 2005, the source process for a sustained sequence of repetitive seismic LP events at Mount St. Helens (drumbeats) also generated impulsive broadband pressure signals traveling through the atmosphere at acoustic velocity. Finite-difference simulation of the seismo-acoustic wave field indicates that the infrasonic signals could not result simply from seismic-acoustic coupling from a common source-time function. The seismic LP event is typically modeled as an impulsive broadband pressure excitation mechanism followed by a long-duration coda resulting from the resonant response of a fluid-filled cavity. The infrasonic signal associated with the LP may be considered a record of the broadband pressure excitation mechanism or trigger mechanism initiating the resonance, while the resonant component couples only weakly through the elastic solid to the overlying atmosphere. The preferential coupling of the trigger component to the atmosphere is consistent with periodic pressure release from a shallow buried hydrothermal crack into a near-surface layer of highly fractured dome rock, and loosely consolidated talus and glacier ice. If the crack is very shallow, variations in crater topography above the crack may also enhance the preferential coupling of the trigger component into the atmosphere. Pressure may build in a sealed hydrothermal crack due to heating from magmatic activity. Periodically, pressure in the crack exceeds the containment pressure, leading to the sudden opening of a "valve", the production of the impulsive infrasonic signal, and the venting of steam through a network of cracks in the near-surface permeable material. Such a porous, highly permeable layer may permit transmission of the infrasonic pressure signals while filtering a periodic steam release to a steady surface effusion. Meanwhile, the sudden loss of pressure in the crack causes the crack to collapse, and initiates resonance of the remaining fluid, generating the seismic LP event. After pressure is lost, lithostatic pressure may reseal the valve, closing a cycle of pressure recharge and collapse that may be responsible for the periodic occurrence of drumbeat LPs.

Since the infrasonic signals were of relatively low amplitude, they were detected intermittently at an array 13.4 km to the NW of the volcano. We attribute the intermittency primarily to changes in amplitude at the source and time-varying atmospheric propagation effects. Waveform cross-correlation and preliminary modeling using ray tracing and finite-differences suggest that wind in the atmospheric boundary layer is the dominating atmospheric factor. However, more detailed information on the mesoscale meteorological structure is required to better understand the causes of amplitude spread and subtle waveform variability.

Chapter acknowledgments

Data for CDWR were collected by the Acoustic Surveillance for Hazardous Eruptions (ASHE) project [McCormack et al., 2005]. CVO data were provided by Seth Moran, Wes Thelen, and IRIS. Thanks to Bob Parker for PSD, Steve Schilling for the DEM, Garth Ferber for the NWAC met data, Doug Drob for the G2S model, and Larry Baker for help with WETC3D. Documentation and publication of ASTAROTH is currently in preparation by LD. Cluster access was kindly provided by Debi Kilb and Atul Nayak (NSF grant ANI-0225642 and the ANF), as well as Sofia Akber and Steve Constable. I would like to thank Hank Bass, David Fee, David Green, Seth Moran, Jim Sabatier, and Roger Waxler for enlightening discussions. The manuscript was diligently reviewed by Seth Moran and John Power (USGS), and two anonymous referees. This work was funded by NSF grant EAR-0609669. Chapter 3, in full, has been published as Matoza, R.S., M.A. Garces, B.A. Chouet, L. D'Auria, M.A.H. Hedlin, C. De Groot-Hedlin, and G.P. Waite (2009), The source of infrasound associated with long-period events at Mount St. Helens, *J. Geophys. Res.*, **114**, B04305, doi:10.1029/ 2008JB006128.

4. Infrasonic jet noise from volcanic eruptions

The lowermost section of a sustained vulcanian or plinian volcanic eruption column may be thought of as a momentum-driven, turbulent, free-shear[1] jet flow. We propose that large-amplitude and long-duration infrasonic (<20 Hz) signals recorded at ranges of tens of kilometers during powerful eruptions at Mount St. Helens, USA, and Tungurahua, Ecuador, represent a low-frequency form of jet noise. A preliminary test of this hypothesis is made by comparing the observed infrasonic spectra to the empirically-derived similarity spectra for pure-air jets. Although the spectral shapes are in approximate agreement, the observed volcanic signals have additional complexities not present in the pure-air laboratory data. These features may result from multiphase flow containing solid particles and liquid droplets, very high temperatures, and perhaps complex crater morphology. However, the overall similarity between the volcanic signals and jet noise indicates that broadband infrasound measurements at volcanoes may provide a quantitative link to eruption jet dynamics, and would aid substantially in the remote assessment of volcanic hazard.

---

[1] Inhomogeneous flow resulting from mean-velocity gradients in the absence of solid boundaries.

4.1 Introduction

Since volcanoes have large length-scales, the majority of their atmospheric acoustic radiation is infrasonic (<20 Hz) [Wilson and Forbes, 1969; Ripepe et al., 1996; Garces and Hansen, 1998; Vergniolle and Caplan-Auerbach, 2006]. As observed with volcano seismology [Chouet, 1996b], a variety of volcanological processes act as sources in this frequency band, each with distinct temporal and spectral characteristics. A continuous vibration of the ground or air is classified as seismic or infrasonic tremor respectively. However, different seismic and infrasonic tremor-generating processes may occur at different volcanoes, and at the same volcano to some degree.

Here we focus on one particular type of infrasonic tremor that was found to accompany powerful vulcanian and plinian eruptions at Mount St. Helens (MSH), USA and Tungurahua, Ecuador. The infrasonic tremor signals are of high-amplitude, long-duration, and broadband. If they were to couple into ground vibration and be recorded seismically, they would be classified as eruption tremor [McNutt, 2000]. However, the data presented here strongly suggest that the source is within the erupted jet in the atmosphere, and is hence more naturally observed with infrasonic sensors recording atmospheric pressure fluctuations.

Large vulcanian and plinian volcanic eruptions may be thought of as turbulent, free-shear jet flows that transition with altitude into buoyancy-driven volcanic plumes [Wilson, 1976; Kieffer and Sturtevant, 1984; Ogden et al., 2008]. Although the acoustic radiation from these fluid dynamic processes remains poorly understood, it has been proposed [Woulff and McGetchin, 1976] that turbulence within small-scale volcanic jets may act as a quadrupole source according to Lighthill's acoustic analogy [Lighthill, 1954], or a dipole source if solid particles or boundaries are present [Woulff and McGetchin, 1976]. However, measurement of the sound radiation pattern from large volcanic eruptions has proven challenging, and poor scaling between acoustic and eruption intensity has been reported

[Johnson et al., 2005].

Our data indicate that infrasonic tremor signals recorded at ranges of tens of kilometers during vulcanian and plinian eruptions represent a low-frequency form of jet noise. Rather than quadrupole radiation from fine-scale turbulence, the signals have spectral properties more characteristic of large-scale turbulence noise. We propose that dynamic similarity in jet flow results in similar physical noise-generation mechanisms in volcanic jets as in audible jet noise from flight vehicles (i.e., jet flow from aircraft and rockets). Since the length-scales for a volcanic jet are much larger, the jet noise is expected to have much lower frequencies. Furthermore, we find that as the length-scale and mass flux of the volcanic jet increase, acoustic radiation shifts to lower frequencies with greater power output. This indicates that eruption intensity and acoustic power output scale over a broad acoustic bandwidth.

4.2 Infrasound from large eruptions

Figure 4.1 shows the infrasonic waveforms recorded during a short-lived phreatic eruption (dominantly steam with entrained ash) at MSH on 8 March 2005, and three magmatic eruptions (heavily particle-laden) at Tungurahua that occurred on 14-15 July 2006, 16-17 August 2006, and 6 February 2008. Hereafter, we refer to these eruptions respectively as eruptions A-D (Figure 4.1). The MSH eruption (A) is best classified as vulcanian based on its relatively brief duration. The Tungurahua eruptions (B-D) range between vulcanian, sub-plinian, and plinian based on the duration of jetting. The data were recorded on four-element small-aperture arrays of broadband infrasonic sensors deployed at ranges of 13.4 km from MSH (chapter 2) and 36.9 km from Tungurahua [Garces et al., 2008]. The systems deployed at MSH and Tungurahua have a flat response in the 0.01-17 Hz and 0.1-17 Hz bands, respectively. Array processing (chapter 2) confirms the signals as coherent acoustic waves arriving from the azimuth of the volcano. Although each signal has different amplitude-scale and duration, the signals in Figure 4.1 are emergent and broadband, with amplitude envelopes that change over time. Discrete, impulsive explosion signals are recorded at Tungurahua (eruptions B-D) in addition to the emergent broadband signals. Note that the final hour of C is marked by a dramatic increase in signal amplitude with lower dominant frequency, before the tremor ends abruptly. This hour corresponds to a drastic change in the eruptive activity [Barba et al., 2006], characterised by an increase in jet diameter to $>$400 m, lava fountaining to a height of $\sim$6 km, and a plume height of $\sim$25 km [Steffke et al., 2008].

Despite the apparent complexity of the recorded signals, the dynamic self-similarity of jet flows [Pope, 2005], and the similarity of radiated jet noise spectra [Tam et al., 1996; Tam, 1998] suggest that infrasonic tremor signals from volcanic eruptions and audible jet noise from flight vehicles may be generated by comparable physical mechanisms occurring at different length and time-scales. An illustration of this is achieved by applying time-compression to the digital infrasonic signals (see Supplementary Material in Matoza et al. [2009a]). After speeding-up the recordings by multiples of a hundred, the signals are audible, and sound qualitatively similar to jet noise from aircraft and rockets.

4.3 Comparison with jet noise spectra

The study of jet noise is intimately related to the study of turbulence, and for this reason a first-principles noise prediction theory is far from complete [Tam, 1998]. However, it is known that quadrupole radiation attributed to fine-scale turbulence [Lilley, 1991] is just one component of jet noise. Noise attributed to large-scale orderly turbulence structures [Crow and Champagne, 1971], screech, and broadband shock can be important depending on the jet operating conditions [Tam, 1995]. In addition, laboratory studies of pure-air jets have documented precisely the empirical dependence of audible jet noise spectra and radiation patterns

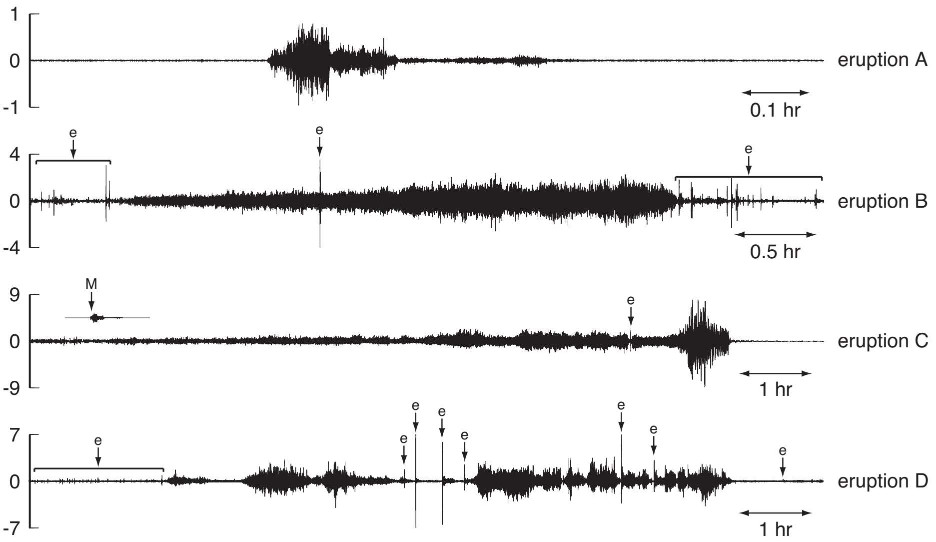

Figure 4.1: Infrasonic signals recorded during vulcanian-plinian volcanic eruptions. From top to bottom, upper trace: 8 March 2005 MSH eruption recorded at 13.4 km (chapter 2) (eruption A), lower three traces: 14-15 July 2006 (eruption B), 16-17 August 2006 (eruption C), and 6 February 2008 (eruption D) Tungurahua eruptions recorded at 36.9 km. Each trace represents a time-domain beam across four array elements with unit gain. Amplitude scale (left) is in pressure (Pa). Time scale (hours) indicated at lower right of each trace. Discrete explosion occurrences marked by "e". The signal labelled "M" on the third trace is the MSH eruption (upper trace) plotted at the same scale for comparison.

on jet operating parameters such as the jet diameter, Mach number, and temperature [Seiner, 1984]. A key discovery has been that jet noise spectra exhibit self-similarity, with the overall shape and curvature of the spectra dependent solely on whether fine-scale or large-scale turbulence is the dominant noise source in a particular direction [Tam et al., 1996]. The frequency band in which jet noise is radiated is related to the expanded jet diameter[2] and velocity via the Strouhal number ($St = fD_j/U_j$, where f, D_j, and U_j are the frequency, expanded jet diameter, and jet velocity respectively) [Seiner, 1984]. For a constant St and U_j, a jet with larger D_j will radiate at lower acoustic frequency f.

To test whether the self-similarity of jet noise extends to infrasonic eruption tremor signals, we compare the shape of the infrasonic spectra with the similarity spectra [Tam et al., 1996] for audible jet noise. Figure 4.3 shows power spectral density (PSD) estimates of the signals shown in Figure 4.1. Since the eruption signals are non-stationary over their full duration, the PSDs were estimated using a multitaper method from isolated 10 min, 50% overlapping data segments where the assumption of stationarity is reasonable (see Figure 4.2). These individual spectra were then progressively averaged to form an ensemble averaged power spectrum of each signal. In the case of eruption C, the final hour of data was treated as a separate ensemble (blue lines, Figure 4.3c). In the case of eruption A, only one 6.6 min data segment was used due to the relatively brief duration of high-amplitude eruption signal. The solid red and gray lines in Figure 4.3 represent the empirically-derived similarity spectra [Tam et al., 1996] for large-scale and fine-scale turbulence respectively. These empirical functions represent a curve-fit to 1900 audible noise spectra measured at the NASA Langley Research Center for axisymmetric, pure-air jets sampling a wide range of Mach number and temperature [Tam et al., 1996]. The overall shape and curvature of the similarity spectra are fixed, while the two free parameters are the position of the peak frequency, and

---

[2] The diameter of the jet once expanded to equilibrium with atmospheric pressure.

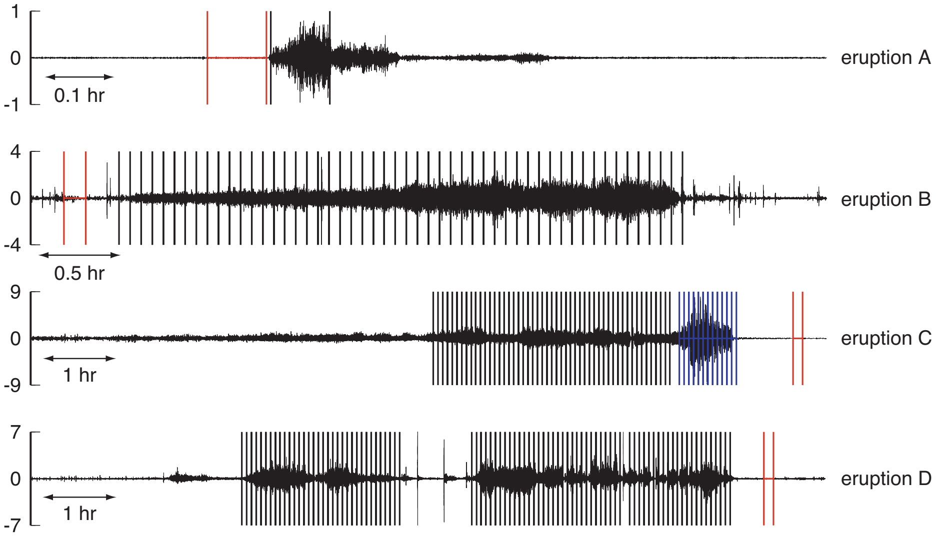

Figure 4.2: Data ensembles used in power spectral density estimates of Figure 4.3. Traces from top to bottom: eruptions A-D (see Figure 4.1). Vertical black bars indicate time range of data segments used for PSD estimates in Figure 4.3. For eruption A, only one 6.6 min data segment was used. For eruptions B-D, 50% overlapping 10 min data segments were used. PSDs estimated using a multitaper method from the data segments were progressively averaged as a function of time (left to right) to create the spectra of Figure 4.3. Red bars indicate the sample of ambient noise used to compute background noise spectra shown by dashed lines in Figure 4.3. Blue lines represent data segments for the final hour of eruption C, which were treated as a separate ensemble (Figure 4.3). In all cases, the data segments were chosen to avoid impulsive explosion signals.

the sound pressure level (SPL) in dB. The similarity spectra should fit the entire measured spectrum. With this constraint, the best fits to the observed spectra were found for a peak frequency of 0.2 Hz for eruption A (Figure 4.3a), and 0.4 Hz for eruptions B-D, excluding the last hour of eruption C (Figure 4.3b-d). The peak frequency for the last hour of eruption C is below the low-frequency response of the sensors (<0.1 Hz), but the slope of the spectrum is matched by the large-scale turbulence noise spectrum (Figure 4.3c).

4.4 Discussion

The peak frequencies of 0.2 Hz and 0.4 Hz are ∼3 orders of magnitude lower than those typical of the NASA data [Tam et al., 1996]. However, the length-scale of the volcanic jet D_j is ∼3 orders of magnitude larger than that of the NASA data, so that the Strouhal numbers of the jet noise peak frequencies are roughly equivalent. Figure 4.4 shows two images that can be used to constrain the jet length-scales at Tunguruhua Volcano. Figure 4.4a is an aerial photograph of the Tungurahua summit crater taken from a helicopter after the 2006 eruptions (eruptions B and C), just before eruption D. The diameter of the crater is ∼300-400 m - an approximate measure of the jet diameter that eroded the crater. Figure 4.4b is a FLIR infrared image of the 16-17 August event (eruption C) taken at 17 August 04:52:22 UTC. The height of the incandescent part of the jet is estimated at ∼1.8-1.9 km, and the jet diameter fills the entire summit region. Jet muzzle velocities at the vent are ∼300 m/s based on field studies of ballistics [Arellano and Hall, 2006]. Eruption A was a smaller-scale event, perhaps having a jet diameter ∼30 m, and a muzzle velocity ∼100 m/s [Mastin, 2007]. Although very approximate, these values for D_j and U_j suggest that peak frequencies of the infrasound spectra (Figure 4.3) correspond to $St \sim 0.06$ for eruption A, and $St \sim 0.4$ for eruptions B-D (excluding the final hour of eruption C). These values of St are within the observed range of St values for laboratory jets [Tam et al., 1996], jet engines, and rockets. Since the

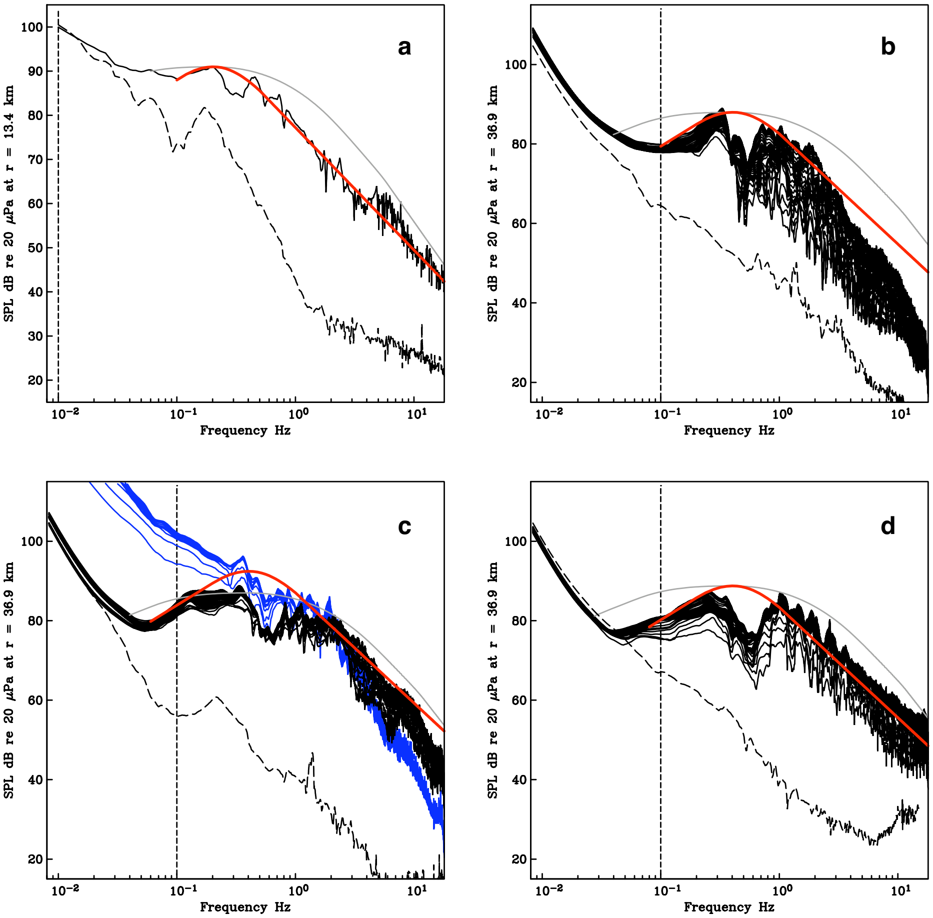

Figure 4.3: Power spectra of signals shown in Figure 4.1. Spectra expressed as sound pressure level (SPL) at the array in dB re 20 μPa. (a) 8 March 2005 MSH eruption (eruption A), (b) 14-15 July 2006 Tungurahua eruption (eruption B), (c) 16-17 August 2006 Tungurahua eruption (eruption C), (d) 6 February 2008 Tungurahua eruption (eruption D). Solid black lines represent the progressive ensemble averaged PSD of 10 min data segments (only one 6.6 min data segment in a). Dashed lines represent the background noise spectra immediately prior to or after each eruption signal (peak at ~0.2 Hz in ambient noise for a and c is the microbarom peak). Blue lines in c represents the final hour of signal. The spectra have been corrected for instrument response. Vertical dashed lines indicate lower frequency limit of flat instrument response (3 dB point). Solid red and gray lines show the large-scale and fine-scale turbulence similarity spectra [Tam et al., 1996] respectively, with peak frequency and amplitude adjusted for comparison to data.

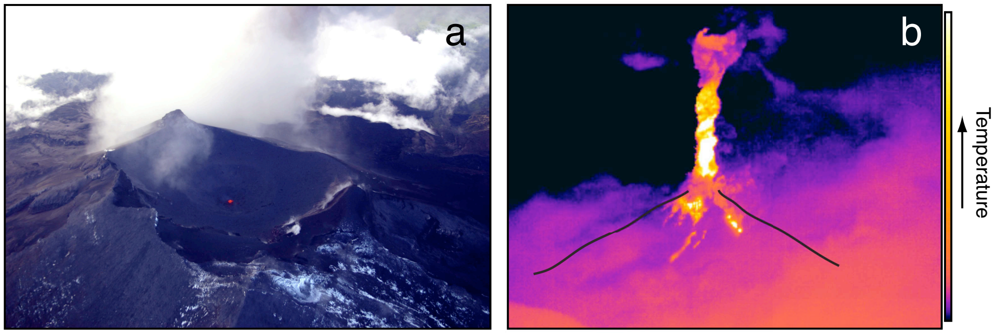

Figure 4.4: Constraints on the length-scale of Tungurahua eruption jets. (a) Aerial view of crater taken from a helicopter in February 2008, ∼5 hours before eruption D. The crater diameter is estimated at 300-400 m. (b) FLIR infrared image of 16-17 August 2006 eruption taken at 04:52:22 17 August 2006 UTC. Black lines indicate approximate mountain topography. The incandescent part of the jet reaches a height ∼1.8-1.9 km above the vent. The jet-like nature of the flow is apparent. The lowermost portion of the jet is obscured by ash from pyroclastic flows descending the mountain.

jet length-scales are very large, the amplitudes of the infrasonic signals are also extremely high considering the source-receiver range (Figures 4.1, 4.3).

The large-scale turbulence (LST) similarity spectrum matches the shape of the infrasonic spectra reasonably well (red lines, Figure 4.3), while the fine-scale turbulence (FST) similarity spectrum [Tam et al., 1996] (gray lines, Figure 4.3) does not match as well. In laboratory studies, LST noise is usually dominant in a narrow beam surrounding the downstream direction of the jet, while FST noise is dominant at ∼90° from the jet axis, the relevant angle for far-field ground observations of a vertical volcanic jet. However, the low frequencies considered may lead to strong diffraction effects, such that source directionality may be less prominent. Furthermore, as jet temperature increases, LST noise is dominant over a wider angular sector for hot jets [Tam et al., 1996]. Core temperatures are high for a volcanic jet, and higher for the magmatic eruptions B-D than for the phreatic eruption A.

The LST similarity spectrum matches the shape of the spectrum for the full range of frequencies[3] for eruption A (Figure 4.3a), but has discrepancies for eruptions B-D (Figure 4.3b-d). The spectra for B-D have a significant notch of diminished amplitudes centred at ~0.4-0.6 Hz, and the roll-off at high frequencies (>3 Hz) is not well matched for B and C. These features could be explained by complexities of the volcanic source not found in pure-air laboratory jets. The phreatic eruption A had a different fluid composition and quantity of solid particle-loading than the magmatic eruptions B-D. Although the pseudogas approximation is often used to model volcanic jets [Kieffer and Sturtevant, 1984], two-phase jet flows are known to be different to pure-air jet flows. For instance, particle image velocimetry (PIV) measurements have shown that turbulent Reynolds stresses are modified by the presence of heavy particles [Seiner et al., 2003]. Drag force on particles can lower the flow velocity of a mixture [Chojnicki et al., 2006], which may result in a lower frequency of acoustic radiation. It is also possible that large particles travel with a separate, slower velocity to the gas phase, which may explain the double-peaked nature of the spectra for B-D. In addition, since the particles are incompressible, they may generate boundary layer noise in the turbulent flow [Woulff and McGetchin, 1976]. Turbulent interaction with solid particles or crater walls may generate one frequency peak, while the other is generated by LST noise within the jet. The difference between the magmatic eruptions B-D and the phreatic eruption A may also be attributable to temperature effects. We note that the notch at ~0.4-0.6 Hz for B-D was observed at an identical array ~250 km north of Tungurahua, suggesting that this is a source feature rather than a propagation effect such as ground-bounce interference.

---

[3] We note that the ambient noise microbarom peak at 0.2 Hz is only ~10 dB below the data for this eruption signal. The presence of the microbarom may therefore affect the fit to the large-scale turbulence similarity spectrum in the case of eruption A.

4.5 Conclusions

Despite the complexities discussed above, the overall features of the infrasonic signals accompanying volcanic eruptions are remarkably similar to those of jet noise. In addition, the fact that eruptions A and D have spectra following the overall shape of the LST similarity spectrum suggests that, despite a length-scale difference of ~3 orders of magnitude, the fundamental noise-generation mechanisms occurring in volcanic jets are similar to those occurring in man-made jets. However, the additional complexities in the volcanic signals point to directions of future research necessary for a better understanding of volcanic jet noise. Laboratory aeroacoustic studies are required to study the effects of heavy particulate loading, very high temperatures, and complex crater morphology on radiated jet noise spectra and acoustic power. A long-term goal of these studies would be to estimate volcanic jet parameters such as the expanded jet diameter and velocity, volume flux, fluid composition, and vent overpressure from broadband acoustic recordings. These parameters are essential for a quantitative understanding of explosive volcanic eruption dynamics, and would aid substantially in ash dispersal modelling and the remote assessment of volcanic hazard.

Chapter acknowledgments

We thank Bernard Chouet, Kent Gee, and Larry Mastin for thoughtful suggestions, and Maurizio Ripepe for a critical review. The infrasound data were collected by the Acoustic Surveillance for Hazardous Eruptions (ASHE) program. We used a multitaper PSD code written by Bob Parker. This work was funded by NSF grant EAR-0609669. We dedicate this chapter to the memory of our friend and mentor Henry E. Bass, who was fascinated by this research and would have been a co-author. Chapter 4, in full, has been published as Matoza, R.S., D. Fee, M.A. Garces, J.M. Seiner, P.A. Ramon, and M.A.H. Hedlin (2009), Infrasonic jet noise from volcanic eruptions, *Geophys. Res. Lett.*, **36**, L08303, doi:10.1029/2008GL036486.

5. Infrasonic tremor wavefield of the Pu‘u Ō‘ō crater complex and lava tube system, Hawaii, in April 2007

Long-lived effusive volcanism at the Pu‘u ‘Ō‘ō crater complex, Kilauea Volcano, Hawaii produces persistent infrasonic tremor that has been recorded almost continuously for months to years. Previous studies showed that this infrasonic tremor wavefield can be recorded at a range of >10 km. However, the low signal power of this tremor relative to ambient noise levels results in significant propagation effects at this range. In April 2007 we supplemented a broadband infrasound array ~12.5 km from Pu‘u ‘Ō‘ō (MENE) with a similar array ~2.4 km from the source (KIPU). The additional closer-range data enable further evaluation of tropospheric propagation effects and provide higher signal-to-noise ratios for studying volcanic source processes. The infrasonic tremor source appears to consist of at least two separate physical processes. We suggest that bubble cloud oscillation in a roiling magma conduit beneath the crater complex may produce a broadband component of the tremor. Low-frequency sound sourced in a shallow magma conduit may radiate infrasound efficiently into the atmosphere due to the anomalous transparency of the magma-air interface. We further propose

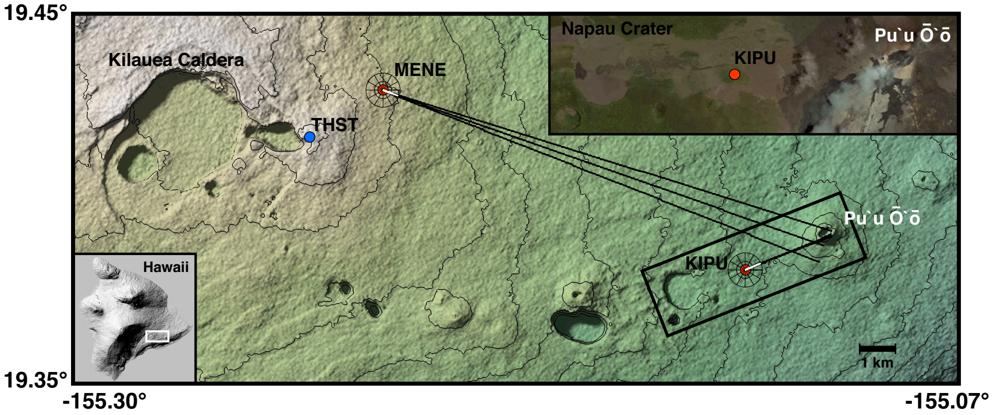

Figure 5.1: Location of broadband infrasound arrays KIPU and MENE, ∼2.4 km and ∼12.5 km from Puʻu ʻŌʻō respectively, and Thurston wind tower (THST). Contours at 50 m intervals. Radial histograms of PMCC detection azimuths are shown at array locations, while solid black lines extending from arrays are great circle paths of the median and inter-quartile range of detection azimuths during the data period Julian day 109-117 2007 UTC (see Figure 5.2). Box around KIPU and Puʻu ʻŌʻō shows area of upper right inset. Lower left inset indicates area of figure.

that more sharply-peaked tones with complex temporal evolution may result from oscillatory interactions of a low-velocity gas jet with solid vent boundaries in a process analogous to the hole tone or whistler-nozzle. The infrasonic tremor arrives with a median azimuth of ∼67° at KIPU. Additional infrasonic signals and audible sounds originating from the extended lava tube system to the south of the crater complex (median azimuth ∼77°) coincided with turbulent degassing activity at a new lava tube skylight. Our observations indicate that acoustic studies may aid in understanding persistent continuous degassing and unsteady flow dynamics at Kilauea Volcano.

5.1 Introduction

The Puʻu ʻŌʻō-Kūpaianaha eruption of Kilauea Volcano, Hawaii, has been ongoing since 1983, and activity at Puʻu ʻŌʻō between 1992 and 2007 was dominated by persistent effusive eruption, lava tube emplacement, and surface lava flows [Heliker and Mattox, 2003]. Although some early volcano acoustic studies provided qualitative descriptions of audible sounds associated with hawaiian eruptive activity [Perret, 1950; Richards, 1963], it has only recently been recognized that persistently active hawaiian eruptions represent near-continous and energetic sources of low-frequency sound (infrasound, <20 Hz) [Garces et al., 2003; Fee and Garces, 2007]. In contrast to the impulsive transient signals characteristic of strombolian eruptions [Ripepe et al., 2007; Johnson et al., 2008], infrasound radiated by Pu‘u ‘Ō‘ō prior to June 2007 consisted of unceasing broadband and harmonic infrasonic tremor, with only minor variation in signal properties over durations of weeks to months. In June 2007 the eruption of Pu‘u ‘Ō‘ō paused temporarily before entering a new phase [Poland et al., 2008]. Infrasonic signals associated with this change in eruptive style are not addressed in this study. Here we focus on the continuous tremor source that was characteristic of the eruption prior to June 2007. The first array analysis of the sustained infrasonic tremor wavefield by Garces et al. [2003] revealed a distributed source, consisting of the Pu‘u ‘Ō‘ō crater complex and lava tube system flowing along the south flank to the ocean. Garces et al. [2003] postulated that the infrasonic source consisted of the continuous acoustic excitation of a shallow lava-gas mixture beneath the crater area and in horizontal lava tubes, and that this sound could radiate to the atmosphere via vents and skylights. However, the array geometry and instrumental limitations did not allow the accurate localization of infrasound sources to individual vents or regions of the lava flow field.

Further investigations of this persistent infrasonic tremor wavefield by Fee and Garces [2007] revealed that, at a range of ∼12.5 km from Pu‘u ‘Ō‘ō, tremor signal power exhibited clear diurnal variations that were anti-correlated with wind speed. Weather balloon data also indicated the formation and break-up of a nocturnal boundary layer for this region, correlated with the diurnal cycle of infrasonic signal reception. These observations indicate the importance of tropospheric (mesoscale and microscale) atmospheric propagation effects on infrasonic signal reception at the ∼10 km range. In particular, this range corresponds to the classical acoustic shadow zone predicted by high-frequency ray theory for ordinary diurnal atmospheric conditions, and it was proposed that the presence of a nocturnal boundary layer may act to duct the tremor signal to the array [Fee and Garces, 2007]. However, the accuracy of ray theory begins to fail for the wavelengths and scale-lengths considered due to low-frequency effects such as diffraction. For instance, a typical nocturnal boundary layer may extend to ∼200-300 m in height above the ground, while the wavelength of a 1 Hz infrasonic signal is ∼340 m for a sound speed of ∼340 m/s in air. These propagation effects therefore remain incompletely understood.

In order to further investigate the source and regional propagation of Pu'u 'Ō'ō's infrasonic tremor wavefield, we conducted a campaign-style field deployment of infrasound and seismic sensors in the vicinity of Pu'u 'Ō'ō from 17-27 April 2007, and used an infrared camera to help identify candidate infrasonic sources. This paper presents a preliminary investigation of this data set. In addition to characterizing the observed propagation effects, we describe the spectral properties of the continuous infrasonic tremor and discuss potential source processes.

5.2 Field deployment

A broadband infrasound array has been operating continuously at MENE (Figure 5.1) since September 2006 [Fee et al., 2009], and has captured the entire range in Kilauea's eruptive activity from 2006 to present [Fee et al., 2009]. During 17-27 April (Julian day 107-117) 2007, we deployed an additional array, KIPU, ∼2.4 km to the southwest of the Pu'u 'Ō'ō crater complex, perpendicular to the lava tube system that extends from the crater complex on the south flank (Figure 5.1). Each array consisted of four Chaparral 2.2 microphones (flat response

0.1-200 Hz). At KIPU, the infrasound sensors were deployed as a centered triangle with ~90 m aperture in a Kipuka (area of surviving land surrounded by lava flows) consisting of densely overgrown ferns within tall trees, providing excellent wind shelter (Figure 5.1). Initially, one 15-m porous hose was attached to each infrasonic sensor for additional spatial wind filtering. However, heavy rainfall during the first 3-4 days of the experiment resulted in the hoses becoming water-saturated, affecting the system response. Consequently, we removed the hoses (see section 5.3). A 3-component Nanometrics Trillium 40 broadband seismometer (flat response 0.025-50 Hz) was deployed in addition to the infrasound array at KIPU. Data were sampled at 40 Hz with a Reftek 24-bit digitizer. Infrared imaging was performed using an Indigo TVS 700.

5.3 Propagation of the tremor wavefield

The array data were processed using PMCC [Cansi, 1995], (window length 10 s, time step 1 s, 10 frequency bands between 0.5-5 Hz). Figure 5.2 shows PMCC detection azimuths as a function of time for both MENE and KIPU during the period of KIPU data coverage, color-scaled by the r.m.s. signal power of the detection in dB re 20 μPa. The results are shown underlain by the ambient noise spectrum at the central array element of each array in the 0-1 Hz band, and wind speed at Thurston wind tower (THST, Figure 5.1). THST is above the forest canopy and the data are therefore likely representative of winds in the study region. Fee and Garces [2007] noted that noise in the 0.02-0.3 Hz band is well-correlated with the regional wind speed. Here we observe that this wind noise extends up to ~0.5 Hz, possibly because the porous hose wind filters were removed, or perhaps simply because different wind noise conditions existed during the time of this experiment than during the data period considered in Fee and Garces [2007] [e.g., Raspet et al., 2006, 2008].

At MENE, azimuthal scatter (azimuthal standard deviation ~18.9°) and variation in signal power (∼7-8 dB) is observed for the continuous infrasonic tremor signal originating from Puʻu ʻŌʻō during the study period (Figure 5.2). Occasionally, full loss of coherent signal is observed and is correlated with an increase in regional wind speed (e.g., end of Julian day 113, end of Julian day 115). As described by Fee and Garces [2007], this switching on and off of PMCC detections at MENE is not simply a result of coherent infrasonic signals being overwhelmed by increasing wind noise levels. Overall power spectral levels actually decrease in the bandwidth of the tremor signal (∼0.5-3 Hz) during the times in which wind noise in the 0.02-0.5 Hz band increases, indicating that propagation of the tremor signal is somehow inhibited by the change in atmospheric conditions associated with the wind noise increase [Fee and Garces, 2007]. Despite similar atmospheric conditions, scatter in azimuth values and signal power variations are minimal at KIPU. There, an unceasing tremor signal is received from the direction of the Puʻu ʻŌʻō crater complex with a smaller azimuthal deviation (azimuthal standard deviation ∼6.4°), which may correspond to a distributed source (section 5.4). Signal power variations ∼2-3 dB at KIPU may result from changes in the source signal power in addition to propagation effects.

Two of the signal power changes shown in Figure 5.2 are the result of equipment changes, and are not the result of real changes in the source power or propagation effects. We removed the porous hoses from KIPU at ∼0230 UTC Julian day 109 2007, and from MENE at ∼0000 UTC Julian day 112 2007 since they had become saturated by heavy rainfall. In each case, removing the hoses resulted in a ∼5 dB increase in observed signal power (Figure 5.2, white arrows). This large change in the system response is probably a result of the pores in the hoses being filled by water, limiting effective acoustic transmission into the hoses and to the sensor. Such a large change in response is not expected for dry hoses operating under less humid conditions.

We note that the median azimuth for tremor signal at MENE is ∼110.4°,

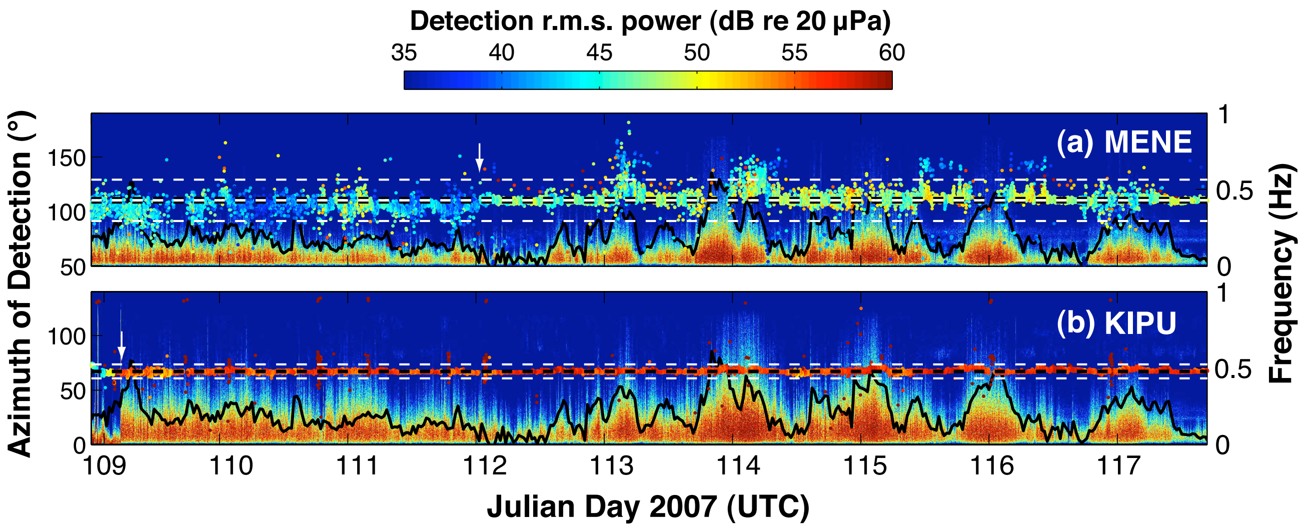

Figure 5.2: PMCC array processing results (0.5-5 Hz) superimposed upon low-frequency noise spectrogram (0-1 Hz) of the central array element for each array, at a) MENE and b) KIPU for the data period Julian day 109-117 2007 UTC. Solid black lines denote wind speed at THST (relative scale, peak value ∼9 m/s). PMCC detection azimuths plot as a function of time and color-scaled for r.m.s. power of detected signal in dB re 20 μPa (top color scale). Increases in signal power at KIPU at ∼0230 UTC Julian day 109 and at MENE at ∼0000 UTC Julian day 112 (white arrows) result from the removal of water-saturated porous hoses from the infrasonic sensors. Horizontal dashed lines are the median (central white), inter-quartile range (black), and standard deviation from the 10 % trimmed mean (outer white) for all detections in the data period (see Figure 5.1). Noise in the 0.02-0.5 Hz band at each array is well-correlated with regional wind speed. KIPU's proximity to the source and downwind direction assure that wind propagation effects on detection azimuth and signal power are minimal. A greater degree of scatter in azimuth values and signal power variation is observed at MENE, well-correlated with regional wind-speed variations.

∼1-2° higher than the true Puʻu ʻŌʻō azimuth of ∼108.9° (Figures 5.1, 5.2). This can be partially attributed to deflection of the signal by the prevailing east-northeasterly trade wind as observed at THST for this time period. Assuming a sound speed of ∼340 m/s, the time of flight for infrasound from Puʻu ʻŌʻō to MENE (12.5 km) is ∼37 s. During this time a wind speed of ∼9 m/s blowing from the ENE (approximately perpendicular to the propagation path) would deflect the signal $\sim 37 \times 9 \sim 330$ m to the SW of the array causing an azimuth deviation of $\sim \tan^{-1}(330/12500) \sim 1.5°$. This is in good agreement with the observed median azimuthal deviation. A wind speed of ∼9 m/s is at the upper bound of wind speeds measured at the 25 m tower at THST during the study period (Figure 5.2).

Taken together, the KIPU and MENE data confirm the results of Fee and Garces [2007], and give an indication of the propagation effects on signal power, intermittency of coherent detection, and scatter in azimuth values expected at the ∼10 km range. The KIPU data suggest that such propagation effects are minimal at the ∼2-3 km range. However, KIPU is in the prevailing downwind direction of Puʻu ʻŌʻō and effects in the upwind direction may be more severe. We note that the wind speed variations are diurnal between Julian days 113 and 118, but more random between Julian days 109 and 113. This illustrates the complexity of boundary layer dynamics and infrasonic propagation effects at the ∼10 km range. These data will provide a reference for future studies aimed at modeling infrasonic propagation in the boundary layer.

5.4 Tremor source properties

KIPU provided high signal-to-noise ratio recordings of Puʻu ʻŌʻō's infrasonic tremor. We focus primarily on observations from KIPU in the remaining sections. Figure 5.3a shows a log-scale frequency spectrogram of time-delay beamformed [DeFatta et al., 1988] infrasound data at KIPU for a 24-hour time period beginning at 0000 UTC Julian day 111 2007. Two distinct persistent tremor components are visible, each with different frequency content and time dependence, indicative of the continuous action of two separate physical source processes. The first component is a broadband signal concentrated between 0.5-15 Hz (Figure 5.3b). Array processing shows this to be coherent acoustic signal originating from the direction of the crater complex area. The second component consists of prominent spectral peaks in the ∼0.6-0.9 Hz band (Figure 5.3b) that exhibit complex temporal dependence (Figure 5.3a). The relative power in the individual peaks changes with time. For example, the peak at ∼0.6 Hz appears to switch on between 0600 and 0900 UTC, and again between 1200 and 1500 UTC, while the peak at ∼0.8 Hz is more persistent, but switches off between 1200 and 1500 UTC (Figure 5.3a). Gliding or subtle changes in the frequency of these individual peaks [Garces et al., 1998] is also observed as a function of time. This signal also originates from the crater complex area and is observed throughout the KIPU deployment. Both components are recorded at MENE (Figure 5.3b). Although we cannot define ambient noise conditions for MENE during this time period due to the presence of the continuous tremor signal, we infer that the tremor signal lies just above the ambient noise floor at MENE (diagonal dashed line, Figure 5.3b).

The median azimuth for the tremor signal at KIPU is ∼67.0°, which points to the southern section of the Puʻu ʻŌʻō crater complex. During the time of the experiment, this southern section of the crater complex contained numerous active vents and pits such as the South Wall pit and vent complex, Puka Nui vents and pit, MLK vents and pit, Beehive vent, East Pond vent, and Tephra Berm vent [*http://hvo.wr.usgs.gov/*]. These can be seen in Figure 5.4a as numerous steaming openings in the southern section of the crater complex. During the experiment we were able to observe several active incandescent vents in the MLK region, and activity at the East Pond vent and Beehive vent. However, several of the areas in the South Wall complex were more difficult to access, and it is likely that multiple vents in the system could be sources of infrasound. It is

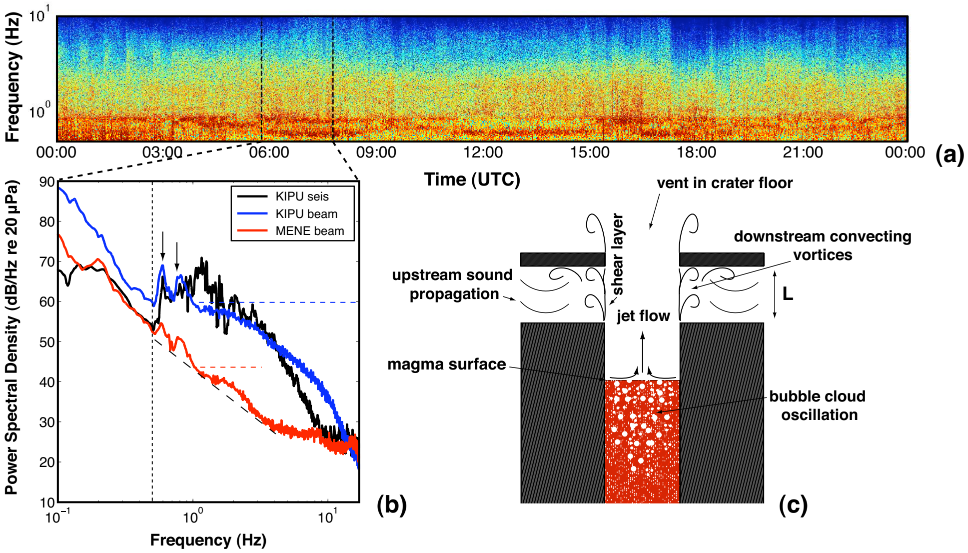

Figure 5.3: Tremor source considerations. a) Log-frequency spectrogram for 24 hours of beamed infrasound data from KIPU beginning at 0000 UTC Julian day 111 2007. Vertical dashed lines indicate time of data used in b, b) Power spectral density of beamed infrasound data at KIPU (blue) and MENE (red) expressed in dB/Hz re 20 μPa. Power spectrum of KIPU vertical seismic data (black) shown with arbitrary scale adjusted for comparison to infrasound data. Energy below ~0.5 Hz (vertical dashed line) is ambient noise (see Figure 5.2). There are two prominent spectral peaks at ~0.6 Hz and ~0.8 Hz (indicated by arrows) in all data (including seismic) which exhibit complex evolution with time (Figure 5.3a). Additional persistent broadband infrasonic tremor is visible in KIPU data between ~0.5-17 Hz (band indicated by horizontal dashed blue line) and in MENE data between ~1-3 Hz (band indicated by horizontal dashed red line). Diagonal dashed line indicates inferred ambient noise floor at MENE. KIPU seismic data have a complicated spectrum above 0.8 Hz. c) Schematic of infrasonic tremor source model for both broadband and harmonic components. Broadband noise may be generated by bubble cloud oscillation in a vigorously degassing magma conduit, while harmonic components may be generated by interaction of gas flow with the vent and near-surface cavities in a process analogous to the hole tone or whistler-nozzle. Although depicted with infinite width, the cavity of length L would in reality be a finite volume between the magma surface and vent with resonant modes.

therefore not clear whether one dominant vent was the primary source of infrasonic tremor, or whether the tremor resulted from the collective sum of contributions from two or possibly many more spatially distributed vents. Since no single vent seemed larger or more energetic in degassing activity than any of the other vents (Figure 5.4a), the latter case seems most plausible. The standard deviation of azimuths derived from PMCC for the deployment period is $\sim$6.4°, corresponding to $\sim$270 m distance at Pu‘u ‘Ō‘ō. Although not a formal estimate of the uncertainty in the calculated azimuth values, this standard deviation can be taken to represent the variability of calculated signal azimuth, which may result from source variability (individual spatially separated vents may have contributed more significantly to the tremor power during different times of the deployment), propagation effects (up to $\sim$1-2° for a wind of $\sim$9 m/s blowing perpendicular to the propagation direction), and uncertainty in the azimuth calculation as a result of noise and array response. From KIPU, the difference in azimuth between the most northerly and southerly points in the crater complex ($\sim$260 m) is $\sim$6.2°. This is of the same order as the observed azimuthal standard deviation and indicates that we do not have the azimuthal resolution from KIPU to identify which particular vents in the crater complex acted as the main contributing tremor sources during the deployment. We note that the observed azimuthal standard deviation could also be explained by a distributed source with multiple vents in the crater complex acting as sources. To resolve individual vents within the crater complex would require a closer-range infrasonic sensor deployment [e.g., Ripepe et al., 2007], which could be corroborated by infrared imaging or other thermal measurements [Marchetti and Harris, 2008] of the numerous active vents. This style of experiment was being planned when the new stage of Kilauea and Pu‘u ‘Ō‘ō’s eruption began in June 2007 [Poland et al., 2008], which included the collapse of the Pu‘u ‘Ō‘ō crater floor and the destruction of all of the active vents and pits which presumably acted as sources in this study (Figure 5.4b).

5.5 Tremor source considerations

The persistent tremor source under consideration is arguably highly complex. During the study period, Puʻu ʻŌʻō was in a constant, elevated state of degassing in comparison to previous years [Poland et al., 2008], and it is probable that this continuous degassing took the form of a roiling, bubbly lava body beneath the crater complex area. Direct observation of such a lava body was not possible in April 2007, as it was capped by a solid lid forming the crater floor (punctured by several distinct active vents, Figure 5.4a). However, in June 2007 deflation at Puʻu ʻŌʻō, attributed to a disrupted magma supply, caused the solid crater floor to collapse by as much as 80 m [Poland et al., 2008]. Shortly afterwards, eruptive activity resumed and a lava lake quickly filled the crater to within 30 m of the rim (Figure 5.4b) [Poland et al., 2008]. Furthermore, recent observations at the similar but more open Halemaʻumaʻu vent revealed a lava body in such a state of vigorous degassing at the base of an open cavity, and similar infrasonic tremor was recorded [Fee et al., 2009]. Within a vigorously degassing basaltic lava system, numerous candidate acoustic source processes may be considered, including noise from turbulent lava overturning and spattering, the oscillations of bubbles [Lu et al., 1990; Chouet, 1996b], degassing noise [Woulff and McGetchin, 1976], resonance of gas or lava-filled cavities [Garces et al., 1998], and possibly thermoacoustic processes [Busse et al., 2005; Swift, 2007]. A full investigation of each of these mechanisms is beyond the scope of the present study, however, one process that is likely to be important is the collective oscillations of bubble clouds within this degassing source [Chouet, 1996b]. Bubbles act as monopole sources, and are therefore often the most efficient sound sources in flows containing them, including breaking ocean waves, waterfalls, and rivers [Leighton, 1994; Park et al., 2008]. Due to this source efficiency, bubble cloud oscillation seems a strong candidate for a tremor source at Puʻu ʻŌʻō. Bubbles also play a critical role in the coupling between the sound field in a magma column and the atmosphere, and this is addressed in section 5.5.2.

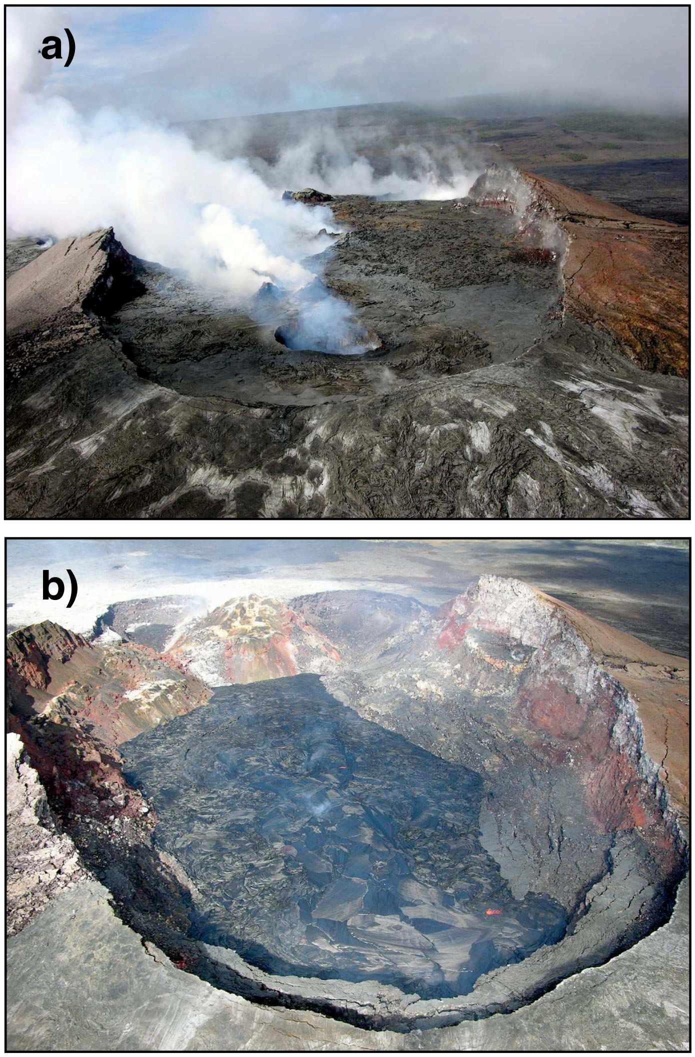

Figure 5.4: Photographs of the Pu‘u ‘Ō‘ō crater complex a) on 22 February 2007 prior to our field deployment, and b) on 13 July 2007 after our field deployment. (a) is representative of the state of the crater complex during our deployment, while by the time (b) was taken the solid lid within the crater complex area had collapsed and had been filled by a lava lake. View in each case is approximately from the northeast looking to the southwest. In (a) the pit in the foreground is the East Pond vent, while the steaming behind it and to the south is coming from a collection of active vents and pits in the southern portion of the Pu‘u ‘Ō‘ō crater complex, e.g., the January vent, South Wall pit and vent complex, and MLK vents and pits. The infrasonic tremor azimuths point to that general area of the crater complex but lack the azimuthal resolution to pinpoint individual vents. Photographs courtesy of U.S. Geological Survey, Hawaiian Volcano Observatory (HVO).

5.5.1 Bubble cloud oscillation

An individual millimeter-scale bubble within shallow molten basalt may oscillate with a characteristic frequency of several kilohertz [Lu et al., 1990; Chouet, 1996b]. However, bubbles in a cloud are coupled oscillators, and the normal modes of bubble clouds can be much lower in frequency than those of the individual bubbles [Lu et al., 1990; Yoon et al., 1991]. The resonant frequency f_0 of a single bubble is approximated by [van Wijngaarden, 1972; Chouet, 1996b]

$$f_0 \sim \frac{1}{2\pi}\sqrt{\frac{3P_0}{\rho_l R^2}}, \tag{5.1}$$

where P_0 is the static pressure in the liquid, ρ_l is the liquid density, and R is the bubble radius. In contrast, for a bubble cloud with characteristic length-scale L_b we may expect eigenfrequencies:

$$f_n \sim \frac{nc_{eff}}{2L_b}, \tag{5.2}$$

where $n = 1, 2, 3, \ldots$, and c_{eff} is the effective sound speed of the liquid-bubble mixture, given by Wood's equation [Wood, 1964]

$$c_{eff} = \{[(1-\phi)\rho_l + \phi\rho_g][(1-\phi)\kappa_l + \phi\kappa_g]\}^{-1/2}, \tag{5.3}$$

where ϕ is the void fraction (gas-volume fraction), ρ_g is the density of the gas, and κ_l and κ_g are the compressibilities of the liquid and gas respectively. Considering that $\rho_l >> \rho_g$ and $\kappa_l << \kappa_g$, equation (5.3) can be approximated as [e.g., van Wijngaarden, 1972; Wilson and Roy, 2008]:

$$c_{eff} \sim \sqrt{\frac{\nu P_0}{\rho_l \phi(1-\phi)}}, \tag{5.4}$$

where ν is the polytropic index of the gas in the bubble. For ϕ in the range 10^{-4} to 10^{-1}, and considering that $\nu \sim 1$, equation (5.4) further reduces to [e.g., Lu et al., 1990; Chouet, 1996b; Hahn et al., 2003]:

$$c_{eff} \sim \sqrt{\frac{P_0}{\rho_l \phi}}. \tag{5.5}$$

Assuming $\phi \sim (R/L_b)^3 N$, where N is the number of bubbles in the cloud, combining equations (5.1), (5.2), and (5.5) gives the ratio f_n/f_0 as [Lu et al., 1990; Chouet, 1996b]:

$$\frac{f_n}{f_0} \sim \frac{n}{\phi^{1/6} N^{1/3}}. \tag{5.6}$$

For instance, Chouet [1996b] illustrated that a single bubble in shallow liquid basalt with $R \sim 1$ mm, $\rho_l \sim 2500$ kg/m^3 and $P_0 \sim 2.5$ MPa (depth $z \sim 100$ m for $P_0 = \rho_l g z$ where g is the acceleration due to gravity) may oscillate at $f_0 \sim$ 10 kHz (equation 5.1). In contrast, a bubble cloud in basalt of the same density and pressure, with characteristic length-scale $L_b \sim 50$ m, void fraction $\phi \sim 10^{-2}$, and constant individual bubble radius $R \sim 1$ mm may radiate at a frequency of $f_1 \sim 2$ Hz (equation 5.6), which is in agreement with the infrasonic frequencies observed. We hypothesize that noise from bubble cloud oscillation is the source of broadly peaked tremor between 0.5-17 Hz. Whereas the turbulent overturning of lava would itself be an inefficient sound source, this turbulence may play a role in driving the collective oscillations of bubbles. A random arrangement of bubbles with various radii within a heterogeneous pressure and flow field may result in a continuous emission of low-frequency broadband noise in contrast to the harmonic series defined in equation (5.2).

Bubble cloud oscillation has typically been investigated in water [Commander and Prosperetti, 1989; Lu et al., 1990; Yoon et al., 1991; Park et al., 2008], where the effect of liquid viscosity is negligible. Ichihara and Kameda [2004] extended the theory to include the effects of liquid viscosity and volatile diffusion on bubble oscillation in magma. They found that attenuation and dispersion of pressure waves in magma are severe for frequencies lower than the characteristic frequency τ_g^{-1} of mass transfer into and out of the bubbles by diffusion of volatiles, or close to the characteristic frequency τ_b^{-1} of the viscous response of the bubble in the magma. Such effects could also inhibit the tremor source outlined above, as they may inhibit cloud oscillation and thus prevent the bubbles from

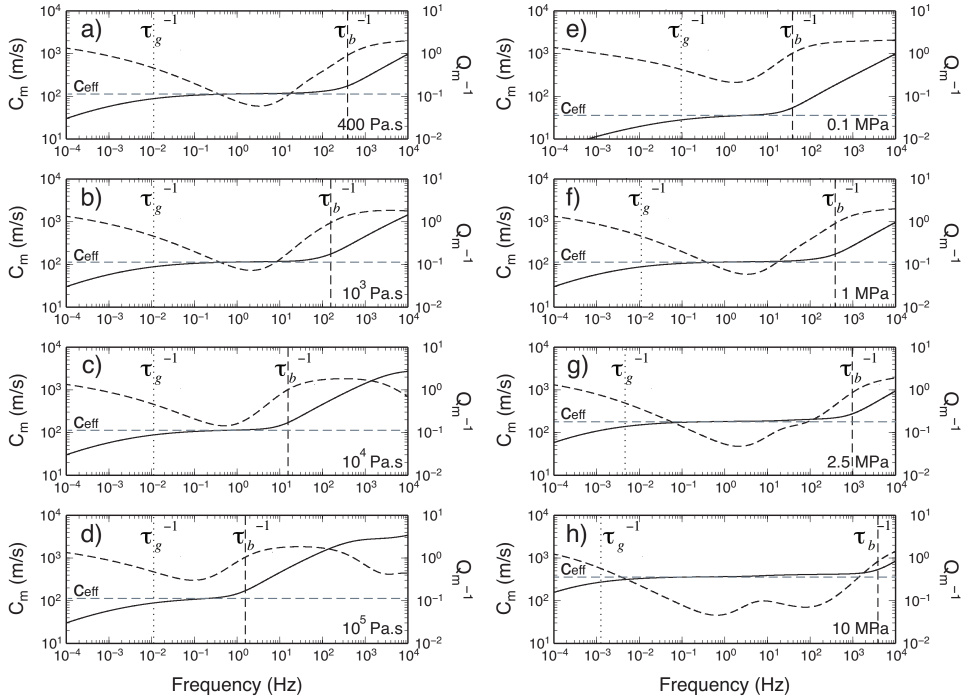

Figure 5.5: Sound speed c_m (m/s) (left axis, solid curve) and attenuation Q_m^{-1} (right axis, dashed curve) of pressure waves in a bubbly liquid including effects of volatile diffusion and melt viscosity according to the model of Ichihara and Kameda [2004]. The material parameters are those assumed for H_2O vapor in basalt at a temperature of 1273 K by Ichihara and Kameda [2004] (their Figures 6 and 7). In a-d, the hydrostatic pressure is set to 1 MPa and the viscosity is varied: a) 400 Pa.s, b) 10^3 Pa.s, c) 10^4 Pa.s, and d) 10^5 Pa.s. In e-h, the viscosity is held at 400 Pa.s and the hydrostatic pressure is varied: e) 0.1 MPa (depth $\sim$ 4 m assuming $\rho_l = 2600$ kg/m^3), f) 1 MPa (depth $\sim$ 40 m), g) 2.5 MPa (depth $\sim$ 100 m), h) 10 MPa (depth $\sim$ 400 m). The horizontal dashed gray line indicates the effective sound speed c_{eff} (equation 5.5). The characteristic frequencies (in Hz) for volatile diffusion (τ_g^{-1}, vertical dotted line) and viscous effects on bubble expansion (τ_b^{-1}, vertical dashed line) are also shown. In the frequency range between these two characteristic frequencies $\tau_g^{-1} \leq f \leq \tau_b^{-1}$ attenuation and dispersion due to viscosity and volatile diffusion are small, and the sound speed c_m agrees with the effective sound speed c_{eff}. The effects of viscosity and volatile diffusion are therefore negligible in the frequency band 0.5-17 Hz of the observed tremor (Figure 5.3) for the parameters used here according to the model of Ichihara and Kameda [2004]

generating sound. These effects have negligible influence in the frequency range $\tau_g^{-1} \leq f \leq \tau_b^{-1}$ where here τ_g^{-1}, τ_b^{-1} and f are frequencies in Hz. The time-scale for volatile diffusion τ_g is given by [Ichihara and Kameda, 2004]:

$$\tau_g = \frac{2\pi R^2}{9\kappa_{gl}} \left(\frac{\rho_l P_0}{\rho_g} \frac{\partial C_{eq}}{\partial P} \right)^{-2}, \tag{5.7}$$

where κ_{gl} is the diffusivity of the volatile in the liquid and $C_{eq}(P)$ is the equilibrium volatile concentration at pressure P. The bubble volume relaxation time τ_b due to melt viscosity is given by:

$$\tau_b = \frac{8\pi\eta_0}{3K_g}, \tag{5.8}$$

where η_0 is the melt shear viscosity, and K_g is the bulk modulus of the bubble for an adiabatic process with $K_g = \gamma P_0$, where γ is the ratio of specific heats, $\gamma \sim 1.3$ [Ichihara and Kameda, 2004]. We note that here we are considering the raw melt viscosity η_0 of the liquid magma, and not the effective viscosity η_{eff} of the bubbly mixture. The effective viscosity of a bubbly mixture increases with the void fraction ϕ, and is the relevant parameter when dealing with bulk properties of the fluid, such as the attenuation of an acoustic wave passing through the bubbly mixture [Garces, 1997, 2000; Marchetti et al., 2004]. The raw melt viscosity is the viscosity experienced by the individual bubbles oscillating within the melt. Note that this assumes a relatively low void fraction where bubbles do not touch (i.e., we are assuming that the magma-gas mixture is not a foam). The importance of effective viscosity for the propagation of the sound field in a magma column to the atmosphere is addressed in section 5.5.2.

Following Ichihara and Kameda [2004], we first assume $R \sim 1$ mm, $\kappa_{gl} \sim 10^{-9}$ m^2/s, $\rho_l \sim 2600$ kg/m^3 and $P_0 \sim 1$ MPa. We then use the values in Table 1 of Ichihara and Kameda [2004] for the quantity $A_g = \frac{\rho_l P_0}{\rho_g} \frac{\partial C_{eq}}{\partial P}$ in equation (5.7) assuming H_2O vapor at a temperature of 1273 K for the gas phase. This yields a characteristic frequency for volatile diffusion $\tau_g^{-1} \sim 0.01$ Hz, which is much lower than the frequencies of infrasonic tremor considered (0.5-17 Hz), suggesting that the effect of volatile diffusion can be neglected. The melt viscosity η_0 may be $\sim$ 400 Pa.s for shallow molten basalt [Shaw, 1972; following Vergniolle and Brandeis, 1996], yielding a value of $\tau_b^{-1} \sim 1$ kHz. This is much higher than the infrasonic tremor frequencies considered, indicating that the effect of a viscous melt may also be neglected for this value of viscosity. However, given the poor constraints on melt viscosity at Pu‘u ‘Ō‘ō of which we are aware, and the fact that melt viscosity is a strong function of water content [Shaw, 1972], it is important to investigate the effects of a larger range of melt viscosity.

A more thorough investigation of variations in melt viscosity and magmastatic pressure is presented in Figure 5.5. Figure 5.5 shows the sound speed and attenuation of pressure waves in a liquid-bubble mixture according to the model of Ichihara and Kameda [2004] for different values of the melt viscosity η_0 and magmastatic pressure P_0. Ichihara and Kameda [2004] employ a linear viscoelastic rheology for the melt [Webb, 1997], in which the shear and bulk moduli of the viscoelastic material are complex functions of the frequency of an applied sinusoidal oscillation. As in Ichihara and Kameda [2004], we assume an unrelaxed bulk modulus $K_\infty = 30$ GPa, an unrelaxed shear modulus $\mu_\infty = 10$ GPa and a relaxed bulk modulus $K_0 = 20$ GPa for the parameters describing the linear viscoelastic rheology [Webb, 1997]. We further assume that the void fraction $\phi = 0.03$ (compare with Figures 5.6-5.7 in Ichihara and Kameda [2004]). In Figures 5.5a-d the magmastatic pressure is held fixed at 1 MPa ($\sim$ 40 m depth assuming a magma density $\rho_l = 2600$ kg/m^3) while the melt viscosity is varied at 400 Pa.s, 10^3 Pa.s, 10^4 Pa.s, and 10^5 Pa.s. The characteristic frequencies τ_g^{-1} and τ_b^{-1} are also shown. In the frequency range between these two characteristic frequencies, $\tau_g^{-1} \leq f \leq \tau_b^{-1}$, attenuation and dispersion due to melt viscosity and volatile diffusion are small, and the sound speed of the liquid-bubble mixture agrees with the effective sound speed (equation 5.5) [Ichihara and Kameda, 2004]. Between these characteristic frequencies we also assume that the effects of volatile diffusion and melt viscosity on the oscillation of bubbles are small, so that bubble clouds could oscillate freely and produce tremor. Here we find that for a depth of $\sim$ 40 m in a basaltic conduit, a melt viscosity several orders of magnitude higher than 400 Pa.s, i.e., $\eta_0 \sim 10^4$–10^5 Pa.s is necessary to lower τ_b^{-1} into the observed frequency range (0.5-17 Hz) and to make viscous effects important in this analysis.

In Figures 5.5e-h the melt viscosity is instead held fixed at 400 Pa.s while the magmastatic pressure is now varied at 0.1 MPa (depth $\sim$ 4 m), 1 MPa ($\sim$ 40 m), 2.5 MPa (depth $\sim$ 100 m), and 10 MPa (depth $\sim$ 400 m). These figures indicate that for a melt viscosity of 400 Pa.s, τ_g^{-1} and τ_b^{-1} are outside of the observed tremor frequency range (0.5-17 Hz) except in the upper few meters of the conduit. We find that further investigation using the same values of pressure but for different values of viscosity supports the conclusion from Figures 5.5a-d that a melt viscosity on the order of $\sim 10^4$–10^5 Pa.s would be required to bring τ_g^{-1} and τ_b^{-1} into the observed tremor frequency range for the shallowest section of the conduit. We note, however, that bubble growth would be most vigorous close to the magma surface where pressure is lower, and with increasing depth in the magma column the increased pressure would inhibit bubble growth and oscillation [Marchetti et al., 2004]. Radiation of the sound field from the magma into the atmosphere would also be most efficient with a very shallow source location, i.e., within a few tens of meters of the magma surface (Figure 5.3c) [Garces et al., 1998; Marchetti et al., 2004; Godin, 2006], and this is discussed in the following section.

5.5.2 Coupling between the sound field in a magma conduit and the atmosphere

Of critical concern in volcano acoustics is the coupling of the sound field in a magma column to the atmosphere. In a canonical investigation of this phenomenon, Buckingham and Garces [1996] proposed that the magma surface may be treated as a pressure-release boundary due to the strong impedance contrast between the two media. This is also conventional in ocean acoustics (the ocean surface is generally treated as a pressure-release boundary). In Buckingham and Garces [1996], weak radiation into the atmosphere of the resonant sound field trapped in a magma conduit was possible due to the diaphragm-like vertical motion of the magma surface acting as a piston set in an infinite baffle (c.f., a loudspeaker cone). Later, Garces and McNutt [1997] and Garces et al. [1998] proposed that a region of low sound speed close to the magma surface corresponding to a bubbly mixture with high void fraction (see equation 5.5) may lower the impedance contrast between the magma and atmosphere, and enable more efficient radiation of sound into the atmosphere. However, a region of high void fraction would also have a high effective viscosity η_{eff}:

$$\eta_{eff} = \frac{3}{4}\eta_b + \eta_s \tag{5.9}$$

where η_b is the bulk viscosity and η_s is the shear viscosity, and both η_b and η_s are non-linear functions of the void fraction [Garces, 1997, 2000; Marchetti et al., 2004]. Marchetti et al. [2004] showed that a basaltic melt with viscosity $\eta_0 \sim 500$ Pa.s, but a high void fraction ($\phi > 0.4$), could have an effective viscosity $\eta_{eff} \sim 10^4$–10^5 Pa.s close to the magma surface, resulting in strong attenuation of acoustic waves. Marchetti et al. [2004] proposed that such attenuation would limit the ability of sound sources deep in a bubbly magma conduit to radiate to the atmosphere. However, sound sources in the uppermost conduit section could be coupled to the atmosphere.

Recent theoretical work [Godin, 2006, 2007] on the boundary at the ocean surface may have important implications for this problem in volcano acoustics. Godin [2006, 2007] showed that, contrary to conventional wisdom, the interface between a liquid with high sound speed (e.g., the ocean with sound speed $\sim$ 1500 m/s) and the overlying atmosphere (sound speed $\sim$ 330 m/s) is in fact anomalously transparent to low-frequency sound. Whereas high-frequency ray theory predicts that only a negligible amount of sound could be transmitted from the ocean into

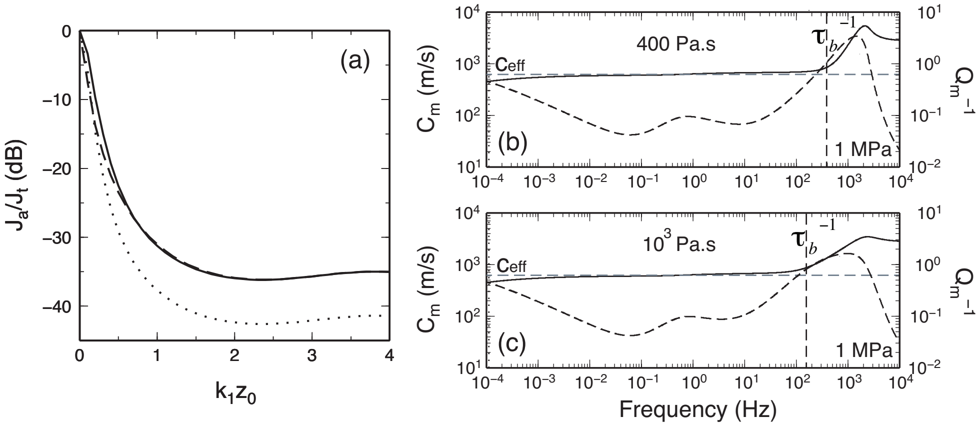

Figure 5.6: (a) Transparency (J_a/J_t in dB) for a monopole source at depth z_0 below a liquid-air interface with wavenumber in the liquid $k_1 = 2\pi/\lambda$ [Godin, 2006, 2007] for water ($c_w = 1500$ m/s, $\rho_w = 1000$ kg/m^3, solid line, compare with Figure 5.4 of Godin [2006]), bubbly magma ($c_{eff} = 620$ m/s, $\rho_l = 2600$ kg/m^3, dotted line), and liquid magma with no gas ($c_{eff} = 2500$ m/s, $\rho_l = 2600$ kg/m^3, dashed line). Energy within $k_1z_0 \sim 1$ of the surface is propagated efficiently into the atmosphere due to inhomogeneous waves. (b) and (c) Sound speed c_m (m/s) (left axis, solid curve) and attenuation Q_m^{-1} (right axis, dashed curve) of pressure waves in a bubbly liquid [Ichihara and Kameda, 2004] where bubble radius $R \sim 1$ cm, and void fraction $\phi \sim 0.001$, the pressure and viscosity are indicated on the plots, and all other parameters are as in Figure 5.5. The effective sound speed c_{eff} is $\sim$ 620 m/s, and is a good approximation to the sound speed in the frequency range of the observed tremor. This value of c_{eff} used in (a) is therefore justified.

the atmosphere, Godin [2006, 2007] showed that almost all of the energy at infrasonic frequencies can be transmitted for shallow sources (i.e., sources within approximately one wavelength of the ocean surface) due to the role of inhomogeneous waves. This phenomenon could enable the shallow sound field in a magma column to radiate efficiently into the atmosphere without the need for a high void fraction and low sound speed layer.

For instance, suppose that we now have a relatively low void fraction $\phi \sim 10^{-3}$ near the magma surface, a bubble radius $R \sim 1$ cm, and a bubble cloud with characteristic length scale $L_b \sim 50$ m. The value of R was chosen to give a value of f_1 (equation 5.6) in the range of the observed infrasonic tremor for this low value of ϕ; i.e., this would correspond to $N \sim 10^8$ bubbles, or ~ 240 bubbles/m^3 assuming $\phi \sim \frac{4}{3}\pi R^3 N/V$, where V is the volume 1 m^3. In this case, equation (5.1) with $P_0 \sim 1$ MPa and $\rho_l \sim 2600$ kg/m^3 yields $f_0 \sim 540$ Hz, equation (5.5) yields $c_{eff} \sim 620$ m/s, and equation (5.6) yields $f_1 \sim 3$ Hz. We note that bubbles with the larger radius of 1 cm used here would also probably result in more powerful sound production than the radius of 1 mm used in the previous section, although a quantitative assessment of the sound power output from volcanic bubble clouds is beyond the scope of the present study. The sound speed $c_{eff} \sim 620$ m/s compared to the atmospheric sound speed $c_a \sim 330$ m/s, together with the density $\rho_l \sim 2600$ kg/m^3 compared to the atmospheric density $\rho_a \sim 1.2$ kg/m^3 result in a large impedance mis-match $(\rho_l c_{eff}/\rho_a c_a)$, which according to high frequency theory would result in poor acoustic transmission from the magma to the atmosphere. However, in Figure 5.6a we show the acoustic transparency J_a/J_t of this magma-air surface ($c_{eff} = 620$ m/s, $\rho_l = 2600$ kg/m^3, dashed line, Figure 5.6a), where J_a is the acoustic power flux into the atmosphere from a monopole source in the liquid and J_t is the total power output of the source, calculated according to Godin [2006, 2007]. The transparency is plotted against the non-dimensional source depth $k_1 z_0$, where k_1 is the wavenumber of the acoustic wave in the liquid (wavenumber $k = 2\pi f/c$), and z_0 is the source depth. For comparison, we also show the transparency for the ocean-air surface ($c_w = 1500$ m/s, $\rho_w = 1000$ kg/m^3, solid line, Figure 5.6a) and the surface of liquid magma with no gas ($c_l = 2500$ m/s [Garces et al., 1998], $\rho_l = 2600$ kg/m^3, dotted line). We find that, as in the ocean environment, anomalous transparency is predicted for the magma-air surface for $k_1 z_0 < 1$. For $c_{eff} = 620$ m/s and frequency ~ 3 Hz this would correspond to a depth ~ 30 m, whereas for $c_{eff} = 2500$ m/s this would correspond to a depth of 132 m. This indicates that the sound field radiated by oscillating bubbles within the upper few tens of meters in a bubbly magma column may be propagated into the atmosphere via anomalous transparency without requiring a low sound speed and high void fraction, while anomalous transparency may be expected up to a greater depth in a degassed conduit with higher sound velocity. In Figure 5.6b and c we show the curves for c_m and Q_m^{-1} predicted by the model of Ichihara and Kameda [2004] for the parameters used for the bubbly magma here. These figures justify the use of $c_{eff} \sim 620$ m/s and the neglect of melt viscosity and volatile diffusion effects on bubble oscillation for the parameters considered above.

Taken together with the results of section 5.5.1, this suggests that the collective oscillations of a cloud of small bubbles (R of millimeters up to centimeters) within the upper few tens of meters of a magma column with melt viscosity $\sim$ 400–1000 Pa.s may be an efficient source of sound into the atmosphere. Anomalous transparency of the magma-air interface may allow the transmission of the low-frequency sound field in the magma conduit into the atmosphere, without requiring a large void fraction near the magma surface. This transparency effect would be reduced at high frequencies (Figure 5.6a). However, the void fraction may inevitably rise sharply in the upper few meters of a magma conduit. In this case, effective viscous attenuation effects may act on the higher frequencies of observed tremor [Garces, 1997, 2000; Marchetti et al., 2004]. Such frequency-dependent effects of liquid-bubble mixtures and the magma-air acoustic transmission may partially explain why the observed tremor power spectrum is peaked between ∼1-3 Hz, and acoustic power is reduced at higher frequencies (Figure 5.3a). We note that this general view of the continuous degassing process (i.e., vigorous degassing taking place within the upper few tens of meters of a conduit) is consistent with that proposed by Edmonds and Gerlach [2007] based on measurements of volcanic gas composition at Puʻu ʻŌʻō in 2004-2005 using open path Fourier transform infrared spectroscopy.

This proposed mechanism for the generation of continuous hawaiian infrasonic tremor can also be related to models for more impulsive infrasonic signal production by moderate to large bubble bursts observed in numerous strombolian and hawaiian systems [Vergniolle and Brandeis, 1996; Ripepe et al., 2007; Johnson et al., 2008; Gerst et al., 2008b; Fee et al., 2009]. The difference being that to generate an observable impulsive signal, small bubbles must coalesce into larger bubbles, which eventually explode energetically at the lava surface with high overpressure [Johnson et al., 2008; Gerst et al., 2008b]. Ripepe et al. [2007] observed numerous small-amplitude impulsive signals at Stromboli Volcano which were more persistent and lower in amplitude than typical strombolian explosion signals. They attributed these signals to the persistent bursting of relatively small bubbles at the top of the magma column in contrast to the larger bubble bursts that generate the typical explosion signals. The proposed system for Puʻu ʻŌʻō's broadband infrasonic tremor can be thought of as an end-member of this spectrum of processes, where the tremor is generated by a population of bubbles that have not coalesced into large exploding bubbles, and are driven into continuous oscillation by lava motion. Continuous bursting of the bubbles at the lava surface would provide a continuous flux of gas. The ascent of this gas through near surface cavities to the atmosphere is discussed in the following section.

5.5.3 Self-sustained shear-layer oscillations

Although bubbles offer a promising mechanism for the production of broadband infrasonic tremor in a shallow magma conduit, it is difficult to explain the observed sharply-peaked harmonic tremor component with the same model. The sharply-peaked harmonic tremor in the ∼0.6-0.9 Hz band has a spectral signature and temporal dependence distinct from the broadband signal, and likely results from a separate physical process (Figure 5.3). Sharply-peaked spectra in volcanic seismic and acoustic signals are usually attributed to resonance in fluid-filled cavities. However, the physics of the driving mechanisms (trigger mechanisms) sustaining the resonance for long-duration tremor sources remains poorly understood [Chouet, 1996b]. One type of self-sustained oscillation that may be relevant to the harmonic tremor source at Pu‘u Ō‘ō is that which results from the aeroacoustic interaction of the shear-layer of a low-velocity gas jet with a solid boundary. Rockwell and Naudascher [1979] provide a comprehensive summary of the phenomena of discrete acoustic frequencies (tones) produced by shear-layers impinging on solid objects. Since there are different types of shear-layers (i.e., jets and mixing layers of various geometries) and many possibilities for the geometry of the solid boundaries (e.g., edges, holes, rings, plates, flaps, and cavities), these interactions give rise to a diverse family of processes with common characteristics and similar underlying physical mechanisms. This family of processes includes the edge tone, which results from the impingement of a planar jet on a solid edge [Nyborg et al., 1952], periodic noise produced by air-flow (i.e., a mixing layer) over a rectangular cavity [Rossiter, 1964], the hole tone, which is produced by the flow of an axisymmetric jet from one plate impinging on a second plate with a hole in it [Chanaud and Powell, 1965; Langthjem and Nakano, 2005], and many other possible configurations [Rockwell and Naudascher, 1979]. Each of these processes is thought to involve a similar complex feedback mechanism. When the flow encounters the solid object, it is impeded slightly and a hydrodynamic or acoustic disturbance is sent back upstream where it then interacts with a sensitive area of the shear-layer upstream to create vortices. These vortical oscillations in the shear-layer then propagate downstream again, forming a closed feedback loop and self-sustained oscillations at specific frequencies [Rockwell and Naudascher, 1979]. The frequencies f of tones produced are non-dimensionalized as the tonal Strouhal number $St = fL/U$, where L is the length-scale of the feedback process and U is the free-stream velocity. For instance, L can be the length of the cavity or distance from the jet nozzle to the solid object, and U the mean flow velocity of the jet in the absence of the solid boundary. The Strouhal numbers of the resulting acoustic signals were found empirically by Rossiter [1964] to agree with:

$$St_m = \frac{(m-\gamma)}{(\frac{1}{K}+M)}, \tag{5.10}$$

where m is a mode number, $m = 1, 2, 3, \ldots$, M is the Mach number ($M = U/c_0$, where U is the free-stream velocity of the flow and c_0 is the sound speed), and K and γ are empirical constants, $K, \gamma < 1$. Equivalently, the observed frequencies of oscillation or Rossiter modes can be expressed as:

$$f_m = \frac{U}{L}\frac{(m-\gamma)}{(\frac{1}{K}+M)}. \tag{5.11}$$

Rossiter [1964] further proposed that the constant K corresponds to the ratio of the vortex convection velocity U_c to the free-stream velocity, i.e., $U_c = KU$, and K is typically around ∼0.4-0.6 for most processes [Howe, 1998]. γ remains an empirical constant, interpreted as a phase lag. The phase lag is due to both 1) the time-delay between the vortex impingement on the solid boundary and the emission of the acoustic/hydrodynamic disturbance, and 2) the delay between the arrival of the acoustic/hydrodynamic disturbance at the upstream shear-layer and the release of new vortices. Equation (5.11) can therefore be expressed in terms of the physical parameters of the system:

$$\frac{L}{U_c} + \frac{L}{c_0} = \frac{(m-\gamma)}{f_m}, \tag{5.12}$$

which is known as Rossiter's equation [Howe, 1998]. Here, the quantity L/U_c represents the time taken for a vortex to travel downstream from the source to the impingement object, and L/c_0 is the time taken for the acoustic disturbance to travel upstream from the impingement object to the vortex source. Delprat [2006] has further proposed that by setting $m = 1$ and $\gamma = 0$, equation (5.12) can be expressed in terms of the fundamental aeroacoustic loop frequency f_a of the feedback process:

$$\frac{L}{U_c} + \frac{L}{c_0} = \frac{1}{f_a}. \tag{5.13}$$

The phase shift γ in equations (5.11) and (5.12) then results in the observed Rossiter mode frequencies f_m being offset from integer multiples of the aeroacoustic loop frequency f_a, as $f_m = (m - \gamma)f_a$ [Howe, 1998; Delprat, 2006].

Several of the shear-layer and solid object impingement geometries that can result in tone production [Rockwell and Naudascher, 1979] may be appropriate to volcanic settings. In particular, the edge tone [Nyborg et al., 1952], hole tone [Chanaud and Powell, 1965], and jet flow through flaring horns [Hirschberg et al., 1989], could be considered as small laboratory-scale analogues for volcanic degassing past solid vent walls, through near surface cavities, and from a vent set in an upward flaring crater respectively. Since the spatial scales for a volcano are large, a similar aeroacoustic flow process operating with the same St but at a volcanic length scale could produce low-frequency (infrasonic) acoustic radiation.

The hole tone geometry seems particularly appropriate to the vent geometry at Puʻu Ōʻō in April 2007 (Figure 5.4a, Figure 5.7c). The hole tone, also known as the Rayleigh bird call [Rayleigh, 1976], is generated in the laboratory when an axisymmetric jet issuing from a nozzle in a plate impinges on a second plate with a hole in it [Chanaud and Powell, 1965]. The jet continues through the hole in the second plate but is impeded slightly as it does so, resulting in the impingement distburbance. The acoustic disturbance propagates back upstream where it interacts with the jet near the nozzle outlet, and the resultant vortical oscillations propagate back downstream towards the second plate, and so on. A common example of this phenomenon is a whistling tea kettle. It is conceivable that a similar process could have occurred within the shallow degassing region underneath the crater complex of Puʻu ʻŌʻō if a similar geometry were present (Figure 5.3c).

In applying equation (5.13) to the hole tone, L is the length-scale between the jet outlet and the second hole or vent (Figure 5.3c), and $U_c = KU$ where U is the mean jet velocity and K is estimated at ∼0.6-0.7 from laboratory experiments [Langthjem and Nakano, 2005]. Suppose a low-velocity gas jet streams from a vent overlying a magma conduit, travels through a small near-surface cavity, and escapes through a second vent in the overlying crater floor (Figure 5.3c). This gas jet may consist of volatiles escaping the magma in addition to locally entrained air. A similar geometry consisting of a vigorously convecting lava body at the base of a subsurface cavity which opens to the atmosphere has been observed recently at the more accessible Halemaʻumaʻu vent [Fee et al., 2009], and this type of geometry also seems reasonable for several of the active vents at Puʻu ʻŌʻō during April 2007 (e.g., see Figure 5.7c). For Puʻu Ōʻō, let the distance from jet origin to the vent be $L \sim 15$ m, the mean jet flow speed may be $U \sim 8$ m/s, which gives $U_c \sim 0.65{\times}8 \sim 5$ m/s. Then for a dominantly steam-filled cavity with sound speed $c_0 \sim 450$ m/s [Fee et al., 2009] we obtain the fundamental aeroacoustic loop frequency $f_a \sim 0.33$ Hz. Since a reasonable value for γ is 0.25 for a wide range of flow conditions [Rossiter, 1964], the first three Rossiter modes are given by $f_m = (m - 0.25)f_a$ for $m = 1, 2, 3$, yielding $f_1 \sim 0.25$ Hz, $f_2 \sim 0.6$ Hz, and $f_3 \sim 0.9$ Hz. The values for f_2 and f_3 from this simple discussion are roughly consistent with the observed frequencies of sharply-peaked harmonic tremor (Figure 5.3b), suggesting that a process similar to the hole tone is a plausible source for the observed infrasonic tremor. We note that the constants γ and K can vary spatially and with Mach number [Malone et al., 2009] indicating that other physically plausible values for the length L and jet flow speed U could lead to a better match to the observed infrasonic frequencies. Rossiter's equation is useful for predicting possible excitation frequencies, but does not predict which particular frequencies will be excited or the most dominant tones in a given system [Malone et al., 2009]. In particular, absence of the fundamental mode $f_1 \sim 0.25$ Hz predicted in our analysis would not be surprising [Malone et al., 2009].

The Rossiter modes are not usually integer harmonics of a fundamental frequency, and in general do not correspond to acoustic modes of the cavity [Howe, 1998; Delprat, 2006]. Nevertheless, resonators can exert their influence on self-sustained shear-layer tones to create more stable spectral peaks [Nyborg et al., 1952; Rockwell and Naudascher, 1978]. For instance, if there is a resonant pipe or Helmholtz cavity in the section L through which a jet flows, the dominant Rossiter mode tends to coincide with the acoustic or Helmholtz cavity modes, and the sound output at these frequencies is particularly high. This type of process occurs in the "whistler-nozzle" phenomenon thought to be responsible for human whistling [Hussain and Hasan, 1983; Wilson et al., 1970]. In this case, both the cavity modes (Helmholtz or acoustic modes) and the jet dynamics are important in sustaining the tone. The gap of length L depicted in Figure 5.3c could be generated by a process such as a solid lid forming over the lava, and the subsequent fall of the lava level. In reality this would form a finite cavity, the resonant properties of which would influence the frequency of sound produced. We note that Julian [1994] proposed a mechanism of continuous tremor excitation by self-sustained oscillations resulting from fluid flow through a conduit with elastic walls. The model of Julian [1994] is somewhat analogous to the mechanism of tone excitation in a clarinet, where vibrations of the elastic walls of the conduit are analogous to the vibrations of the reed in a clarinet mouthpiece [Fletcher, 1999; Fletcher and Rossing, 2008]. The mechanism discussed here is more analogous to that in reedless musical instruments such as the flute, where the interaction of an air jet from the player's lips with a solid edge in the mouthpiece generates edge tones which are coupled closely to the resonant modes of the flute cavity [Fletcher, 1999; Fletcher and Rossing, 2008].

One general qualitative characteristic of flow-induced oscillations caused by jet shear-layers impinging on solid objects is that the oscillation frequencies can change depending on the length-scale L or the flow speed of the jet U, and can exhibit sudden discontinuous frequency jumps [Rockwell and Naudascher, 1979]. The various stable modes of operation between the frequency jumps are referred to as *stages*, and several stages and their harmonics can exist simultaneously [Nyborg et al., 1952]. In this framework, the complex time evolution (e.g., gliding and mode switching) of frequency peaks of the observed tremor may relate to fluctuations in gas velocity U issuing from the vent and the transition between different stages. L could also change if the lava level were to fluctuate up and down. In the multi-vent Pu‘u ‘Ō‘ō system it is also possible that different frequencies of tone production relate to the activity of different vents. In this case, the switching on and off of different tremor frequencies at ∼0.6 Hz and ∼0.8 Hz (Figure 5.3a) may simply correspond to intermittent activity at separate vents. However, between 0300 and 0600 UTC Julian day 111 2007 (Figure 5.3a), the lower frequency peak of ∼0.6 Hz appears to diverge progressively from the peak at ∼0.8 Hz at a bifurcation in the frequency domain. This property suggests that both frequency peaks are related to a single mechanism such as sound production by evolving flow conditions at a single vent. We note that the seismic tremor data at KIPU have a complicated spectrum (Figure 5.3b), but with sharp peaks between ∼0.6-0.9 Hz in common with the infrasound data.

Finally, we comment that fully turbulent volcanic flows can generate powerful infrasound, which may be analogous to audible jet noise produced by smaller-scale turbulent jet flows (chapter 4). However, the mechanism discussed here refers to lower speed and therefore lower Reynolds number flows. In fact, a laminar jet

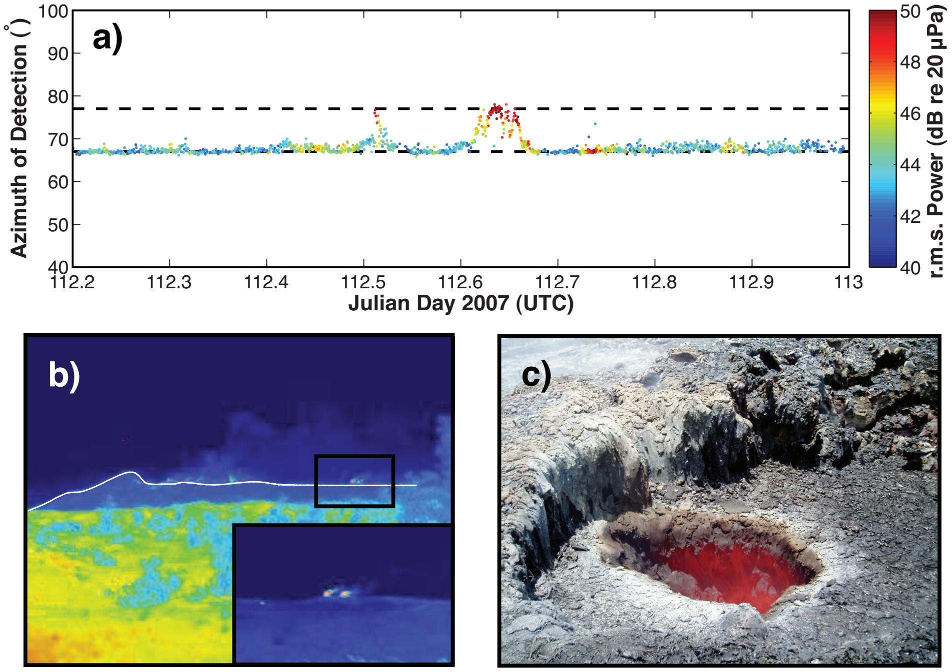

Figure 5.7: Infrasonic signal variation associated with lava tube activity as corroborated by audible noises and infrared imaging. a) 5-10 Hz band PMCC processing during Julian day 112.2 to 113 2007. Note that coherent signal detection azimuths deviate from that of the crater complex and begin to arrive from the greater azimuth of ∼77°. This coincides with the time in which audible noises were heard coming from that approximate direction. The crater complex source at ∼67° does not end during these times, but is no longer the dominant sound source in the 5-10 Hz band. PMCC array processing is unable to differentiate between the two competing signals during these times. b) Infrared image taken from KIPU array location towards Puʻu ʻŌʻō, revealing incandescent sources to the south of the main crater complex. White line indicates approximate topography of Puʻu ʻŌʻō. Area in box is expanded in the inset. In inset, right hand incandescent source corresponds to new lava tube skylight described in text. Left hand incandescent source is the acoustically quiescent kiln hornito. c) New skylight vent (corresponding to right hand source in b) from which the infrasound and audible sounds originated, photographed on Julian day 115 2007.

can produce self-sustained oscillations when impinging on a solid object [Rockwell and Naudascher, 1979; Chanaud and Powell, 1965; Howe, 1998], and it is typically observed that laminar flows produce more intense and better defined flow-induced spectral peaks [Chanaud and Powell, 1965; Howe, 1998]. When the flows become more turbulent, the tones generated by impingement feedback become less defined, and can be overwhelmed by the broadband noise from turbulence (although supersonic jet flows can exhibit additional spectral peaks referred to as jet screech [Tam, 1995]). In this sense, the sharply-peaked harmonic tremor observed at Puʻu ʻŌʻō, and at other volcanoes [Garces et al., 2008], may be related to the more energetic and broadband tremor associated with more vigorous vulcanian and plinian volcanic eruptions (chapter 4). Both may result from jet aeroacoustic processes, with the Reynolds number of the flow being a key parameter determining whether harmonic or more broadband (jet noise-like) infrasonic tremor is produced. In this framework, the geometry of the volcanic vent and nozzle, and the resonant modes of the upper conduit section would be other critical factors controlling the spectral nature of infrasonic tremor resulting from degassing at various flow speeds.

5.6 Signals from the lava tube system

At intermittent times throughout the field deployment, audible noises resembling jet noise, chugging [Johnson and Lees, 2000], and more resonant harmonic tremor could be heard for up to several hours at a time and originated from south of the main crater complex area. At most of these times, little or no change in the KIPU infrasound data was observed. However, during at least one time (1200 to 1700 UTC Julian day 112 2007), very intense audible chugging and jet noise sounds were heard at the same time that PMCC processing results show additional infrasonic energy in the 5-10 Hz band arriving from a location on the south flank (Figure 5.7a). However, the infrasound arrays with aperture of ∼100 m have an array response which results in spatial aliasing above frequencies of ∼5 Hz. Thus, array processing in the 5-10 Hz band for KIPU results in numerous spurious signals and the results must be interpreted with caution. Nevertheless, PMCC processing can perform well on ground-truth signals with frequencies extending well above the optimal array response (see Figure 2.16 of chapter 2 where a similar array geometry and aperture were used). In addition, we applied strict post-processing parsing of the 5-10 Hz PMCC results to remove the spurious azimuth detections (Figure 5.7a), and correlated the PMCC results with changes in the waveform envelope during these time periods. During the times in which intense audible sounds were heard, PMCC detections in the 5-10 Hz band shift to the south and point to a location along the lava tube system. This does not indicate cessation of the crater complex source, which is seen to be continuous in the 0.5-5 Hz band (Figure 5.2), but suggests instead that the source to the south dominated in the 5-10 Hz band.

Infrared imaging from the KIPU array site revealed an incandescent source in the approximate direction from which audible sound and infrasound originated (Figure 5.7b). Subsequent investigation of this area revealed a new skylight opening in the lava tube system which had not been previously documented (Figure 5.7c). The vent was surrounded by spatter indicative of increased degassing/spattering activity (Figure 5.7c). These observations indicate that vents in the extended lava tube system can be sources of infrasonic tremor in addition to the vents in the crater complex area and suggest that infrasound arrays could help to monitor the lava tube system for new vent openings. The evidence for degassing activity is consistent with the acoustic source process outlined in section 5.5.3. The smaller size of this vent in comparison to the larger vents in the crater complex area may explain why these signals had higher dominant frequencies than the signals from the crater complex area.

The intermittent acoustic and degassing activity of the vent shown in Figure 5.7c has implications for skylight formation, lava tube dynamics, and acoustic source dynamics in the lava tube system. On the night of Julian day 115 after the photograph shown in Figure 5.7c was taken, the audible jet noise sounds were heard again, indicating that vigorous (turbulent) degassing had reinitiated at the vent. On the following day (Julian day 116) we returned to the skylight, and found that the skylight opening had been eroded and heavily spattered, and that the vent area features were unrecognizable. Lava in this downstream section of the lava tube system is usually considered essentially degassed of volatiles other than water [Edmonds and Gerlach, 2007], yet the jetting activity and erosion/dynamics of the vent region suggest vigorous degassing activity from an abundant volatile source. It is possible that a pocket of gas intermittently managed to make it downstream to this location, where it was then released causing erosion of the skylight and the jetting activity. In another scenario, solid pieces of the lava tube may have intermittently collapsed into the lava, triggering degassing. Alternatively, heavy rainfall during the experiment may have provided meteoric input to the system [Keszthelyi, 1995], providing an intermittent volatile flux. A sudden change in the lava tube geometry such as a step down in elevation (lava fall), or a constriction in the tube diameter, might be responsible for disrupting the flow and releasing the gas at this specific location. Some of the questions pertaining to lava tube dynamics [Greeley, 1987; Helz et al., 2003] and skylight formation could be addressed with future focussed acoustic studies.

5.7 Conclusions

The temporary deployment of a broadband infrasound array ~2.4 km from Puʻu ʻŌʻō, in conjunction with a semi-permanent array at ~12.5 km range, enabled clarification of the propagation effects on the infrasonic tremor wavefield at Kilauea Volcano. The deployment of the array closer to Puʻu ʻŌʻō also enabled recordings of the tremor signal that had higher signal-to-noise ratios and were relatively free from propagation effects. The persistent infrasonic tremor source contains at least two components: 1) a broadband component concentrated between 0.5-15 Hz, and 2) more sharply-peaked tones in the 0.6-0.9 Hz band that exhibit complex temporal evolution. We speculate that (1) may be generated primarily by bubble cloud oscillations in a roiling lava body beneath the crater complex, while (2) may result from interaction of the escaping stream of gas with the vent and near-surface cavities in a process similar to the hole tone or whistler-nozzle phenomenon. However, further work is required to assess the theoretical source power and radiation properties of these processes. Additional infrasonic and audible sounds originating from the south flank coincided with increased degassing activity at a relatively new lava tube skylight, suggesting that acoustic studies may aid in monitoring and understanding flow dynamics in the lava tube system.

Chapter acknowledgments

KIPU was deployed with helicopter field support from HVO. We are very grateful to Frank Trusdell for hosting the MENE array in his backyard, and to Tim Orr for advice on accessible vents. James Robertson and Emily Crawford helped with the field deployment and KIPU array site survey. THST wind tower data were provided by Thomas Giambelluca, Guangxia Cao and Kate Brauman. Bernard Chouet provided some insightful comments on an early version of the manuscript. This work was funded by NSF grant EAR-0609669. Chapter 5, in part, has been submitted for publication as Matoza, R.S., Fee, D., and Garces, M.A., Infrasonic tremor wavefield of the Puʻu Ōʻō crater complex and lava tube system, Hawaii, in April 2007, *J. Geophys. Res.*, *submitted.*

6. Future work

The purpose of this final chapter is to highlight some possible avenues of future research. We discuss several ways in which the source models initiated in this dissertation could be further tested and evaluated using analogue and numerical experiments and dense seismo-acoustic sensor deployments.

6.1 Laboratory experiments

6.1.1 Aeroacoustic experiments

In chapter 4 it was argued that laboratory aeroacoustic experiments could investigate the effects of particulate loading on radiated jet noise spectra, noise radiation patterns, and noise power. Since jet flows and jet noise appear self-similar across a broad range of length-scales, small-scale laboratory experiments may produce results that are applicable to the physics of noise emissions in large-scale volcanic jet flows. Kieffer and Sturtevant [1984] performed shock-tube investigations of volcanic jets using pure gases Freon 12, Freon 22, Helium, and Nitrogen. The Freons were considered good analogues of particle-laden volcanic gases given a pseudogas assumption. N-waves recorded by microphones placed near the shock tubes for the Helium and Nitrogen gases showed similarity to barograph recordings of the 1883 eruption of Krakatoa [Kieffer and Sturtevant, 1984]. However, the acoustics of two-phase jet noise is likely to deviate from a pseudogas approximation as interaction between the solid particles and the gas phase is likely to be significant. Recently, Chojnicki et al. [2006] used 1D shock-tube experiments to investigate the fluid dynamics of gas-particle mixtures. More advanced laboratory aeroacoustic experiments [Seiner, 1984] could be devised for measuring the acoustic radiation from sustained jetting of particle-laden gases in an anechoic chamber. The sizes of particles used should scale with typical volcanic ash grain sizes. Such studies could address whether the presence of small particles in the flow acts to lower the frequency of sound produced, or results in a spectrum that is different from the similarity spectra for pure-air jets [Tam et al., 1996]. Other parameters that could be considered include the temperature of the gas-particle mixture, and the nozzle and crater geometry. These factors are probably significant in volcanic jets.

6.1.2 Explosive properties of water

Thiéry and Mercury [2009] have recently provided a summary of the thermodynamic properties of water and their implications for volcanic explosions. Under certain conditions, water can be placed into a metastable or unstable field, from where adjustment back to a stable state can be violent and explosive. LP events at Mount St. Helens appear to result from the interaction of the magmatic and hydrothermal system [Waite et al., 2008]. Metastable and unstable activity of water in a hydrothermal crack heated by magmatic activity is an attractive explanation for the sudden pressure transients that lead to LP events [Ohminato, 2006]. Laboratory experiments aimed at measuring the pressure waveforms from water in heated and pressurized containers may lead to further insights on the trigger mechanism of LP events at Mount St. Helens and other volcanoes.

6.2 Numerical experiments

6.2.1 Seismic-acoustic coupling

In chapter 3 it was concluded that seismic-acoustic wave propagation through permeable and porous near-surface volcanic material is important for explaining joint infrasonic and seismic observations of long-period events. Since long-period seismicity is commonly located at shallow depth within a volcanic edifice, it is likely that similar coupling to the atmosphere will be recorded for LPs, tremor and explosions signals at many volcanoes. In order to proceed with quantifying this coupling mechanism, it will be necessary to incorporate the theory for wave transmission through unconsolidated material, i.e., *Biot theory*, or its alternatives [Hickey and Sabatier, 1997, *and references therein*], into the numerical finite-difference calculations of low frequency seismic-acoustic transmission. This work would benefit from laboratory studies of geo-acoustic properties of geological field samples from Mount St. Helens and other volcanoes to constrain the properties of the volcanic materials [e.g., Scheu et al., 2006].

6.2.2 Multiphase fluids

The source mechanism for seismic and infrasonic LP events advanced in chapter 3 consists of a complex multiphase (gas-liquid) fluid process. The model consists of the rapid transformation of superheated liquid contained in a pressurized hydrothermal crack into vapor. The infrasound signal was attributed to an acoustic wave generated by this fluid expansion into porous material, while the seismic LP event was attributed to the collapse of the crack and resonance of the remaining fluid (steam and bubbly water). More detailed numerical modeling of this process requires a method that is able to incorporate the thermodynamics of the liquid-gas mixture with the elastodynamics of seismic and acoustic wave propagation. The phase-field method or diffuse-interface model is one approach that holds great promise for achieving the first component of this goal [Chouet, 2009]. This theory deals with a description of the interface between gas and liquid. The interface is modeled as a thin diffuse layer (rather than a sharp boundary) in which the gas and liquid components are mixed [Chouet, 2009]. Numerical implementations of the phase field method have shown success in modeling a wide variety of two-phase physical phenomena. Success has also been achieved with this method in modeling gas slug ascent in a magma conduit [D'Auria and Martini, 2009], with results consistent with analogue laboratory experiments [James et al., 2006]. This approach may therefore be useful for assessing physicochemical conditions that may lead to LP events in a hydrothermal crack, and for calculating the elastodynamic wavefield resulting from cavitation and spinodal decomposition [Thiéry and Mercury, 2009] in a buried fluid container.

6.2.3 Computational aeroacoustics

In chapter 4, we proposed that broadband infrasonic tremor signals from sustained vulcanian and plinian eruptions represent a low frequency form of jet noise. Recently, advances have been made in modeling compressible supersonic volcanic jet flows using computational fluid dynamics (CFD) [Ogden et al., 2008]. However, modeling acoustic radiation from such flows with computational aeroacoustics (CAA) represents a separate and formidable challenge [Bailly and Bogey, 2004; Tam, 2004]. To resolve small acoustic pressure perturbations upon a turbulent flow field, the turbulence simulation must have very low noise. In addition, there are large disparities between the grid spacings and size of computational domain required to resolve acoustic propagation (out to the far field) and the grid spacings required to resolve turbulent flow [Tam, 2004]. As the Reynolds number increases, direct numerical simulation of turbulence becomes increasingly difficult [Pope, 2005]. Consequently, current CAA simulations can only predict the noise emissions from the most simple jet flows. Nevertheless, approaches based on direct numerical simulation (DNS) or large eddy simulation (LES) of turbulent (possibly two-phase) volcanic jet flows, coupled with solutions of the linearized Euler equations, and the use of adaptive meshes, could in principle provide a way to model the infrasonic signals reported in chapter 4. Given the significant challenges involved, application of CAA to exploring the noise emissions from peculiar volcanic jet flows with peculiar physics should be coupled with analogue laboratory experiments. Laboratory aeroacoustic experiments would help to ground-truth the CAA simulations. The harmonic tremor source process outlined in chapter 5 may also be amenable to numerical simulation. A numerical simulation of the hole-tone feedback cycle and its acoustic radiation has already been presented by Langthjem and Nakano [2005]. This formulation could be adapted for volcanic length-scales, fluids, and infrasonic frequencies.

6.2.4 Infrasonic propagation

As outlined in chapters 1 and 2, locating infrasonic sensors at ranges >10 km from a volcano, rather than directly on top of a volcanic edifice, has the following advantages: 1) the risk to field personnel and equipment during a volcanic crisis is reduced, 2) data continuity is improved since sensors are less likely to be destroyed during an explosion, 3) greater flexibility in site selection means that sensors can be placed in low wind noise sites such as forests, and 4) the sensors are in the far-field for many volcano acoustic sources, where near-field source directivity and non-linear wave propagation effects are minimal [Garces et al., submitted]. Since vulcanian and plinian eruptions represent powerful infrasonic sources, arrays located at $\sim$10-50 km range can record these signals with high signal-to-noise ratio (chapter 4). However, the results and analysis of chapters 2, 3, and 5 indicate significant propagation effects for low-amplitude infrasonic signals recorded at this range. Further characterization and modeling of infrasonic propagation effects will therefore be critical for future studies of volcanic infrasound. Fortunately, atmospheric specifications on the mesoscale are currently improving dramatically. Numerical, observationally nudged, mesoscale models such as the Weather Research and Forecasting (WRF) system or the the Rapid Update Cycle (RUC) operational weather prediction system of the National Oceanic and Atmospheric Administration (NOAA) may be able to provide atmospheric specifications at the resolution required to study infrasonic propagation at the ∼10 km range [Douglas Drob, NRL, *personal communication*]. It would be useful to assess the validity of these specifications for explaining observed signal variability. Furthermore, infrasonic data from continuous volcanic sources could be used to ground-truth such specifications, or even to improve them, as has been done on a larger global scale [Le Pichon et al., 2005b]. Studies of volcanic infrasound propagation to greater ranges (>100 km) are also important. In particular, the importance and effects of seasonal stratospheric ducting at mid-latitudes [Le Pichon et al., 2009] and scattering and diffraction into acoustic ray shadow zones should be assessed.

6.3 Field experiments

The infrasound array deployments described in this dissertation represented proof-of-concept stage experiments. When the arrays were initially deployed, it was not known whether infrasonic signals would be recorded at the ranges considered from a relatively closed-vent system such as Mount St. Helens. In future, deployments could be designed with more optimal infrasonic sensor configurations. In addition, supplementary data could help to constrain infrasonic source and propagation effects.

6.3.1 Array design

The four-element arrays used were optimized for frequencies of ∼3 Hz and have a limited signal-to-noise gain. Larger arrays consisting of more sensors could yield higher signal-to-noise gains, enabling the recording of lower-amplitude signals at the same range. Wider-aperture arrays would permit the array analysis of longer-period signals, and would improve signal azimuth estimates. However, a single array effectively represents a point sample of the infrasonic wavefield radiated by a volcano. In order to investigate source directivity effects and wind propagation effects, multiple array deployments around a volcano would be useful. For instance, arrays in the prevailing upwind and downwind directions would be able to examine the preliminary conclusion in chapter 3 that wind is the dominating atmospheric factor affecting propagation at these ranges.

6.3.2 Seismo-acoustic networks

Dense seismic network deployments around an active volcano permit the inversion for point-source moment-tensor and single-force representations of the seismic source [e.g., Waite et al., 2008]. The addition of infrasonic sensors to these networks could allow for analysis of the radiation pattern of volcanic infrasound sources, and detailed source inversions when the signal-to-noise ratio is high. With careful network design, discrimination between volcanic signals of interest and ambient infrasonic noise sources may be possible using network or array processing techniques. In chapter 3 we showed that a dynamic atmosphere can lead to variability in acoustic waveforms, which should be taken into account for inversions of acoustic waveform data. Averaging many waveforms for repetitive events to form a master event for each station (chapter 3) would lead to more robust acoustic inversions.

6.3.3 Additional instruments

Volcano acoustic studies have a significant advantage over volcano seismic studies, in that the source processes are often amenable to visual, infrared, or radar observation. For instance, Moran et al. [2008] used field geological observations and video data to constrain and improve a volcano acoustic source model for a rockfall event. This study used a camera sampling image frames every 3 minutes with one image relayed back to CVO per hour. High-frame-rate visual or infrared recordings of rockfalls, jetting, explosions, or pyroclastic flows would provide valuable data on infrasonic source mechanisms. Video cameras could be set up to start high-frame-rate recording when triggered by motion-activation or by seismic or acoustic data. Finally, studies of infrasound propagation near volcanoes could benefit from more meteorological data. Wind sensors in more exposed and geographically separate sites, and echosondes imaging the structure of the lower atmosphere could provide valuable input to propagation models and mesoscale atmospheric specifications.

A. Beamforming

In this appendix we describe briefly the application of beamforming methods to the MSH infrasound array data set. The time-delay beamformer (A.1) is used throughout the dissertation (Chapters 2, 3, 4, 5) in conjunction with PMCC [Cansi, 1995]. Although the adaptive beamforming methods (A.2) are not used in the remainder of the dissertation, we include their description for two reasons: 1) it is instructive to compare the performance and results of the adaptive beamformers with those of the PMCC algorithm, and 2) these methods show promise in the processing of infrasound array data sets and could be explored in future work.

A.1 Time-delay beamforming

Here we analyze data from the CDWR array (Figures 2.1 and 2.2, individual array elements: MSH21, MSH22, MSH23, MSH24) using a conventional time-delay beamformer [DeFatta et al., 1988]. In section 2.3.1, PMCC was used to identify acoustic arrivals with low signal-to-noise ratio (SNR) coming from the direction of MSH (back azimuth to dome center: 153°) on 11 November 2004 (Julian day 316). At this array there are also three continuous coherent interferers during this time: 1) low frequency ocean noise coming from ∼270°, 2) high frequency noise associated with the city of Portland, Oregon, at ∼200°, and 3) high frequency noise associated with Kelso/Longview, Washington, at ∼240° (Fig 2.3). The aim is to coherently stack the volcanic signals in order to increase their SNR with respect to the ambient incoherent noise and coherent interferers. Two data segments are used for illustration: 1) a 13-second window containing a 6-second signal that had the highest SNR on 11 November 2004 (Figure A.1a), and 2) a 10-minute time window containing ∼20 of the low-amplitude 11 November events (Figure A.1b).

A.1.1 Method

The time-delay beamformer produces a broadband stack of signals coming from a particular direction. For each "look direction" or beam angle $0^\circ \leq \theta_m < 360^\circ$, the stacked beam $b_m(t)$ is computed [DeFatta et al., 1988]:

$$b_m(t) = \sum_{n=1}^{N} w_n e_n \left(t - \frac{\mathbf{E_n}.\mathbf{B_m}}{c} \right), \tag{A.1}$$

where N is the number of array elements, w_n is a weight vector or shading function, $e_n(t)$ is the sensor time series for array element n, $\mathbf{E_n}$ is the spatial coordinates for array element n (relative to central element), c is the sound speed, and $\mathbf{B_m}$ is the beam vector:

$$\mathbf{B_m} = \left[\sin(\theta_m), \cos(\theta_m) \right], \tag{A.2}$$

where θ_m is the azimuth clockwise from North ($0^\circ \leq \theta_m < 360^\circ$). For the weight vector w_n, we initially use a rectangle function (equal weighting to all array elements) with no normalization in order to demonstrate the increase in SNR gained by beamforming. This sum over n is most efficiently performed as a vector dot product for vectors of length n. We used linear interpolation of the sensor time series data in order to achieve time-delays consisting of a non-integer number of time samples.

In order to obtain the values of the phase velocity c, and azimuth corresponding to the maximum energy beam, the time-delay beam (equation A.1) was computed over a grid search of values in the phase velocity c, and azimuth θ_m, and the r.m.s. amplitude of the beam was plotted against the value of c and

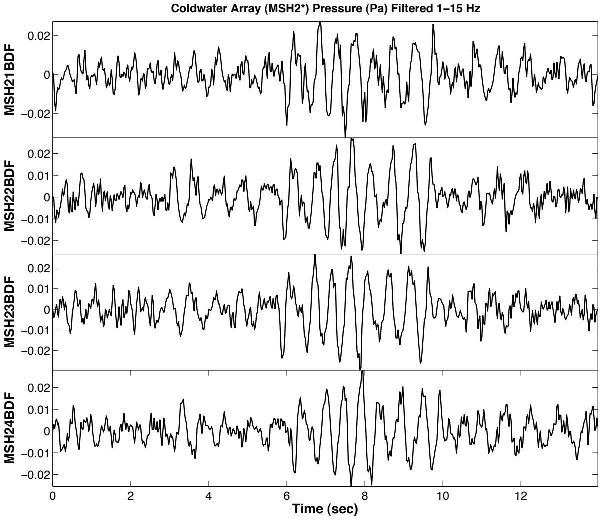

(a) The 13-second time window containing the 6-second pulse of energy occurring on 11 November 2004. It is the largest of a series of low-amplitude detections from the volcano occurring on that day.

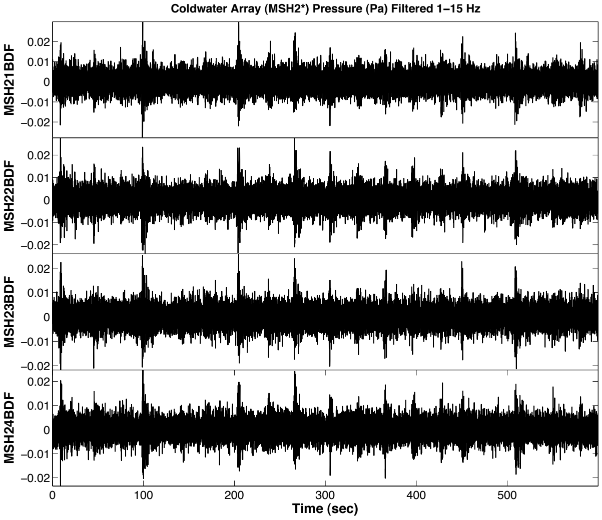

(b) The 10-minute time window containing ∼20 low-amplitude events on 11 November 2004.

Figure A.1: Data used to test time-delay beamformer. Panels correspond to the four array element channels of CDWR (MSH21, MSH22, MSH23, MSH24).

azimuth (Fig A.2). The data were filtered 1-5 Hz prior to time-delay beamforming. A clearly-defined maximum in the beam amplitude is observed at an azimuth pointing towards the 2004-2008 lava dome (∼153.5°) and a phase velocity of ∼340 m/s. This indicates that these are acoustic signals originating from MSH that are traveling through the atmosphere. Seismic signals would have higher phase velocity (∼2000-4000 m/s).

A.1.2 Result

Figures A.3a and A.3b show the time-delay beam at the azimuth and velocity that give the maximum beam power, plotted with the original data of the individual sensor elements. The beamformer enhances the SNR of the low-amplitude impulsive signals, enabling better characterization of their waveform. Throughout the remainer of this dissertation, we set the signal gain as a result of beamforming to unity by dividing the final beam by N (i.e., we set each element of w_n to $1/N$), where N is the number of array elements ($N = 4$). This allows for a more physical interpretation of the beamformed signals.

A.2 Adaptive beamforming

In this section, we briefly investigate the application of the frequency domain Conventional BeamFormer (CBF), Minimum Variance Distortionless Response (MVDR) adaptive beamformer, and White Noise Constrained (WNC) adaptive beamformer to the MSH infrasound array data. Frequency domain beamforming is more computationally efficient than time-domain beamforming, and allows beamforming to be performed at exact narrow band frequencies. The MVDR adaptive beamformer represents an optimal solution to the beamforming problem, i.e., the problem of maximizing the SNR or array gain of a signal in the presence of coherent interferers and incoherent (spatially diffuse) noise [Cox et al., 1987; Van

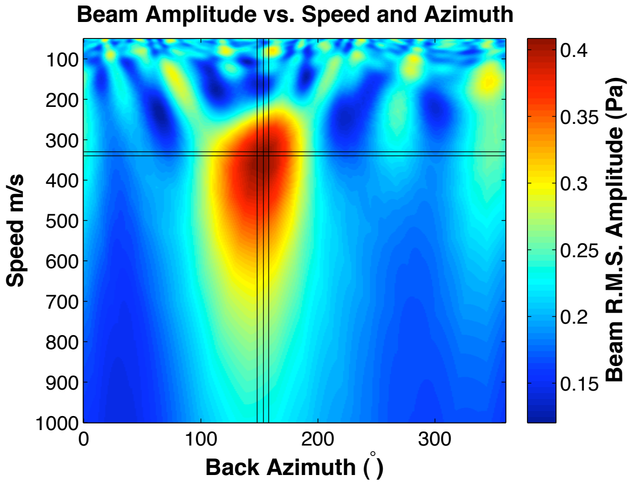

Figure A.2: Time-delay beamformer beampattern for pulse shown in Figure A.1(a) computed by grid search over phase velocity c and azimuth. Vertical black lines indicate upper and lower azimuth bounds ∼148.09° and ∼157.94° of the MSH crater as viewed from CDWR (Figure 2.1), and the azimuth of the 2004-2008 lava dome (∼153.5°). Horizontal black lines indicate sound speeds of 330 m/s and 340 m/s.

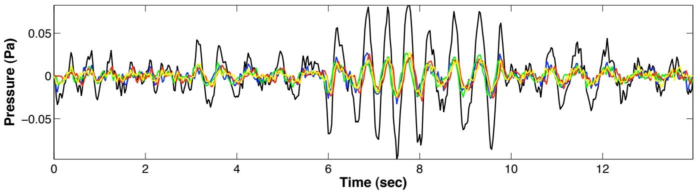

(a) Beam (black) for the data shown in Fig A.1(a). The individual array channels are shown in color.

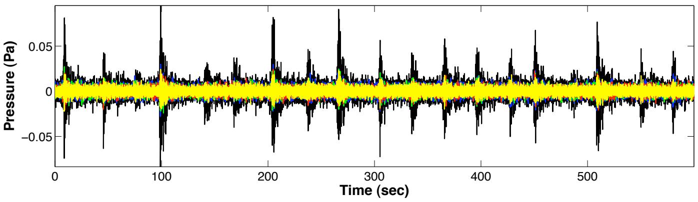

(b) Beam (black) for the data shown in Fig A.1(b). The individual array channels are shown in color.

Figure A.3: Time-delay beamformer.

Trees, 2002]. For each look direction, the dominant signal in that look direction is treated as the desired signal, and a weight vector is calculated that places nulls at the azimuths of all other coherent signals (interferers) [Van Trees, 2002]. The resulting beamwidths are narrower than for the CBF, allowing discrimination between separate sources with smaller angular separation than is possible with the CBF. However, the MVDR beamformer generally fails in the ocean acoustics environment as it does not include a robustness constraint [Cox et al., 1987]. Small errors in the phase of sensors or array element location error of hydrophone arrays leads to large errors with the algorithm. The WNC beamformer was developed to overcome this problem. However, both the MVDR and WNC beamformers are found to perform well for our array on land, as array element location error is small. More details on the theory for this material can be found in Cox et al. [1987] and Van Trees [2002]. We use the 10-minute data segment shown in Figure A.1b for illustration.

A.2.1 Covariance matrix R (CSDM)

We assess the degree to which signals are correlated across all sensors (elements) of the array at specific frequencies using the covariance matrix **R**, or cross-spectral density matrix (CSDM) [Cox et al., 1987; Van Trees, 2002]:

$$\mathbf{R} = \mathbf{x_i}\mathbf{x_i}^H, \tag{A.3}$$

where H denotes the Hermitian operator (complex conjugate transpose), and $\mathbf{x_i}$ is the N-length vector consisting of complex FFT amplitudes of data from all N sensors at the i^{th} frequency bin. In other words, vector $\mathbf{x_i}$ is the i^{th} row of the matrix $\mathbf{X}$ given by:

$$\boldsymbol{X} = \begin{bmatrix} FFT(e_1) & FFT(e_2) & FFT(e_3) & \dots & FFT(e_N) \\ \vdots & \vdots & \vdots & \vdots & \vdots \end{bmatrix}, \tag{A.4}$$

where FFT denotes the Fast Fourier Transform, and $e_n(t)$ is the sensor time series for array element n. We note that coherent signals and interferers would be correlated between the various elements of the array and would lead to non-zero off-diagonal elements in $\mathbf{R}$ while spatially diffuse (incoherent) noise will appear only along the diagonal of $\mathbf{R}$.

In order to gain a robust estimate of the covariance matrix $\mathbf{R}$, a separate estimate is calculated at each of 15, 50 % overlapping time windows of the 10-minute data sequence (Figure A.1b) at the frequency bin of interest (i) at each of 5 frequencies (1, 2, 3, 4, 5 Hz). For each frequency, these 15 estimates of $\mathbf{R}$ are then averaged to form a single average estimate of matrix $\mathbf{R}$. We note that the number of averages (15) used in estimating $\mathbf{R}$ is much greater than the number of array elements ($N = 4$), which should lead to a good estimate of $\mathbf{R}$. We note further that this averaging procedure assumes stationarity of the signals for the 10-minute duration of the data. We believe this is a reasonable assumption given the highly repetitive nature of the volcanic detections, and the truly continuous sources of sound from the ocean and settlements.

A.2.2 Beamformer output

To obtain the beamformer output power P_m at an azimuth θ_m, we use the quadratic form:

$$P_m = \mathbf{W}^H \mathbf{R} \mathbf{W}, \tag{A.5}$$

where $\mathbf{W}$ is the weight vector particular to the beamformer being used (CBF, MVDR, WNC). This choice of weight function $\mathbf{W}$ is the main variable controlling the type of beamformer used, and we introduce the three choices of weight vector $\mathbf{W_{CBF}}$, $\mathbf{W_{MVDR}}$, and $\mathbf{W_{WNC}}$ below.

A.2.3 Conventional (CBF)

For the CBF, we use a unit shading function normalized to give unit signal gain on beamforming (i.e., $\mathbf{w} = 1/N$). This shading function $\mathbf{w}$ is multiplied by

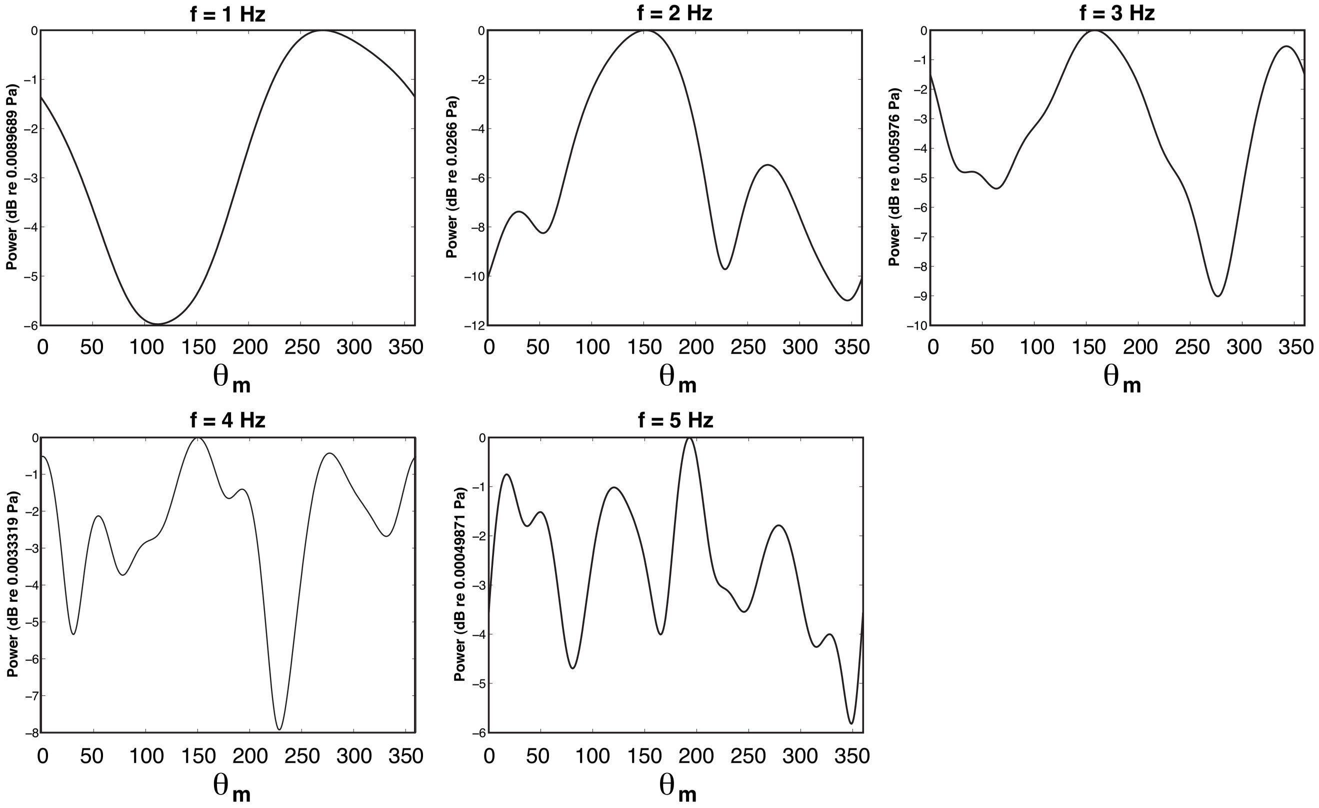

Figure A.4: Conventional beamformer power output at frequencies 1-5 Hz. Power in dB relative to max power.

the vector of phase delays **d** to obtain the weight vector $\mathbf{W_{CBF}}$ for a particular azimuth and frequency f [DeFatta et al., 1988]:

$$\mathbf{W_{CBF}} = \mathbf{w}.\mathbf{d} = \frac{\mathbf{d}}{N}. \tag{A.6}$$

The vector of phase delays **d** is given by:

$$\boldsymbol{d} = \begin{bmatrix} e^{-2\pi j f \tau_{m1}} \\ e^{-2\pi j f \tau_{m2}} \\ \vdots \\ e^{-2\pi j f \tau_{mn}} \end{bmatrix}, \tag{A.7}$$

where τ_{mn} is the time delay for array element n and a beam look direction m, computed as:

$$\tau_{mn} = \frac{\mathbf{E_n}.\mathbf{B_m}}{c}. \tag{A.8}$$

The CBF outputs are shown at various frequencies (f = 1, 2, 3, 4, and 5 Hz) in Figure A.4. We find that the CBF results are generally consistent with those from the PMCC method (Chapter 2, Figures 2.3 and 2.4). For instance, in Figure A.4, at 1 Hz, the CBF power output is maximum at an azimuth of ∼270°, which is consistent with 1 Hz energy from the direction of the Pacific Ocean as observed in the PMCC results (Chapter 2, Figures 2.3 and 2.4). At 2 and 3 Hz, the CBF power output is peaked at ∼153°, which is the direction of MSH. At 4 Hz, peaks are observed at azimuths of ∼153° (MSH), ∼200° (Portland), ∼0°, and ∼270° (unknown sources). At 5 Hz, signal from ∼200° (Portland) is dominant.

A.2.4 Minimum variance distortionless response (MVDR)

For the MVDR beamformer, the data-adaptive weight vector is constructed as [Cox et al., 1987; Van Trees, 2002]:

$$\mathbf{W_{MVDR}} = \frac{\mathbf{R}^{-1}\mathbf{d}}{\mathbf{d}^H\mathbf{R}^{-1}\mathbf{d}}. \tag{A.9}$$

The presence of $\mathbf{R}^{-1}$ in the numerator makes the weight vector data-adaptive, while the denominator achieves normalization in passing the signal through the array with unit signal gain. The MVDR power outputs P_m are shown for frequencies f = 1, 2, 3, 4, and 5 Hz in Figure A.5. The results shown in Figure A.5 are consistent with those shown in Figure A.4. However, in Figure A.5, the beamwidths are narrower, and it is evident that the MVDR beamformer provides better azimuthal resolution than the CBF (Figure A.4). One clear illustration of this is in the results at 3 Hz. Here, two distinct peaks are seen at ∼153° (MSH) and ∼200° (Portland) in the MVDR results of Figure A.5, whereas the CBF only shows one clear peak at ∼153° (Figure A.4). In the CBF case, the signal from ∼200° appears to be obscured by the wide beam of the ∼153° signal.

A.2.5 White Noise Constrained (WNC)

The WNC beamformer is similar to the MVDR beamformer, except that the CSDM matrix $\mathbf{R}$ used in computing the data-adaptive weight vector $\mathbf{W}$ is diagonally loaded with a value ϵ [Cox et al., 1987; Van Trees, 2002]:

$$\mathbf{W}_{\mathbf{WNC}} = \frac{(\mathbf{R} + \epsilon\mathbf{I})^{-1}\mathbf{d}}{\mathbf{d}^H(\mathbf{R} + \epsilon\mathbf{I})^{-1}\mathbf{d}}, \tag{A.10}$$

where $\mathbf{I}$ is the identity matrix. This corresponds to introducing a chosen quantity of uncorrelated (spatially diffuse) noise to the data used in the data-adaptive process. The value of ϵ is selected subject to the constraint:

$$N \geq [G_w = (\mathbf{W}^{\mathbf{H}}_{\mathbf{WNC}}\mathbf{W}_{\mathbf{WNC}})^{-1}] \geq \delta^2, \tag{A.11}$$

where N is the number of array elements ($N = 4$) and here we choose δ^2 values of $0.25N$, $0.5N$, and $0.9N$ (see below). The quantity G_w is the gain against white noise or "white noise gain". It is the improvement in SNR due to beamforming when the noise is spatially white, i.e., uncorrelated from sensor to sensor, and is therefore a measure of the robustness to errors [Cox et al., 1987].

The approach for determining this ϵ satisfying the white noise constraint is as follows:

1. Test G_w according to equation A.11 with $\epsilon = 0$.
2. If the white noise constraint (WNC, equation A.11) is not satisfied, start with ϵ set to 60 dB below the average of the eigenvalues of $\mathbf{R}$, then bracket the desired ϵ by repeating the test of equation A.11 while incrementing ϵ first in steps of 10 dB, then 1 dB, then 0.1 dB.
3. Stop incrementing ϵ if $\epsilon \geq$ the maximum eigenvalue of $\mathbf{R}$ + 30 dB.

In practice this was implemented by using three “while” loops (a block of code that is executed repeatedly only while some boolean condition is true) that progressively increment ϵ until the WNC is satisfied or $\epsilon \geq$ the maximum eigenvalue of $\mathbf{R}$ + 30 dB. The first “while” loop increments in steps of 10 dB. Once this loop is finished, 10 dB is subtracted from ϵ, and then the next “while” loop increments in steps of 1 dB, then 1 dB is subtracted and the third loop increments by 0.1 dB.

The WNC beampower outputs are shown at frequencies $f = 1, 2, 3, 4,$ and 5 Hz in Figure A.6 for the three different values of δ^2. The quantity δ^2 acts as a parameter which can be varied to give the desired degree of adaptation in beamforming. At the low value of $\delta^2 = 0.25N$, diagonal loading (equation A.10) is low, and the WNC adaptive beamformer approaches the MVDR beamformer (Figure A.5), which gives the maximum possible adaptation to the data. For the larger value of $\delta^2 = 0.9N$, the WNC beamformer behavior approaches that of the conventional beamformer (Figure A.4) with no adaptation to the data.

A.2.6 Results

The results are generally consistent with those derived using PMCC (section 2.3.1, Figures 2.3 and 2.4). At 1 Hz, in all three beamformer cases: CBF

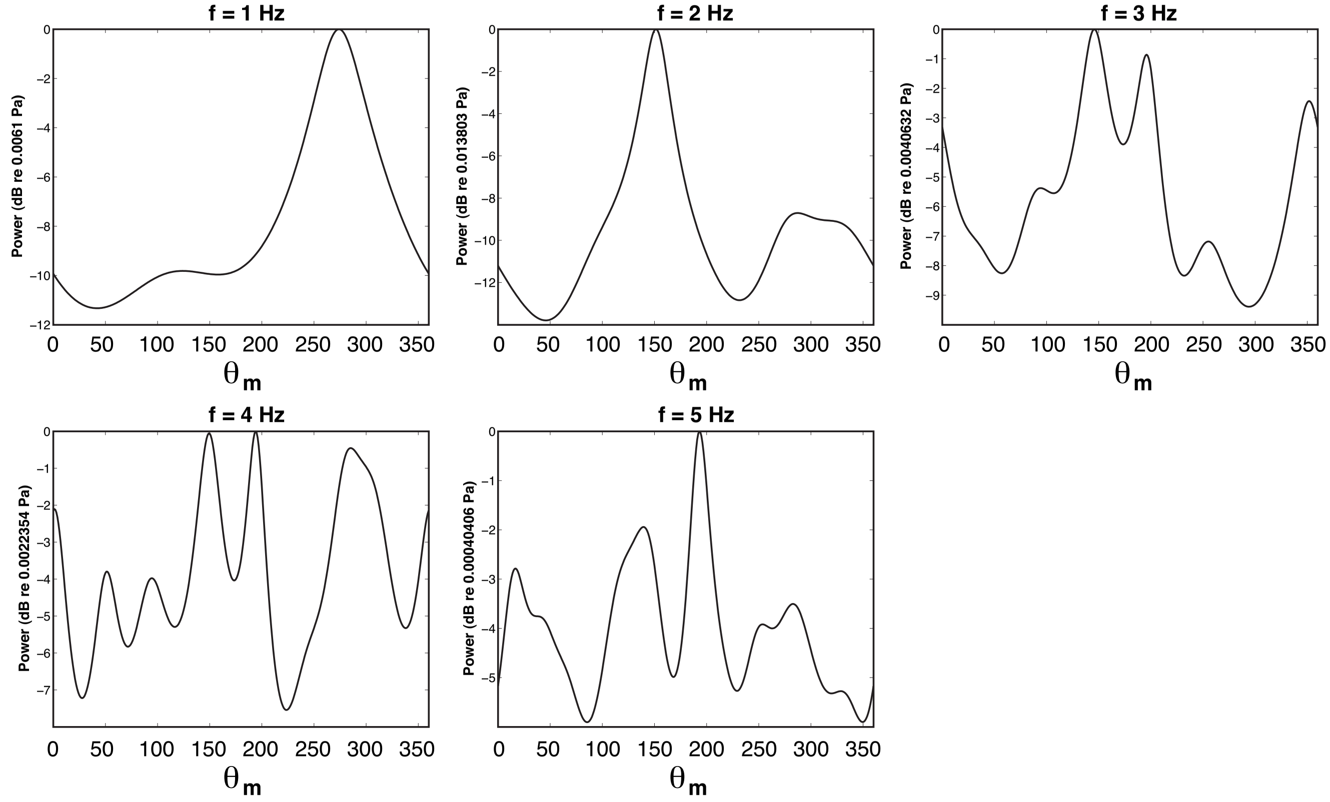

Figure A.5: MVDR beamformer power output at frequencies 1-5 Hz. Note the much narrower beamwidth at 1 Hz for the ocean noise signal at ∼270°, in contrast to the CBF results of Figure A.4. At 2 Hz, signal from MSH (∼153°) is the dominant energy.

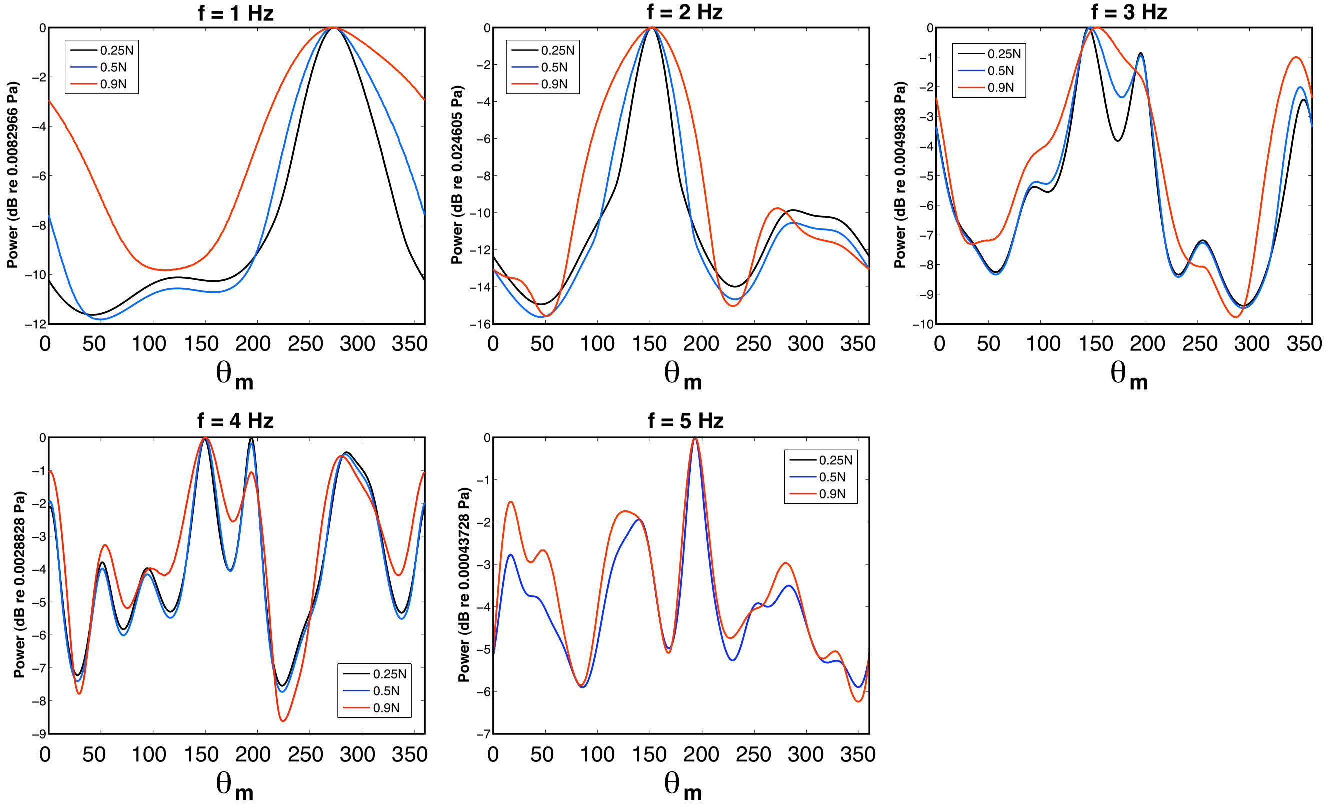

Figure A.6: WNC beamformer power output at frequencies 1-5 Hz, for three values of δ^2: $0.25N$ (black), $0.5N$ (blue), and $0.9N$ (red).

(Figure A.4), MVDR (Figure A.5), and WNC (Figure A.6), there is a strong peak at ∼270°, consistent with the PMCC results (interpreted as ocean infrasound from surf). At 2 Hz, the volcanic signals are dominant, and a very strong peak is observed at ∼153° in all three beamformer cases. At 3 Hz, there is a double peak in beamformer output at ∼153° (MSH) and ∼200° (city of Portland, OR). This indicates that both the volcano and Portland are sources of infrasound at 3 Hz. There is also a peak at ∼350-360° indicating that there is another source of infrasound at that azimuth. Close inspection of the PMCC output (Figures 2.3 and 2.4) shows that PMCC also detects signals at ∼330° in the 3 Hz band, but not at ∼350-360°. At 4 Hz, the MVDR and WNC adaptive beamformers show all four signals (∼153°, ∼200°, ∼270°, and ∼350°) at approximately the same amplitude, indicating that all four sources have energy at roughly the same power level in the 4 Hz band. At 3 and 4 Hz, the CBF lacks the angular resolution required to differentiate between the signal at ∼153° and the signal at ∼200°, whereas the adaptive MVDR and WNC beamformer outputs show two distinct peaks. At 5 Hz, for all three beamformers, the Portland infrasound at ∼200° has the strongest power level.

A.2.7 Summary of adaptive beamforming

The MVDR and WNC adaptive beamformers perform effectively for the MSH infrasound array data in discriminating signals of interest from incoherent and coherent ambient noise. In general, the results are consistent with those obtained by the PMCC method. We note that, in practice, the MVDR beamformer is not usually used in ocean acoustics, as Array Element Location (AEL) error renders the MVDR beamformer ineffective [Cox et al., 1987]. A surprise finding in this study was that the MVDR beamformer performed well for this data set, probably as a result of the very accurately known (and non-moving) station coordinates. In principle, the adaptive beamforming methods described in this section could be applied to long-duration data segments by dividing the data into a series of window lengths (as is done in PMCC), and conducting grid searches over frequency, azimuth, and time. These methods provide some attractive advantages over PMCC for infrasound data processing, such as 1) beam patterns and uncertainty in angular resolution could be more quantitatively addressed than with PMCC, 2) frequency space is explored precisely by using individual frequency bins of the FFT, whereas PMCC uses selective narrow-band-pass filtering (with potential for energy leakage), 3) PMCC essentially computes a conventional beam, whereas adaptive beamforming techniques could provide better angular resolution and allow the separation of infrasonic sources with a smaller incident azimuth separation. Nevertheless, for simplicity, we use PMCC in conjunction with time-delay beamforming throughout the remainder of this dissertation.

Acknowledgments

This work was undertaken as an assignment for a class on array processing taught by Bill Hodgkiss.

References

Aki, K., Fehler, M., and Das, S., 1977: Source mechanism of volcanic tremor: Fluid driven crack models and their application to the 1963 Kilauea eruption. *J. Volcanol. Geotherm. Res.*, **2**, 259–287.

Aki, K., and Koyanagi, R., 1981: Deep volcanic tremor and magma ascent mechanism under Kilauea, Hawaii. *J. Geophys. Res.*, **86**, 7095–7109.

Aki, K., and Richards, P. G., 2002: *Quantitative Seismology.* University Science Books, second edition.

Almendros, J., Chouet, B., and Dawson, P., 2001: Spatial extent of a hydrothermal system at Kilauea Volcano, Hawaii, determined from array analyses of shallow long-period seismicity 2. Results. *J. Geophys. Res.*, **106**, 13581–13597.

Arellano, S., and Hall, M., 2006: Velocidades de emisión de bombas expulsadas por el Volcán Tungurahua el 16 - 17 de Agosto de 2006. *Resúmenes extendidos de las 6th Jornadas en Ciencias de la Tierra, EPN - DG, Quito - Ecuador*, 185–188.

Arrowsmith, S. J., and Hedlin, M. A. H., 2005: Observations of infrasound from surf in southern California. *Geophys. Res. Lett.*, **32**(9), L09810. doi: 10.1029/2005GL022761.

Aster, R., Mah, S., Kyle, P., McIntosh, W., Dunbar, N., Johnson, J., Ruiz, M., and McNamara, S., 2003: Very long period oscillations at Mount Erebus Volcano. *J. Geophys. Res.*, **108**, 2522. doi:10.1029/2002JB002101.

Aster, R., McIntosh, W., Kyle, P., Esser, R., and Bartel, B., 2004: Real-time data received from Mount Erebus volcano, Antarctica. *EOS Trans. Am. Geophys. Union*, **85:97100-1**.

Bailly, C., and Bogey, C., 2004: Contributions of computational aeroacoustics to jet noise research and prediction. *International Journal of Computational Fluid Dynamics*, **18**(6), 481491.

Barba, D., Arellano, S., Ramón, P., Mothes, P., Alvarado, A., Ruiz, G., and Troncoso, L., 2006: Cronología de los Eventos Eruptivos de Julio y Agosto del 2006 del Volcan Tungurahua. *Resúmenes extendidos de las 6th Jornadas en Ciencias de la Tierra, EPN - DG, Quito - Ecuador*, 177 – 180.

Bass, H. E., 1991: Atmospheric acoustics. In *Encyclopedia of Applied Physics*, volume 2, 145–179. VCH, New York.

Bass, H. E., Bolen, L. N., Cress, D., Lundien, J., and Flohr, M., 1980: Coupling of airborne sound into the Earth: Frequency dependence. *J. Acoust. Soc. Am.*, **67**(5), 1502–1506.

Battaglia, J., Aki, K., and Ferrazzini, V., 2005: Location of tremor sources and estimation of lava output using tremor source amplitude on the Piton de la Fournaise volcano: 1. Location of tremor sources. *J. Volcanol. Geotherm. Res.*, **147**.

Battaglia, J., Got, J.-L., and Okubo, P., 2003: Location of long-period events below kilauea volcano using seismic amplitudes and accurate relative relocation. *J. Geophys. Res.*, **108**(B12), 2553. doi:10.1029/2003JB002517.

Bedard, A. J., and Georges, T. M., 2000: Atmospheric Infrasound. *Physics Today*, **53(3)**, 32–37.

Bedrosian, P. A., Burgess, M., and Hotovec, A., 2008: Groundwater Hydrology within the crater of Mount St. Helens from geophysical constraints. *Eos Trans. AGU*, **89**(53), Fall Meet. Suppl., Abstract V43E–2191.

Bedrosian, P. A., Unsworth, M. J., and Johnston, M. J. S., 2007: Hydrothermal circulation at Mount St. Helens determined by self-potential measurements. *J. Volcanol. Geotherm. Res.*, **160**(1-2), 137–146.

Benioff, H., Ewing, M., and Press, F., 1951: Sound waves in the atmosphere generated by a small earthquake. *Proc. Natl. Acad. Sci. U.S.A.*, **37**(9), 600–603.

Benz, H. M., Chouet, B. A., Dawson, P. B., Lahr, J. C., Page, R. A., and Hole, J. A., 1996: Three-dimensional P and S wave velocity structure of Redoubt Volcano, Alaska. *J. Geophys. Res.*, **101**, 8111–8128.

Berenger, J. P., 1996: Three-dimensional perfectly matched layer for the absorption of electromagnetic waves. *J. Comput. Phys.*, **127**(2), 363–379.

Biot, M. A., 1952: Propagation of elastic waves in a cylindrical bore containing a fluid. *Journal of Applied Physics*, **23**, 997–1005.

Bolt, B. A., 1964: Seismic air waves from the great 1964 Alaskan earthquake. *Nature*, **202**(493), 1095–1096.

Braun, T., and Ripepe, M., 1993: Interaction of seismic and air waves as recorded at Stromboli volcano. *Geophys. Res. Lett.*, **20**, 65–68.

Brekhovskikh, L. M., 1980: *Waves in Layered Media.* Academic, New York, second edition.

Buckingham, M. J., and Garces, M. A., 1996: Canonical model of volcano acoustics. *J. Geophys. Res.*, **101**, 8129–8151.

Burlini, L., Vinciguerra, S., Di Toro, G., De Natale, G., Meredith, P., and Burg, J.-P., 2007: Seismicity preceding volcanic eruptions: New experimental insights. *Geology*, **35**, 183–186.

Busse, F. H., Monkewitz, P. A., and Hellweg, M., 2005: Are harmonic tremors self-excited thermoacoustic oscillations? *Earth Planet. Sci. Lett.*, **240**, 302–306.

Campus, P., 2006: Monitoring volcanic eruptions with the IMS infrasound network. *InfraMatics (September)*, **15**, 6–12.

Cansi, Y., 1995: An automatic seismic event processing for detection and location: The P.M.C.C. method. *Geophys. Res. Lett.*, **22**(9), 1021–1024.

Cansi, Y., and Klinger, Y., 1997: An automated data processing method for mini-arrays. *Newsletter of the European-Mediterranean Seismological Centre.*, **11**, 2–4.

Caplan-Auerbach, J., and Petersen, T., 2005: Repeating coupled earthquakes at Shishaldin Volcano, Alaska. *J. Volcanol. Geotherm. Res.*, **145**(1-2), 151–172.

Cashman, K. V., Thornber, C. R., and Pallister, J. S., 2008: From dome to dust: Shallow crystallization and fragmentation of conduit magma during the 2004-2006 dome extrusion at Mount St. Helens, Washington. In *A Volcano Rekindled: The Renewed Eruption of Mount St. Helens, 2004-2006*, editors D. R. Sherrod, W. E. Scott, and P. H. Stauffer. U.S. Geological Survey Professional Paper 1750.

Chanaud, R. C., and Powell, A., 1965: Some experiments concerning the Hole and Ring Tone. *J. Acoust. Soc. Am.*, **37(5)**, 902–911.

Chojnicki, K., Clarke, A. B., and Phillips, J. C., 2006: A shock-tube investigation of the dynamics of gas-particle mixtures: Implications for explosive volcanic eruptions. *Geophys. Res. Lett.*, **33**, L15309. doi:10.1029/2006GL026414.

Chouet, B., 1979: Sources of seismic events in the cooling lava lake of Kilauea Iki, Hawaii. *J. Geophys. Res.*, **84**, 2315–2330.

Chouet, B., 1981: Ground motion in the near field of a fluid-driven crack and its interpretation in the study of shallow volcanic tremor. *J. Geophys. Res.*, **86**, 5985–6016.

Chouet, B., 1982: Free surface displacements in the near field of a tensile crack expanding in three dimensions. *J. Geophys. Res.*, **87**, 3868–3872.

Chouet, B., 1983: Ground motion near an expanding preexisting crack. *J. Volcanol. Geotherm. Res.*, **19**, 367–379.

Chouet, B., 1985: Excitation of a buried magmatic pipe: A seismic source model for volcanic tremor. *J. Geophys. Res.*, **90**, 1881–1893.

Chouet, B., 1986: Dynamics of a fluid-driven crack in three dimensions by the finite difference method. *J. Geophys. Res.*, **91**, p13967–13992.

Chouet, B., 1988: Resonance of a fluid-driven crack: radiation properties and implications for the source of long-period events and harmonic tremor. *J. Geophys. Res.*, **93**, p4375–4400.

Chouet, B., 2003: Volcano Seismology. *Pure Appl. Geophys.*, **160**, 739–788.

Chouet, B., 2009: Volcanoes, Non-linear processes in. In *Encyclopedia of Complexity and System Science*, editor R. Meyer, 9872–9899. Springer.

Chouet, B., Dawson, P., and Arciniega-Ceballos, A., 2005: Source mechanism of Vulcanian degassing at Popocatepetl Volcano, Mexico, determined from waveform inversions of very long period signals. *J. Geophys. Res.*, **110**, B070301. doi:10.1029/2004JB003524.

Chouet, B., Dawson, P., and Martini, M., 2008: Shallow-conduit dynamics at Stromboli Volcano, Italy, imaged from waveform inversions. In *Fluid Motions in Volcanic Conduits: A Source of Seismic and Acoustic Signals*, editors S. J. Lane, and J. S. Gilbert, volume 307, 57–84. Geological Society, London, Special Publications.

Chouet, B., Dawson, P., Ohminato, T., Martini, M., Saccorotti, G., Giudicepietro, F., Luca, G. D., Milana, G., and Scarpa, R., 2003: Source mechanisms of explosions at Stromboli Volcano, Italy, determined from moment tensor inversions of very-long-period data. *J. Geophys. Res.*, **108**(B1), 2019. doi: 10.1029/2002JB001919.

Chouet, B., and Julian, J. R., 1985: Dynamics of an expanding fluid-filled crack. *J. Geophys. Res.*, **90**, 11187–11198.

Chouet, B. A., 1992: A seismic model for the source of long-period events and harmonic tremor. In *Volcanic Seismology: IAVCEI Proceedings in Volcanology 3*, editors P. Gasparini, and R. Scarpa, 133–156. Springer-Verlag.

Chouet, B. A., 1996a: Long-period volcano seismicity: its source and use in eruption forecasting. *Nature*, **380**, 309–316.

Chouet, B. A., 1996b: New methods and future trends in seismological volcano monitoring. In *Volcanic Seismology: IAVCEI Proceedings in Volcanology 3*, editors R. Scarpa, and R. Tilling, 23–97. Springer-Verlag.

Chouet, B. A., Page, R. A., Stephens, C. D., Lahr, J. C., and Powers, J. A., 1994: Precursory swarms of long-period events at Redoubt Volcano (1989-1990), Alaska: Their origin and use as a forecasting tool. *J. Volcanol. Geotherm. Res.*, **62**, 95–135.

Christiansen, R. L., and Peterson, D. W., 1981: Chronology of the 1980 Eruptive Activity. In *The 1980 eruptions of Mount St. Helens, Washington*, editors P. Lipman, and D. Mullineaux, 17–30. USGS Professional Paper 1250.

Christie, D. R., 2006: Wind noise reuction at infrasound monitoring stations. *Infrasound Technology Workshop, Fairbanks.*

Clynne, M., Calvert, A., Wolfe, E., Evarts, R., Fleck, R., and Lanphere, M., 2008: The Pleistocene eruptive history of Mount St. Helens, Washington – From 300,000 to 12,800 Years Ago. In *A Volcano Rekindled: The Renewed Eruption of Mount St. Helens, 2004-2006*, editors D. R. Sherrod, W. E. Scott, and P. H. Stauffer. U.S. Geological Survey Professional Paper 1750.

Commander, K. W., and Prosperetti, A., 1989: Linear pressure waves in bubbly liquids: Comparison between theory and experiments. *J. Acoust. Soc. Am.*, **85(2)**, 732–746.

Cox, H., Zeskind, R. M., and M.M.Owen, 1987: Robust adaptive beamforming. *IEEE Transactions on Acoustics, Speech, and Signal Processing*, **ASSP-35(10)**, 1365–1376.

Crandell, D. R., Mullineaux, D. R., and Meyer, R., 1975: Mount St. Helens volcano: recent and future behavior. *Science*, **187**, 438–441.

Crow, S. C., and Champagne, F. H., 1971: Orderly structure in jet turbulence. *J. Fluid Mech.*, **48**, 547–591.

D'Auria, L., 2006: Numerical modelling of gas slugs rising in basaltic volcanic conduits: Inferences on Very-Long-Period event generation. *The Physics of Fluid Oscillations in Volcanic Systems workshop, Lancaster, UK.*

D'Auria, L., and Martini, M., 2007: 3-D finite difference modeling of the seismo-acoustic wave field. *Seismol. Res. Lett.*, **59**, 2.

D'Auria, L., and Martini, M., 2009: Slug flow: modeling in a conduit and associated elastic radiation. In *Encyclopedia of Complexity and System Science*, editor R. Meyer, 8153–8168. Springer.

Dawson, P. B., Chouet, B. A., Okubo, P. G., Villasenor, A., and Benz, H. M., 1999: Three-dimensional Velocity Structure of Kilauea Caldera, Hawaii. *Geophys. Res. Lett.*, **26**, 2805–2808.

de Groot-Hedlin, C., 2004: Criteria for discretization of seafloor bathymetry when using a stairstep approximation: Application to computation of T-phase seismograms. *J. Acoust. Soc. Am.*, **115**(3), 1103–1113.

DeFatta, D., Lucas, J., and Hodgkiss, W., 1988: *Digital Signal Processing: A System Design Approach.* NY. John Wiley.

Delclos, C., Blanc, E., Broche, P., Glangeaud, F., and Lacoume, J. L., 1990: Processing and interpretation of microbarograph signals generated by the explosion of Mount St. Helens. *J. Geophys. Res.*, **95**, 5485–5494.

Delprat, N., 2006: Rossiter's formula: A simple spectral model for a complex amplitude modulation process? *Physics of Fluids*, **18**, 071703.

Dibble, R. R., 1989: Infrasonic recordings of Strombolian Eruptions of Erebus, Antarctica, March - December 1984, Covering the jump in activity on 13 September 1984. In *Volcanic Hazards, Assessment and Monitoring*, editor J. Latter, 536–553. Springer, New York.

Drob, D. P., Picone, J. M., and Garces, M., 2003: Global morphology of infrasound propagation. *J. Geophys. Res.*, **108**, 4680–4691.

Dzurisin, D., Vallance, J., Gerlach, T., Moran, S., and Malone, S., 2005: Mount St. Helens Reawakens. *EOS*, **86(3)**, 25–29.

Edmonds, M., and Gerlach, T. M., 2007: Vapor segregation and loss in basaltic melts. *Geology*, **35**, 751–754.

Embleton, T. F. W., 1996: Tutorial on sound propagation outdoors. *J. Acoust. Soc. Am.*, **100**(1), 31–48.

Evers, L. G., 2008: *The inaudible symphony: on the detection and source identification of atmospheric infrasound.* PhD thesis, Delft University of Technology, The Netherlands.

Fairfield, C., 1980: OMSI sound project, the acoustic effects of the Mount St. Helens eruption on May 18, 1980. *Or. Geol.*, **42(12)**, 200–202.

Fee, D., and Garces, M., 2007: Infrasonic tremor in the diffraction zone. *Geophys. Res. Lett.*, **34**(16). doi:10.1029/2007GL030616.

Fee, D., Garces, M., and Matoza, R., 2007: Characterization of Explosion Signals from Tungurahua Volcano. *Infrasound Technology Workshop, Tokyo.*

Fee, D., Garces, M., and Patrick, M., 2009: Infrasonic harmonic tremor and explosions from Halema‘uma‘u Crater, Kilauea. *J. Volcanol. Geotherm. Res.*, in prep.

Fehler, M., 1983: Observations of volcanic tremor at Mount St. Helens Volcano. *J. Geophys. Res.*, **88**, 3476–3484.

Fehler, M., and Chouet, B., 1982: Operation of a digital seismic network on Mount St. Helens volcano and observations of long period seismic events that originate under the volcano. *Geophys. Res. Lett.*, **9**, 1017–1020.

Ferrazzini, V., and Aki, K., 1987: Slow waves trapped in a fluid-filled infinite crack: Implication for volcanic tremor. *J. Geophys. Res.*, **92**, 9215–9223.

Ferrick, M. G., and Qamar, A., 1982: Source mechanism of volcanic tremor. *J. Geophys. Res.*, **87**, 8675–8683.

Festa, G., and Nielsen, S., 2003: PML absorbing boundaries. *Bull. Seismol. Soc. Am.*, **93**(2), 891–903.

Firstov, P. P., and Kravchenko, N. M., 1996: Estimation of the amount of explosive gas released in volcanic eruptions using air waves. *Volc. Seis.*, **17**, 547–560.

Fletcher, N. H., 1999: The nonlinear physics of musical instruments. *Rep. Prog. Phys.*, **62**, 723764.

Fletcher, N. H., and Rossing, T. D., 2008: *The Physics of Musical Instruments.* Springer, second edition.

Garces, M., 1997: On the volcanic waveguide. *J. Geophys. Res.*, **102**(B10), 22547–22564.

Garces, M., Aucan, J., Fee, D., Caron, P., Merrifield, M., Gibson, R., Bhattacharyya, J., and Shah, S., 2006: Infrasound from large surf. *Geophys. Res. Lett.*, **33**, L05611. doi:10.1029/2005GL025085.

Garces, M., Fee, D., McCormack, D., Servranckx, R., Bass, H., Hetzer, C., Hedlin, M., Matoza, R., and Yepes, H., 2008: Prototype ASHE volcano monitoring system captures the acoustic fingerprint of stratospheric ash injection. *Eos Trans. AGU*, **89**(40), 377–379.

Garces, M., Harris, A., Hetzer, C., Johnson, J., Rowland, S., Marchetti, E., and Okubo, P., 2003: Infrasonic tremor observed at Kilauea Volcano, Hawaii. *Geophys. Res. Lett.*, **30**(20). doi:10.1029/2003GL018038.

Garces, M., Iguchi, M., Ishihara, K., Morrissey, M., Sudo, Y., and Tsutsui, T., 1999: Infrasonic precursors to a Vulcanian eruption at Sakurajima Volcano, Japan. *Geophys. Res. Lett.*, **26**, 2537–2540.

Garces, M., and Le Pichon, A., 2009: Infrasound: Applications for earthquakes, tsunamis and volcanoes. In *Encyclopedia of Complexity and Systems Science*, editor W. H. K. Lee. Springer.

Garces, M. A., 1995: The Acoustics of Volcanic Explosions. *Ph.D. Thesis, Scripps Institution of Oceanography, University of California, San Diego.*

Garces, M. A., 2000: Theory of acoustic propagation in a multi-phase stratified liquid flowing within an elastic-walled conduit of varying cross-sectional area. *J. Volcanol. Geotherm. Res.*, **101**, 1–17.

Garces, M. A., Fee, D., and Matoza, R. S., submitted: Volcano acoustics. In *Modeling Volcanic Processes*, editors S. Fagents, T. Gregg, and R. Lopes. Cambridge University Press.

Garces, M. A., Hagerty, M. T., and Schwartz, S. Y., 1998: Magma acoustics and time-varying melt properties at Arenal Volcano, Costa Rica. *Geophys. Res. Lett.*, **25**, 2293–2296.

Garces, M. A., and Hansen, R. A., 1998: Waveform analysis of seismoacoustic signals radiated during the Fall 1996 eruption of Pavlof volcano, Alaska. *Geophys. Res. Lett.*, **25**, 1051–1054.

Garces, M. A., Hansen, R. A., and Lindquist, K. G., 1998: Traveltimes for infrasonic waves propagating in a stratified atmosphere. *Geophys. J. Int.*, **135**(1), 255–263.

Garces, M. A., and McNutt, S. R., 1997: Theory of the airborne sound field generated in a resonant magma conduit. *J. Volcanol. Geotherm. Res.*, **78**, 155–178.

Garces, M. A., McNutt, S. R., Hansen, R. A., and Eichelberger, J. C., 2000: Application of wave-theoretical seismoacoustic models to the interpretation of explosion and eruption tremor signals radiated by Pavlof volcano, Alaska. *J. Geophys. Res.*, **105**, 3039–3058.

Gasparini, P., Scarpa, R., and Aki, K., 1992: Preface. In *Monitoring and Mitigation of Volcano Hazards*, editors P. Gasparini, R. Scarpa, and K. Aki, v–vii. Springer-Verlag.

Gerlach, T. M., McGee, K. A., and Doukas, M. P., 2008: Emission rates of CO2, SO2, and H2S, scrubbing, and preeruption excess volatiles at Mount St. Helens. In *A Volcano Rekindled: The Renewed Eruption of Mount St. Helens, 2004-2006*, editors D. R. Sherrod, W. E. Scott, and P. H. Stauffer. U.S. Geological Survey Professional Paper 1750.

Gerst, A., Hort, M., and Kyle, P. R., 2006: The first second of a strombolian eruption. *The Physics of Fluid Oscillations in Volcanic Systems workshop, Lancaster, UK.*

Gerst, A., Hort, M., Kyle, P. R., and Voege, M., 2008a: A Technique to Measure Energy Partitioning and Absolute Gas Pressures of Strombolian Explosions Using Doppler Radar at Erebus Volcano. *Eos Trans. AGU*, **89**(53), Fall Meet. Suppl., Abstract V51E–2076.

Gerst, A., Hort, M., Kyle, P. R., and Voge, M., 2008b: 4D velocity of Strombolian eruptions and man-made explosions derived from multiple Doppler radar instruments. *J. Volcanol. Geotherm. Res.*, **177**, 648–660.

Gil Cruz, F., and Chouet, B. A., 1997: Long-period events, the most characteristic seismicity accompanying the emplacement and extrusion of a lava dome in Galeras Volcano, Colombia, in 1991. *J. Volcanol. Geotherm. Res.*, **77**, 121–158.

Godin, O. A., 2006: Anomalous transparency of water-air interface for low-frequency sound. *Physical Review Letters*, **97**, 164301.

Godin, O. A., 2007: Transmission of low-frequency sound through the water-to-air interface. *Acoustical Physics*, **53**(3), 305–312.

Goerke, V. H., Young, J. M., and Cook, R. K., 1965: Infrasonic observations of the May 16, 1963, volcanic explosion on the island of Bali. *J. Geophys. Res.*, **70**, 6017–6022.

Gorshkov, G. S., 1960: Determination of the explosion energy in some volcanoes according to barograms. *Bulletin of Volcanology*, **23**, 141–144.

Goto, A., 1999: A new model for volcanic earthquakes at Unzen Volcano: melt rupture model. *Geophys. Res. Lett.*, **26**, 2541–2544.

Graves, R. W., 1996: Simulating seismic wave propagation in 3D elastic media using staggered-grid finite differences. *Bull. Seismol. Soc. Am.*, **86**(4), 1091–1106.

Greeley, R., 1987: The role of lava tubes in Hawaiian volcanoes. In *Volcanism in Hawaii*, editors R. W. Decker, T. L. Wright, and P. H. Stauffer, 1589–1602. U.S. Geological Survey Professional Paper 1350.

Green, D. N., and Neuberg, J., 2005: Seismic and infrasonic signals associated with an unusual collapse event at the Soufriere Hills volcano, Montserrat. *Geophys. Res. Lett.*, **32**, L07308. doi:10.1029/2004GL022265.

Green, D. N., and Neuberg, J., 2006: Waveform classification of volcanic low-frequency earthquake swarms and its implication at Soufriere Hills Volcano, Montserrat. *J. Volcanol. Geotherm. Res.*, **153**, 51–63.

Grover, F. H., 1971: Experimental noise reducers for an active microbarograph array. *Geophys. J. R. astr. Soc.*, **26**, 41–52.

Hagerty, M. T., Schwartz, S. Y., Garces, M. A., and Protti, M., 2000: Analysis of seismic and acoustic observations at Arenal Volcano, Costa Rica, 1995-1997. *J. Volcanol. Geotherm. Res.*, **101**, 27–65.

Hahn, T. R., Berger, T. K., and Buckingham, M. J., 2003: Acoustic resonances in the bubble plume formed by a plunging water jet. *Proc. R. Soc. Lond. A*, **459**, 1751–1782.

Harrington, R. M., and Brodsky, E. E., 2007: Volcanic hybrid earthquakes that are brittle-failure events. *Geophys. Res. Lett.*, **34**(6). doi:10.1029/2006GL028714.

Harris, A., and Ripepe, M., 2007: Synergy of multiple geophysical approaches to unravel explosive eruption conduit and source dynamics – A case study from Stromboli. *Chemie der Erde*, **67**, 1–35.

Hedlin, M. A. H., Alcoverro, B., and D'Spain, G., 2003: Evaluation of rosette infrasonic noise-reducing spatial filters. *J. Acoust. Soc. Am.*, **114**, 1807–1820.

Hedlin, M. A. H., Garces, M., Bass, H., Hayward, C., Herrin, G., Olson, J., and Wilson, C., 2002: Listening to the secret sounds of Earth's atmosphere. *EOS*, **83**, 557–565.

Heliker, C., and Mattox, T. N., 2003: The first two decades of the Pu‘u ‘Ō‘ō-Kūpaianaha Eruption: Chronology and selected bibliography. In *The Pu‘u ‘O‘o-Kupaianaha Eruption of Kilauea Volcano, Hawai‘i: The First 20 Years*, editors C. Heliker, D. Swanson, and T. Takahashi, 1–28. U.S. Geological Survey Professional Paper 1676.

Hellweg, M., 2000: Physical models for the source of Lascar's harmonic tremor. *J. Volcanol. Geotherm. Res.*, **101**, 183–198.

Helz, R. T., Heliker, C., Hon, K., and Mangan, M., 2003: Thermal efficiency of lava tubes in the Puʻu ʻŌʻō-Kūpaianaha Eruption. In *The Puʻu ʻOʻo-Kupaianaha Eruption of Kilauea Volcano, Hawaiʻi: The First 20 Years*, editors C. Heliker, D. Swanson, and T. Takahashi, 105–120. U.S. Geological Survey Professional Paper 1676.

Hetzer, C., and Garces, M., 2003: Coherent ambient noise field at IMS infrasound stations I56US, I57US, I59US, I24FR, and I52GB. *ISLA report*.

Hickey, C. J., and Sabatier, J. M., 1997: Measurements of two types of dilatational waves in an air-filled unconsolidated sand. *J. Acoust. Soc. Am.*, **102**(1), 128–136.

Hidayat, D., Chouet, B., Voight, B., Dawson, P., and Ratdomopurbo, A., 2002: Source mechanism of very-long-period signals accompanying dome growth activity at Merapi volcano, Indonesia. *Geophys. Res. Lett.*, **29**(23).

Hirschberg, A., Bruggeman, J. C., Wijnands, A. P. J., and Smits, N., 1989: The "whistler nozzle" and horn as aero-acoustic sound sources in pipe systems. *ACUSTICA*, **68**, 157–160.

Howe, M. S., 1998: *Acoustics of Fluid-Structure Interactions.* Cambridge University Press.

Hussain, A. K. M. F., and Hasan, M. A. Z., 1983: The 'whistler-nozzle' phenomenon. *J. Fluid Mech.*, **134**, 431–458.

Ichihara, M., and Kameda, M., 2004: Propagation of acoustic waves in a visco-elastic two-phase system: influences of the liquid viscosity and the internal diffusion. *J. Volcanol. Geotherm. Res.*, **137**(1-3), 73–91.

Ichihara, M., Ripepe, M., Goto, A., Oshima, H., Aoyama, H., Iguchi, M., Tanaka, K., and Taniguchi, H., 2009: Airwaves generated by an underwater explosion: Implications for volcanic infrasound. *J. Geophys. Res.*, **114**, B03210. doi: 10.1029/2008JB005792.

Iguchi, M., and Ishihara, K., 1990: Comparison of earthquakes and air-shocks accompanied with explosive eruptions at Sakurajima and Suwanosejima volcanoes. *Annuals. Disas. Prev. Res. Inst. Kyoto Univ.*, **33B-1**, 1–11 (in Japanese).

Iverson, R. M., Dzurisin, D., Gardner, C. A., Gerlach, T. M., LaHusen, R. G., Lisowski, M., Major, J. J., Malone, S. D., Messerich, J. A., Moran, S. C., Pallister, J. S., Qamar, A. I., Schilling, S. P., and Vallance, J. W., 2006: Dynamics of seismogenic volcanic extrusion at Mount St. Helens in 2004-05. *Nature*, **444**, 439–443.

Jagger, T. A., 1920: Seismometric investigations of the Hawaiian lava column. *Bull. Seism. Soc. Am.*, **6 (4)**, 204.

James, M. R., Lane, S. J., Chouet, B., and Gilbert, J. S., 2004: Pressure changes associated with the ascent and bursting of gas slugs in liquid-filled vertical and inclined conduits. *J. Volcanol. Geotherm. Res.*, **129**, 61–82.

James, M. R., Lane, S. J., and Chouet, B. A., 2006: Gas slug ascent through changes in conduit diameter: Laboratory insights into a volcano-seismic source process in low-viscosity magmas. *J. Geophys. Res.*, **111**, B05201. doi: 10.1029/2005JB003718.

Johnson, J., Aster, R., Jones, K. R., Kyle, P., and McIntosh, B., 2008: Acoustic source characterization of impulsive Strombolian eruptions from the Mount Erebus lava lake. *J. Volcanol. Geotherm. Res.*, **177(3)**, 673–686.

Johnson, J. B., 2003: Generation and propagation of infrasonic airwaves from volcanic explosions. *J. Volcanol. Geotherm. Res.*, **121**, 1–14.

Johnson, J. B., 2007: On the relation between infrasound, seismicity, and small pyroclastic explosions at Karymsky Volcano. *J. Geophys. Res.*, **112**, B08203. doi:10.1029/2006JB004654.

Johnson, J. B., and Aster, R. C., 2005: Relative partitioning of acoustic and seismic energy during Strombolian eruptions. *J. Volcanol. Geotherm. Res.*, **148**, 334–354.

Johnson, J. B., Aster, R. C., and Kyle, P. R., 2004: Volcanic eruptions observed with infrasound. *Geophys. Res. Lett.*, **31**, L14606. doi:10.1029/2004GL020020.

Johnson, J. B., Aster, R. C., Ruiz, M. C., Malone, S. D., McChesney, P. J., Lees, J. M., and Kyle, P. R., 2003: Interpretation and utility of infrasonic records from erupting volcanoes. *J. Volcanol. Geotherm. Res.*, **121**, 15–63.

Johnson, J. B., and Lees, J. M., 2000: Plugs and chugs - seismic and acoustic observations of degassing explosions at Karymsky, Russia and Sangay, Ecuador. *J. Volcanol. Geotherm. Res.*, **101**, 67–82.

Johnson, J. B., Lees, J. M., and Yepes, H., 2006: Volcanic eruptions, lightning, and a waterfall: Differentiating the menagerie of infrasound in the Ecuadorian jungle. *Geophys. Res. Lett.*, **33**, L06308. doi:10.1029/2005GL025515.

Johnson, J. B., Ruiz, M. C., Lees, J. M., and Ramon, P., 2005: Poor scaling between elastic energy release and eruption intensity at Tungurahua Volcano, Ecuador. *Geophys. Res. Lett.*, **32**, L15304. doi:10.1029/2005GL022847.

Jones, K. R., Johnson, J. B., Aster, R., Kyle, P. R., and McIntosh, W., 2008: Infrasonic tracking of large bubble bursts and ash venting at Erebus Volcano, Antarctica. *J. Volcanol. Geotherm. Res.*, **177**, 661–672.

Julian, B. R., 1994: Volcanic tremor: Nonlinear excitation by fluid flow. *J. Geophys. Res.*, **99**, 11859–11877.

Kamo, K., Ishihara, K., and Tahira, M., 1994: Infrasonic and seismic detection of explosive eruptions at Sakurajima volcano, Japan, and the PEGASAS-VE early-warning system. In *Proceedings of the First International Symposium on Volcanic Ash and Aviation Safety*, 357–365. U.S. Geological Survey Bulletin 2047.

Kanamori, H., and Given, J., 1982: Analysis of long-period seismic waves excited by the May 18, 1980 eruption of Mount St. Helens - a terrestrial monopole? *J. Geophys. Res.*, **87**, 5422–5432.

Kanamori, H., Given, J., and Lay, T., 1984: Analysis of seismic body waves excited by the Mount St. Helens eruption of May 18, 1980. *J. Geophys. Res.*, **89**, 1856–1866.

Kanamori, H., Mori, J., and Harkrider, D. G., 1994: Excitation of atmospheric oscillations by volcanic eruptions. *J. Geophys. Res.*, **99**, 21947–21961.

Kaneshima, S., Kawakatsu, H., Matsubayashi, H., Sudo, Y., Tsutsui, T., Ohminato, T., Ito, H., Uhira, K., Yamasato, H., Oikawa, J., Takeo, M., and T.Iidaka, 1996: Mechanism of phreatic eruptions at Aso Volcano inferred from near-field broadband seismic observations. *Science*, **273**, 642–645.

Kawakatsu, H., Kaneshima, S., Matsubayashi, H., Ohminato, T., Sudo, Y., Tsutsui, T., Uhira, K., Yamasato, H., Ito, H., and Legrand, D., 2000: Aso94: Aso seismic observation with broadband instrumnents. *J. Volcanol. Geotherm. Res.*, **101**, 129–154.

Kawakatsu, H., Ohminato, T., Ito, H., Kuwahara, Y., Kato, T., Tsuruga, K., Honda, S., and Yomogida, K., 1992: Broad-band seismic observation at the Sakurajima volcano, Japan. *Geophys. Res. Lett.*, **19**, 1959–1962.

Keszthelyi, L., 1995: A preliminary thermal budget for lava tubes on the Earth and planets. *J. Geophys. Res.*, **100 (B10)**, 20411–20420.

Kieffer, S., 1981: Blast dynamics at Mount St. Helens on 18 May 1980. *Nature*, **291**, 568–570.

Kieffer, S. W., and Sturtevant, B., 1984: Laboratory studies of volcanic jets. *J. Geophys. Res.*, **89**, 8253–8268.

Kitov, I., Murphy, J., Kusnetsov, O., Barker, B., and Nedoshivin, N., 1997: An analysis of seismic and acoustic signals measured from a series of atmospheric and near-surface explosions. *Bull. Seismol. Soc. Am.*, **87**(6), 1553–1562.

Koyanagi, R. Y., Chouet, B., and Aki, K., 1987: Origin of volcanic tremor in Hawaii. Part I: compilation of seismic data from the Hawaiian Volcano Observatory, 1972 to 1985. In *Volcanism in Hawaii*, editors R. Decker, T. Wright, and R. Stauffer, 1221–1258. U.S. Geological Survey Prof. Paper 1350.

Kubotera, A., 1974: Volcanic tremors at Aso volcano. In *Physical Volcanology*, editors L. Civetta, P. Gasparini, G. Luongo, and A. Rapolla, 29–48. Elsevier, New York.

Kumagai, H., and Chouet, B., 1999: The complex frequencies of long-period seismic events as probes of fluid composition beneath volcanoes. *Geophys. J. Int.*, **138**, F7–F12.

Kumagai, H., and Chouet, B. A., 2000: Acoustic properties of a crack containing magmatic or hydrothermal fluids. *J. Geophys. Res.*, **105**, 25493–25512.

Kumagai, H., and Chouet, B. A., 2001: The dependence of acoustic properties of a crack on the resonance mode and geometry. *Geophys. Res. Lett.*, **28**(17), 3325–3328.

Kumagai, H., Chouet, B. A., and Dawson, P. B., 2005: Source process of a long-period event at Kilauea volcano, Hawaii. *Geophys. J. Int.*, **161**, 243–254.

Kumagai, H., Chouet, B. A., and Nakano, M., 2002: Temporal evolution of a hydrothermal system in Kusatsu-Shirane Volcano, Japan, inferred from the complex frequencies of long-period events. *J. Geophys. Res.*, **107**(B10), 2236. doi: 10.1029/2001JB000653.

Kumazawa, M., Imanishi, Y., Fukao, Y., Furumoto, M., and Yamamoto, A., 1990: A theory of spectral analysis based on the characteristic property of a linear dynamic system. *Geophys. J. Int.*, **101**, 613–630.

Lahr, J. C., Chouet, B. A., Stephens, C. D., Power, J. A., and Page, R. A., 1994: Earthquake classification, location, and error analysis in a volcanic environment: Implications for the magmatic system of the 1989-1990 eruptions of Redoubt Volcano, Alaska. *J. Volcanol. Geotherm. Res.*, **63**, 137–151.

Landau, L. D., and Lifshitz, E. M., 1987: *Fluid Mechanics.* Pergamon, New York, second edition.

Lane, S., and Gilbert, J., 2007: The Physics of Fluid Oscillations in Volcanic Systems. *EOS*, **88**, 29–30.

Lane, S. J., Chouet, B. A., Phillips, J. C., Dawson, P., Ryan, G. A., and Hurst, E., 2001: Experimental observations of pressure oscillations and flow regimes in an analogue volcanic system. *J. Geophys. Res.*, **106**, 6461–6476.

Langthjem, M. A., and Nakano, M., 2005: A numerical simulation of the hole-tone feedback cycle based on an axisymmetric discrete vortex method and Curle's equation. *Journal of Sound and Vibration*, **288**, 133–176.

Larsson, C., and Israelsson, S., 1991: Effects of meteorological conditions and source height on sound propagation near the ground. *Appl. Acoust.*, **33**(2).

Latter, J. H., 1979: Volcanological observations at Tongariro National Park, 2, Types and classification of volcanic earthquakes, 1976-1979. *N.Z. Dep. of Sci. and Ind. Res., Geophys. Div.*, **Rep. 150**, 60.

Lawrence, W. S., and Qamar, A., 1979: Hydraulic transients: A seismic source in volcanoes and glaciers. *Science*, **203**, 654–656.

Le Pichon, A., Blanc, E., Drob, D., Lambotte, S., Dessa, J. X., Lardy, M., Bani, P., and Vergniolle, S., 2005a: Infrasound monitoring of volcanoes to probe high-altitude winds. *J. Geophys. Res.*, **110**, D13106. doi:10.1029/2004JD005587.

Le Pichon, A., Guilbert, J., Vallee, M., Dessa, J., and Ulziibat, M., 2003: Infrasonic imaging of the Kunlun Mountains for the great 2001 China earthquake. *Geophys. Res. Lett.*, **30**(15).

Le Pichon, A., Guilbert, J., Vega, A., Garces, M., and Brachet, N., 2002: Ground-coupled air waves and diffracted infrasound from the Arequipa earthquake of June 23, 2001. *Geophys. Res. Lett.*, **29**(18).

Le Pichon, A., Herry, P., Mialle, P., Vergoz, J., Brachet, N., Garces, M., Drob, D., and Ceranna, L., 2005b: Infrasound associated with 2004-2005 large Sumatra earthquakes and tsunami. *Geophys. Res. Lett.*, **32**, L19802. doi: 10.1029/2005GL023893.

Le Pichon, A., Mialle, P., Guilbert, J., and Vergoz, J., 2006: Multistation infrasonic observations of the Chilean earthquake of 2005 June 13. *Geophys. J. Int.*, **167**(2), 838–844.

Le Pichon, A., Vergoz, J., Blanc, E., Guilbert, J., Ceranna, L., Evers, L., and Brachet, N., 2009: Assessing the performance of the International Monitoring Systems infrasound network: Geographical coverage and temporal variabilities. *J. Geophys. Res.*, **114**, D08112. doi:10.1029/2008JD010907.

Lees, J. M., and Crosson, R. S., 1989: Tomographic inversion for three-dimensional velocity structure at Mount St. Helens using earthquake data. *J. Geophys. Res.*, **94**, 5716–5728.

Leet, R. C., 1988: Saturated and subcooled hydrothermal boiling in groundwater-flow channels as a source of harmonic tremor. *J. Geophys. Res.*, **93**, 4835–4849.

Leighton, T. G., 1994: *The Acoustic Bubble.* Academic, New York.

Lighthill, M. J., 1954: On sound generated aerodynamically II. Turbulence as a source of sound. *Proc. Roy. Soc. London Ser. A*, **222**, 1–32.

Lighthill, M. J., 2001: *Waves in Fluids.* Cambridge Univ. Press, Cambridge, U.K., second edition.

Lilley, G. M., 1991: Jet Noise Classical Theory and Experiments. In *Aeroacoustics of Flight Vehicles: Theory and Practice, Vol. 1*, editor H. H. Hubbard. Acoustical Society of America.

Lingevitch, J. F., Collins, M. D., Dacol, D. K., Drob, D. P., Rogers, J. C. W., and Siegmann, W. L., 2002: A wide angle and high Mach number parabolic equation. *J. Acoust. Soc. Am.*, **111**(2), 729–734.

Lu, N. Q., Prosperetti, A., and Yoon, S. W., 1990: Underwater noise emissions from bubble clouds. *IEEE Journal of Oceanic Engineering*, **15(4)**, 275–281.

Magliozzi, B., Hanson, D. B., and Amiet, R., 1991: Propeller and Propfan Noise. In *Aeroacoustics of Flight Vehicles: Theory and Practice, Vol. 1*, editor H. H. Hubbard. Acoustical Society of America.

Major, J., Scott, W., Driedger, C., and Dzurisin, D., 2005: Mount St. Helens Erupts Again: Activity from September 2004 through March 2005. *USGS Fact Sheet 2005-3036.*

Malone, J., Debiasi, M., Little, J., and Samimy, M., 2009: Analysis of the spectral relationships of cavity tones in subsonic resonant cavity flows. *Physics of Fluids*, **21**, 055103.

Malone, S. D., 1983: Volcanic Earthquakes: Examples from Mount St. Helens. In *Earthquakes: Observations, theory and interpretation*, 436–455. Bologna, Italy, Societa Italiana di Fisica.

Marchetti, E., and Harris, A. J. L., 2008: Trends in activity at Pu‘u O‘o during 2001-2003: insights from the continuous thermal record. *Geological Society, London, Special Publications*, **307**, 85–101.

Marchetti, E., Ichihara, M., and Ripepe, M., 2004: Propagation of acoustic waves in a viscoelastic two-phase system: influence of gas bubble concentration. *J. Volcanol. Geotherm. Res.*, **137**(1-3), 93–108.

Marchetti, E., Ripepe, M., Harris, A. J. L., and Delle Donne, D., 2009: Tracing the differences between Vulcanian and Strombolian explosions using infrasonic and thermal radiation energy. *Earth Planet. Sci. Lett.*, **279**, 273–281.

Mastin, L. G., 2007: A user-friendly one-dimensional model for wet volcanic plumes. *Geochem. Geophys. Geosyst.*, **8**, 1–24.

Matoza, R. S., Fee, D., Garces, M. A., Seiner, J. M., Ramon, P. A., and Hedlin, M. A. H., 2009a: Infrasonic jet noise from volcanic eruptions. *Geophys. Res. Lett.*, L08303. doi:10.1029/2008GL036486.

Matoza, R. S., Garces, M. A., Chouet, B. A., D'Auria, L., Hedlin, M. A. H., De Groot-Hedlin, C., and Waite, G. P., 2009b: The source of infrasound associated with long-period events at Mount St. Helens. *J. Geophys. Res.*, **114**. doi:10.1029/2008JB006128.

McChesney, P. J., Couchman, M. R., Moran, S. C., Lockhart, A. B., Swinford, K. J., and Husen, R. G. L., 2008: Seismic monitoring changes and the remote deployment of seismic stations (Seismic Spider) at Mount St. Helens. In *A Volcano Rekindled: The Renewed Eruption of Mount St. Helens, 2004-2006*, editors D. R. Sherrod, W. E. Scott, and P. H. Stauffer. U.S. Geological Survey Professional Paper 1750.

McCormack, D., Bass, H., Garces, M., and Yepes, H., 2005: Acoustic surveillance for hazardous eruptions (ASHE). *J. Acoust. Soc. Am.*, **117**, 2419.

McNutt, S. R., 2000: Seismic Monitoring. In *Encyclopedia of Volcanoes*, editor H. Sigurdsson, 1095–1119. Academic Press.

McNutt, S. R., 2005: Volcanic Seismology. *Annu. Rev. Earth Planet. Sci.*, **32**, 461–491.

Mikumo, T., 1968: Atmospheric pressure waves and tectonic deformation associate with the Alaskan earthquake of March 28, 1964. *J. Geophys. Res.*, **73**(6), 20092025.

Miller, A., Stewart, R., White, R., Luckett, R., Baptie, B., Aspinall, W., Latchman, J., Lynch, L., and Voight, B., 1998: Seismicity associated with dome growth and collapse at the Soufriere Hills Volcano Montserrat. *Geophys. Res. Lett.*, **25 (18)**, 3401–3404.

Moran, S., McChesney, P., and Lockhart, A., 2008a: Seismicity and infrasound associated with explosions at Mount St. Helens, 2004-2005. In *A Volcano Rekindled: The Renewed Eruption of Mount St. Helens, 2004-2006*, editors D. R. Sherrod, W. E. Scott, and P. H. Stauffer. U.S. Geological Survey Professional Paper 1750.

Moran, S. C., 2003: Multiple seismogenic processes for high-frequency earthquakes at Katmai National Park, Alaska: Evidence from stress tensor inversions of fault-plane solutions. *Bull. Seis. Soc. Am.*, **93**, 94–108.

Moran, S. C., 2005: Overview of seismicity associated with the 2004-2005 Eruption of Mount St. Helens. *Session V52B, AGU Fall Meeting.*

Moran, S. C., Malone, S. D., Qamar, A. I., Thelen, W., Wright, A. K., and Caplan-Auerback, J., 2008b: 2004-2005 seismicity associated with the renewed dome-building eruption of Mount St. Helens. In *A Volcano Rekindled: The Renewed Eruption of Mount St. Helens, 2004-2006*, editors D. R. Sherrod, W. E. Scott, and P. H. Stauffer. U.S. Geological Survey Professional Paper 1750.

Moran, S. C., Matoza, R. S., Garces, M. A., Hedlin, M. A. H., Bowers, D., Scott, W. E., Sherrod, D. R., and Vallance, J. W., 2008: Seismic and acoustic recordings of an unusually large rockfall at Mount St. Helens, Washington. *Geophys. Res. Lett.*, **35**(19). doi:10.1029/2008GL035176.

Morrissey, M. M., and Chouet, B. A., 1997a: Burst Conditions of Explosive Volcanic Eruptions Recorded on Microbarographs. *Science*, **275**, 1290–1293.

Morrissey, M. M., and Chouet, B. A., 1997b: A numerical investigation of choked flow dynamics and its application to the triggering mechanism of long-period events at Redoubt Volcano, Alaska. *J. Geophys. Res.*, **102**, 7965–7983.

Morrissey, M. M., and Chouet, B. A., 2001: Trends in long-period seismicity related to magmatic fluid compositions. *J. Volcanol. Geotherm. Res.*, **108**, 265–281.

Mullineaux, D., and Crandell, D., 1981: The Eruptive History of Mount St. Helens. In *The 1980 eruptions of Mount St. Helens, Washington*, editors P. Lipman, and D. Mullineaux, 3–15. USGS Professional Paper 1250.

Mutschlecner, J., and Whitaker, R., 2005: Infrasound from earthquakes. *J. Geophys. Res.*, **110**(D1). doi:10.1029/2004JD005067.

Nakano, M., Kumagai, H., Chouet, B., and Dawson, P., 2007: Waveform inversion of volcano-seismic signals for an extended source. *J. Geophys. Res.*, **112**, B02306. doi:10.1029/2006JB004490.

Nakano, M., Kumagai, H., Kumazawa, M., Yamaoka, K., and Chouet, B. A., 1998: The excitation and characteristic frequency of the long-period volcanic event: An approach based on an inhomogeneous autoregressive model of a linear dynamic system. *J. Geophys. Res.*, **103**, 10031–10046.

Neuberg, J., Luckett, R., Baptie, B., and Olsen, K., 2000: Models of tremor and low-frequency earthquake swarms on Montserrat. *J. Volcanol. Geotherm. Res.*, **101**, 83–104.

Neuberg, J., Luckett, R., Ripepe, M., and Braun, T., 1994: Highlights from a seismic broadband array on Stomboli Volcano. *Geophys. Res. Lett.*, **21**, 749–752.

Neuberg, J., and Pointer, T., 2000: Effects of volcano topography on seismic broadband waveforms. *Geophys. J. Int.*, **143**, 1–14.

Neuberg, J. W., Tuffen, H., Collier, L., Green, D., Powell, T., and Dingwell, D., 2006: The trigger mechanism of low-frequency earthquakes on Montserrat. *J. Volcanol. Geotherm. Res.*, **153**, 37–50.

Newhall, C. G., and Self, S., 1982: The Volcanic Explosivity Index: An estimate of explosive magnitude for historical volcanism. *J. Geophys. Res.*, **87**(C2), 1231–1238.

Nishimura, T., and Chouet, B., 2003: A numerical simulation of magma motion, crustal deformation, and seismic radiation associated with volcanic eruptions. *Geophys. J. Int.*, **153**, 699–718.

Nyborg, W. L., Burkhard, M. D., and Schilling, H. K., 1952: Acoustical characteristics of jet-edge and jet-edge-resonator systems. *J. Acoust. Soc. Am.*, **24 (3)**, 293304.

Obara, K., 2002: Nonvolcanic deep tremor associated with subduction in southwest Japan. *Science*, **296**, 1679–1681.

Ogden, D. E., Wohletz, K. H., Glatzmaier, G. A., and Brodsky, E. E., 2008: Numerical simulations of volcanic jets: Importance of vent overpressure. *J. Geophys. Res.*, **113**, B02204. doi:10.1029/2007JB005133.

Ohminato, T., 2006: Characteristics and source modeling of broadband seismic signals associated with the hydrothermal system at Satsuma-Iwojima volcano, Japan. *J. Volcanol. Geotherm. Res.*, **158**(3-4), 467–490.

Ohminato, T., and Chouet, B. A., 1997: A free-surface boundary condition for including 3D topography in the finite-difference method. *Bull. Seismol. Soc. Am.*, **87**, 494–515.

Ohminato, T., Chouet, B. A., Dawson, P., and Kedar, S., 1998: Waveform inversion of very long period impulsive signals associated with magmatic injection beneath Kilauea Volcano, Hawaii. *J. Geophys. Res.*, **103**, 23839–23862.

Omer, G. C., 1950: Volcanic Tremor (Part Two: The Theory of Volcanic Tremor). *Bull. Seismol. Soc. Am.*, **40**, 175–194.

Omori, F., 1912: The Eruptions and Earthquakes of the Asama-Yama. *Bulletin of the Imperial Earthquake Investigation Commitee*, **6 (1)**.

Oshima, H., and Maekawa, T., 2001: Excitation process of infrasonic waves associated with Merapi-type pyroclastic flow as revealed by a new recording system. *Geophys. Res. Lett.*, **28**, 1099–1102.

Ostashev, V. E., 1997: *Acoustics in Moving Inhomogeneous Media.* E & FN SPON, London.

Pallister, J. S., Cashman, K. V., and Hagstrum, J. T., 2008: Conduit-margin faulting at Mount St. Helens - A seismogenic process? *Eos Trans. AGU*, **89**(53), Fall Meet. Suppl., Abstract V43E–2186.

Pallister, J. S., Thornber, C. R., Cashman, K. V., Clynne, M. A., Lowers, H. A., Mandeville, C. W., Brownfield, I. K., and Meeker, G. P., 2008: Petrology of the 2004-2006 Mount St. Helens lava dome-implications for magmatic plumbing and eruption triggering. In *A Volcano Rekindled: The Renewed Eruption of Mount St. Helens, 2004-2006*, editors D. R. Sherrod, W. E. Scott, and P. H. Stauffer. U.S. Geological Survey Professional Paper 1750.

Park, J., Garces, M., Fee, D., and Pawlak, G., 2008: Collective bubble oscillations as a component of surf infrasound. *J. Acoust. Soc. Am.*, **123 (5)**, 25062512.

Perret, F. A., 1950: *Volcanological Observations.* Carnegie Inst. Wash. Publ.

Petersen, T., 2007: Swarms of repeating long-period earthquakes at Shishaldin Volcano, Alaska, 20012004. *J. Volcanol. Geotherm. Res.*, **166**, 177192.

Petersen, T., DeAngelis, S., Tytgat, G., and McNutt, S. R., 2006: Local infrasound observations of large ash explosions at Augustine Volcano, Alaska, during January 11-28, 2006. *Geophys. Res. Lett.*, **33**, L12303. doi:10.1029/2006GL026491.

Petersen, T., and McNutt, S. R., 2007: Seismo-acoustic signals associated with degassing explosions recorded at Shishaldin Volcano, Alaska, 2003-2004. *Bull. Volcanol.*, **69**(5), 527–536.

Piercy, J., Embleton, T., and Sutherland, L., 1977: Review of noise propagation in the atmosphere. *J. Acoust. Soc. Am.*, **61**(6), 1403–1418.

Pinatubo Volcano Obsevatory Team, 1991: Lessons from a major eruption: Mt. Pinatubo, Philippines. *EOS, Trans. Am. Geophys. Union*, **72**, 545–555.

Poland, M., Miklius, A., Orr, T., Sutton, J., Thornber, C., and Wilson, D., 2008: New episodes of volcanism at Kilauea Volcano, Hawaii. *EOS, Trans. AGU*, **89**(5).

Pope, S. B., 2005: *Turbulent Flows.* Cambridge Univ. Press, New York.

Press, F., and Ewing, M., 1951: Ground roll coupling to atmospheric compressional waves. *Geophysics*, **16**, 416–438.

Pringle, P., 1993: *Roadside geology of the Mount St. Helens national volcanic monument and vicinity.* Washington Department of Natural Resources Information Circular 88.

Raspet, R., Webster, J., and Dillion, K., 2006: Framework for wind noise studies. *J. Acoust. Soc. Am.*, **119 (2)**, 834843.

Raspet, R., Yu, J., and Webster, J., 2008: Low frequency wind noise contributions in measurement microphones. *J. Acoust. Soc. Am.*, **123 (3)**, 1260–1269.

Rayleigh, J. W. S., 1976: *The Theory of Sound, Volume 2.* Dover Classics of Science and Mathematics, second edition.

Reed, J. W., 1987: Air-pressure waves from Mount St. Helens eruptions. *J. Geophys. Res.*, **92**, 11979–11992.

Reynolds, O., 1873: On the refraction of sound by the atmosphere. *Proc. R. Soc. London*, **22**, 531548.

Rice, J. A., 1995: *Mathematical Statistics and Data Analysis.* Duxbury, Belmont, Calif., second edition.

Richards, A. F., 1963: Volcanic sounds: Investigation and analysis. *J. Geophys. Res.*, **68**, 919–928.

Riedel, K., and Sidorenko, A., 1995: Minimum bias multiple taper spectral estimation. *IEEE Trans. Signal Process.*, **43**(1), 188–195.

Ripepe, M., De Angelis, S., Lacanna, G., Poggi, P., Williams, C., Marchetti, E., Delle Donne, D., and Ulivieri, G., 2009: Tracking Pyroclastic Flows at Soufriere Hills Volcano. *Eos Trans. AGU*, **90**(2), 229230.

Ripepe, M., and Marchetti, E., 2002: Array tracking of infrasonic sources at Stromboli volcano. *Geophys. Res. Lett.*, **29(22)**, 33–1–33–4.

Ripepe, M., Marchetti, E., and Ulivieri, G., 2007: Infrasonic monitoring at Stromboli volcano during the 2003 effusive eruption: Insights on the explosive and degassing process of an open conduit system. *J. Geophys. Res.*, **112**, B09207. doi:10.1029/2006JB004613.

Ripepe, M., Poggi, P., Braun, T., and Gordeev, E., 1996: Infrasonic waves and volcanic tremor at Stromboli. *Geophys. Res. Lett.*, **63**, 181–184.

Rockwell, D., and Naudascher, E., 1978: Review - Self-sustaining oscillations of flow past cavities. *ASME Trans. J. Fluids Eng.*, **100**, 152–165.

Rockwell, D., and Naudascher, E., 1979: Self-sustained oscillations of impinging free shear layers. *Ann. Rev. Fluid Mech.*, **11**, 67–94.

Roman, D. C., and Cashman, K. V., 2006: The origin of volcano-tectonic earthquake swarms. *Geology*, **34**(6), 457–460.

Roman, D. C., De Angelis, S., Latchman, J. L., and White, R., 2008: Patterns of volcanotectonic seismicity and stress during the ongoing eruption of the Soufriere Hills Volcano, Montserrat (1995-2007). *J. Volcanol. Geotherm. Res.*, **173**, 230–244.

Roman, D. C., Neuberg, J., and Luckett, R. R., 2006: Assessing the likelihood of volcanic eruption through analysis of volcanotectonic earthquake fault-plane solutions. *Earth Planet. Sci. Lett.*, **248**, 244–252.

Rossiter, J. E., 1964: Wind-tunnel experiments on the flow over rectangular cavities at subsonic and transonic speeds. *Ministry of Aviation Reports and Memoranda*, (3438).

Ruiz, M. C., Lees, J. M., and Johnson, J. B., 2006: Source constraints of Tungurahua volcano explosion events. *Bull. Volcanol.*, **68**, 480–490.

Sabatier, J., and Raspet, R., 1988: Investigation of possibility of damage from the acoustically coupled seismic waveform from blast and artillery. *J. Acoust. Soc. Am.*, **84**(4), 1478–1482.

Sabatier, J. M., Bass, H. E., Bolen, L. N., and Attenborough, K., 1986: Acoustically induced seismic waves. *J. Acoust. Soc. Am.*, **80**, 646649.

Sahetapy-Engel, S. T., Harris, A. J. L., and Marchetti, E., 2008: Thermal, seismic and infrasound observations of persistent explosive activity and conduit dynamics at Santiaguito lava dome, Guatemala. *J. Volcanol. Geotherm. Res.*, **173**(1-2), 1–14.

Sakai, T., Yamasato, H., and Uhira, K., 1996: Infrasound accompanying C-type tremor at Sakurajima volcano. *Bull. Volcanol. Soc. Japan*, **41**, 181–185 (in Japanese).

Scheu, B., Kern, H., Spieler, O., and Dingwell, D., 2006: Temperature dependence of elastic P- and S-wave velocities in porous Mt. Unzen dacite. *J. Volcanol. Geotherm. Res.*, **153**(1-2), 136–147.

Schilling, S. P., Thompson, R. A., Messerich, J. A., and Iwatsubo, E. Y., 2008: Use of digital aerophotogrammetry to determine rates of lava dome growth, Mount St. Helens, 2004-2005. In *A Volcano Rekindled: The Renewed Eruption of Mount St. Helens, 2004-2006*, editors D. R. Sherrod, W. E. Scott, and P. H. Stauffer. U.S. Geological Survey Professional Paper 1750.

Scott, W., Sherrod, D., and Gardner, C., 2008: Overview of 2004 to 2005, and continuing, eruption of Mount St. Helens, Washington. In *A Volcano Rekindled: The Renewed Eruption of Mount St. Helens, 2004-2006*, editors D. R. Sherrod, W. E. Scott, and P. H. Stauffer. U.S. Geological Survey Professional Paper 1750.

Seiner, J. M., 1984: Advances in high speed jet aeroacoustics. *AIAA Pap.*, **84-2275**.

Seiner, J. M., Gui, L. G., Ukeiley, L., and Jansen, B. J., 2003: Particle laden jet PIV experiments and simulations. *JANNAF Spirits*, **4B**.

Shaw, H. R., 1972: Viscosities of magmatic silicate liquids: an empirical method of prediction. *Am. J. Sci.*, **272**, 870–893.

Shields, F. D., 2005: Low-frequency wind noise correlation in microphone arrays. *J. Acoust. Soc. Am.*, **117**, 3489–3496.

Shima, M., 1958: On the Second volcanic micro-tremor at volcano Aso. *Bull. Disaster Prev. Res. Inst. Kyoto Univ.*, **22**, 1–6.

Shimozuru, D., 1961: Volcanic microseisms - Discussion on the origin. *Bull. Volcanol. Soc. Jpn.*, **5**, 154–162.

Simkin, T., and Siebert, L., 1994: *Volcanoes of the World.* Smithsonian Institution, Washington DC, second edition.

Snodgrass, J. M., and Richards, A. F., 1956: Observations of undwerwater volcanic acoustics at Barcena volcano, San Benedicto Island, Mexico, and in Shelikof Strait, Alaska. *Trans. Am. Geophys. Union*, **37**, 97–104.

Steffke, A., Fee, D., Garces, M. A., and Harris, A., 2008: Detecting plume heights and eruption intensities using thermal infrared satellite data at Tungurahua Volcano. in prep.

Steinberg, G. S., and Steinberg, A. S., 1975: On Possible Causes of Volcanic Tremor. *J. Geophys. Res.*, **80**, 1600–1604.

Stephens, C. D., and Chouet, B. A., 2001: Evolution of the December 14, 1989 precursory long-period event swarm at Redoubt Volcano, Alaska. *J. Volcanol. Geotherm. Res.*, **109**, 133–148.

Strachey, R., 1888: On the air waves and sounds caused by the eruption of Krakatoa in August, 1883. In *Krakatau 1883 (published 1983)*, editors T. Simkin, and R. S. Fiske, 368–374. Smithsonian Institution Press.

Stump, B., 1985: Constraints on explosive sources with spall from near-source waveforms. *Bull. Seismol. Soc. Am.*, **75**(2), 361–377.

Sutherland, L. C., and Bass, H. E., 2004: Atmospheric absorption in the atmosphere up to 160 km. *J. Acoust. Soc. Am.*, **115**, 1012–1032.

Swift, G. W., 2007: Thermoacoustics. In *Springer Handbook of Acoustics*, editor T. Rossing, 239–255. Springer, New York.

Sylvander, M., C., P., Benahmed, S., and Fels, J. F., 2007: Seismoacoustic recordings of small earthquakes in the Pyrenees: Experimental results. *Bull. Seismol. Soc. Am.*, **97**(1, Part B Sp. Iss. S), 294–304.

Tahira, M., 1982: A Study of the Infrasonic Wave in the Atmosphere: (II) Infrasonic Waves Generated by the Explosions of the Volcano Sakura-jima. *Journal of the Meteorological Society of Japan*, **60**, 896–907.

Tahira, M., Nomura, M., Sawada, Y., and Kamo, K., 1996: Infrasonic and Acoustic-Gravity Waves generated by the Mount Pinatubo Eruption of June 15, 1991. In *Fire and Mud: Eruptions and Lahars of Mount Pinatubo, Philippines*, editors C. G. Newhall, and R. S. Punongbayan, 1095–1119. USGS.

Tam, C., Golebiowski, M., and Seiner, J., 1996: On the two components of turbulent mixing noise from supersonic jets. *AIAA*, **96-1716**.

Tam, C. K. W., 1995: Supersonic jet noise. *Annu. Rev. Fluid Mech.*, **27**, 17–43.

Tam, C. K. W., 1998: Jet noise: Since 1952. *Theoret. Comput. Fluid Dynamics*, **10**, 393–405.

Tam, C. K. W., 2004: Computational aeroacoustics: An overview of computational challenges and applications. *International Journal of Computational Fluid Dynamics*, **18**(6), 547–567.

Tempest, A., and Flett, J. S., 1903: Report on the Eruptions of the Soufriere, in St. Vincent, in 1902, and on a Visit to Montagne Pelee, in Martinique - Part I. *Philosphical Transactions of the Royal Society of London. Series A.*, **200**, 353–553.

Thelen, W. A., Crosson, R. S., and Creager, K. C., 2008: Absolute and relative locations of earthquakes at Mount St. Helens, Washington using continuous data: Implications for magmatic processes. In *A Volcano Rekindled: The Renewed*

Eruption of Mount St. Helens, 2004-2006, editors D. R. Sherrod, W. E. Scott, and P. H. Stauffer. U.S. Geological Survey Professional Paper 1750.

Thiéry, R., and Mercury, L., 2009: Explosive properties of water in volcanic and hydrothermal systems. *J. Geophys. Res.*, **114**, B05205. doi:10.1029/2008JB005742.

Tilling, R. L., Topinka, L. T., and Swanson, D. A., 1984: *Eruptions of Mount St. Helens: Past, Present, and Future.* U.S. Geological Survey.

Tuffen, H., and Dingwell, D., 2005: Fault textures in volcanic conduits: evidence for seismic trigger mechanisms during silicic eruptions. *Bull. Volcanol.*, **67**(4), 370–387.

Tuffen, H., Smith, R., and Sammonds, P. R., 2008: Evidence for seismogenic fracture of silicic magma. *Nature*, **453**(7194), 511–514.

USGS, 2000: Mount St. Helens - From the 1980 Eruption to 2000. *USGS Fact Sheet 036-00.*

Vallance, J. W., Schneider, D. J., and Schilling, S. P., 2008: Growth of the 2004-2006 lava-dome complex at Mount St. Helens. In *A Volcano Rekindled: The Renewed Eruption of Mount St. Helens, 2004-2006*, editors D. R. Sherrod, W. E. Scott, and P. H. Stauffer. U.S. Geological Survey Professional Paper 1750.

Van Trees, H. L., 2002: *Optimum Array Processing - Part IV, Detection, Estimation, and Modulation Theory.* Wiley-Interscience.

van Vossen, R., Robertsson, J., and Chapman, C., 2002: Finite-difference modeling of wave propagation in a fluid-solid configuration. *Geophysics*, **67**(2), 618–624.

van Wijngaarden, L., 1972: One-dimensional flow of liquids containing small gas bubbles. *Annu. Rev. Fluid Mech.*, **4**, 369–396.

Vergniolle, S., and Brandeis, G., 1994: Origin of the sound generated by Strombolian explosions. *Geophys. Res. Lett.*, **21**, 1959–1962.

Vergniolle, S., and Brandeis, G., 1996: Strombolian explosions 1. A large bubble breaking at the surface of a lava column as a source of sound. *J. Geophys. Res.*, **101**, 20433–20447.

Vergniolle, S., Brandeis, G., and Mareschal, J. C., 1996: Strombolian explosions 2. Eruption dynamics determined from acoustic measurements. *J. Geophys. Res.*, **101**, 20449–20466.

Vergniolle, S., and Caplan-Auerbach, J., 2006: Basaltic thermals and Subplinian plumes: Constraints from acoustic measurements at Shishaldin volcano, Alaska. *Bull. Volcanol.*, **68**, 611–630.

Viktorov, I. A., 1967: *Rayleigh and Lamb Waves: Physical Theory and Applications.* Plenum, New York.

Virieux, J., 1986: P-SV wave propagation in heterogeneous media: Velocity-stress finite-difference method. *Geophysics*, **51**(4), 889–901.

Voight, B., 1981: Time scale for the first moments of the May 18 eruption. In *The 1980 eruptions of Mount St. Helens, Washington*, editors P. Lipman, and D. Mullineaux, 69–86. USGS Professional Paper 1250.

Waite, G. P., Chouet, B. A., and Dawson, P. B., 2008: Eruption dynamics at Mount St. Helens imaged from broadband seismic waveforms: Interaction of the shallow magmatic and hydrothermal systems. *J. Geophys. Res.*, **113**(B2). doi:10.1029/2007JB005259.

Waite, G. P., and Moran, S. C., 2009: V_p Structure of Mount St. Helens, Washington, USA, imaged with local earthquake tomography. *J. Volcanol. Geotherm. Res.*, **182**, 113–122.

Waxler, R., and Gilbert, K. E., 2006: The radiation of atmospheric microbaroms by ocean waves. *J. Acoust. Soc. Am.*, **119**(5), 2651–2664.

Waxler, R., Gilbert, K. E., and Talmadge, C., 2008: A theoretical treatment of the long range propagation of impulsive signals under strongly ducted nocturnal conditions. *J. Acoust. Soc. Am.*, **124**(5), 2742–2754.

Waxler, R., Talmadge, C., Dravida, S., and Gilbert, K., 2006: The near-ground structure of the nocturnal sound field. *J. Acoust. Soc. Am.*, **119**(1), 86–95.

Webb, S., 1997: Silicate melts: relaxation, rheology, and the glass transition. *Reviews of Geophysics*, **35**(2), 191–218.

Wiemer, S., and McNutt, S. R., 1997: Variations in the frequency-magnitude distribution with depth in two volcanic areas: Mount St. Helens, Washington, and Mt Spurr, Alaska. *Geophys. Res. Lett.*, **24**(2), 189–192.

Wilcox, R. E., 1947: Activity of Paricutin volcano from September 18 to November 30, 1946. *Trans. Am. Geophys. Union*, **23**, 567–572.

Willis, M., Garces, M., Hetzer, C., and Businger, S., 2004: Infrasonic observations of open ocean swells in the Pacific: Deciphering the song of the sea. *Geophys. Res. Lett.*, **31**, L19303. doi:10.1029/2004GL020684.

Wilson, C. R., and Forbes, R. B., 1969: Infrasonic Waves from Alaskan Volcanic Eruptions. *J. Geophys. Res.*, **74**, 4511–4522.

Wilson, C. R., Nichparenko, S., and Forbes, R. B., 1966: Evidence of two sound channels in the polar atmosphere from infrasonic observations of the eruption of an Alaskan volcano. *Nature*, **5045**, 163–165.

Wilson, L., 1976: Explosive Volcanic Eruptions-III. Plinian Eruption Columns. *Geophys. J. R. Astr. Soc.*, **45**, 543–556.

Wilson, P. S., and Roy, R. A., 2008: An audible demonstration of the speed of sound in bubbly liquids. *Am. J. Phys.*, **76**(10), 975–981.

Wilson, T. A., Beavers, G. S., DeCoster, M. A., , Holger, D. K., and Regenfuss, M. D., 1970: Experiments on the fluid mechanics of whistling. *J. Acoust. Soc. Am.*, **50**, 366–372.

Wood, A. B., 1964: *A Textbook of Sound*. G. Bell, London, third edition.

Woulff, G., and McGetchin, T. R., 1976: Acoustic noise from volcanoes: Theory and experiments. *Geophys. J. R. Astr. Soc.*, **45**, 601–616.

Yamasato, H., 1997: Quantitative analysis of pyroclastic flows using infrasonic and seismic data at Unzen Volcano, Japan. *J. Phys. Earth*, **45**, 397–416.

Yamasato, H., 1998: Nature of infrasonic pulse accompanying low frequency earthquake at Unzen Volcano, Japan. *Bull. Volcanol. Soc. Japan*, **43**, 1–13.

Yamasato, H., Miyamura, J., Mori, H., Usui, Y., Sakuma, K., Watanabe, A., Sato, J., Takahashi, Y., and Sakai, T., 2002: Eruptive activity inferred from infrasound associated with the 2000 eruption of Usu Volcano (in Japanese, English abstract). *Bull. Volcanol. Soc. Japan*, **47**, 255262.

Yokoo, A., , Tameguri, T., and Iguchi, M., 2009: Swelling of a lava plug associated with a Vulcanian eruption at Sakurajima Volcano, Japan, as revealed by infrasound record: case study of the eruption on January 2, 2007. *Bull. Volcanol.*, **71**, 619630.

Yokoo, A., and Ishihara, K., 2007: Analysis of pressure waves observed in Sakurajima eruption movies. *Earth Planets Space*, **59**, 177–181.

Yokoo, A., and Taniguchi, H., 2004: Application of video image processing to detect volcanic pressure waves: A case study on archived images of Aso Volcano, Japan. *Geophys. Res. Lett.*, **31**, L23604. doi:10.1029/2004GL021183.

Yoon, S. W., Crum, L. A., Prosperetti, A., and Lu, N. Q., 1991: An investigation of the collective oscillations of a bubble cloud. *J. Acoust. Soc. Am.*, **89(2)**, 700–706.

Zumberge, M. A., Berger, J., Hedlin, M. A. H., Husmann, E., Nooner, S., Hilt, R., and Widmer-Schnidrig, R., 2003: An optical fiber infrasound sensor: A new lower limit on atmospheric pressure noise between 1 and 10 Hz. *J. Acoust. Soc. Am.*, **113**, 2474–2479.